THESIS FOR THE DEGREE OF DOCTOR OF PHILOSOPHY
IN
THERMO AND FLUID DYNAMICS

Spatial Decompositions of a Fully-developed Turbulent Round Jet Sampled with Particle Image Velocimetry

MAJA WÄNSTRÖM

Department of Applied Mechanics

CHALMERS UNIVERSITY OF TECHNOLOGY

Göteborg, Sweden, 2009

Spatial Decompositions of a Fully-developed Turbulent Round Jet Sampled with Particle Image Velocimetry

MAJA WÄNSTRÖM
ISBN 978-91-7385-352-1

Doktorsavhandling vid Chalmers tekniska högskola
Ny serie nr 3033
ISSN 0346-718X

Division of Fluid Dynamics
Department of Applied Mechanics
Chalmers University of Technology
SE-412 96 Göteborg, Sweden

Tel.: +46-(0)31-7721000
Fax: +46-(0)31-180976

Printed at Chalmers Reproservice
Göteborg, Sweden 2009

Spatial Decompositions of a Fully-developed Turbulent Round Jet Sampled with Particle Image Velocimetry

MAJA WÄNSTRÖM

Division of Fluid Dynamics
Department of Applied Mechanics
Chalmers University of Technology

Abstract

Spatial decompositions of the turbulence in a far, axisymmetric jet at exit Reynolds number of 20, 000 have been performed. Equilibrium similarity theory applied to the two-point Reynolds stresses has shown that the turbulence statistics in the far, fully developed region of an axisymmetric jet should be independent of origin in the streamwise direction when evaluated on the similarity coordinates system $\xi = ln[(x - x_o)D]$, $\eta = r/\delta_{1/2}(x)$. The homogeneity was confirmed in a planar PIV experiment that measured the streamwise and radial velocity components in a (0.4m by 0.7 m) composite field-of-view intersecting the centerline. The homogeneity allowed for spatial spectra to be estimated in the streamwise direction. Radial Proper Orthogonal Decomposition was subsequently performed based on the two-point cross-spectral tensor elements. The obtained eigenspectra and eigenvectors reflect the high-dimensional nature of of the far jet as the rates of convergence to the available spectral density decreased with increasing wavenumber.

In addition, radial Proper Orthogonal Decomposition was performed on three-component stereoscopic PIV velocity data from cross-planes in the far turbulent jet. Fourier series expansion of the azimuthally homogeneous turbulence again highlighted the dynamic complexity of the far jet. In particular, it was shown that several azimuthal modes are needed to expand the primary Reynolds shear stress which is associated with the process by which the turbulence extracts kinetic energy from the mean flow gradient. This in turn implies that the far jet turbulence should not be expected to be dominated by any one azimuthal mode, as has been inferred from linear stability analysis.

Keywords: axisymmetric turbulent jet, equilibrium similarity, PIV, spatial spectral analysis, proper orthogonal decomposition,

ACKNOWLEDGMENTS

This work was conducted at the Division of Fluid Dynamics at Chalmers University of Technology and at the Technical University of Denmark.

I would like to express my sincere gratitude to Professor William K.George for his never-ending support and enthusiasm throughout the course of this work.

I would like to thank Associate Professor Knud Erik Meyer for generously making the Fluid Mechanics Laboratory available to me and for the all the support he has provided in Denmark.

In addition, I would like to acknowledge my helpful current and former research group members, Murat Tutkun, Farzad Shiri, Lars-Uno Axelsson, Carlos Arroyoos and also Docent Gunnar Johansson.

I also would like to thank Ulla Lindberg-Thieme and Monica Vargman for their administrative support and supportive attitude.

Financial support from the Swedish Research Council has provided the financing for this work and I would like to express my gratitude to the Swedish tax-payers and the Swedish government for making this possible.

My heartfelt sense of gratitude goes to my family for their support and understanding.

CONTENTS

1. INTRODUCTION

This introductory chapter contains, a contextual rationale for the work attempted and accomplished in this dissertation and a brief paragraph describing the structure of this document.

1.1 Rationale and objectives of this work

Turbulent jets form one of the most important classes of turbulent free shear flows. Not only are they technologically important in their own right because of their omnipresence, they are among the few flows for which we have found similarity solutions that appear to describe the flows we can produce in the laboratory. This means that we can readily spot the role played by boundary and upstream conditions, and as well any errors in measurement or changes to the flow introduced by the measurement techniques. This is very important for the evaluation and development of turbulence models, which are primarily local and presumed to be independent of a particular flow, and especially independent of boundary conditions.

There have been a number of important developments over the past two decades which motivated this dissertation. First, it was the recognition by George [1] that turbulent free shear flows could retain an asymptotic dependence on their upstream (or initial) conditions. The fact of this now seems to be beyond dispute (Cater and Soria [2], Wong et al.[3], Slessor et al. [4]). The second important development was the recognition that the axisymmetric jet flow in particular admitted to two-point similarity solutions; i.e., the two-point Reynolds stress equations themselves had Reynolds number independent similarity solutions (Ewing and George[5], Ewing [6], Ewing et al.[7]). This meant that the axisymmetric jet belonged to a very small class of turbulent shear flows for

which all the scales of motion could be collapsed with a single similarity length scale, and was one of only two flows for which the local Reynolds number was constant during decay (the plane wake is the other).

The two-point similarity analysis deduced that the streamwise coordinate scaled as the logarithm of the downstream distance, while the radial coordinate scaled with the local half-width. These had the immediate consequence that the asymptotic jet was homogeneous in the logarithmic streamwise coordinate, and homogeneous periodic in the azimuthal coordinate. Gamard et al. [8] provided the first experimental evidence for that the azimuthal similarity was in fact observed in the two-point correlations and cross-spectra. Subsequently, Ewing et al. [7] provided the first experimental evidence for the logarithmic scaling of the axisymmetric coordinate and for the homogeneity of the jet when represented in it. This experimental evidence consisted of correlations computed from PIV data obtained in a jet at very low Reynolds number (2000) based on jet exit diameter and velocity), and from correlations computed from simultaneous hot-wire/LDA data at higher Reynolds number (33,000) but only along the jet centerline. One of the goals of this dissertation was further test the two-point similarity hypothesis by carrying out full-field PIV measurements at higher Reynolds number. Another was to use stereo PIV to repeat and extend the measurements of Gamard et al.[8] , both to test the sensitivity of the results to the particular domain and to eliminate any bias arising from the large rake of 139 hotwires which was used to obtain them.

There are a number of further consequences of the single and two-point similarity theories described above, some of which have been noted before, others of which are new, none of which have been tested. The most important of these further consequences was that the homogeneity in the logarithmic streamwise coordinate implied that there was no need to carry out a standard POD (Proper Orthogonal Decomposition) analysis, since the POD integral could be solved analytically. In fact, the eigenfunctions can be shown to be harmonic functions (Ewing [6], George [9]) of the logarithmic streamwise coordinate with continuous (dimensionless) wavenumber, say κ. Statistical stationarity in time implies directly that the POD eigenfunctions are also harmonic functions in time with continuous frequency, say ω (Lumley [10], George [11]); while the fact that the azimuthal coordinate is periodic homogenous implies that the POD eigenfunctions must also be harmonic, but at integer

multiples of 2π.

Thus, *if the two-point theory and its implications for the streamwise decomposition can be confirmed*, the remaining representation problem reduces to simply the radial coordinate, the individual contributions to the velocity field of the eigenfunctions being themselves functions of κ, ω and m. Decomposition of the Navier-Stokes equations results in non-linear coupled equations in the single variable $\eta = r/\delta_{1/2}$ with κ, ω and m as parameters. Linearization of these in turn yields equations which closely resemble the parallel stability analysis of Batchelor and Gill [12], Michalke [13] and others, but with the important difference that the growth of the jet is fully represented without the need for any localization or perturbation analysis (Leib and Goldstein [14], Wu and Huerre [15]). A primary objective of this dissertation was to test the fundamental deduction that the instantaneous jet could be so represented. This was accomplished by using planar PIV and performing Fourier analysis on very large streamwise cuts. The very large fields were necessary in order to minimize the effects of windowing and aliasing on the spatial Fourier transforms.

It was originally our objective to make simultaneous cross-plane - streamwise plane measurements in order to see how the various modes described above couple together. This proved to be technologically beyond our capabilities at this time. In addition there were many aspects of the PIV that were not well-understood (at least by us), and especially as it applied to this problem. Therefore a significant portion of this dissertation is devoted to a detailed analysis and discussion of the influences of quantization noise, the effects of spatial averaging, and the effects of windowing and filtering on the data and the inferences from it.

1.2 Thesis structure

Chapter 2 this thesis focusses on the the theory of equilibrium similarity as applied to the momentum-conserving axisymmetric far jet and the conclusions that can be drawn from it with. The material is to be considered as a review of the previous work of George et al [16] in general and of the theoretical work of Ewing in particular [7]. The outstanding

result of the equilibrium similarity is that it is possible to find a coordinate system in which the turbulence exhibit streamwise homogeneity. This result is exploited in chapter , in which the theory for the subsequent composite spatial decompositions are detailed. Following this are I and II describing the two experimental investigations that provided the data for the spatial decompositions. The results of the data analysis are given in the respective parts. Concluding remarks are given in chapter 11.

2. EQUILIBRIUM SIMILARITY OF THE AXISYMMETRIC TURBULENT JET

In an attempt to reduce the dimensionality of the equations of motion for fluid flow similarity solutions are often sought (Batchelor[17], George[1]). These are solutions to the equations of motion mapped onto a coordinate system which eliminates their dependence on at least one independent spatial (or temporal) dimension and renders the equations dimensionless. For single-point equations such mappings consist of scaling out the growth along one coordinate axis by absorbing it into another and choosing appropriate velocity scales for the velocity quantities. The choice of the relevant scaling quantity is important and is often established by the researchers own insight into the expected behavior of the flow in question (Tennekes & Lumley[18], Townsend[19]). It is then inevitable that erroneous scalings are sometimes presumed, leading to un-physical solutions. And even if the solutions found are physical, the constraint utilized could leave families of solutions undiscovered. In short, a certain measure of arbitrariness influences the similarity analysis. In an effort to counteract this arbitrariness, a method of identifying both if a similarity mapping exists and in that case what the scaling parameters are, the theory of equilibrium similarity was developed by George [20].

Equilibrium similarity proposes unknown scaling variables for all relevant terms which are then substituted back into the equations. Then an assumption is made that in order for the flow to develop as a similarity flow, the terms of the averaged equations may not change in relation with each other, i.e., all the terms must be in mutual balance with respect to each other at every stage of the flow progression - hence the epithet *equilibrium* similarity. This requirement places constraints on the scaling variables in terms of their relation to each other and to the axis of progression. If some functional dependence of the scaling vari-

ables can be found that simultaneously satisfies all such constraints, an equilibrium similarity solution to the flow equations exists.

The theoretical analysis as well as experimental results reported in this work relies crucially on the conclusions that can be made from equilibrium similarity theory applied to the far, stationary, round turbulent jet. The theory has been developed largely by George and his co-workers over the past two decades, continuing in this dissertation with investigation of it's implications for the decomposition of the far, turbulent round jet. Consequently there is no single reference prior to this which presents the current state of our understanding. In light of this, the theory and its consequences will be discussed in some detail.

2.1 Equilibrium similarity applied to the single-point RANS equations of motion

The equations are most naturally expressed in cylindrical coordinates x, r, θ. The nomenclature for the velocity components is $\vec{v} = (u, v, w)$ where v is the radial component and w the azimuthal one. Following Batchelor [17] the full governing equations in cylindrical coordinates are listed in Appendix A. Reynolds-decomposition and ensemble-averaging yields single-point equations for the mean velocity and the turbulent quantities. The flow is to be considered statistically homogeneous in the azimuthal direction and stationary in time. There is no mean swirling velocity. As the jet flow is a rotationally symmetric shear flow the boundary layer approximation applies. The Reynolds number for the flow is assumed to be large enough that the viscous effect on the mean flow are negligible. In summary the following reductions can be made to all equations for averaged quantities:

$$\frac{\partial}{\partial \theta} = 0 \;\; ; \;\; \frac{\partial}{\partial t} = 0 \;\; ; \;\; \frac{\partial}{\partial x} \ll \frac{\partial}{\partial r} \tag{2.1}$$

Further simplification to specific equations will be justified as necessary.

2.1.1 Momentum and mass conservation

By integrating the radial mean momentum equation, neglecting viscous terms and all second order terms in the turbulence intensity, the

streamwise pressure gradient can be shown to be zero to leading order. Thus the streamwise momentum equation for high Reynolds number and to first order in turbulence intensity reduces to:

$$U\frac{\partial U}{\partial x} + V\frac{\partial U}{\partial r} = -\frac{1}{r}\frac{\partial}{\partial r}r\langle uv\rangle \tag{2.2}$$

The radial mean velocity V is obtained via the mean continuity equation,

$$\frac{\partial U}{\partial x} + \frac{1}{r}\frac{\partial}{\partial r}(rV) = 0 \tag{2.3}$$

which can be integrated from the centerline (where r=0 and the radial velocity is presumed to be zero) to any position r to yield:

$$V(x,r) = -\frac{1}{r}\int_0^r \frac{\partial U}{\partial x}\bar{r}d\bar{r}. \tag{2.4}$$

Substitution of equation 2.4 into the mean momentum equation 2.2 gives

$$U\frac{\partial U}{\partial x} - \frac{1}{r}\frac{\partial U}{\partial r}\int_0^r \frac{\partial U}{\partial x}\bar{r}d\bar{r} = -\frac{1}{r}\frac{\partial}{\partial r}r\langle uv\rangle \tag{2.5}$$

The only remaining velocity variables are U and $\langle uv\rangle$ which both vary along the streamwise axis x and radial axis r. The objective of similarity analysis is find some x-dependent scalings of U and $\langle uv\rangle$ that remove all dependency on x from equation 2.5.

Defining the radial similarity coordinate η as

$$\eta = r/\delta(x,\star) \tag{2.6}$$

where the length scale $\delta(x,\star)$ is to be determined, the mean velocity and Reynolds shear stress can be expressed as:

$$U(x,r) = U_s(x,\star)f(\eta,\star) \tag{2.7}$$
$$\langle uv\rangle(x,r) = R_s(x,\star)g_{uv}(\eta,\star) \tag{2.8}$$

where the '$\star$' denotes an unknown, but possible dependence on the upstream conditions. Note that the point of including the '$\star$' is that it passes through all of the analysis unchanged; hence such a dependence cannot be ruled out *a priori*.

Substitution of equations 2.7 and 2.8 into equation 2.5 yields

$$U_s f\left[f\frac{dU_s}{dx}+U_s\frac{df}{d\eta}\frac{\partial\eta}{\partial x}\right]-U_s\frac{df}{d\eta}\frac{\partial\eta}{\partial r}\frac{1}{\eta\delta}\int_0^\eta\left[f\frac{dU_s}{dx}+U_s\frac{df}{d\eta}\frac{\partial\eta}{\partial x}\right]\delta^2\bar{\eta}d\bar{\eta} = -\frac{1}{\eta\delta}\frac{\partial}{\partial\eta}\left(\eta\delta R_s g_{uv}\right)\frac{\partial\eta}{\partial r} \quad (2.9)$$

The partial derivatives can be evaluated via the chain rule of differentiation to be $\partial\eta/\partial x = -r\delta^{-2}d\delta/dx = -(\eta/\delta)d\delta/dx$ and $\partial\eta/\partial r = 1/\delta$ so that

$$\left[U_s\frac{dU_s}{dx}\right]f^2-\left[\frac{U_s^2}{\delta}\frac{d\delta}{dx}\eta\right]f\frac{df}{d\eta}-\left[U_s\frac{dU_s}{dx}\right]\frac{1}{\eta}\frac{df}{d\eta}\int_0^\eta f\bar{\eta}d\bar{\eta} + \left[\frac{U_s^2}{\delta}\frac{d\delta}{dx}\right]\frac{1}{\eta}\frac{df}{d\eta}\int_0^\eta\frac{df}{d\bar{\eta}}\bar{\eta}^2d\bar{\eta} = -\left[\frac{R_s}{\delta}\right]\frac{1}{\eta}\frac{d}{d\eta}\left(\eta g_{uv}\right) \quad (2.10)$$

Integration by parts of the second integral term in 2.10 gives:

$$\int_0^\eta\frac{df}{d\bar{\eta}}\bar{\eta}^2d\bar{\eta} = f\bar{\eta}^2\big|_0^\eta-\int_0^\eta 2f\bar{\eta}d\bar{\eta} = f\eta^2-2\int_0^\eta f\bar{\eta}d\bar{\eta} \quad (2.11)$$

So equation 2.10 reduces to

$$\left[U_s\frac{dU_s}{dx}\right]\left\{f^2-\frac{1}{\eta}\frac{df}{d\eta}\int_0^\eta f\bar{\eta}d\bar{\eta}\right\}-\left[2\frac{U_s^2}{\delta}\frac{d\delta}{dx}\right]\frac{1}{\eta}\frac{df}{d\eta}\int_0^\eta f\bar{\eta}d\bar{\eta} = -\left[\frac{R_s}{\delta}\right]\frac{1}{\eta}\frac{d}{d\eta}\left(\eta g_{uv}\right) \quad (2.12)$$

As outlined in the introduction to this chapter, the conceptual idea of equilibrium similarity is that the functional dependency of the scaling variables (in this case $\delta(x)$, $U_s(x)$ & $R_s(x)$) must be found by requiring the x-dependent parts of the terms in the governing differential

equation to deviate at most by a constant factor. Any other variation in functional dependency would fail to eliminate the x-dependence from all terms simultaneously and thus fail in reducing the dependent variables in the single-point equations from (x, r) to $\eta = r/\delta(x)$ only. Applying the equilibrium criteria to equation 2.12, i.e., requiring that all terms must be proportional to within a constant factor at all downstream positions x, results in the scaling constraints:

$$U_s \frac{dU_s}{dx} \propto \frac{U_s^2}{\delta} \frac{d\delta}{dx} \tag{2.13}$$

$$\frac{R_s}{\delta} \propto U_s \frac{dU_s}{dx} \tag{2.14}$$

$$\frac{R_s}{\delta} \propto \frac{U_s^2}{\delta} \frac{d\delta}{dx} \tag{2.15}$$

where the constant factors of proportionality can at most depend on the upstream conditions at the jet generator. Constraint 2.13 gives a functional relationship between the velocity scale and the length scale

$$\frac{1}{U_s} \frac{dU_s}{dx} \propto \frac{1}{\delta} \frac{d\delta}{dx} \tag{2.16}$$

which can be integrated from some virtual origin in along the streamwise axis, x_o, to a downstream position x to obtain:

$$U_s(x) = U_s(x_o) \left[\frac{\delta(x)}{\delta(x_o)} \right]^n \propto \delta(x)^n \tag{2.17}$$

As neither $\delta(x)$ nor $U_s(x)$ are hitherto known, the exponent n cannot be immediately determined. Nor does the other independent constraint, 2.15, provide such information. Instead, it dictates the scaling of the primary Reynolds shear stress in the jet flow to be

$$R_s \propto U_s^2 \frac{d\delta}{dx} \tag{2.18}$$

Again, as δ remains unknown, there is no logical foundation for assuming that the similarity scaling for the Reynolds stress $\langle uv \rangle$ is simply the square of the scaling of the mean streamwise velocity (c.f. Tennekes &

Lumely [18] and Townsend[19]). Clearly, the growth rate of the length scale δ will influence the magnitude of this quantity.

Thus there are really only two independent relationships needed to describe the mean momentum equation, one relating the x-dependence of the mean velocity to that of the variation of the length scale, and a second relating the Reynolds shear stress to both. In fact, it is possible to absorb the ratio $R_s/(U_s^2 d\delta/dx)$ into the definition of $g_{uv}(\eta, \star)$ by defining:

$$\tilde{g}_{uv}(\eta) = \left[\frac{R_s}{U_s^2 d\delta/dx}\right] g_{uv}(\eta, \star) \tag{2.19}$$

Using this the streamwise momentum equation becomes completely independent of the scaling parameters :

$$-f^2 - \frac{1}{\eta}\frac{df}{d\eta}\int_0^\eta f\bar{\eta}d\bar{\eta} = -\frac{1}{\eta}\frac{d}{d\eta}\left(\eta\tilde{g}_{uv}\right) \tag{2.20}$$

An immediate consequence of this is that any dependence on exit Reynolds number or upstream conditions will not appear in the properly normalized profiles. They will only appear in $d\delta/dx$, which has been fully absorbed into expression 2.20 above. As a final note, the conclusions are based on a set of equations in which the viscous terms have been neglected. If they are not truly negligible, then extra terms must be retained, and these can result in differential equations relating $f(\eta)$ and $\tilde{g}_{uv}(\eta)$ that are different from 2.20.

In order to establish the the exponent n, which relates the velocity scale U_s to the length scale δ, one must consider the equilibrium similarity applied to the momentum integral. For the round jet, the conservation of momentum requires that the momentum crossing any downstream plane equals the rate at which momentum is added at the source, M_o, minus any work done by the streamwise pressure difference. By integrating the radial and streamwise momentum equations it follows that (v. Appendix I of Hussein et al.[16]):

$$\frac{M_o}{2\pi} = \int_0^\infty \left[U^2 + \langle u^2\rangle - \left(\frac{\langle v^2\rangle + \langle w^2\rangle}{2}\right)\right] r dr \tag{2.21}$$

In the subsequent chapter it will be shown that the normal Reynolds stresses are all proportional to the square of the mean velocity scale. Substitution of the similarity relations yields:

$$\frac{M_o}{2\pi} = U_s^2\delta^2\int_0^\infty\left[f^2+g_{uu}-\frac{1}{2}[g_{vv}+g_{ww}]\right]\eta d\eta \tag{2.22}$$

where the normal Reynolds stresses $\langle u^2\rangle$, $\langle v^2\rangle$, and $\langle w^2\rangle$ scale as U_s^2 leaving the radial profiles g_{uu}, g_{vv}, and g_{ww}. The radial integral in 2.22 is simply some constant, so that the product of the velocity scale and the length scale must stay constant at every downstream position, i.e.,

$$U_s(x,\star)\propto\delta(x,\star)^{-1} \tag{2.23}$$

This implies immediately that the Reynolds number based on the similarity scales $Re_s(\star) = U_s(x,\star)\delta(x,\star)/\nu$ remains constant as the flow develops. The star symbol represents the fact that the scaling is dependent on the conditions at the jet exit, in particular the exit Reynolds number $Re_D = U_eD/\nu$. Thus a given flow develops its own similarity solution in accordance with only its upstream conditions and Reynolds number. This has important consequences for all that follows, since it implies that all length scales (integral, pseudo-integral scale, Taylor microscale, Kolmogorov microscale) remain proportional to each other as the flow develops. This in turn implies that the role of terms neglected in the original first order analysis does not change downstream, so they do not grow back into the problem (like the axisymmetric wake of Johansson et al [21]), nor become more negligible (like the plane jet of George [22]).

Once the relation between the velocity scale and the length scale has been determined, the scaling for the radial mean velocity can be derived directly. As previously stated, the radial mean velocity is given by equation 2.4, which in similarity scaling is

$$V(x,\eta) = -\left\{\left[\delta\frac{dU_s}{dx}\right]+2\left[U_s\frac{d\delta}{dx}\right]\right\}\frac{1}{\eta}\int_0^\eta f(\overline{\eta})\overline{\eta}d\overline{\eta}+\left[U_s\frac{d\delta}{dx}\right]\eta f \tag{2.24}$$

Since momentum conservation requires that $U_s\propto\delta^{-1}$, $\delta(dU_s/dx) = -U_s(d\delta/dx)$, and it follows that:

$$V(x,\eta) = -\left[U_s \frac{d\delta}{dx}\right]\left\{\frac{1}{\eta}\int_0^\eta f(\overline{\eta})\,\overline{\eta}\,d\overline{\eta} \;-\; \eta f\right\} \tag{2.25}$$

Note that the proportionality to $d\delta/dx$ makes sense since it is V that is responsible for the growth of the jet.

2.1.2 Transport equation for the turbulent kinetic energy q^2

For a statistically stationary, incompressible flow without swirl which is homogeneous in the azimuthal coordinates, the kinetic energy equation (c.f., Hussein et al.[16] for the turbulence can be written as:

$$\begin{aligned}\left[U\frac{\partial}{\partial x} + V\frac{\partial}{\partial r}\right]\left(\frac{1}{2}\langle q^2\rangle\right) \;=\; & \frac{1}{r}\frac{\partial}{\partial r} r\left[-\frac{1}{\rho}\langle pv\rangle - \frac{1}{2}\langle q^2 v\rangle + \nu\frac{\partial}{\partial r}\left(\frac{1}{2}\langle q^2\rangle\right)\right] \\ & + \frac{\partial}{\partial x}\left[-\frac{1}{\rho}\langle pu\rangle - \frac{1}{2}\langle q^2 u\rangle + \nu\frac{\partial}{\partial x}\left(\frac{1}{2}\langle q^2\rangle\right)\right] \\ & - \langle u^2\rangle\frac{\partial U}{\partial x} - \langle v^2\rangle\frac{\partial V}{\partial r} - \frac{V}{r}\langle w^2\rangle - \langle uv\rangle\left[\frac{\partial U}{\partial r} + \frac{\partial V}{\partial x}\right] \\ & - \varepsilon_{hom}\end{aligned} \tag{2.26}$$

where $q^2 \equiv u^2 + v^2 + w^2$. The left-hand side represents the convection by the mean flow, while the terms on the right-hand side represent respectively the turbulence transport in the radial and streamwise directions, the production by the working of the Reynolds stresses against the mean flow gradients, and the 'homogeneous dissipation'. Note that the 'homogeneous dissipation' is not really the dissipation (which involves only the fluctuating strain-rates), but is given by:

$$\varepsilon_{hom} = \nu\langle\frac{\partial u_i}{\partial x_j}\frac{\partial u_i}{\partial x_j}\rangle \tag{2.27}$$

For high Reynolds number turbulence the true dissipation and homogenous 'dissipation' are virtually equivalent due to the local homogeneity at the dissipative scales. This particular form has been chosen here to simplify the viscous term in the transport equation, and has no impact on all subsequent considerations.

If the turbulence Reynolds number is assumed to be high enough to neglect the viscous transport terms, the turbulence kinetic energy equation to second order in the turbulence intensities reduces to:

$$\left[U\frac{\partial}{\partial x}+V\frac{\partial}{\partial r}\right]\left(\frac{1}{2}\langle q^2\rangle\right)=-\frac{1}{r}\frac{\partial}{\partial r}\left(r\left[\frac{1}{\rho}\langle pv\rangle+\frac{1}{2}\langle q^2v\rangle\right]\right)-\langle uv\rangle\frac{\partial U}{\partial r}-\epsilon_{hom} \tag{2.28}$$

Thus the high Reynolds number turbulent jet (to second-order in turbulence intensities) consists only of a balance among mean convection, radial turbulence transport, production and dissipation. Only in the immediate neighborhood of the centerline do the neglected production terms become important (since the Reynolds shear stress vanishes there). Hussein et al.[16] have shown in fact that to first order the dissipation and production are nearly in balance. The mean convection and turbulence transport are smaller in magnitude and also nearly in balance.

Recalling the first order scaling $U \propto U_s$, $V \propto U_s d\delta/dx$ and $\langle uv\rangle \propto U_s^2 d\delta/dx$ and proposing the following scaling for remaining terms in the kinetic energy balance 2.28 as

$$\frac{1}{2}\langle q^2\rangle = K_s(x)k(\eta) \tag{2.29}$$

$$\frac{1}{\rho}\langle pv\rangle+\frac{1}{2}\langle q^2v\rangle = T_s(x)t(\eta) \tag{2.30}$$

$$\epsilon_{hom} = D_s(x)d(\eta) \tag{2.31}$$

gives, after substitution and differentiation,

$$\left[\frac{K_sU_s}{\delta}\frac{d\delta}{dx}\right]\eta f\frac{dk}{d\eta}+\left[U_s\frac{dK_s}{dx}\right]fk-\left[\frac{U_sK_s}{\delta}\frac{d\delta}{dx}\right]\frac{1}{\eta}\frac{dk}{d\eta}\int_0^\eta f\overline{\eta}d\overline{\eta}= -\left[\frac{T_s}{\delta}\right]\left\{\frac{t}{\eta}+\frac{dt}{d\eta}\right\}-\left[\frac{R_sU_s}{\delta}\right]g_{uv}\frac{df}{d\eta}-[D_s]\,d \tag{2.32}$$

The equilibrium similarity constraint can be satisfied only if all terms have the same functional dependence, which is possible only if the following relations hold (recalling that $R_s = U_s^2(d\delta/dx)$):

$$\frac{K_s}{\delta}\frac{d\delta}{dx}\propto\frac{dK_s}{dx}\propto\frac{T_s}{U_s\delta}\propto\frac{U_s^2}{\delta}\frac{d\delta}{dx}\propto\frac{D_s}{U_s} \tag{2.33}$$

Solving these, one can see immediately that the turbulence kinetic energy must have the same functional dependence on x as the mean velocity squared; i.e.,

$$K_s \propto U_s^2 \tag{2.34}$$

Also, the radial turbulence transport term must vary as the mean velocity raised to the third power times the growth rate of the length scale; i.e.,

$$T_s \propto U_s^3 \frac{d\delta}{dx} \tag{2.35}$$

Note that this resembles closely the Reynolds shear stress term, a feature that is common to all the radial transport moments regardless of the order.

The functional dependency for the dissipation can be satisfied only if:

$$D_s \propto \frac{U_s K_s}{\delta}\frac{d\delta}{dx} \propto \frac{U_s^3}{\delta}\frac{d\delta}{dx} \tag{2.36}$$

2.1.3 Transport equations for the normal Reynolds stresses

The component Reynolds stress equations for the normal stresses for high Reynolds number and to second order are given by:

Streamwise normal Reynolds stress

$$\left[U\frac{\partial}{\partial x} + V\frac{\partial}{\partial r}\right]\langle u^2\rangle = +2\langle\frac{p}{\rho}\frac{\partial u}{\partial x}\rangle - \frac{1}{r}\frac{\partial}{\partial r}r\langle u^2 v\rangle - 2\langle uv\rangle\frac{\partial U}{\partial r} - 2\varepsilon_u \tag{2.37}$$

Radial normal Reynolds stress

$$\left[U\frac{\partial}{\partial x} + V\frac{\partial}{\partial r}\right]\langle v^2\rangle = +2\frac{1}{r}\langle\frac{p}{\rho}\frac{\partial}{\partial r}rv\rangle - \frac{1}{r}\frac{\partial}{\partial r}r\left[\frac{1}{\rho}\langle pv\rangle + \langle v^2 v\rangle\right] - 2\varepsilon_v \tag{2.38}$$

Azimuthal normal Reynolds stress

$$\left[U\frac{\partial}{\partial x}+V\frac{\partial}{\partial r}\right]\langle w^2\rangle=+2\frac{1}{r}\langle\frac{p}{\rho}\frac{\partial w}{\partial\theta}\rangle-\frac{1}{r}\frac{\partial}{\partial r}r\langle w^2v\rangle-2\varepsilon_w \tag{2.39}$$

While each component of turbulent kinetic energy loses energy through dissipation, only the streamwise normal stress equation retains the terms that allows for production of turbulence kinetic energy. Thus the only possible way to distribute energy among the component equations is through a coupling facilitated by the pressure-strain rate terms. But due to the continuity equation for the turbulent fluctuations the sum of these terms are zero i.e.,

$$\langle\frac{p}{\rho}\frac{\partial u}{\partial x}\rangle+\frac{1}{r}\langle\frac{p}{\rho}\frac{\partial}{\partial r}rv\rangle+\frac{1}{r}\langle\frac{p}{\rho}\frac{\partial w}{\partial\theta}\rangle=0 \tag{2.40}$$

Each term in equations 2.37 through 2.40 is written in similarity form according to:

$$\langle u^2\rangle=K_u(x,\star)k_u(\eta,\star)\ \ ;\ \varepsilon_u=D_u(x,\star)d_u(\eta,\star)\ \ ;\ \langle\frac{p}{\rho}\frac{\partial u}{\partial x}\rangle=P_u(x,\star)p_u(\eta,\star) \tag{2.41}$$

$$\langle v^2\rangle=K_v(x,\star)k_v(\eta,\star)\ \ ;\ \varepsilon_v=D_v(x,\star)d_v(\eta,\star)\ \ ;\ \frac{1}{r}\langle\frac{p}{\rho}\frac{\partial}{\partial r}rv\rangle=P_v(x,\star)p_v(\eta,\star) \tag{2.42}$$

$$\langle w^2\rangle=K_w(x,\star)k_w(\eta,\star)\ ;\ \varepsilon_w=D_w(x,\star)d_w(\eta,\star)\ ;\ \frac{1}{r}\langle\frac{p}{\rho}\frac{\partial w}{\partial\theta}\rangle=P_w(x,\star)p_w(\eta,\star) \tag{2.43}$$

Equation 2.40 gives:

$$P_u\propto P_v\propto P_w \tag{2.44}$$

Substitution of the relations 2.41 into equation 2.37 gives

$$U_s\frac{dK_u}{dx}\propto\frac{U_sK_u}{\delta}\propto P_u\propto\frac{U_s^3}{\delta}\frac{d\delta}{dx}\propto D_u \tag{2.45}$$

while equations 2.38 and 2.39 give:

$$U_s\frac{dK_v}{dx}\propto\frac{U_sK_v}{\delta}\propto P_v\propto D_u \tag{2.46}$$

and

$$U_s \frac{dK_w}{dx} \propto \frac{U_s K_w}{\delta} \propto P_w \propto D_w \tag{2.47}$$

So that

$$P_u \propto P_v \propto P_w \propto \frac{U_s^3}{\delta}\frac{d\delta}{dx} \propto \frac{U_s K_u}{\delta} \propto \frac{U_s K_u}{\delta} \propto \frac{U_s K_w}{\delta} \propto D_u \propto D_v \propto D_w \tag{2.48}$$

Moreover since $P_u(x)$ must at least balance the production term in the $\langle u^2 \rangle$ equation, they must all be proportional to $R_s U_s/\delta = (U_s^3/\delta)d\delta/dx$.

2.1.4 Transport equations for the Reynolds shear stresses

So far the single-point equation analysis has provided no direct constraint on the scaling length $\delta(x)$ or its growth rate $d\delta/dx$. However, the equation for the Reynolds shear stress to leading order:

$$\left[U\frac{\partial}{\partial x} + V\frac{\partial}{\partial r}\right]\langle uv\rangle = +\langle \frac{p}{\rho}\left[\frac{\partial u}{\partial r} + \frac{\partial v}{\partial x}\right]\rangle - \frac{1}{r}\frac{\partial}{\partial r} r\langle uvv\rangle - \langle v^2\rangle \frac{\partial U}{\partial r} - \frac{\langle uw^2\rangle}{r} \tag{2.49}$$

Note that a ε_{uv} could also have been included, but is usually neglected because of the assumed local isotropy (or local axisymmetry) at high Reynolds numbers.

Substituting the similarity relations we know, and keeping only the first mean convection term on the left-hand-side and the production term from the right yields:

$$\left[U_s\frac{dR_s}{dx}\right] f g_{uv} - \left[\frac{U_s R_s}{\delta}\frac{d\delta}{dx}\right]\eta f \frac{dg_{uv}}{d\eta} - \left[\frac{U_s R_s}{\delta}\frac{d\delta}{dx}\right]\frac{1}{\eta}\frac{dg_{uv}}{d\eta}\int_0^\eta f\bar{\eta}d\bar{\eta}$$
$$= [P_{uv}]\, p_{uv} + \left[K_v\frac{U_s}{\delta}\right] g_{vv}\frac{df}{d\eta} + \cdots \tag{2.50}$$

Equilibrium similarity requires that:

$$U_s \frac{dR_s}{dx} \propto U_s \frac{R_s}{\delta} \frac{d\delta}{dx} \propto K_v \frac{U_s}{\delta} \tag{2.51}$$

where previous results required $R_s \propto U_s^2 d\delta/dx$ and $K_v \propto U_s^2$. Thus the constraints are

$$U_s^2 \frac{dU_s}{dx} \frac{d\delta}{dx} \propto U_s^3 \frac{d^2\delta}{dx^2} \propto \frac{U_s^3}{\delta} \left(\frac{d\delta}{dx} \right)^2 \propto \frac{U_s^3}{\delta} \tag{2.52}$$

where the streamwise derivative $dU_s/dx \propto U_s/\delta(d\delta/dx)$ so that the first terms on the left is identical to the second from the right in 2.52. The remaining constraints are thus:

$$\frac{d^2\delta}{dx^2} \propto \frac{1}{\delta} \left(\frac{d\delta}{dx} \right)^2 \propto \frac{1}{\delta} \tag{2.53}$$

Clearly these can all be satisfied only if the growth rate is constant:

$$\frac{d\delta}{dx} = A(\star) \tag{2.54}$$

where the star symbol serves as a reminder that while $A(\star)$ is fixed for a given flow, it will not necessarily be universal to all similar flows, which are influenced by the exit Reynolds number and other exit parameters.

2.1.5 Conclusions from single-point equilibrium similarity

Equilibrium similarity constraints applied to the single point equations governing the fully developed turbulent jet shows, in conjunction with

overall momentum conservation, that

$$\begin{aligned} U(x,r) &= U_s(x)f(\eta) \propto \delta^{-1} \\ \langle uv \rangle &= R_s(x)g_{uv}(\eta) \propto U_s^2 \frac{d\delta}{dx} \\ \langle uu \rangle &= K_u(x)g_{uu}(\eta) \propto U_s^2 \\ \langle vv \rangle &= K_v(x)g_{vv}(\eta) \propto U_s^2 \\ \langle ww \rangle &= K_w(x)g_{ww}(\eta) \propto U_s^2 \\ \delta &\propto x \end{aligned} \tag{2.55}$$

A natural choice for the velocity scale $U_s(x)$ is the centerline velocity $U_c(x)$ and the length scale $\delta(x)$ is chosen to be represented by the velocity half-width $\delta_{1/2}(x)$ defined as the radial location at which the velocity as dropped to half its centerline value; i.e., the value of r satisfying $1/2 = f(r/\delta_{1/2})$. Then we expect that the centerline velocity decays inversely with downstream position and that the half-width grows linearly, both from some common virtual origin $x_o(\star)$, i.e.,

$$U_c(x) = B(\star)M_o^{1/2}/(x - x_o(\star)) \tag{2.56}$$

$$\delta_{1/2}(x) = A(\star)(x - x_o(\star)) \tag{2.57}$$

2.2 Similarity of the multi-point equations

There are very few flows for which the two-point equations admit to fully self-similar solutions: decaying (grid) turbulence (George [23, 24], George & Wang [25]), homogeneous shear flow turbulence (George & Gibson[26]), the two-dimensional wake (George [1]), the axisymmetric wake (Johansson et al. [21]) and the axisymmetric jet (Ewing et al. [7]).

A contribution of this thesis is the confirmation of the two-point similarity equations developed by Ewing 1995, Ewing et al. 2007. By two-point, we mean the joint statistics between two quantities, one evaluated at one point, say $(\vec{x}, t)$, and another point, say $(\vec{x'}, t')$. Of primary interest herein will be the two point cross-correlation given by $\langle u_i(\vec{x}, t)u_j(\vec{x'}, t')$ In this dissertation our only be concern is with the case where $t = t'$. Since the jet flow is statistically stationary, this implies that all two-point moments of interest can be obtained by time-

averaging data taken simultaneously at both points. For this reason the time-variable will be suppressed in the analysis that follows.

2.2.1 Similarity of The two-point equations for the fluctuating velocity

The similarity analysis as presented in Ewing et al.[7] is non-trivial and long due to the complex nature of the equations for the two-point correlations. As the objective of this work is to explore the consequences of Ewing's work on similarity, the analysis will be presented here in as condensed form as possible. In order to facilitate this, the following equations are in Ewing's more compact notation where (x_1, x_2, x_3) correspond to (x, r, θ) and (u_1, u_2, u_3) to (u, v, w). Following Ewing et al. 2007 (Appendix) the governing equations for the two-point velocity correlation in the axisymmetric jet can be written as [27]:

$$
\begin{aligned}
&U_k \frac{1}{h^{(k)}} \frac{\partial \overline{u_i u'_j}}{\partial x_k} + U'_k \frac{1}{h^{(k)\prime}} \frac{\partial \overline{u_i u'_j}}{\partial x'_k} + \frac{U_2 \overline{u_3 u'_j}}{x_2} \delta_{i3} + \frac{U'_2 \overline{u_i u'_3}}{x'_2} \delta_{j3} = \\
&-\frac{1}{\rho} \frac{1}{h^{(i)}} \frac{\partial \overline{p u'_j}}{\partial x_i} - \frac{1}{\rho} \frac{1}{h^{(j)\prime}} \frac{\partial \overline{p' u_i}}{\partial x'_j} - \frac{1}{h^{(k)}} \frac{\partial \overline{u_k u_i u'_j}}{\partial x_k} - \frac{1}{h^{(k)\prime}} \frac{\partial \overline{u'_k u_i u'_j}}{\partial x'_k} \\
&-\frac{\overline{u_2 u_i u'_j}}{x_2} - \frac{\overline{u'_2 u_i u'_j}}{x'_2} + \frac{\overline{u_3^2 u'_j}}{x_2} \delta_{i2} + \frac{\overline{u_3^{2\prime} u_i}}{x'_2} \delta_{j2} - \frac{\overline{u_2 u_3 u'_j}}{x_2} \delta_{i3} - \frac{\overline{u'_2 u_i u'_3}}{x'_2} \delta_{j3} \\
&-\overline{u'_j u_k} \frac{\partial U_i}{\partial x_k} - \overline{u_i u'_k} \frac{\partial U'_j}{\partial x'_k} + \nu \nabla^2 \overline{u_i u'_j} + \nu \nabla'^2 \overline{u_i u'_j} \\
&-\nu \left(\frac{\overline{u_2 u'_j}}{x_2^2} + \frac{2}{x_2^2} \frac{\partial \overline{u_3 u'_j}}{\partial x_3} \right) \delta_{i2} - \nu \left(\frac{\overline{u_i u'_2}}{x_2^{2\prime}} + \frac{2}{x_2'^2} \frac{\partial \overline{u_i u'_3}}{\partial x'_3} \right) \delta_{j2} \\
&-\nu \left(\frac{\overline{u_3 u'_j}}{x_2^2} - \frac{2}{x_2^2} \frac{\partial \overline{u_2 u'_j}}{\partial x_3} \right) \delta_{i3} - \nu \left(\frac{\overline{u_i u'_3}}{x_2^{2\prime}} - \frac{2}{x_2'^2} \frac{\partial \overline{u_i u'_2}}{\partial x'_3} \right) \delta_{j3}, \qquad (2.58)
\end{aligned}
$$

where the unprimed variables are evaluated at one point in the jet, and the primed variables are evaluated at a second arbitrary point in the jet at the same point in time. Here, u_3 is the fluctuating velocity in the azimuthal coordinate direction, x_3, and $h^j = (1, 1, x_2)$ is the metric of the coordinate system. It should be noted that the summation convention is not applied to the superscripts in brackets on the metric. Instead, the

value of the superscript has the same value as the index of the differential coordinate next to the metric.

As for the single-point equations, solutions are sought which reduce the dimensions of the problem. Ewing proposes a logarithmic transformation of the streamwise position variable

$$\xi = \ln \frac{x_1}{l} \tag{2.59}$$

where l is some constant length and x_1 is Cartesian distance relative to some virtual origin. He then proposes equilibrium similarity scaling that reduces the functional dependency of equations 2.58 from depending explicitly on ξ or ξ' to depending on the separation variable $\zeta = \xi' - \xi$ only. The proposed scaling is:

$$\overline{u_i u_j'} = Q_s^{(i,j)}(x_1, x_1') q_{i,j}(\zeta, \eta, \eta', \theta), \tag{2.60}$$

$$\overline{u_k u_i u_j'} = T_{s,1}^{(ki,j)}(x_1, x_1') t_{ki,j}^1(\zeta, \eta, \eta', \theta), \tag{2.61}$$

$$\overline{u_k' u_i u_j'} = T_{s,2}^{(i,kj)}(x_1, x_1') t_{i,kj}^2(\zeta, \eta, \eta', \theta), \tag{2.62}$$

$$\overline{p u_j'} = \Pi_{s,1}^{(,j)}(x_1, x_1') \pi_j^1(\zeta, \eta, \eta', \theta), \tag{2.63}$$

$$\overline{p' u_i} = \Pi_{s,2}^{(i,)}(x_1, x_1') \pi_i^2(\zeta, \eta, \eta', \theta). \tag{2.64}$$

Note that thee superscripts on the scales in brackets are not indices, and should not be considered when applying the summation convection.

Substituting the previously obtained similarity solutions for the mean velocity and the two-point correlations into the equation 2.58 yields, for $\delta \propto x$ and $U_s \propto \delta^{-1}$,

$$\left[U_s(x_1) \frac{\partial Q_s^{(i,j)}}{\partial x_1} \right] f(\eta) q_{i,j} + \left[\frac{Q_s^{(i,j)} U_s(x_1)}{x_1} \right] \left\{ f(\eta) \frac{\partial q_{i,j}}{\partial \zeta} \right.$$

$$\left. - \left(\frac{\partial q_{i,j}}{\partial \eta} + \frac{q_{3,j}}{\eta} \delta_{i3} \right) \frac{1}{\eta} \int_0^\eta \tilde{\eta} f(\tilde{\eta}) d\tilde{\eta} + f(\eta) q_{3,j} \delta_{i3} \right\} + \left[U_s(x_1') \frac{\partial Q_s^{(i,j)}}{\partial x_1'} \right] f(\eta') q_{i,j} +$$

$$\left[\frac{Q_s^{(i,j)} U_s(x_1')}{x_1'} \right] \left\{ -f(\eta') \frac{\partial q_{i,j}}{\partial \zeta} - \left(\frac{\partial q_{i,j}}{\partial \eta'} + \frac{q_{i,3}}{\eta'} \delta_{j3} \right) \frac{1}{\eta'} \int_0^{\eta'} \tilde{\eta} f(\tilde{\eta}) d\tilde{\eta} + f(\eta') q_{i,3} \delta_{j3} \right\} =$$

$$-\frac{1}{\rho} \left\{ \left[\frac{\partial \Pi_{s,1}^{(,j)}}{\partial x_1} \right] \pi_j^1 \delta_{i1} + \left[\frac{\Pi_{s,1}^{(,j)}}{x_1} \right] \left(-\eta \frac{\partial \pi_j^1}{\partial \eta} + \frac{\partial \pi_j^1}{\partial \zeta} \right) \delta_{i1} - \left[\frac{\Pi_{s,1}^{(,j)}}{\delta(x_1)} \right] \left(\frac{\partial \pi_j^1}{\partial \eta} \delta_{i2} + \frac{1}{\eta} \frac{\partial \pi_j^1}{\partial \theta} \delta_{i3} \right) \right\}$$

$$-\frac{1}{\rho}\left\{\left[\frac{\partial\Pi^{(i,)}_{s,2}}{\partial x'_1}\right]\pi_i^2\delta_{j1}+\left[\frac{\Pi^{(i,)}_{s,1}}{x'_1}\right]\left(-\eta'\frac{\partial\pi_i^2}{\partial\eta'}-\frac{\partial\pi_i^2}{\partial\zeta}\right)\delta_{j1}-\left[\frac{\Pi^{(i,)}_{s,2}}{\delta(x'_1)}\right]\left(\frac{\partial\pi_i^2}{\partial\eta'}\delta_{j2}-\frac{1}{\eta'}\frac{\partial\pi_i^2}{\partial\theta}\delta_{j3}\right)\right\}$$

$$-\left[\frac{\partial T^{(1i,j)}_{s,1}}{\partial x_1}\right]t^1_{1i,j}+\left[\frac{T^{(1i,j)}_{s,1}}{x_1}\right]\left(+\eta\frac{\partial t^1_{1i,j}}{\partial\eta}-\frac{\partial t^1_{1i,j}}{\partial\zeta}\right)-\left[\frac{T^{(2i,j)}_{s,1}}{\delta(x_1)}\frac{1}{\eta}\right]\frac{\partial\eta t^1_{2i,j}}{\partial\eta}-\left[\frac{T^{(3i,j)}_{s,1}}{\delta(x_1)}\right]\frac{1}{\eta}\frac{\partial t^1_{3i,j}}{\partial\theta}$$

$$-\left[\frac{\partial T^{(i,1j)}_{s,2}}{\partial x'_1}\right]t^2_{i,1j}+\left[\frac{T^{(i,1j)}_{s,2}}{x'_1}\right]\left(\eta'\frac{\partial t^2_{i,1j}}{\partial\eta'}+\frac{\partial t^2_{i,1j}}{\partial\zeta}\right)-\left[\frac{T^{(i,2j)}_{s,2}}{\delta(x'_1)}\right]\frac{1}{\eta'}\frac{\partial\eta' t^2_{i,2j}}{\partial\eta'}+\left[\frac{T^{(i,3j)}_{s,2}}{\delta(x'_1)}\right]\frac{1}{\eta'}\frac{\partial t^2_{i,3j}}{\partial\theta}$$

$$+\left[\frac{T^{(33,j)}_{s,1}}{\delta(x_1)}\right]\frac{t^1_{33,j}}{\eta}\delta_{i2}-\left[\frac{T^{(23,j)}_{s,1}}{\delta(x_1)}\right]\frac{t^1_{23,j}}{\eta}\delta_{i3}+\left[\frac{T^{(i,33)}_{s,2}}{\delta(x'_1)}\right]\frac{t^2_{i,33}}{\eta'}\delta_{j2}-\left[\frac{T^{(i,23)}_{s,2}}{\delta(x'_1)}\right]\frac{t^2_{i,23}}{\eta'}\delta_{j3}$$

$$-\left\{-\left[\frac{Q^{(i,j)}_s U_s(x_1)}{x_1}\right]q_{1,j}\left(f(\eta)+\eta\frac{df}{d\eta}\right)+\left[\frac{Q^{(2,j)}_s U_s(x_1)}{\delta(x_1)}\right]q_{2,j}\frac{df}{d\eta}\right\}\delta_{i1}+$$

$$\left\{\left[\frac{Q^{(1,j)}_s U_s(x_1)}{x_1}\frac{d\delta}{dx_1}\right]q_{1,j}\left(\eta f(\eta)+\eta^2\frac{df}{d\eta}\right)-\left[\frac{Q^{(2,j)}_s U_s(x_1)}{x_1}\right]q_{2,j}\left(\eta\frac{df}{d\eta}+\frac{1}{\eta^2}\int_0^\eta\tilde{\eta}f d\tilde{\eta}\right)\right\}\delta_{i2}$$

$$-\left\{-\left[\frac{Q^{(i,1)}_s U_s(x'_1)}{x'_1}\right]q_{i,1}\left(f(\eta')+\eta'\frac{df}{d\eta'}\right)+\left[\frac{Q^{(i,2)}_s U_s(x'_1)}{\delta(x'_1)}\right]q_{i,2}\frac{df}{d\eta'}\right\}\delta_{j1}+$$

$$\left\{\left[\frac{Q^{(i,1)}_s U_s(x'_1)}{x'_1}\frac{d\delta}{dx'_1}\right]q_{i,1}\left(\eta' f(\eta')+\eta'^2\frac{df}{d\eta'}\right)-\left[\frac{Q^{(i,2)}_s U_s(x'_1)}{x'_1}\right]q_{i,2}\left(\eta'\frac{df}{d\eta'}+\frac{1}{\eta'^2}\int_0^{\eta'}\tilde{\eta}f d\tilde{\eta}\right)\right\}\delta_{j2}$$

$$+\nu\left\{\left[\frac{\partial^2 Q^{(i,j)}_s}{\partial x_1^2}\right]q_{i,j}+\left[\frac{2Q^{(i,j)}_s}{x_1^2}-\frac{2}{x_1}\frac{\partial Q^{(i,j)}_s}{\partial x_1}\right]\eta\frac{\partial q_{i,j}}{\partial\eta}+\left[\frac{2}{x_1}\frac{\partial Q^{(i,j)}_s}{\partial x_1}-\frac{Q^{(i,j)}_s}{x_1^2}\right]\frac{\partial q_{i,j}}{\partial\zeta}\right.$$

$$\left.-\left[\frac{2Q^{(i,j)}_s}{x_1^2}\right]\eta\frac{\partial^2 q_{i,j}}{\partial\eta\partial\zeta}+\left[\frac{Q^{(i,j)}_s}{x_1^2}\right]\left(\eta^2\frac{\partial^2 q_{i,j}}{\partial\eta^2}+\frac{\partial^2 q_{i,j}}{\partial\zeta^2}\right)+\left[\frac{Q^{(i,j)}_s}{\delta^2(x_1)}\right]\left(\frac{1}{\eta}\frac{\partial}{\partial\eta}\eta\frac{\partial q_{i,j}}{\partial\eta}+\frac{1}{\eta^2}\frac{\partial^2 q_{i,j}}{\partial\theta^2}\right)\right\}$$

$$-\nu\left\{\left[\frac{Q^{(2,j)}_s}{\delta^2(x_1)}\right]\frac{q_{2,j}}{\eta^2}+\left[\frac{2Q^{(3,j)}_s}{\delta^2(x_1)}\right]\frac{1}{\eta^2}\frac{\partial q_{3,j}}{\partial\theta}\right\}\delta_{i2}-\nu\left\{\left[\frac{Q^{(3,j)}_s}{\delta^2(x_1)}\right]\frac{q_{3,j}}{\eta^2}-\left[\frac{2Q^{(2,j)}_s}{\delta^2(x_1)}\right]\frac{1}{\eta^2}\frac{\partial q_{2,j}}{\partial\theta}\right\}\delta_{i3}$$

$$+\nu\left\{\left[\frac{\partial^2 Q^{(i,j)}_s}{\partial x'^2_1}\right]q_{i,j}+\left[\frac{2Q^{(i,j)}_s}{x'^2_1}-\frac{2}{x'_1}\frac{\partial Q^{(i,j)}_s}{\partial x'_1}\right]\eta'\frac{\partial q_{i,j}}{\partial\eta'}-\left[\frac{2}{x'_1}\frac{\partial Q^{(i,j)}_s}{\partial x'_1}-\frac{Q^{(i,j)}_s}{x'^2_1}\right]\frac{\partial q_{i,j}}{\partial\zeta}+\right.$$

$$\left.\left[\frac{2Q^{(i,j)}_s}{x'^2_1}\right]\eta'\frac{\partial^2 q_{i,j}}{\partial\eta'\partial\zeta}+\frac{Q^{(i,j)}_s}{x'^2_1}\left(\eta'^2\frac{\partial^2 q_{i,j}}{\partial\eta'^2}+\frac{\partial^2 q_{i,j}}{\partial\zeta^2}\right)+\left[\frac{Q^{(i,j)}_s}{\delta^2(x'_1)}\right]\left(\frac{1}{\eta'}\frac{\partial}{\partial\eta'}\eta'\frac{\partial q_{i,j}}{\partial\eta'}+\frac{1}{\eta'^2}\frac{\partial^2 q_{i,j}}{\partial\theta^2}\right)\right\}$$

$$-\nu\left\{\left[\frac{Q^{(i,2)}_s}{\delta^2(x'_1)}\right]\frac{q_{i,2}}{\eta'^2}-\left[\frac{2Q^{(i,3)}_s}{\delta^2(x'_1)}\right]\frac{1}{\eta'^2}\frac{\partial q_{i,3}}{\partial\theta}\right\}\delta_{j2}$$

$$-\nu\left\{\left[\frac{Q_s^{(i,3)}}{\delta^2(x_1')}\right]\frac{q_{i,3}}{\eta'^2}+\left[\frac{2Q_s^{(i,2)}}{\delta^2(x_1')}\right]\frac{1}{\eta'^2}\frac{\partial q_{i,2}}{\partial\theta}\right\}\delta_{j3} \tag{2.65}$$

According to the equilibrium similarity principle, similarity solutions for 2.58 exists if the terms in square brackets in equation 2.65 have the same dependence on the downstream positions x_1 and x_1', i.e. if they are proportional to within a function of the separation similarity variable ζ. Ewing then shows that if the scales for the similarity solutions are chosen such that the two-point velocity correlation is

$$Q_s^{(i,j)}(x_1,x_1')=U_s(x_1)U_s(x_1')\frac{d\delta}{dx_1}^{b(i,j)}, \tag{2.66}$$

and the transport and pressure are terms proportional according to

$$T_1^{(1i,j)}(x_1,x_1')\propto U_s(x_1)Q^{(i,j)}(x_1,x_1'), \tag{2.67}$$

$$T_1^{(2i,j)}(x_1,x_1')\propto T_1^{(3i,j)}\propto U_s(x_1)Q^{(i,j)}(x_1,x_1')\frac{d\delta}{dx_1}, \tag{2.68}$$

$$T_2^{(i,1j)}(x_1,x_1')\propto U_s(x_1')Q^{(i,j)}(x_1,x_1'), \tag{2.69}$$

$$T_2^{(i,2j)}(x_1,x_1')\propto T_2^{(i,3j)}\propto U_s(x_1')Q^{(i,j)}(x_1,x_1')\frac{d\delta}{dx_1}, \tag{2.70}$$

$$\Pi_1^{(,j)}(x_1,x_1')\propto U_s(x_1)Q^{(i,j)}(x_1,x_1'), \tag{2.71}$$

and

$$\Pi_2^{(i,)}(x_1,x_1')\propto U_s(x_1')Q^{(i,j)}(x_1,x_1'). \tag{2.72}$$

that the terms in equation 2.65 can be split into two groups which are internally proportional. The ratio of these groups of terms to each other are given by

$$\frac{Q^{i,j}U_s(x_1)}{x_1}\frac{x_1'}{Q_s^{(i,j)}U_s(x_1')}\propto\frac{x_1'^2}{x_1^2}=e^{-2\zeta}, \tag{2.73}$$

which satisfies the similarity constraint of depending on ζ only. Therefore, when the similarity scales are chosen as in equations 2.66-2.72, it follows that the governing equations for the two-point velocity correlation tensor admit equilibrium similarity solutions.

The scales for the viscous terms in equation 2.65 are proportional to the convective terms if

$$\frac{U_s(x_1)Q^{i,j}}{x_1}\propto\nu\frac{Q^{i,j}}{x_1^2} \tag{2.74}$$

or

$$\frac{U_s(x_1)x_1}{\nu}\propto\frac{U_s\delta}{\nu}\propto const \tag{2.75}$$

which is the same constraint deduced from the integral momentum equation. Therefore, the governing equations for the two-point velocity correlations indeed admit to equilibrium similarity solutions, even for finite Reynolds number jets. However, Ewing also finds that there is no unique set of scaling variables that removes the dependence on the jet growth rate from the two-point equations. Nor was it possible to scale out the dependence on the scaling Reynolds number.

2.2.2 Conclusions from similarity of the multi-point equations

The similarity analysis of Ewing shows that scaled properly the two-point equations are independent of position in ξ, i.e.,

$$\begin{aligned} \langle u_i(\vec{x}) u_j(\vec{x'}) \rangle &= Q_s^{i,j}(x, x') q_{i,j}(\zeta, \eta, \eta', \vartheta) \\ &= U_s(x) U_s(x') \left[\frac{d\delta}{dx} \frac{d\delta'}{dx'} \right]^{b_{ij}} q_{i,j}(\xi' - \xi, \eta, \eta', \theta' - \theta) \end{aligned} \quad (2.76)$$

where $b_{ij} = 0$ if $i = j$ and $1/2$ for $i \neq j$. The velocity scale $U_s(x)$and the length scale $\delta(x)$ are the ones obtained from the previous single point equilibrium similarity analysis. Note that b_{ij} corresponds to the incorporation of the growth rate in the shear stresses, but not in the normal stresses. Equation 2.76 reduces directly to the single-point results and correctly reflects the effect of the source conditions on the jet.

In particular, it is now evident that the turbulence can be expected to be streamwise homogenous in the similarity coordinate system (ξ, η, θ), $\xi = ln(x)$ and $\eta = r/\delta$. The semi-infinite Cartesian streamwise axis x has been mapped into the infinite domain ξ.

3. MULTI-SCALE DECOMPOSITION OF THE TURBULENT VELOCITY IN THE FAR JET

Turbulence manifests as a continuously changing field of vortices. From flow visualization one can appreciate the great diversity of size of vortical structures, but also that the structures often seem to form and un-form. Sometimes structures are visually more persistent and last longer, as well as re-appear in a predictable manner, awarding them the epithet coherent structures. A great challenge in turbulence research lies in understanding how these structures form and change as they interact with each other and the flow in which they are embedded.

Much is known about the symptoms of turbulence. From the single point Reynolds averaged differential equations for the mean velocity field and the turbulence kinetic energy it is clear that on the average, turbulent kinetic energy increases at the expense of that of the mean flow by means of the expected value of the product of the fluctuating shear stresses and the mean gradient. Through this interaction, the nature of which is currently not established, turbulence gains energy of motion, which is then distributed among the velocity components via the pressure strain-rate. The interaction among the multitude of fluctuations of the turbulent field is non-linear, causing the energy to manifest in less than predictable configurations. Finally, energy can be shown to be leaving the turbulent flow via friction. The work done by the fluid elements in resisting the deformative action of the fluctuating strain dissipates energy from the fluctuations.

From such descriptions one can conclude only that energy of motion enters the system by some process involving some quantities and that energy leaves the system by some other process. The more precise nature of the processes by which the turbulent velocity fluctuations sustain themselves and re-distribute their kinetic energy remain to be established. In order to glean some insight into the internal goings on of the turbulence one can attempt to assess what happens at various scales of motion. Of particular interest is exactly how motion of a certain scale interacts with motions at other scales. Classically, and contemporarily, this can be done with the aid of Fourier analysis of the velocity field realizations, but only when the turbulence is homogeneous, i.e. when

the statistical quantities are independent of position. In that case turbulence kinetic energy is attributed to a continuum of scales, on the average. The equations for the turbulence expressed on this basis elucidate that the non-linear energy transportation among the different size structures can be viewed as an exchange between triads of wavenumbers, facilitating energy transport among very different sized structures.

The turbulent round jet has been shown to exhibit several homogeneous flow directions when expressed in the coordinate system ξ, η, θ, t. Of the four space-time axes, the turbulence remains inhomogeneous only along the radial η-axis. Section 3.1 describes the expansion of the turbulence in terms of Fourier modes along ξ, θ, t. An empirical method for establishing some workable orthogonal basis for the radial variation of fluctuation is given in section 3.2. The full composite expansion is then assembled in section 3.3. Lastly, section 3.4 addresses what sources of useful turbulence data is available and the subsection 3.5 outlines the experiments that were performed.

3.1 Fourier analysis in homogeneous coordinate directions

Expressing the turbulent fluctuating velocity field in terms of Fourier modes amounts to Fourier transformation along axes where the flow is non-periodic, i.e. along ξ and t, and Fourier series expansion along the 2π-periodic flow direction θ.

3.1.1 Fourier series expansion in θ

The Fourier series expansion provides a countably infinite number of modes which correspond the complex exponentials of integer multiples of the period. A basis formed from the Fourier modes is orthogonal on $[0, 2\pi]$ since

$$(e^{in\theta}, e^{im\theta}) = \int_{-\pi}^{\pi} e^{i\theta(m-n)} d\theta = 2\pi\delta_{mn} \tag{3.1}$$

With this in mind the 2π-periodic velocity field can be expanded as

$$u_i(\theta) = \sum_{-\infty}^{\infty} c_i^m e^{im\theta} \tag{3.2}$$

$$c_i^m = \frac{1}{2\pi}(e^{im\theta}, u_i)_{[-\pi,\pi]} = \frac{1}{2\pi}\int_{-\pi}^{\pi} u_i(\theta) e^{-im\theta} d\theta \tag{3.3}$$

where the standard notation for the coefficient of mode number 'm' has been modified to make room for the index notation. Note also that the use of 'i'

serves both as an independent tensor index and as the definition $i = \sqrt{-1}$ and should not be interpreted as a repeated index.

The the expected value of the product of any two Fourier coefficients is

$$\langle c_i^{n*} c_j^m \rangle = \left(\frac{1}{2\pi}\right)^2 \langle (u_i, e^{in\theta})(e^{im\theta'}, u_j) \rangle \tag{3.4}$$

$$= \left(\frac{1}{2\pi}\right)^2 \int_{-\pi}^{\pi} d\theta \int_{-\pi}^{\pi} d\theta' \langle u_i(\theta) u_j(\theta + \vartheta) \rangle e^{i(n\theta - m(\theta+\vartheta))} \tag{3.5}$$

$$= \delta_{mn} \frac{1}{2\pi} \int_{-2\pi}^{2\pi} B_{i,j}(\vartheta) e^{-in\vartheta} d\vartheta \tag{3.6}$$

3.1.2 Fourier transformation in ξ and t

The Fourier transform can be viewed as a generalization of the Fourier series as the period which defines the domain approaches infinity. The discrete nature of the Fourier series melds into a continuous space of frequencies. Orthogonality properties of the transform dictate that,

$$\lim_{T\to\infty} \frac{1}{T} (e^{it(2\pi n/T)}, e^{it(2\pi m/T)})_{[-T/2,T/2]} = \delta(\omega' - \omega) = \int_{-\infty}^{\infty} e^{it(\omega'-\omega)} dt \tag{3.7}$$

where it is presumed that $\lim_{T\to\infty} 2\pi n/T = 2\pi f = \omega$. Thus any non-periodic, square integrable function $g(t)$ can be represented as an infinite sum of uncountably many complex trigonometric functions:

$$g(t) = \int_{-\infty}^{\infty} \hat{g}(\omega) e^{i\omega t} d\omega \tag{3.8}$$

$$\hat{g}(\omega) = \frac{1}{2\pi} \int_{-\infty}^{\infty} g(t) e^{-i\omega t} dt \tag{3.9}$$

The turbulent fluctuations along the temporal and streamwise axes are non-periodic, homogeneous functions. While the homogeneity is what enables the use of Fourier analysis (due to the non-developing statistical nature of these flows) it also introduces concern for the convergence criteria for the representation, namely the square-integrability of the represented function. Clearly a non-periodic homogeneous velocity field is of infinite extent and therefor not a candidate of Fourier transformation in the ordinary sense. This inconvenience is by-passed by defining the transforms in the sense of generalized functions (Lumley [28], George[29]). This ensures the ability to treat infinite functions by standard integral methods of calculus by introducing a function with a more compact nature with limit 1.

The velocity field can then be defined as the inverse Fourier transform of the Fourier transformed velocity, defined as

$$u_i(\xi,t) = \int_{-\infty}^{\infty} d\kappa \int_{-\infty}^{\infty} df \hat{\hat{u}}_i(\kappa,f) e^{i(\kappa\xi+2\pi ft)} \tag{3.10}$$

$$\hat{\hat{u}}_i(\xi,t)_{g.f.} = \frac{1}{2\pi}\int_{-\infty}^{\infty} d\xi \int_{-\infty}^{\infty} dt u_i(\kappa,f) e^{-i(\kappa\xi+2\pi ft)} \tag{3.11}$$

Due to orthogonality, the transforms are un-correlated in non-overlapping wavenumber bands:

$$\langle \hat{\hat{u}}_i^*(\kappa,f)\hat{\hat{u}}_j(\kappa',f')\rangle = \delta(\kappa'-\kappa)\delta(f'-f)\int_{-\infty}^{\infty} d\tau \int_{-\infty}^{\infty} d\zeta B_{i,j}(\zeta,\tau) e^{-i(\kappa\zeta+2\pi f\tau)} \tag{3.12}$$

3.2 Proper Orthogonal Decomposition

The remaining space axis is the radial η- direction. The turbulence is not homogeneous along this axis so that the standard continuous space of Fourier modes does not constitute an orthogonal basis for the variation along η. Thus some other means of establishing a workable basis should be found. One such method is the proper orthogonal decomposition (POD), which can be used to establish a space of orthogonal functions from *a priori* knowledge of sampled data. As the name implies, POD is can yield a set of mutually orthogonal functions that are properly ordered with respect to the most efficient convergence to the cross-correlation of the function so approximated. The methodology is centered on the concept of the inner product of two functions as a means of establishing a best approximation of one to the other. For example, one can approximate one realization of the random turbulent velocity field $u_i(x), x \in \Omega$ by some deterministic function $\phi_i(x)$. If both the velocity field and ϕ are square integrable functions in Ω their inner product can be stated as

$$\alpha = (\phi_i, u_i)_\Omega = \int_\Omega u_i(x)\phi_i^*(x)dx \tag{3.13}$$

where '*' indicates complex conjugate and Einstein summation over the repeated index is implied. Further, assume ϕ_i to be of unit length so that $|\phi_i| = (\phi_i,\phi_i)^{1/2} = 1$ and proceed to constrain the available functions to the one that maximizes the projection $|\alpha|^2$ in an ensemble average sense, i.e.,

$$\langle|\alpha|^2\rangle = \frac{\langle(\phi_i,u_i)(u_k,\phi_k)\rangle}{|\phi|^2} = \frac{\int\int_\Omega \langle u_i(x)u_k^*(y)\rangle\phi_i^*(x)\phi_k(y)dxdy}{\int_\Omega \phi_i^*(x)\phi_i(x)dx} \tag{3.14}$$

where $\langle\rangle$ indicates the expected value of the ensemble.

By perturbing $\phi_i(x)$ with some small variation $\delta\phi_i(x)$ and requiring that the projection $\langle|\alpha|^2\rangle$ remains unchanged, one deduces an equation which constrains the unknown functions ϕ_i:

$$\int_\Omega B_{i,k}(x,y)\phi_k(y)dy = \lambda\phi_i(x) \tag{3.15}$$

This equation is a homogeneous Fredholm integral equation of the second kind where kernel $B_{i,k}(x,y) = \langle u_i(x)u_k(y)^*\rangle$ is the two-point correlation tensor function and the scalar $\lambda = \langle|\alpha|^2\rangle$. If there exist non-trivial solutions $\phi_i(x)$ to equation 3.15, then $1/\lambda$ is referred to as the the characteristic value of the equation. The non-trivial solutions are called the eigenfunctions of the equation. If $1/\lambda$ is a characteristic value of 3.15 then λ is called an eigenvalue of the integral equation [30]. The eigenfunctions will form a denumerably infinite space of orthogonal functions

$$(\phi_i^{(n)}, \phi_i^{(m)}) = \delta_{mn} \tag{3.16}$$

where $n = 1, 2, ...$ is the POD mode number. This sequence of integers is established by the size of the corresponding eigenvalues λ_n so that $\lambda_1 > \lambda_2$, etc. If the kernel is real symmetric or Hermitian symmetric in its argument the eigenvalues will be real and positive.

As stated in equation 3.15 the purpose of establishing the basis $\phi_i^{(n)}(x)$ is to expand the individual velocity realizations on it. It should be noted that the optimization equation 3.14 pertains to the expected value of the total energy of the field in the domain Ω, not to the velocity fields themselves. Nonetheless, once a basis has been established from the solutions to equation 3.15, one can proceed to establish the distribution of instantaneous kinetic energy over the space by means of the inner product:

$$a_n = (\phi_i^{(n)}, u_i)_\Omega = \int_\Omega u_i(x)\phi_i^{(n)*}(x)dx \tag{3.17}$$

where summation over $i = 1, 2, 3$ is implied. Note that since ϕ_i is a deterministic function, the stochastic nature of the velocity fluctuation u_i has been transferred to the coefficients a_n. However, the expected value of the magnitude of products of the coefficients corresponding to different mode numbers is zero. This can be shown using the definition 3.15 and the orthogonality of the basis:

$$\begin{aligned}\langle a_n^* a_m\rangle &= \langle(u_i, \phi_i^{(n)})(\phi_j^{(m)}, u_j)\rangle = \int_\Omega dx\ \phi_i^{(n)}(x)\int_\Omega \langle u_i(x)u_j(x')\rangle\phi_j^{(m)*}(x')dx' \\ &= \lambda_m(\phi_i^{(m)}, \phi_i^{(n)}) = \lambda_n\delta_{mn}\end{aligned} \tag{3.18}$$

Given equation 3.18 and orthogonality it is easy to see that the correlation

function is recovered as

$$B_{i,j}(x,x') = \sum_{n=1}^{\infty} \lambda_n \phi_i^{(n)}(x) \phi_j^{(n)*}(x') \tag{3.19}$$

and that the expected total energy of the turbulence is simply the full sum of the eigenvalues λ_n:

$$B_{i,i}(x,x) = \langle u_i(x) u_i(x) \rangle = \sum_{n=1}^{\infty} \lambda_n \tag{3.20}$$

Due to the monotonously decreasing magnitudes of λ_n with increasing mode number n, it is clear that the sequence of eigenfunctions so ordered are optimized with respect to the energy.

Depending on the nature of the kernel and the domain Ω, the solution set will vary. Analytical solution can be found for several forms of the kernel, such as when the kernel is separable or for a kernel constructed from known polynoms, exponential or trigonometric functions [30]. However, for the non-homogenous turbulence correlation tensor function this is not the case. Therefor the issue of determining the eigenfunctions and corresponding eigenvalues is typically approached by discretizing the integral equation using a kernel formed from known turbulence cross-correlation data and solving the resulting to a matrix eigenvalue problem. The correlation data can be found from sampling laboratory experiments (George et al.[31], Glauser[32], Glauser & George [33], Delville et al. [34], Citriniti[35], Gordyev & Thomas [36], Citriniti & George [37], Tinney et al.[38]) or numerical simulations (Noack et al.[39, 40]).

3.3 Composite Decomposition

Bringing together the decompositions outlined above, the space-time velocity field corresponding to one possible realization for the far round turbulent jet can be expressed as:

$$u_i(\xi,\eta,\theta,t) = \int_{-\infty}^{\infty} df \int_{-\infty}^{\infty} d\kappa \sum_{m=-\infty}^{\infty} e^{i(\kappa\xi + 2\pi f t + im\theta)} \sum_{n=1}^{\infty} a_n(\kappa,m,f) \phi_i^{(n)}(\eta) \tag{3.21}$$

where the POD basis $\phi_i^{(n)}(\eta)$ is determined by the eigenfunctions of the integral equation 3.22:

$$\int_0^{\infty} \Psi_{i,j}(\eta,\eta';\kappa,m,f) \phi_j(\eta') \eta' d\eta' = \lambda(\kappa,m,f) \phi_i(\eta) \tag{3.22}$$

Here the kernel $\Psi_{i,j}(\eta,\eta';\kappa,m,f)$ is what remains of the two-point correlation tensor after Fourier transformation in $\tau = t' - t$ and $\zeta = \xi' - \xi$ and Fourier series expansion in $\vartheta = \theta' - \theta$:

$$\Psi_{i,j}(\eta,\eta';\kappa,m,f) = \frac{1}{(2\pi)^2}\int_{-\infty}^{\infty} d\zeta \int_{-\infty}^{\infty} d\tau \int_{-\pi}^{\pi} d\vartheta R_{i,j}(\zeta,\eta,\eta',\vartheta,\tau) e^{-i(\kappa\zeta + m\vartheta + 2\pi f\tau)} \tag{3.23}$$

which can also be viewed as the expected values of the Fourier transforms of the Fourier expansion coefficients, i.e,

$$\langle \hat{\hat{c}}_i^{m*}(\kappa,\eta,f)\hat{\hat{c}}_j^{p}(\kappa',\eta',f')\rangle = \Psi_{i,j}(\eta,\eta',\kappa,m,f)\delta_{pm}\delta(\kappa'-\kappa)\delta(f'-f) \tag{3.24}$$

Once the basis has been obtained, the random POD coefficients $a_n(\kappa,m,f)$ are found by projecting the realization on the constructed basis, i.e.,

$$a_n(\kappa,m,f) = (\phi_i^n(\eta), \hat{\hat{c}}_i^m(\eta;\kappa,m,f)) = \int_0^{\infty} \hat{\hat{c}}_i^m(\eta;\kappa,m,f)\phi_i^{(n)*}(\eta)\eta d\eta \tag{3.25}$$

where $\hat{\hat{c}}_i^m(\kappa,\eta,m,f)$ is given by

$$\begin{aligned}\hat{\hat{c}}_i^m(\kappa,\eta,m,f) &= \frac{1}{(2\pi)^2}(e^{i(\kappa\xi+m\theta+2\pi ft)}, u_i(\xi,\eta,\theta,t)) \\ &= \frac{1}{(2\pi)^2}\int_{-\infty}^{\infty} d\xi \int_{-\infty}^{\infty} dt \int_{-\pi}^{\pi} u_i(\xi,\eta,\theta,t) e^{-i(\kappa\xi+m\theta+2\pi ft)} d\theta\end{aligned} \tag{3.26}$$

As in section 3.2, the orthogonality of the POD basis ensures that the expected value of products of basis coefficients is non-zero only for self-products. These self-product are identical to the eigenvalues of 3.22, i.e.,

$$\langle a_n^*(\kappa,m,f)a_q(\kappa,m,f)\rangle = \lambda_n(\kappa,m,f)\delta_{qn} \tag{3.27}$$

which indicates that the Fourier represented correlation tensor 3.23 is simply found by:

$$\Psi_{i,j}(\eta,\eta',\kappa,m,f) = \sum_{n=1}^{\infty} \lambda_n(\kappa,m,f)\phi_i(\eta)\phi_j^*(\eta') \tag{3.28}$$

In fact, from relations 3.27 and 3.24 it is then clear that

$$\langle a_n^*(\kappa,m,f)a_q(\kappa',p,f')\rangle = \lambda_n(\kappa,m,f)\delta_{qn}\delta_{pm}\delta(\kappa'-\kappa)\delta(f'-f) \tag{3.29}$$

and the original correlation tensor (the inverse Fourier transform of equation 3.23) is thus constructed as:

$$B_{i,j}(\zeta,\eta,\eta',\vartheta,\tau) = \int_{-\infty}^{\infty} d\kappa \int_{-\infty}^{\infty} df \sum_{m=-\infty}^{\infty} \Psi_{i,j}(\kappa,\eta,\eta',m,f) e^{i(\kappa\zeta+m\vartheta+2\pi f\tau)}$$
$$= \sum_{n=1}^{\infty} \phi_i^{(n)}(\eta)\phi_j^{(n)*}(\eta') \sum_{m=-\infty}^{\infty} \int_{-\infty}^{\infty} d\kappa \int_{-\infty}^{\infty} df \lambda_n(\kappa,m,f) e^{i(\kappa\zeta+m\vartheta+2\pi f\tau)} \tag{3.30}$$

3.4 Choice of data source for POD kernel

The premier requirement on the data set that can facilitate the decomposition is that it allows for Fourier transformation in the streamwise similarity coordinate axis ξ. Further, the flow cannot be expected to behave as homogeneous along this axis until the jet flow has developed past its near field state which is to say that it is fully turbulent across its cross-section and that linear growth has been established, indicating that the turbulence develops in equilibrium with itself. Previous work indicates that this state does not occur until at a downstrem position of approximately $x/D = 30$, where D is the diameter of the jet nozzle exit. Moreover, as shown later, the data must be available from downstream till $x/D > 90$ to avoid spectral leakage due to the finite window Fourier transforms. This effectively rules out any direct numerical simulations (DNS) as a potential source of data, as these are at the time limited $x/D < 30$. The very large domain length requirement makes large eddy simulations (LES) unrealistic. In summary, data resulting from contemporary numerical simulations was deemed unsuitable for the objective of the analysis.

In terms of experimental acquisition of large domain simultaneous turbulent velocity data only one sampling technique was suitable at the time of the thesis proposal, namely particle image velocimetry (PIV). With PIV velocity components within and parallel to a sheet-like laser plane can be estimated from the imaged displacements of light scattered by particles in the flow between two instances in time. With the use of a stereoscopic setup the third component of velocity can be backed out given a careful calibration. At the time of the writing of this thesis it is also possible to use high-repetition PIV systems to provide frequency content. However, at the the onset of the thesis work, this was not an available resource. Thus the methodology could provide data only along planar spatial extents. A more thorough description of the principles of PIV, its capabilities, limitations and influence on the attempted analysis is given in a subsequent chapter.

3.5 Experimental objective and the experiments implemented

Via a collaboration with the Technical University of Denmark (DTU) an experimental venture was proposed that utilized the PIV resources of the Fluid Mechanics Laboratory of the department of Mechanics, Energy and Construction and the jet flow facility was relocated from Sweden to Denmark.

Initially, it was attempted to evaluate the velocity field simultaneously along two planes, one intersecting the centerline axis of the jet to provide measurements for the streamwise Fourier analysis and the other perpendicular to the first, to provide data for the cross-plane Fourier and POD analysis. This configuration of sampling could utilize the inherent rotational symmetries of the flow to make inferences about the full expansion of equation 3.26. In particular it would preserve some foundations for drawing conclusions about the interaction between streamwise modes and radial modes in the samples. This was to be realized by simultaneous two-component (2C) measurements in the streamwise plane and stereoscopic measurements in the cross-plane, facilitated by the use of four cameras and two laser systems.

This approach was indeed attempted in the initial stages of the doctoral work, but eventually proved beyond the capacities of the experimenters as then insurmountable problems with the laser scattering configurations, leading to overexposure of the camera sensors in the vital overlap region of the two systems. It was decided at last to focus on what could be done, namely experimental investigations of the two planes separately. The experiments are described in detail in a subsequent chapter.

Part I

STREAMWISE EXPERIMENT

4. STREAMWISE PLANAR PIV - EXPERIMENTAL SPECIFICATIONS AND IMPLEMENTATION

The previous chapter outlined the analysis that one would like to be able to perform - of a perfectly realized flow, perfectly sampled with a perfect instrument of infinite scope and infinitesimal probe size. However, the chapter also describes the ultimate choice of measurement procedure, both in terms of what correlation entities that will have to suffice and what was finally realized. This chapter concerns itself with the design of the above outlined experiments, with particular emphasis on the domain extent required in order to facilitate the spectral analysis in the streamwise direction, see section 4.1, and the POD analysis in the radial direction, section 4.2. In addition, an estimate of the number of independent samples required to estimate converged statistics is estimated in in section 4.3.

Section 4.4 describes the the planar PIV experiment and the evaluation of the single point statistics of the measured velocity field section 4.5 concludes this chapter.

4.1 Spectral analysis of discrete fields of finite extent

Consider first the idealized case of a homogeneous, non-periodic, continuous velocity $u_i(\xi)$ varying over an infinite domain $\xi \in R$ so that:

$$u_i(\xi) = \int_{-\infty}^{\infty} \hat{u}_i(\kappa) e^{i\kappa\xi} d\kappa \tag{4.1}$$

$$\hat{u}_i(\kappa) = \frac{1}{2\pi} \int_{-\infty}^{\infty} u_i(\xi) e^{-i\kappa\xi} d\xi \tag{4.2}$$

Note that throughout the text $\hat{}$ over the same function name will be used to indicate the Fourier transform; e.g., $\hat{u}$ is the Fourier transform of the function u.

The cross-spectral density is zero in non-overlapping wavenumber bands while the expected value per unit wavenumber is the cross-spectral tensor

function $F_{i,j}(\kappa)$:

$$\langle \hat{u}_i(\kappa)^* \hat{u}_j(\kappa') \rangle d\kappa' d\kappa = F_{i,j}(\kappa)\delta(\kappa' - \kappa)d\kappa \tag{4.3}$$

where

$$B_{i,j}(\zeta) = \int_{-\infty}^{\infty} F_{i,j}(\kappa) e^{i\kappa\zeta} d\kappa \tag{4.4}$$

$$F_{i,j}(k) = \frac{1}{2\pi} \int_{-\infty}^{\infty} B_{i,j}(\zeta) e^{-i\kappa\zeta} d\zeta \tag{4.5}$$

and $B_{i,j}(\zeta) = \langle u_i(\xi) u_j(\xi + \zeta) \rangle$ is the two-point correlation function and $\zeta = \xi' - \xi$. This signal will serve as a baseline case to which will be compared the spectra and correlation functions estimated using finite domain widths and finite spatial resolution.

4.1.1 Windowing - spectral leakage due to finite domain

The spectral distortion effect called windowing is due to failing to sample a large enough contiguous piece of the available process. The windowed velocity signal can be expressed as $u_i^{L_\xi}(\xi) = u_i(\xi) w_{L_\xi}(\xi)$ where $w_{L_\xi}(\xi)$ is any symmetric, continuous window function in ξ-space of width L_ξ. The finite domain width estimator for the spectral tensor function is:

$$F_{i,j}^{L_\xi}(\kappa) = \frac{2\pi}{L_\xi} \langle \hat{u}_i^{L_\xi *}(\kappa) \hat{u}_j^{L_\xi}(\kappa) \rangle \tag{4.6}$$

The convolution theorem for the definition of the Fourier transform used in this work is:

$$h_1(r) = f(x) \otimes g(x) = \int_{-\infty}^{\infty} f(x) g(r - x) dx \tag{4.7}$$

$$h_2(r) = f(x) \odot g(x) = \int_{-\infty}^{\infty} f(x) g(x + r) dx, \tag{4.8}$$

$$\hat{h}_1(k) = 2\pi \hat{f}(k) \hat{g}(k) \tag{4.9}$$

$$\hat{h}_2(k) = 2\pi \hat{f}(k)^* \hat{g}(k) \tag{4.10}$$

$$\widehat{fg} = \hat{f}(k) \otimes \hat{g}(k) \tag{4.11}$$

$$\tag{4.12}$$

Evaluating the finite width estimator 4.6 with the convolution theorem, it can be shown that:

$$F_{i,j}^{L_\xi}(\kappa) = \frac{1}{2\pi L_\xi} \int_{-\infty}^{\infty} B_{i,j}(\zeta) W_{L_\xi}(\zeta) e^{-ik\zeta} d\zeta \tag{4.13}$$

where the ζ - window function $W_{L_\xi}(\zeta)$ is the symmetric convolution of the ξ-space window $w_{L_\xi}(\xi)$. Due to the finite width of the windows this convolution is:

$$W_{L_\xi}(\zeta) = [w_{L_\xi} \odot w_{L_\xi}](\zeta) = \int_{-\infty}^{\infty} w_{L_\xi}(\xi) w_{L_\xi}(\xi+\zeta) d\xi$$
$$= \begin{cases} \int_{\zeta - L_\xi/2}^{L_\xi/2} w_{L_\xi}(\xi) w_{L_\xi}(\xi+\zeta) d\xi & , \quad \zeta > 0 \\ \int_{-L_\xi/2}^{\zeta + L_\xi/2} w_{L_\xi}(\xi) w_{L_\xi}(\xi+\zeta) d\xi & , \quad \zeta < 0 \end{cases} \tag{4.14}$$

This corresponds to:

$$F_{i,j}^{L_\xi}(\kappa) = F_{i,j}(\kappa) \otimes \frac{1}{L_\xi} \hat{W}_{L_\xi}(\kappa) = F_{i,j}(\kappa) \otimes \frac{2\pi}{L_\xi} |\hat{w}_{L_\xi}(\kappa)|^2 \tag{4.15}$$

i.e., the windowed spectrum $F_{i,j}^{L_\xi}(\kappa)$ is obtained as the Fourier space convolution of the true spectrum $F_{i,j}(\kappa)$ and the magnitude of the Fourier transform of window function $w_{L_\xi}(\xi)$ divided by the window width. The influence on the velocity correlation tensor function can immediately be shown to be:

$$B_{i,j}^{L_\xi}(\zeta) = \int_{-\infty}^{\infty} F_{i,j}^{L_\xi}(\kappa) e^{i\kappa\zeta} d\kappa = B_{i,j}(\zeta) \frac{W_L(r)}{L_\xi} = B_{i,j}(\zeta) \frac{[w_{L_\xi} \odot w_{L_\xi}](\zeta)}{L_\xi} \tag{4.16}$$

For a rectangular ξ window function

$$w_{L_\xi}(\xi) = \begin{cases} 1 & , \quad |\xi| \le L_\xi/2 \\ 0 & , \quad |\xi| > L_\xi/2 \end{cases} \tag{4.17}$$

$$\hat{w}_{L_\xi}(\kappa) = \frac{L_\xi}{2\pi} \frac{sin(\kappa L_\xi/2)}{\kappa L_\xi/2} \tag{4.18}$$

the ζ -space window is

$$W_{L_\xi}(\zeta) = \begin{cases} L_\xi - |\zeta| & , \quad |\zeta| \le L_\xi \\ 0 & , \quad |\zeta| > L_\xi \end{cases} \tag{4.19}$$

$$\hat{W}_{L_\xi}(\kappa) = \frac{1}{2\pi} \left[\frac{sin(\kappa L_\xi/2)}{\kappa/2} \right]^2 \tag{4.20}$$

so that the finite domain window spectral and correlation tensor functions for a rectangular unit window is:

$$B_{i,j}^{L_\xi}(\zeta) = B_{i,j}(\zeta) \left[1 - \frac{|\zeta|}{L_\xi} \right] \tag{4.21}$$

$$F_{i,j}^{L_\xi}(\kappa) = F_{i,j}(\kappa) \otimes \frac{L_\xi}{2\pi} \left(\frac{\sin(\kappa L_\xi/2)}{\kappa L_\xi/2} \right)^2 \tag{4.22}$$

NB: For our definition of the Fourier transform, the delta function is:

$$\mathcal{F}[1] = \delta(\kappa) = \lim_{R\to\infty} \frac{R}{\pi}\frac{sin(\kappa R)}{\kappa R} \tag{4.23}$$

$$\mathcal{F}[\delta(x)] = \frac{1}{2\pi} \tag{4.24}$$

so that it is evident that as $L_\xi \to \infty$, $W_{L_\xi}(\zeta) \to 1$ and $F^L_{i,j} \to F_{i,j}(\kappa)$.

Model of effect of windowing on turbulence correlation
In order to establish some measure for the required length of the window L_ξ in the experiment a model for $B(\zeta)$ was used:

$$B_m(\zeta) = Ae^{-|\zeta|/I_\xi} \tag{4.25}$$

where $A = \langle u^2 \rangle$ and I_ξ is the integral scale along the ξ - axis. The spectrum associated with this is given by its Fourier transform which is:

$$S_m(\kappa) \;=\; \frac{A}{2\pi}\int_{-\infty}^{\infty} e^{-|\zeta|/I_\xi}e^{-i\kappa\zeta}d\zeta = \frac{AI_\xi}{\pi}\left[\frac{1}{1+(\kappa I_\xi)^2}\right] \tag{4.26}$$

The finite domain window version of the model spectrum is then :

$$\begin{aligned} F_m^{L_\xi}(\kappa) &= \frac{A}{2\pi}\int_{-L_\xi}^{L_\xi} B_m(\zeta)\left[1-|\zeta|/L_\xi\right]e^{-i\kappa\zeta}d\zeta \\ &= F_m(\kappa)\left\{1 - b^{-1}\left[\frac{1-(\kappa I_\xi)^2}{1+(\kappa I_\xi)^2} - e^{-b}\frac{1-(\kappa I_\xi)^2}{1+(\kappa I_\xi)^2}cos(\kappa L_\xi)\right.\right. \\ &\quad \left.\left. - \; e^{-b}\frac{\kappa I_\xi}{1+(\kappa I_\xi)^2}sin(\kappa L_\xi)\right]\right\} \end{aligned} \tag{4.27}$$

where the scalar $b = L_\xi/I_\xi$ is the ratio of the domain window width to the integral scale.

Figure 4.1(a) and 4.1(b) shows the function 4.27 evaluated for various values of b on linear and logarithmic axes, respectively. As is evident from the graphs, the spectral estimates obtained in this fashion suffer drastically from spectral leakage unless $b = L/I$ is larger than 10. In order to ensure leakage-free spectral estimates from the experimental data a conservative choice of $L_\xi/I_\xi = 20$ was made.

The important length scale is the integral scale along the ξ- axis, but that the measurements must take place in Cartesian laboratory space. Thus the Cartesian domain window width $L_x = x_b - x_a$ which yields the appropriate domain width $L_\xi = 20I_\xi$ is

$$L_x = x_a\left(\frac{x_b}{x_a} - 1\right) = x_a\left(e^{\xi_b - \xi_a} - 1\right) = x_a\left(e^{L_\xi} - 1\right) \tag{4.28}$$

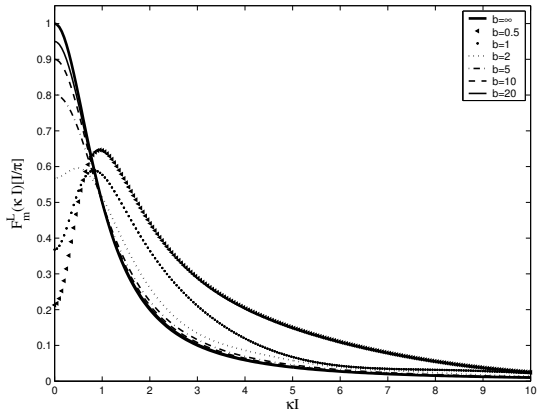

(a)

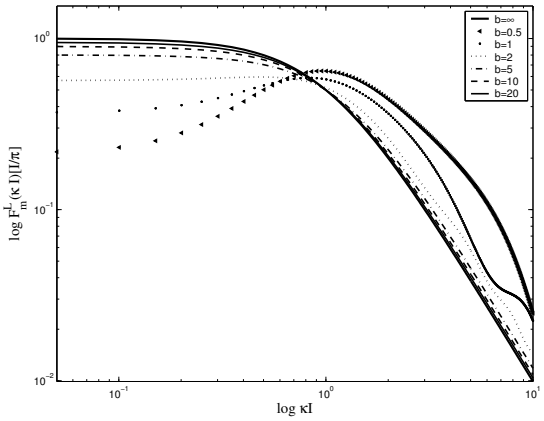

(b)

Fig. 4.1: Model spectrum. Spectral leakage varying with $b = L_\xi / I_\xi$.
(-) b=∞ (–) b=20 (- -) b=10 ($\cdot$ - $\cdot$) b=5 ($\cdots$) b=2 ($*$) b=1 ($\triangleleft$) b=0.5 .

An estimate for the integral scale I_ξ along the jet centerline can be found from the correlation coefficients obtained by Frohnapfel [41] by means of constant temperature anemometry (hotwire) and laser doppler anemometry (LDA) (these are shown in the next chapter as figure 5.3). Integrating under the curves gives $I_\xi \approx 0.055$ so that $L_\xi = 20I_\xi = 1.1$. Thus the domain window length in the laboratory space, $L_x = x_a(e^{1.1} - 1) \approx 2x_a$. Clearly the required domain window length must increase with the position of the upstream boundary point of the window. As mentioned previously, the logarithmic mapping only applies after the flow achieves similarity, i.e., for $x/D \geq 30$. For this choice of the upstream boundary of the window, the window width required is $L_x = 60D$; so the downstream window boundary point will be located at $x_b \geq 90D$. In the jet facility the diameter is $D = 10m$m so that $x_a - x_b = 600m$m.

4.1.2 Spatial resolution of turbulence scales

In this section the output from the PIV will be assumed to produce the same statistics as a probe which averages uniformly across the measuring volume. When representing turbulence at a point x_i with the local average over a measuring volume centered centered at location x_i, the velocity evaluated will be the spatial convolution of the turbulence $u_i(\vec{x})$ with the probe window functions $w_l(\vec{x})$, i.e.,

$$u_i^l(\vec{x}) = \int_{-\infty}^{\infty} u_i(\vec{y}) w_l(\vec{y} - \vec{x}) d\vec{y} \tag{4.29}$$

If the probe window is rectangular in all three spatial directions, and has width l_i, the probe window $w_l(\vec{x})$ is given by

$$w_l(\vec{x}) = \begin{cases} \frac{1}{l_1 l_2 l_3} & , \quad |x_i| \leq l_i/2 \\ \\ 0 & , \quad |x_i| > l_i/2 \end{cases}$$

The effect of sampling turbulence with a finite measuring volume is to filter out fluctuations smaller than the probe volume. As turbulent fluctuations vary over a very large range of scales, it is inevitable that the sampling filters out of the signal. In an attempt to estimate the amount of filtering by a certain volume size, a model for isotropic turbulence was used to define a resolution for the experiment. It should be noted that such a model can never be used to correct data from inhomogeneous turbulence, since the modeled energy spectrum can only be expected to be an adequate representation of the smallest scales, which are considered as locally isotropic. The larger scales in jet turbulence, which are decidedly anisotropic in nature, will be incorrectly represented. Therefore it is important to stress that the objective of investigating the filtering caused by a measuring volume with an isotropic turbulence spectral model is for convenience and lack of appropriate alternatives only. The

results of the analysis are for preparatory use, as they should be indicative of the relative effect of spatial filtering on the data.

4.1.3 Filtering model for isotropic turbulence sampled by 3D rectangular probe

Isotropic turbulence is by definition homogenous, so the three-dimensional spectral tensor can be used:

$$\langle \hat{u}_i^{l*}(\vec{k})\hat{u}_j^{l}(\vec{k'})\rangle = F_{i,j}^{l}(\vec{k})\delta(\vec{k'}-\vec{k}) \tag{4.30}$$

where

$$\hat{u}_i^{l}(\vec{k}) = \int_{-\infty}^{\infty} dx_1 \int_{-\infty}^{\infty} dx_2 \int_{-\infty}^{\infty} dx_1 [u_i(\vec{y}) \otimes w_l(\vec{y})](\vec{x}) e^{-i(\vec{k}\cdot\vec{x})} \tag{4.31}$$

From the convolution theorem,

$$F_{i,j}^{l}(\vec{k}) = (2\pi)^6 F_{i,j}(\vec{k})|\hat{w}_l|^2 \tag{4.32}$$

where

$$\hat{w}_l(\vec{k}) = \frac{1}{(2\pi)^3}\frac{sin(k_1 l_1/2)}{k_1 l_1/2}\frac{sin(k_2 l_2/2)}{k_2 l_2/2}\frac{sin(k_3 l_3/2)}{k_3 l_3/2} \tag{4.33}$$

$$F_{i,j}^{l_p}(k) = F_{i,j}(k)\left[\frac{sin(k_1 l_1/2)}{k_1 l_2/2}\right]^2\left[\frac{sin(k_2 l_2/2)}{k_2 l_2/2}\right]^2\left[\frac{sin(k_3 l_3/2)}{k_3 l_3/2}\right]^2 \tag{4.34}$$

The filtered homogeneous correlation tensor is then

$$B_{i,j}^{l}(\vec{r}) = B_{i,j}(\vec{r}) \otimes \frac{1}{l}\left[1 - \frac{|r|}{l}\right] \tag{4.35}$$

For isotropic turbulence the spectral tensor is

$$F_{i,j}(\vec{k}) = \frac{E(k)}{4\pi k^4}[k^2\delta_{ij} - k_i k_j] \tag{4.36}$$

where $k = |\vec{k}| = (\vec{k}\cdot\vec{k})^{1/2}$ and $E(k)$ is the three-dimensional energy spectrum function defined as

$$E(k) = \frac{1}{2}\int_{k=|\vec{k}|} F_{i,i} dS(k) \tag{4.37}$$

The isotropic energy spectrum model utilized here is the von Karman - Howarth spectrum, which attempts to represent the energetic scales and the scales in the inertial subrange only, while ignoring the exponential behavior observed in the purely dissipative range. The reason for choosing this model

is that the PIV experiments are not expected to be able to resolve any scales in the dissipative range. Again, it should be stressed that the isotropic model used below does not represent jet turbulence in any part of the energy spectrum and the results obtained are to be used for relative comparisons of the measuring volume size only.

The von Karman/Howarth energy spectrum model was parameterized by George & Wang [25]. The model below corresponds to their $p = 4$ version:

$$E(k) = C\frac{(kI)^4}{[1 + (kI/k_eI)^2]^{17/6}} \tag{4.38}$$

where I is the integral scale, C is a constant and the spectral peak k_e can be chosen (for the unfiltered case) to satisfy the energy and integral scale constraints (George and Wang [25]).

The results from such an analysis was performed for a previous experiment and was reported in [42]. A more detailed description of the procedure is available in appendix **??**. The conclusion was that for PIV interrogation window (IW) dimensions smaller than one tenth of the local integral length scale, approximately 12% of the variance of individual velocity fluctuation components was filtered out. This result is supported by Spenser & Hollis [43], and will be seen to be consistent with the turbulence intensities presented below.

In jet turbulence, the local integral length I_x varies with downstream position x. Utilizing the relationship between the local integral length in x and I_ξ, the (constant) integral length in ξ, and the values for I_ξ stated in the previous section, one obtains:

$$\frac{x + I_x}{x} = e^{I_\xi} \Leftrightarrow I_x = x(e^{I_\xi} - 1) = x(e^{0.055} - 1) = 0.056x \tag{4.39}$$

If the local resolution is required to be one tenth of the local integral length scale I_x, then the interrogation window dimension should vary as $d_{IW} \approx 0.006x$ in order to resolve the turbulence as it develops downstream. This was not possible in the experiments reported herein, due to commercial software limitations, so constant dimensions were maintained throughout. As will be seen in the next chapter, this somewhat complicates the interpretation of precisely at which wavenumbers the spatial spectra were affected by spatial filtering.

4.2 Requirements for POD analysis

The degree to which the sampled domain encompasses the jet radially is important for the POD analysis. In order for the POD modes to be uniquely determined the field should be square-integrable, i.e.,

$$\lim_{\bar{\eta}\to\infty} \int_0^{\bar{\eta}} \frac{\langle u_i(\eta) u_i(\eta) \rangle}{U_c(x)^2} \eta d\eta < \infty \tag{4.40}$$

From previous work by Gamard et al. [8] and Wanstrom [44] it appears that the integrand $\langle u_i(\eta) u_i(\eta) \rangle \eta / U_c(x)^2$ is zero for $\eta > 2.5$.

The discretization of the domain over which the POD integrals are computed is also important. Lumley 1970 [28] (see also Glauser and George 1992 [45] for a more complete discussion) showed that the number of POD modes required to capture the energy of an inhomogeneous domain was proportional to the size of the domain containing the energy divided by the integral scale of the process in that direction. As noted above the size of the domain in the radial direction required to capture most of its energy is $2.5\delta_{1/2}$, while the integral scale in the lateral direction can be estimated as approximately $\delta_{1/2}/2$. Thus a minimum of 5 modes is required. Since one vector POD mode is produced for each grid point and component of velocity, this means a minimum of five radial points (including the centerline) are required. For the streamwise experiment, 26 equally-spaced points were used, resulting in $2 \times 26 = 52$ vector POD modes.

4.3 Ensemble requirements

The analysis outlined in this work all consists of the decomposition of statistical quantities, so the quality of the results will be only be as trustworthy as the convergence levels of the finite realization estimators of said quantities. As will be indicated below, the variability, or relative deviation of the estimator from the expected value, decreases as the number of independent realizations increases. Thus a certain number of samples and the time separating them can be determined.

4.3.1 Variability of a finite sample estimator

The variability for finite sample estimator F_N of a function $f(u)$ of a random variable u is a measure for the degree of statistical convergence of the estimator relative to the expected value. If u_n corresponds to the n^{th} realization of the random variable u, its expected value (or ensemble average) $\langle u \rangle$ can be evaluated as the arithmetic average of an infinity of statistically independent realizations for u, i.e.,

$$\langle u \rangle = \lim_{N \to \infty} \frac{1}{N} \sum_{1}^{N} u_n \tag{4.41}$$

Any finite N estimator for $\langle u \rangle$, say U_N, deviates from the expected value due to the inability to perform an infinitude of experiments (or because the estimator is biased, but this will not feature in this outline). The finite estimated value U_N deviates from $\langle u \rangle$ by $U_N - \langle u \rangle$ and this deviation can be characterized by it's variance $var\{U_N\} = \langle (U_N - \langle u \rangle)^2 \rangle$. The relative statistical error, or variability of the finite sample estimator, is then a measure of the expected intensity of the deviation of the estimator,

$$\varepsilon^2_{U_N} = \frac{\langle (U_N - \langle u \rangle)^2 \rangle}{\langle u \rangle^2} = \frac{1}{N} \frac{\langle (u_n - \langle u \rangle)^2 \rangle}{\langle u \rangle^2} = \frac{1}{N} \frac{var\{u\}}{\langle u \rangle^2} \tag{4.42}$$

The expression for the variability can be generalized for any function of the random variable. If $f_n = f(u_n)$ is a function of the random variable u, the expected value is $\langle f \rangle$ and the variability of a finite sample estimator of $\langle f \rangle$, defined as $F_N = (1/N) \sum f_n$, is (if F_N defined this way is unbiased)

$$\varepsilon^2_{F_N} = \frac{\langle (F_N - \langle f \rangle)^2 \rangle}{\langle f \rangle^2} = \frac{1}{N} \frac{var\{f\}}{\langle f \rangle^2} \tag{4.43}$$

The work herein depends on two-point quantities, both in the form of velocity correlations and in the form of spectral representations of velocity realizations. In order to perform such analysis from laboratory data, the number of acquired independent samples must be sufficiently large as to bring down the variability of the estimators used for the evaluation of the statistics.

4.3.2 Spectral estimator

The one-dimensional velocity spectrum function $F_{i,j}(k)$ for homogenous turbulence directly related to the expected value of the product of the Fourier transforms $\hat{u}_i(k)^*$ and $\hat{u}_j(k)$; $\langle F_{i,j}(k) \rangle \delta(k' - k) = \langle \hat{u}^*_i(k) \hat{u}_j(k') \rangle$. As has been shown above, the finite nature of the domain, L, influences the spectral tensor. The spectral tensor estimator for finite domain is given by:

$$F^L_{i,jn}(k) = \frac{2\pi}{L} \hat{u}^{L*}_{in}(k) \hat{u}^L_{jn}(k). \tag{4.44}$$

It can be shown that if the fourth order moments of the turbulence are jointly Gaussian that $\lim_{L \to \infty} var\{F^L_{i,j}\} \propto \langle F_{i,j} \rangle^2$ (George et al. 1978 [46] and Velte 2009 [47]). Thus the absolute error of any random spectrum formed from

the Fourier transforms of a single realization of a turbulent field is proportional to the expected value of the spectrum, at all wavenumbers, i.e., the uncertainty is distributed over the spectrum according to the magnitude of it's expected value and the relative error of a random spectrum is therefore unity and independent of wavenumber.

Because of this high variability, individual spectral estimates must be ensemble averaged over in order to reduce it; i.e.,

$$F^L_{i,jN}(k) = \frac{1}{N}\sum_1^N F^L_{i,jn}(k). \tag{4.45}$$

The variability is now given by:

$$\varepsilon^2_{F^L_{i,jN}} = \frac{\langle (F^L_{i,jN} - \langle F_{i,j}\rangle)^2\rangle}{\langle F_{i,j}\rangle^2} = \frac{1}{N}\frac{var\{F^L_{i,j}\}}{\langle F^L_{i,j}\rangle^2}. \tag{4.46}$$

Clearly the spectral error decreases inversely in proportion to the square root of the number of independent blocks (or frames) in this case.

In the current case, realizations from different frames are statistically independent because of the time-separation which allows the previously sampled field to be completely convected out of the field-of-view. If the local convection velocity is $U_{conv}(x) \approx 0.6U_c(x)$, $U_c(x) = BM_o^{1/2}(x-x_o)^{-1}$ and the nozzle exit velocity profile is a top-hat of velocity U_e, then $U_c(x) = B_uU_eD(x-x_o)^{-1}$, where $B_u = B\sqrt{\pi}/2$. For such a flow the time of passage through an $L = 3a$ long distance in the fully developed jet is

$$T = \int_a^{a+L}\frac{dx}{0.6U_c(x)} = \int_a^{4a}\frac{(x-x_o)}{0.6B_uU_eD}dx \approx \frac{25a^2}{2B_uU_eD} \tag{4.47}$$

In this case $B_u = 5.8$, $U_e = 31m/s$, $D = 0.01m$ and $a = 30D$ so the time between globally independent velocity fields comes out to be $T \approx 0.65s$, corresponding to a maximum allowable sampling frequency of 1.5 Hz. For the experiments reported herein, the sampling frequency was chosen to be 1 Hz.

4.4 Jet Facility and Flow

The jet facility used in these experiments was originally constructed at the State University of New York at Buffalo by Daehan Jung (now professor at the Korean Air Force Academy). It moved to Gothenburg with the move of the Turbulence Research Laboratory to Chalmers in 2000 and was used in the Ph.D. dissertation of Gamard in 2002 [48] (see also Gamard et al. 2004 [8]), and in the award-winning LDA/hot-wire studies of Frohnapfel 2003 [41]. Unfortunately

the space which the facility occupied at Chalmers was thought by the Applied Mechanics departmental administration to be more valuable to the university if unused. Moreover it was not possible to purchase or borrow a PIV system. In order to be able to perform the experimental studies required by the work that constitutes this thesis, the jet facility was moved to the Fluid Mechanics Laboratory of the Technical University of Denmark in the spring of 2005. For that reason the actual implementation of the experiment was carried out at DTU by MW in cooperation with Knud Erik Meyer, who is also a co-advisor to this thesis. The design specifications detailed in the previous section were created by the author while a Ph.D. student at Chalmers Technical University.

4.4.1 Jet Flow Generator

The jet generator used in both experiments described in this work was cubic box of dimensions $58.5 \times 58.5 \times 59cm^3$ fitted with a axisymmetric plexiglas nozzle, tooled into a 5^th order polynomial contraction from an interior diameter $D_1 = 6c$m to an exit diameter of $D = 1c$m. The interior of the box was stacked with foam baffles in order to damp out disturbances from the fan that supplied the generator with pressurized air. The air intake was located inside the the jet enclosure. For further details on the generator box, see Gamard [48]. The flow generating box rested on an aluminum frame which was in turn rigidly attached to a large two-axis traverse. This enabled the relative positioning of the measurements setup to the flow via the coordinate system defined by the axes of the traverse.

The exit velocity was monitored via a pressure tap in the nozzle positioned upstream of the contraction and connected to a digital manometer by a silicon tube. The pressure difference between the ambient and the pressure tap gave the exit velocity as

$$U_e = \sqrt{\frac{p_{amb} - p_{tap}}{\rho_a \left(1 - \left[\frac{D}{D_1}\right]^4\right)}} \tag{4.48}$$

where ρ_a is the density of the air, U_e is the magnitude of a tophat exit velocity profile and D_1 is the cross section diameter of the nozzle upstream of the contraction. This relation is derived from Bernouli's equation applied to a streamtube and assumes irrotational uniform flow at the nozzle exit and at the cross section of the pressure tap location.

The pressure tap output was recorded for each block of sampling. The source conditions of the jet were known from previous investigations (Gamard 2002 [49]), but were confirmed using a hotwire at the end of the experimental program. The exit profile corresponded to a top-hat with a small over-

shoot at the edge which is caused by the continuing curvature of the streamlines after the nozzle exit plane. The fluctuation level at the exit was about 0.3% and the frequency content was mostly broad-band noise with only a few weak peaks (attributed to electronic noise). The ambient pressure was monitored by an independent barometer. Temperature in the jet enclosure by both a thermocouple and an alcohol thermometer. The nominal exit velocity chosen was $U_e = 30.3m/s$, corresponding to an exit Reynolds number of $Re_D = U_e D/\nu = 20000$, where ν is the kinematic viscosity defined as $\nu = \mu/\rho$ for air at standard temperatures and pressure.

4.4.2 The jet flow enclosure

A free jet is a flow that issues into an infinite environment at rest. It's predominant physical characteristic is that the momentum crossing any downstream cross-section must be equal to the rate at which it is being added at the jet exit. In order to successfully mimic such a flow in a confined laboratory setting, the distance from the jet to the walls of the flow enclosure must large enough that the jet entrainment does not cause a significant return flow. The return flow contains negative momentum, which steals momentum from the jet itself (since the rate of momentum crossing any downstream cross-section must be constant), thus causing the momentum conservation which defines the free jet to be violated. Hussein et al. [16], using a simple model for the return flow, estimated the ratio of mean momentum at any downstream cross section, M, to the momentum added at the source, M_o, as

$$\frac{M}{M_o} = \left[1 + \frac{16x^2}{\pi B D^2}\frac{A_o}{A_R}\right]^{-1} \tag{4.49}$$

where $A_o = \pi D^2/4$ is the exit area of the nozzle and A_R is the cross section.

The enclosure utilized in the experiment was a large tent of dimension $2.5 \times 3 \times 10m^3$. The jet generator was positioned at the back of the enclosure, see sketch (generate sketch). The expected momentum conservation, based on equation 4.49 was estimated to be 100% at x/D=30 to 94% at x/D=90, see figure 4.4.2 below.

Thus the jet flow generated in the facility should be expected to correspond to a free jet up until x/D=70, and to be somewhat adversely affected by negative momentum addition beyond that position. If this effect is significant it would be expected to manifest in the data statistics as a decrease in the jet growth rate and in the centerline velocity decay (Hussein et al. [16]).

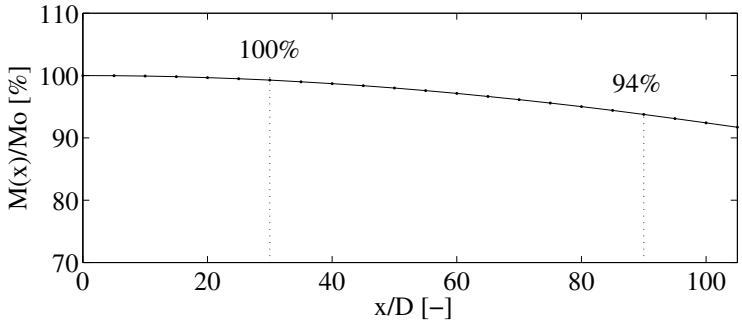

Fig. 4.2: Expected momentum conservation in jet issuing into enclosure. A return flow is caused by wall influence on jet entrainment and adds negative momentum to positive added at source, thereby 'stealing' momentum from the jet itself.

4.4.3 PIV Setup

Illumination was provided by a New Wave double-cavity 120 mJ YAG laser. A spherical lens and a cylindrical lens generated a thin expanding laser sheet which was reflected by a mirror positioned near the jet nozzle. The resulting sheet intersected the jet along its centerline and extended downstream according to figure 4.4.3. The laser sheet thickness in the composite field of view of the cameras was estimated to be approximately 2 mm.

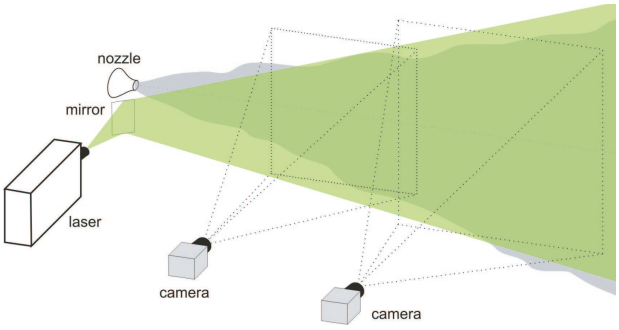

Fig. 4.3: Sketch of experimental setup.

In order to facilitate the large streamwise domain required by the design specification in sections 4.1.1 and 4.2, a composite field of view was created from two 4Mpixel HiSense cameras, generously made available as a loan from Dantec Dynamics. The sensor dimensions of the cameras were 2048 pixels by 2048 pixels where the pixel pitch was 7.4μm. As indicated by figure 4.4.3

the cameras were positioned along side each other on an aluminum beam rig positioned along the side of the tent. The viewing angles with respect to the laser sheet were both 90 degrees. The upstream camera was fitted with a 60 mm focal length lens while the downstream camera had a 50 mm lens. The aperture was $f^{\#} = 2.8$. The difference in magnification was designed adjust the measuring domain to account for the growth of the jet width. The mapping from the sensor coordinates to the laboratory coordinate system was a linear transformation. A set of images of a ruler were taken with the ruler traversed at high precision to different streamwise positions within the composite field of view.

Seeding particles were droplets of DEHS with an average particle diameter was $d_p = 2\mu$m. The corresponding particle time constant was estimated to be two order of magnitude lower than the Kolmogorov microtime throughout the flow. However, the low magnification imaging of these small particles means that the particle image diameters on the sensors are dominated by the diffraction limit, which can be estimated following Raffel et al. [50] to be on the order of the pixel pitch. Therefor the particle image diameter on the sensors is about 1 pixel. This has the effect of reducing the accuracy of the instantaneous particle displacement by reducing the accuracy of the sub-pixel Gaussian peak-fit.

In general, when using particle-based flow measurement techniques, one risks bias in the statistics of the estimated particle velocities if the expected particle density (number of particles per unit volume) varies in the flow, c.f., Buchhave et al. 1979 [51]. Thus it is important, form a fundamental point-of-view, that the seeding particles be uniformly distributed in the entire enclosure. If, for example, the jet flow was seeded with particles but not the rest of the enclosure, then the fluid that the jet entrains would not be represented and the velocity of fluid particles originating from entrainments would not be measured. In order to minimize this bias, a forked tubing system delivered seeding particles both to the vicinity of the fan intake and the surrounding air. After seeding was introduced the facility was left to run, allowing the jet seeding and the entrained flow seeding to be thoroughly mixed with each other. Data was acquired while the particle density in the field-of-view was adequate, then the procedure was repeated.

4.4.4 Data Acquisition and Validation

Particle images were acquired with a time between pulses of $\Delta t = 300\mu$s. The sampling frequency was 1 Hz < 1.5 Hz required to sample statistically independent turbulence in both cameras. A total of 10,850 samples were acquired in a series of blocks. In-between the blocks, the seeding levels were monitored and replenished as needed. Note that it was later discovered that due to an unknown system dysfunction, 9 of the double frames were exposed on the first

frame only. This reduced the total number of double frames per camera to $N = 10,841$.

Once acquired, the particle images were evaluated with the Dynamic Studio software. The interrogation window size was 32 pixels $\times$ 32 pixels for both cameras. With 50 % overlap of the interrogation windows a multi-pass interrogation with window shifting and moving average validation of displacements resulted in 127 $\times$ 127 vectors in each camera field of view. Sub-pixel correlation peak fitting was performed relative a Gaussian curve. As indicated above, the particle image diameter was 1 pixel. Table 4.1 summarizes the output.

	x_a [mm]	x_b[mm]	z_a[mm]	z_b[mm]	W_I[mm]	M	N_x	N_z
C_0	315	632	-166	150	2.5	0.048	127	127
C_1	622	1006	-196	188	3.0	0.039	127	127

Tab. 4.1: Fields of view and resolution for PIV output. Subscripts 0 and 1 indicate the upstream and downstream cameras respectively. Subscripts a and b indicate the boundaries of the fields-of-view in each camera.

4.5 Single Point Statistics

The single point first and centered second moments estimated from the data will be examined below. The estimates were obtained as the arithmetic average according to section 4.3.1.

4.5.1 Optimization of jet data coordinate system

When measuring a free flow like the jet there is no fixed coordinate system relative to which the flow can be expected to develop. Instead the flow coordinate system is one defined by the statistical centerline of the jet itself - the location of which is not *a priori* known. In order to position the laser sheet in the proper plane a preliminary investigation of the alignment of the traverse with the mean streamwise velocity was performed. At several downstream positions the mean velocity was measured with a stereoscopic PIV system and the centerline location was determined. In this fashion a 0.5° lateral deviation of the jet centerline relative to the traverse axis was established. This deviation was accounted for when positioning the laser sheet.

Nonetheless, when the outputted velocity was averaged it was obvious that the coordinate system defined by the traverse and cameras rig was not fully vertically aligned with the jet coordinate system. This was evident from the

fact that the flow centerline did not coincide with the data position of $r = 0$. The statistical centerline is characterized by the mean streamwise velocity U being maximum in any cross section and by the mean radial velocity V going through zero there. As evident from figure 4.5.1 the vertical distance from the data coordinate system streamwise axis to the jet centerline increased linearly with downstream position.

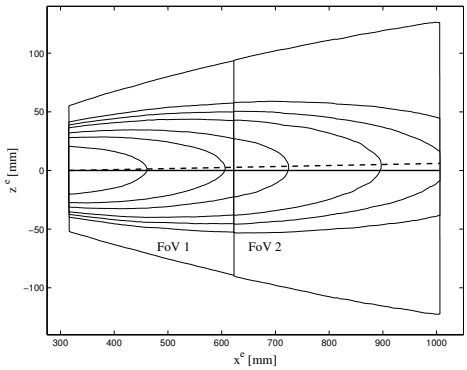

Fig. 4.4: Contour lines of $U(x, z)$ corresponding to 0.5, 1.5, 1.75, 2, 2.5, 3 and 4 m/s. Solid black line indicating x^e axis and maximum of contours, traced by the dashed line, indicate location of x^f axis.

In order to correct for the misalignment an optimization scheme consisting of iterative curve-fitting was performed. In the range $0 \leq \eta \leq 1.5$, the radial curvature of the mean streamwise velocity can be described to a reasonable approximation by a $sech^2(c\eta)$ curve:

$$U_{fit}(x, r) = U_c(x) sech^2(c\frac{r}{\delta 1/2(x)}) \tag{4.50}$$

where $c = asech(1/\sqrt{2})$ and similarity scaling of the mean velocity gives $U_c(x) = BM_o^{1/2}(x - x_o)^{-1}$ and $\delta_{1/2}(x) = A(x - x_o)$. Nonlinear least squares fits of the mean streamwise velocity data from the two cameras were performed separately, yielding initial values for the scaling constants $BM_o^{1/2}$, A and x_o. Then a misalignment consisting of a rotation of α radians about the out-of-plane coordinate axis y and a translation z_o along the vertical axis z was proposed:

$$\begin{bmatrix} x^f \\ z^f \end{bmatrix} = \begin{bmatrix} cos(\alpha) & sin(\alpha) \\ -sin(\alpha) & cos(\alpha) \end{bmatrix} \begin{bmatrix} x^e - 0 \\ z^e - z_o \end{bmatrix} \tag{4.51}$$

$$\begin{bmatrix} u_x^f(x^f, z^f) \\ u_z^f(x^f, z^f) \end{bmatrix} = \begin{bmatrix} cos(\alpha) & sin(\alpha) \\ -sin(\alpha) & cos(\alpha) \end{bmatrix} \begin{bmatrix} u_x^e(x^f, z^f) \\ u_z^e(x^f, z^f) \end{bmatrix} \tag{4.52}$$

where the superscript 'f' stands for 'flow' and the superscript 'e' stands for 'experiment'. The rotations and displacements for the two cameras were found

as the ones that minimize

$$\left| U^f(x^f, z^f) - \frac{B\sqrt{M_o}}{x^f - x_o^f} sech^2 \left[c \frac{|z^f|}{A(x^f - x_o^f)} \right] \right| \tag{4.53}$$

where x^f, z^f are defined in equation 4.51 and

$$U^f(x^f, z^f) \quad = \quad U^e(x^f, z^f)cos(\alpha) + V^e(x^f, z^f)sin(\alpha)$$

Note that the scaling parameters $BM_o^{1/2}$, A, x_o^f are characteristics of the flow coordinate system. Thus the minimization 4.53 must be done iteratively, with alternatively the scaling parameters or the mapping parameters being held fixed. The optimization was considered as completed when the change in outputted velocity profile was negligible. The resulting parameters are summarized in Table 4.2 below. Note the slight differences in coordinate system mapping between camera 0 (upstream position) and camera 1 (downstream position).

	$BM_o^{1/2}$	A	x_o/D	z_o/D	α
C 0	1.754	0.0933	2.05	-0.24	0.008
C 1	1.747	0.0935	2.63	-0.05	0.005

Tab. 4.2: Resulting scaling and mapping parameters.

Figures 4.5(a) through 4.5(d) show the mean velocity components in similarity coordinates before and after the coordinates system optimization. Note that for camera 1 only the first upstream half of the field of view was used, as the gradual influence of the enclosure walls would otherwise adversely influence the fit.

4.5.2 The x-dependence of U_c and $\delta_{1/2}$

Customarily graphs of $\delta_{1/2}(x)$ and U_o/U_c are generated in order to establish the virtual origin x_o of the mean streamwise flow, which reflects the distance for transients from the source to die off and in general is expected to depend on the source conditions. However, as the virtual origin was one of the parameters in the jet coordinate system optimization, it has already been established together with $U_c(x)$ and $\delta_{1/2}(x)$. In order to see if the goodness of the fit was uniform over the domain, figures 4.6 and 4.7 show the local values relative to the a line corresponding to the scales established by the optimization.

A consequence of momentum conservation is that the product of the centerline mean velocity and the half-width must be constant. This is possible

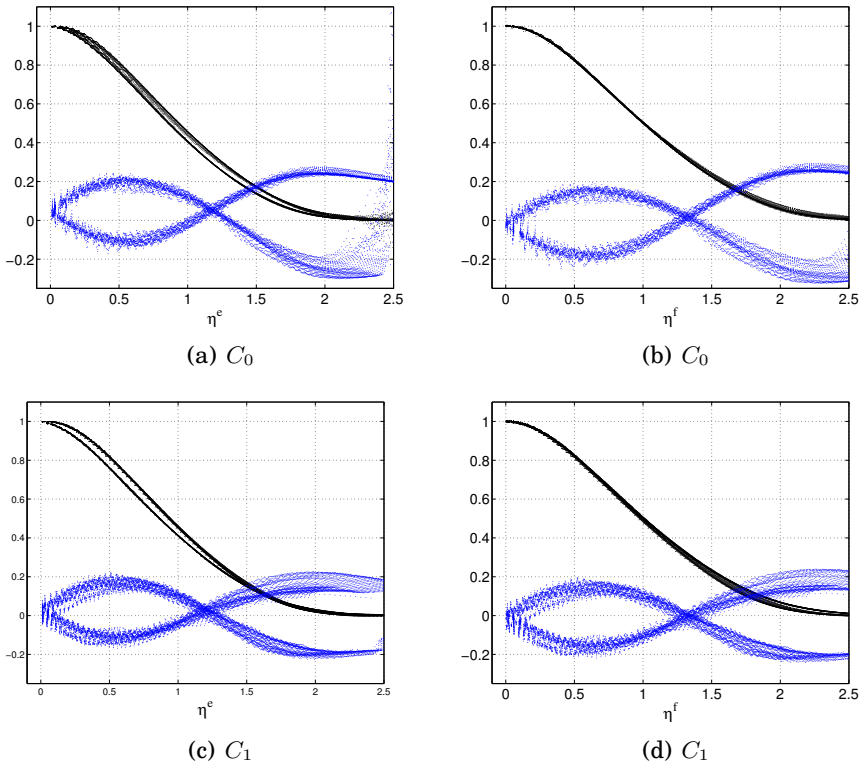

(a) C_0 (b) C_0

(c) C_1 (d) C_1

Fig. 4.5: Comparison of the mean velocity profile collapse. (a) and (c) before coordinate optimization, (b) and (d) after coordinate optimization. • : $U(x,\eta)/U_c(x)$. • : $|V(x,\eta)|/(U_c(x)A)$

only if both have the virtual origin. Note that examples are commonly found in the literature where different virtual origins allow better fits to individual quantities. These are reflections of a lack of real similarity, and can usually be attributed to a failure to satisfy the momentum integral equation due to return flow, experimental error, etc. (Hussein et al.[16]).) For the experiments reported herein:

$$\delta_{1/2}(x) = A(x - x_o) \tag{4.54}$$

$$U_c(x) = BM_o^{1/2}(x - x_o)^{-1} \tag{4.55}$$

where $A = 0.093, B = 6.5$ and $x_o = 2.4$ has been obtained as from the average of the scaling parameters of the upstream and downstream cameras. These

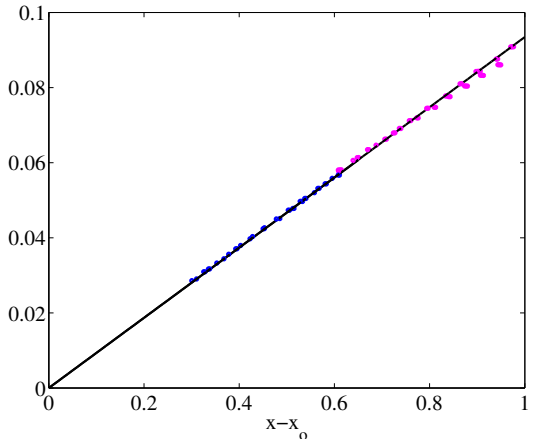

Fig. 4.6: Variation of $\delta_{1/2}$ with downstream distance from the obtained virtual origins. Solid line corresponding to $A(x - x_o)$ where A was obtained from optimization. Data in blue from C_0 and data in magenta from C_1.

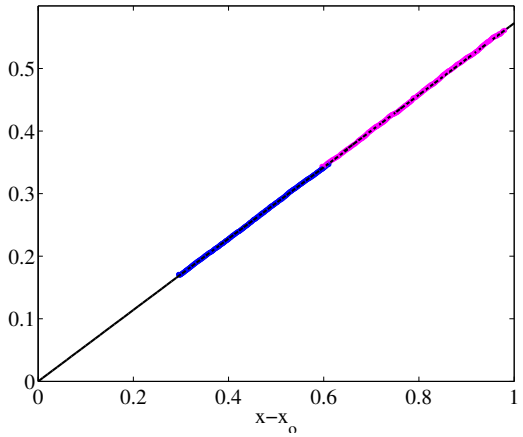

Fig. 4.7: Variation of $(1/U_c)^{-1}$ with downstream distance from the obtained virtual origins. Solid line corresponding to $(x - x_o)/BM_o^{1/2}$ where $BM_o^{1/2}$ was obtained from optimization. Data in blue from C_0 and data in magenta from C_1.

results are in close agreement with the experiment of Hussein et al.[16] at an exit Reynolds number of 100,000, and Panchepakesan and Lumley [52] at 10,000 who obtained (0.094, 6.5, 4) and (0.096, 6.1, 0) respectively. Note that the mean centerline velocity for top-hat exit profiles (which all these jets closely approximate) can also be expressed as:

$$\frac{U_o}{U_c} = \frac{1}{B_u}\left[\frac{x - x_o}{D}\right] \tag{4.56}$$

where $B_u = \frac{2}{\sqrt{\pi}}B$. For this experiment, the exit velocity was 30.3 m/s, so $B_u = 5.8$.

The *local* Reynolds number for these measurements is given by:

$$\frac{U_c \delta_{1/2}}{\nu} = 0.094(5.8)R_D \approx 0.55 R_D \tag{4.57}$$

where R_D is the exit Reynolds number defined as:

$$R_D = \frac{U_o D}{\nu} \tag{4.58}$$

For the experiments reported later, $U_o = 30.3$ m/s, $D = 0.01$m, and $\nu = 14.7 \times 10^{-6} m^2/s$, so $Re \approx 20,000$. Thus the local Reynolds number of the fully-developed jet is approximately 11,000.

4.5.3 The mean velocity profiles

Figure 4.8 shows the final profile plotted together with the LDA and flying hot-wire data obtained by Hussein et al. 1994 in a jet at exit Reynolds number of 100,000. In spite of the large difference in Reynolds number and measurement technique, the profiles are quite similar.

The radial velocity is almost two orders of magnitude smaller than the streamwise one, and as a result exhibits much more scatter. It has been divided by $\delta_{1/2}/dx = 0.093$ before plotting in figures 4.5(c) and 4.5(d). In order to check the validity of the radial measured mean velocity one can calculate it from the smoother streamwise curve via the mean continuity equation in similarity variables:

$$V(x,r)/U_c(x) = -\left[\frac{d\delta}{dx}\right]\left\{\frac{1}{\eta}\int_0^{\eta} f(\overline{\eta})\,\overline{\eta}\,d\overline{\eta} \;-\; \eta f\right\} \tag{4.59}$$

Figures 4.9(a) and 4.9(b) display the results.

Note that in order to perform the numerical integration the scaled profiles $f(\eta)$ had to be interpolated onto a new grid which was equidistant in η. The

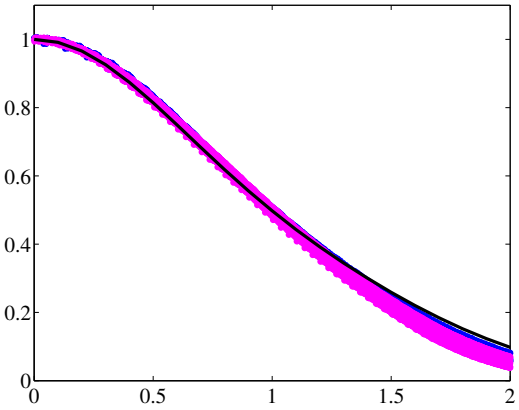

Fig. 4.8: Means streamwise velocity in similarity coordinates, with comparison to the curvefit from Hussein et al.[16]. Data in blue from C_0 and data in magenta from C_1.

agreement between the directly measured V/U_c and that computed from continuity is quite spectacular actually. Thus it seems that V has been determined to an accuracy that is at least at limits of what is commonly believed possible with PIV, in large part perhaps because of the extremely large number of independent samples.

4.5.4 The second order moments

The scaled single point second order moments of the two velocity components are shown in figures 4.10(a) and 4.10(a), together with the corresponding LDA profiles from the experiment of Hussein et al.[16]. The variances are about 10% below those of Hussein et al.[16]. While it is tempting to interpret this as being primarily due to the spatial filtering by the relatively large interrogation volumes, it may be in part due to the much lower Reynolds number (20,000 versus 100,000), since they are actually quite close to the data of Panchepakesan and Lumley [52] at an exit Reynolds number of 10,000. In particular, for the scaled centerline turbulence moments Panchepakesan/Lumley obtained $\langle u^2/U_c^2 \rangle = 0.06$ and $\langle v^2/U_c^2 = 0.036 \rangle = 0.06$ compared to the corresponding values of 0.06 and 0.04 obtained herein. S Interestingly, all three experiments get approximately the same value for the peak in the Reynolds shear stress; i.e. $\langle uv \rangle = 21,19$ and 20 for the Hussein et al.[16], Panchepakesan and Lumley [52]and the present experiment respectively. Note that there was some evi-

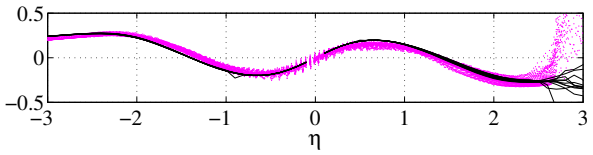

(a) C_0

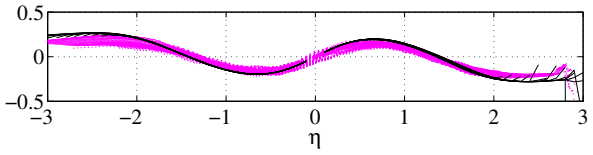

(b) C_1

Fig. 4.9: Measured mean radial velocity profiles in similarity variables, (•) $V/U_c/A$, and calculated from measured mean streamwise velocity and the mean continuity equation, (-) $-\frac{1}{\eta}\int_0^\eta f\bar{\eta}d\bar{\eta} + \eta f$.

dence in the latter for spatial filtering as well, since the streamwise turbulence intensity never reached an equilibrium value.

It should be noted that as only in-plane velocity components can be outputted from the planar PIV, the azimuthal out-of-plane component is folded into the variances above. This error should affect the variances as $(1+tan^2(\alpha))$, where $tan(\alpha) \approx \sqrt{(x-x_c)^2 + \delta_{1/2}(x)^2\eta^2}/Z$, where x_c is the center of each camera and Z is the distance to the lens. In our case the maximum value for $tan^2(\alpha))$ is 0.02, so it is not a significant contributor to the variance. Also note that in the absence of swirl there should be no effect on the mean velocity components.

4.5.5 Spatial filtering versus noise

The fact the Reynolds shear stresses among the different experiments are quite close, while the normal stresses are not, suggests the differences are mostly attributable to spatial filtering, since the shear stresses (as noted below) are much less affected. While figures 4.10(a) and 4.10(b) indicate the general levels of the scaled second moments of velocity, they do not indicate the streamwise spatial variation of those quantities. Figures 4.11(a) through 4.11(c) show contours of the variance and covariance of the streamwise and radial turbulent velocity, with the streamwise growth scaled out. The color scales are different for each plot. Note the progressive increase of the variance in each of the

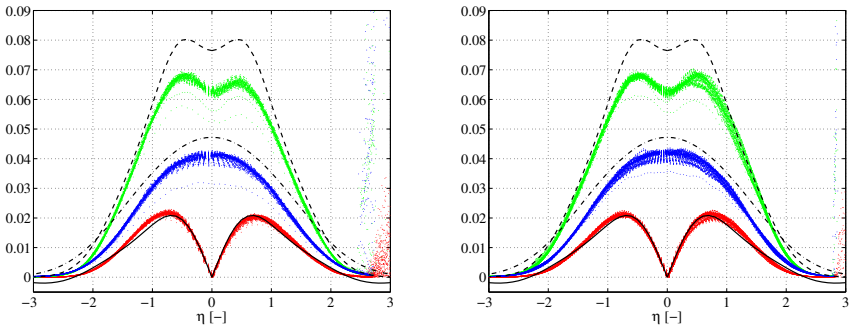

(a) Camera 0

(b) Camera 1

Fig. 4.10: Variance and covariance profiles in similarity variables, compared with LDA data curve fits form Hussein et al.[16]. (●)$\langle u^2 \rangle / U_c^2$, (●)$\langle v^2 \rangle / U_c^2$, (●)$|\langle uv \rangle| / U_c^2$.

two cameras. Since the turbulence is fully developed, the contours of constant color should fall within parallel lines. Only the Reynolds shear stresses do so. The rise in the normal stresses must either be due to an increase in the noise downstream, or a decrease in the spatial filtering.

It will be argued in the next chapter that the only noise source whose mean square value is dependent on interrogation volume size is the quantization noise, and it can be shown to be negligible. Therefore the dominant effect is due to the spatial filtering of the turbulence which decreases linearly in each camera field of view. This is because the interrogation window has constant dimensions for reach camera, 2.5mm and 3 mm respectively, while the scales of the turbulence grows proportionally to $x - x_o$ as shown previously. Thus for each camera, the filtering effect is maximum at the upstream boundary and gradually decreases. At the transition from the upstrem camera to the downstream camera the filtering jumps due to the change in interrogation window physical dimension. The cut-off wave number for the spatial filtering is approximately $2\pi/l_i$, where i is an index for camera. From the figures it is clear that the effect is most prominent in the variance of the radial velocity component. It will be shown later that in the range of wavenumbers which are affected by the filtering, the spectral density of the radial auto correlation has higher values than both the streamwise power spectral density and the cross-spectral density, which indicates that more of the energy would be filtered out for a given cut-off wavenumber. In fact, the relative filtering effect on the Reynolds shear stress is virtually negligible, since its spectrum drops much more rapidly and its primary contribution is from wavenumbers below the cutoff.

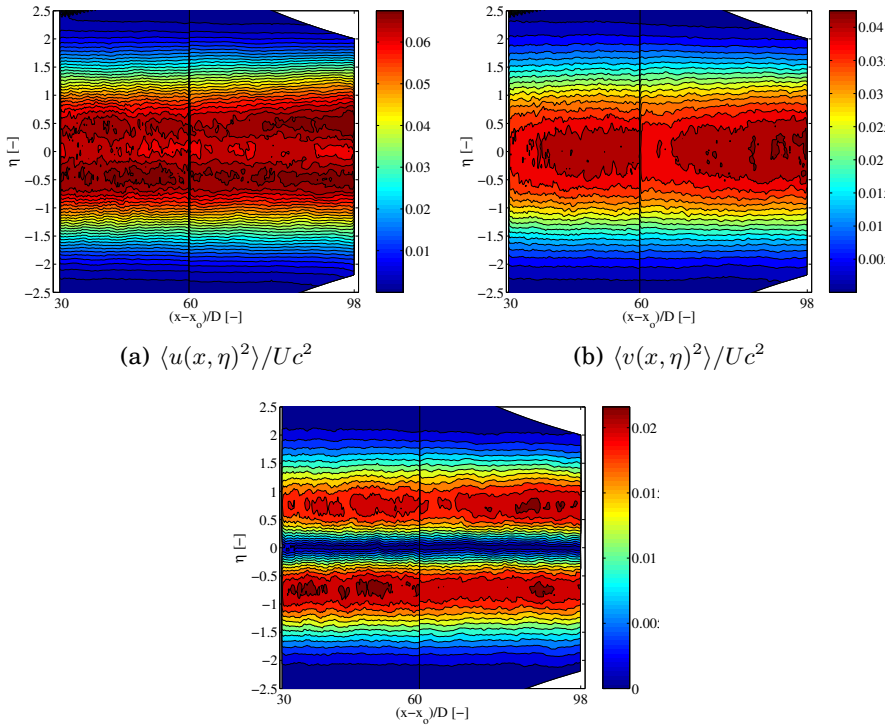

(a) $\langle u(x,\eta)^2 \rangle / Uc^2$

(b) $\langle v(x,\eta)^2 \rangle / Uc^2$

(c) $\langle u(x,\eta)v(x,\eta) \rangle / Uc^2$

Fig. 4.11: Contour plots of second moments of the velocity components in similarity variables for the two fields of view. Note that the color scales are individual.

4.5.6 Noise and bias

There are a number of effects that can affect the single point correlations of measured data. In PIV it is generally established that under good measurement conditions with standard interrogation methods the rms measurement error from all sources (optical imperfections, peak detection, etc.) corresponds to about 0.1 pixel equivalents. In the current case this number could well be larger, due to the small particle images caused by the low magnification. However, if the 0.1 pixel estimate is used as an order of magnitude, and since the mean velocity corresponds to about 3 to 7 pixel displacements over the plane of our measurements, this translates into a nominal value in our experiment of about a 2 % contribution to the rms turbulence moments. More importantly it corresponds to an increase in the scaled rms velocity across one camera of

about 1-2 %. This is clearly not enough to account for the increase along the centerline of the turbulence variances of figure 4.11(a), consistent with the spatial filtering explanation offered above.

A second source of error in the rms values is the quantization arising from the fact that the signal is outputted digitally. This is identical to the usual quantization noise whose mean square value is $\epsilon^2/12$ where ϵ is also given in pixels. It will be argued in the next chapter that this contribution corresponds approximately to 0.01 pixels, which is clearly negligible compared to the effects discussed in the preceding paragraph. Nonetheless, it will turn out in the next chapter to be visible as the last high wavenumber tail of the spectrum, in large part because of the normalization by $U_c(x)$.

Finally, George(2009) has identified a potential source of bias for both the mean and rms values which is a consequence of the fact the the PIV output velocity is based on an average over the particles present at any instant. The problem for estimates of the mean velocity is that the realizations with fewer particles are weighted the same as the realizations with more particles. The net effect is the mean velocity is overestimate by a factor of $(1+1/N_p)$ where N_p is the average number of particles in the interrogation volume. Thus the lower the expected number of particles, the more the bias. This theory is very new, and needs to be tested more thoroughly before conclusions can be definitively drawn, but it has been recognized for a long time that errors result if there are too few particles in the volume. Moreover, to-date, no software provides an estimate of how many particles contribute to the instantaneous results, so at this point the question of correction is moot.

Another consequence of the George (2009) theory is that there is an 'turbulence' noise contribution, the mean square value of which is also inversely proportional to the expected number of particles in the interrogation volume and proportional the mean square fluctuating volume averaged velocity itself; i.e., $\langle u_i u_j \rangle / N_p$. The spectral properties of this 'noise' are discussed in the next chapter, and shown to contribute negligibly to the measured spectra. Unfortunately it is not possible at this point to say whether its contribution to the single point second moments is significant or not.

5. SPECTRAL ANALYSIS IN TWO-POINT SIMILARITY COORDINATES

This chapter exploits the streamwise homogeniety of the logarithmically transformed and scaled velocity field. In particular it develops the two-point correlations and spectra of the scaled velocity field in the 'homogenized' streamwise coordinate.

5.1 Instantaneous velocities into similarity coordinates

As outlined above in the previous chapter, the purpose of the large field of view is to accommodate spectral estimates with a minimum of spectral leakage due to finite domain window width. In order to do so, the two fields of data were interpolated onto a common grid which was equidistant in the multi-point similarity coordinates $\xi = ln[(x - x_o)/D]$ and $\eta = r/\delta_{1/2}(x)$. The resulting new coordinate system has grid points defined by equation 5.1 and table 5.1 below.

$$\begin{aligned} \xi_s &= \xi_a + s\Delta_\xi = \xi_a + s\frac{L_\xi}{N_\xi - 1}, \quad s = 0, 1, ..., S \\ \eta_p &= p\Delta_\eta = p\frac{L_\eta}{N_\eta - 2}, \quad p = 0, \pm 1, ..., \pm P \end{aligned} \tag{5.1}$$

Here the maximum values of the grid indices are defined as $S = N_\xi - 1$ and $P = (N_\eta - 1)/2$.

The velocity data from each camera field of view was normalized by the local mean velocity and interpolated onto the common equidistant similarity coordinate grid above. The interpolation scheme was cubic and the values in the area of field of view overlap were evaluated as the average of the contributions from the two cameras. The resulting data should then correspond to:

$$\upsilon_i(\xi_s, \eta_p) = \frac{u_i(x_s, r_p)}{U_c(x_s)} \tag{5.2}$$

where $x_s = De^{\xi_s} + x_o$ and $r_p = \delta_{1/2}(x_s)\eta_p$. The effect of this mapping is visualized in figures 5.1(a) through 5.1(f) below. Note that though the similarity

Axis	a	L	N	Δ	S
ξ	3.4013	1.1788	512	0.0023	511

Axis	L	N	Δ	P
η	4	51	0.08	25

Tab. 5.1: Equidistant grid in two-point similarity coordinate system. Note that the η - domain spans across the entire jet. The effective number of grid point spanning the upper or lower part of the jet individually is $P + 1 = 26$.

scaled instantaneous velocities appear 'visually homogeneous' in the streamwise direction, exactly as expected from the similarity theory, the true test of homogeneity is that the two-point correlations are independent of origin. This will be shown to be the case in the following section.

5.2 Two-point correlations in similarity coordinates

The similarity scaled two-point Reynolds stress should depend only on the difference variable $\zeta = \xi' - \xi$. Figure 5.2 shows the centerline two-point correlation coefficients of the scaled streamwise fluctuations, i.e.,

$$C_{i,j}(\zeta, 0) = \frac{\langle v_i(\xi, 0) v_j(\xi + \zeta, 0) \rangle}{\langle v_i(\xi, 0) v_j(\xi, 0) \rangle} \tag{5.3}$$

evaluated from four different locations in the ξ domain. The black and blue data points correspond to the auto-correlation coefficients of the streamwise and radial velocity components respectively. The red data points in this particular figure correspond to the *non*-normalized cross-component correlation values inflated by a factor 20. For comparison, figure 5.3 shows the normalized centerline correlation of the streamwise velocity produced by Frohnapfel [41] (see also Ewing et al. [7]) obtained from as the correlation between an upstream LDA probe and a downstream hot wire. Also in figure 5.3 is shown the spatial lag correlation as obtained by time-autocorrelation of hot-wire anemometer data which was converted using Taylor's frozen field hypothesis.

When comparing the correlations in figures 5.2 and 5.3, it should be noted that the combined LDA/hot-wire two-point correlations were based on up to 60,000 independent realizations while the number of independent samples in the PIV experiment was 10,000. Recalling that the variability for the auto-correlation is inversely proportional to the correlation coefficient; i.e., $\epsilon_\rho^2 = (1/N)(1/\rho_{uu}^2)$), it indicates that the PIV results should exhibit larger relative

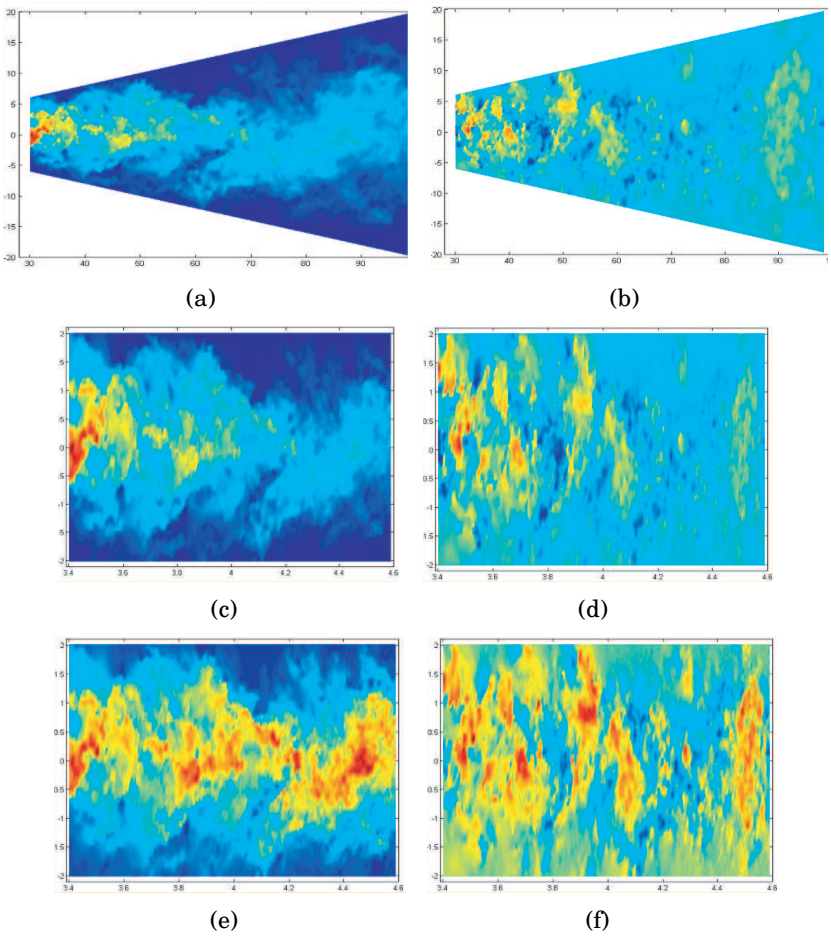

(a) (b)

(c) (d)

(e) (f)

Fig. 5.1: One instantaneous realization of the turbulent jet velocity field. Left column correspond to streamwise velocity and right corresponds to radial. Figures (a) and (b) show the physical velocity in physical coordinates, $\tilde{u}_i(x,r)$, (c) and (d) the physical velocity in similarity coordinates, $\tilde{u}_i(\xi,\eta)$, and (e) and (f) the similarity scaled velocity in similarity coordinates, $\tilde{v}_i(\xi,\eta)$.

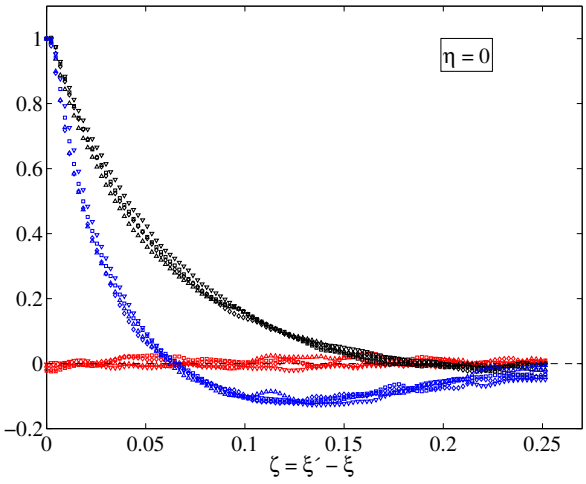

Fig. 5.2: Elements of the correlation coefficient tensor in similarity coordinates, $C_{i,j}(\zeta, \eta, \eta)$, at the centerline and evaluated for several non-overlapping downstream positions in ξ which are indicated by the different symbols. Black symbols correspond to $C_{1,1}(\zeta)$, blue symbols to $C_{2,2}(\zeta)$ and the red ones, in this particular graph, to $20 \times \langle v_1(\xi, 0) v_2(\xi + \zeta, 0) \rangle$, since the expected value of the cross-correlation function is zero along the centerline. Both normal tensor elements show independence of origin and dependence only on $\zeta = \xi' - \xi$. The cross-correlation is indeed zero to within measurement error.

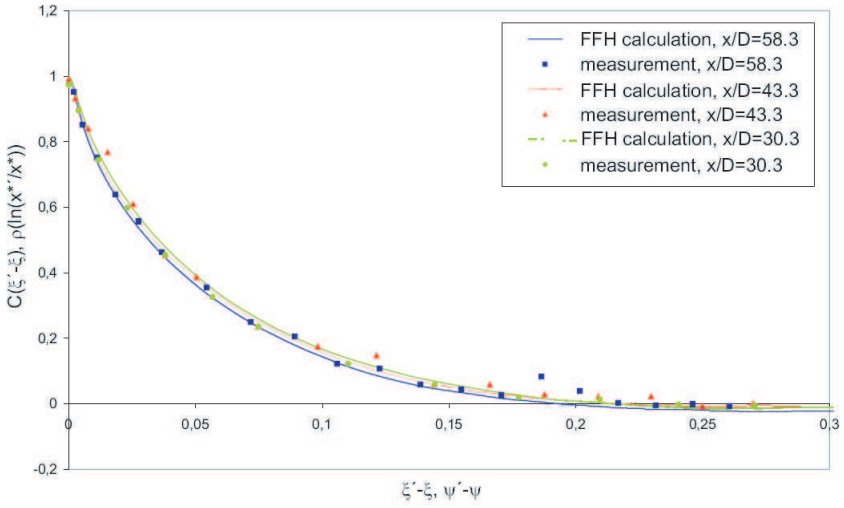

Fig. 5.3: Spatial correlation of the axial velocity fluctuations in similarity coordinates measured with simultaneous LDA and hot-wire, together with the 'spatial' correlation inferred from temporal hot-wire data using Taylor's hypothesis, from Frohnapfel[41].

error for large separations. In addition, a consequence of the decreasing filtering effect in the streamwise direction is that the correlation at zero lag will increase, causing the correlation coefficients to be normalized with a progressively larger value as the origin of the two-point correlations increase in ξ. This leads to an apparent lack of collapse that is not characteristic of the correlations themselves, but an artifact of the normalization.

A striking feature of the results in figures 5.2 and 5.3 is the this correlation remains positive (to within statistical error) for all values of the separation. The same characteristic has has previously been noted for the longitudinal correlations in decaying grid turbulence (c.f. Comte-Bellot & Corrsin [53]), and although not theoretically predicted (to the best knowledge of the author), seems to be a characteristic of homogenous turbulence. The 'homogenized' jet turbulence appears to behave the same way.

Unlike the $C_{1,1}$ correlations, the $C_{2,2}$ correlations go negative. They are also surprisingly like the corresponding correlations for homogeneous turbulence (Comte-Bellot and Corrsin 1971[53]). In isotropic turbulence the changing of sign of the spanwise correlation can be shown to be a consequence of the two-point continuity equation and the monotonic behavior of the longitudinal correlation (Batchelor [54], Lumley [28]). At the present, a corresponding

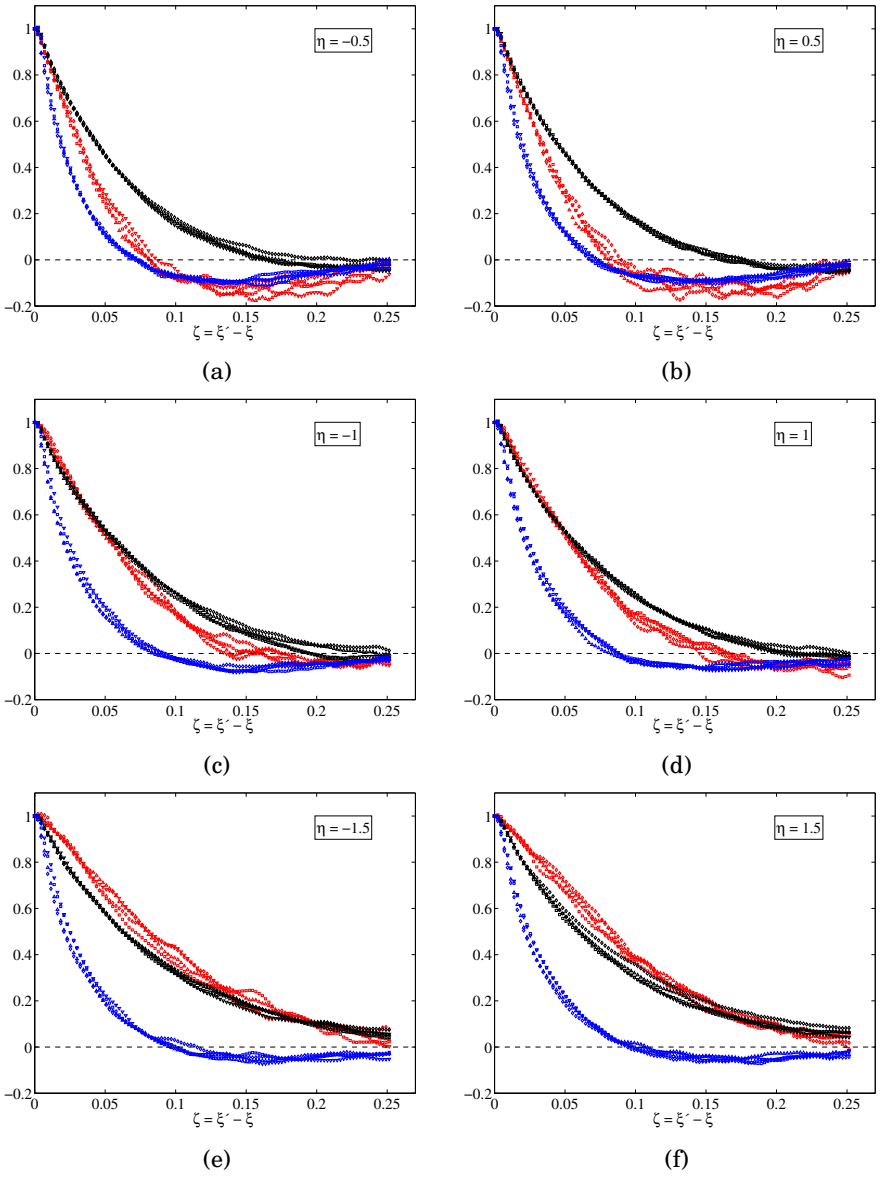

Fig. 5.4: Correlation coefficient tensor elements in similarity coordinates $C_{i,j}(\zeta,\eta,\eta)$ at six radial locations $|\eta| = 0.5, 1$ and 1.5. $C_{i,j}(\zeta)$ is evaluated for several non-overlapping downstream positions in ξ which are indicated by the different symbols. Black symbols correspond to $C_{1,1}(\zeta)$blue symbols to $C_{2,2}(\zeta)$ and red ones to $C_{1,2}(\zeta)$.

causal relation has not been established for the current 'homogenized' flow.

Figures 5.4(a) through 5.4(f) show the correlation coefficients at positions $|\eta| = 0.5, 1$ and $\eta = 1.5$. Like the centerline results, $C_{1,1}(\zeta)$ remains positive for almost all values of ζ. Another obvious feature is the decreased rate of correlation decay with increasing $\xi' - \xi$ with increasing radial distance from the centerline, so much so that the curves at $|\eta| = 1.5$ do not quite reach zero. This result is quite surprising, and indicates that the longitudinal integral scale for the streamwise velocity fluctuations has increased by nearly a factor of 2 with increasing radius. This does not appear to have been previously observed, perhaps due to the great difficulties of measuring in this part of the flow with conventional techniques given the high local turbulence intensity.

In summary, the degree of collapse of the correlation coefficient curves with origin in ξ exhibited in all figures and for all the elements of the correlation coefficient tensor demonstrates unequivocally the independence of position of the two-point statistics in two-point similarity coordinates and confirms the theoretical results of Ewing [55]. Therefore it is legitimate to represent the homogenized turbulence by spectral analysis, which is presented in the following section.

5.3 Spectral analysis in ξ

The homogeneity in ξ for the transformed velocity data opens up the possibility of directly computing the one-dimensional spatial spectra. Most 'spatial' (or wavenumber) spectra in turbulence have been produced from either DNS attempts to simulate homogeneous turbulence, usually with periodic boundary conditions, or have used Taylor's hypothesis together with the corresponding hypothesis of *local homogeneity* to relate frequency spectra obtained by a fixed probe (e.g., Comte-Bellot and Corrsin [53], Kang et al. [56] for decaying grid turbulence). Spatial spectra from PIV data have been estimated by Foucaut et al.[57] as early as 2004. In their paper they showed that spectral analysis can be used as a tool for determining the local interrogation window dimension which optimizes the compromise between resolution and measurement noise due to limited number of particle images in the interrogation volume. More recently, Herpin [58] made comparisons of spatial PIV spectra with DNS data. In both cases, however, streamwise variations of boundary layer turbulence were decomposed under the assumption of local homogeneity. Thus the results in this thesis are, to the best knowledge of the author, the first experimental spatial spectral analysis of a globally 'homogenized' turbulent field.

5.3.1 Evaluation of spectral estimates

The finite Fourier transforms along the similarity coordinate axis ξ were implemented with an FFT algorithm which calculates the Fourier coefficients of the instantaneous fluctuating velocity $\upsilon_i(\xi_n, \eta_p)$ as:

$$\hat{\upsilon}_i^{L_\xi}(\kappa_s, \eta_p) = \Delta\xi \sum_{n=0}^{N_\xi - 1} \upsilon_i(\xi_n, \eta_p) e^{-i\kappa_s \xi_n / N_\xi} \tag{5.4}$$

Note that the fluctuations are relative to the arithmetic average over the whole set of independent realizations, not relative to an average estimated from the $N_\xi = 512$ grid points over which the finite Fourier transform is applied. That means that the instantaneous value of the finite transform corresponding to wavenumber κ_0 is simply the instantaneous average over the ξ domain.

The expected values of the spectral densities were estimated as

$$\Phi_{i,jN}^{(1)L_\xi}(\kappa_m, \eta_p, \eta_q) = \frac{L_\xi}{2\pi N} \sum_{n=1}^{N} \hat{\upsilon}_i^{L_\xi *}(\kappa_m, \eta_p, t_n) \hat{\upsilon}_j^{L_\xi}(\kappa_m, \eta_q, t_n) \tag{5.5}$$

where the superscript (1) reminds us that the spectra are one-dimensional and function of a wavenumber in the streamwise direction only. L_ξ indicates the finite domain length (for clarity, this superscript will be suppressed in the remainder of the section) and subscript n is used to indicate the N independent realizations. Thus the spectral density associated with the artificial wavenumber κ_0 is simply the the variance of the deviations of the instantaneous domain mean velocities relative to the ensemble mean. The theoretical spectral density at wavenumber κ_0 can be found by extrapolating from the lowest resolved wave numbers. The variance of an individual spectral estimator is equal to twice the value of the spectrum itself (for discretely sampled data). Thus if the spectra are averaged over N blocks of data, then relative error (or variability), is equal to $\varepsilon^2_{\Phi_N(\kappa)} = 2/N$. For these experiments, $N \approx 10,000$, so the spectra are remarkably well-converged from all wavenumbers.

5.3.2 Spectra at the centerline

Figure 5.5 shows the streamwise and radial velocity spectra at the centerline. Note that the corresponding cross-spectrum at this location should be zero, since the Reynolds stress (to which it integrates) is identically zero at the centerline. Appendix I below shows how to interpret the logarithmically transformed data produced herein in the more traditional physical coordinates, and *vice versa*. In particular, if the usual *local* physical coordinate wavenumber spectra, say $F_{i,j}^{(1)}(k_1(x); x)$, are scaled as $F_{i,j}^{(1)}(k_1; x)/(U_c^2[x - x_o])$ and the

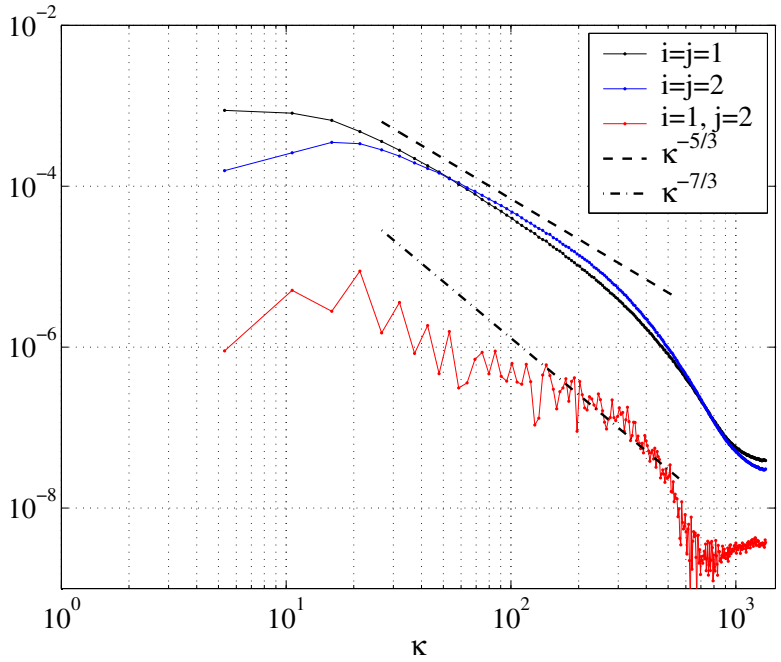

Fig. 5.5: Elements of the one-dimensional spectral tensor estimate $\Phi_{i,j}^{(1)}(\kappa)$ along the jet centerline where $\eta = 0$. (-) $\Phi_{1,1}(\kappa_s, 0, 0)$, (-) $\Phi_{2,2}(\kappa_s, 0, 0)$, (-) $|\Phi_{1,2}(\kappa_s, 0, 0)|$ and the dashed lines indicate slopes of $\kappa^{-5/3}$ and $\kappa^{-7/3}$ respectively.

streamwise wavenumber as $k_1[x - x_o]$, then these are local approximations to the logarithmic spectra $\Phi_{i,j}^{(1)}(\kappa)$.

Figure 5.6 shows the streamwise velocity component spectrum from Figure 5.5 plotted together with spectra obtained from the experimental data of Frohnapfel [41] using the same experimental facility at a slightly higher exit velocity (40 m/s corresponding to an exit Reynolds number of 26,000). The hot-wire data were processed using an FFT, while the LDA data were produced using the randomly arriving samples together with a residence-time weighted algorithm (described in detail in Velte [47]). The LDA spectra have considerably more variability which also increases with wavenumber, a consequence of the random sampling.

All three spectral estimates are exhibit similar behavior at the lower wavenumbers, until the effects of the finite measuring volume begins to influence the PIV data (see discussion below). This lends considerable credibility to the re-

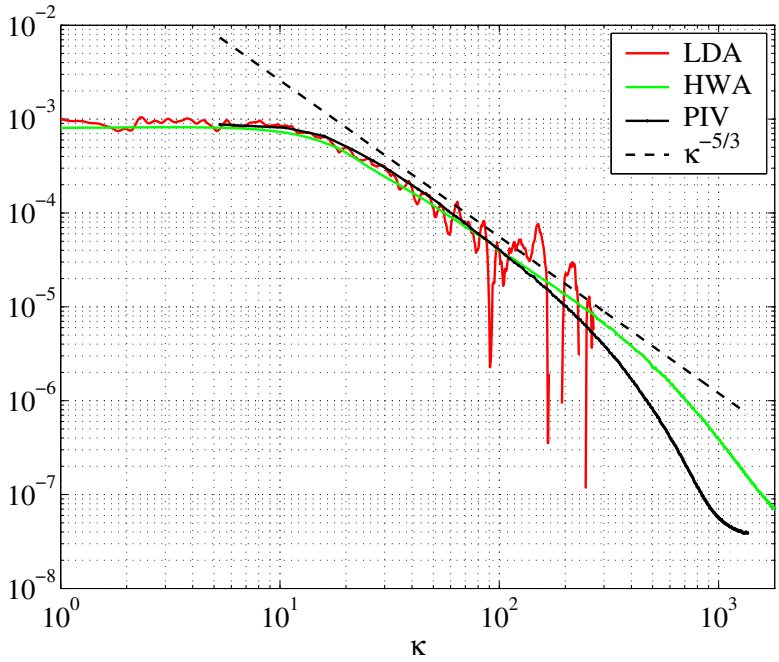

Fig. 5.6: One-dimensional spatial streamwise spectrum $\Phi^{(1)}_{1,1}(\kappa)$ at $\eta = 0$ from PIV in black, together with scaled local one-dimensional spectra computed using Taylor's hypothesis. In green, HWA data from Frohnapfel [41], and in red residence time weighted LDA data processed by Velte [47].

sults of the analysis presented in this thesis. Also as with the correlation data of the previous section, Taylor's hypothesis does remarkably well, at all scales of motion, in spite of the relatively high turbulence intensity (25 %). As noted earlier, this is somewhat surprising, and currently lacks theoretical explanation.

It is perhaps not too surprising, given the observations about the correlations functions in the preceding section, that the centerline spectra show approximately the same overall characteristics as those of isotropic turbulence (c.f. Comte-Bellot and Corrsin [53], Tennekes and Lumley [18]). In particular, the streamwise spectrum, $\Phi^{(1)}_{1,1}$ rolls off monotonically from its maximum (presumably as $\kappa \rightarrow 0$). By contrast, $\Phi^{(1)}_{2,2}$ has its maximum away from the origin, a consequence of the corresponding correlation function going negative somewhere. For isotropic turbulence, the ratio of the auto-spectral densities

$\Phi^{(1)}_{1,1}/\Phi^{(1)}_{2,2} = 2$ in the limit as $\kappa \to 0$. Clearly this is not the case here. Since $\Phi^{(1)}_{1,1}(0) = \langle \upsilon_1^2 \rangle \mathcal{L}_1/\pi$ and $\Phi^{(1)}_{2,2}(0) = \langle \upsilon_2^2 \rangle \mathcal{L}_2/\pi$ where $\mathcal{L}_1$ and $\mathcal{L}_2$ are the streamwise and cross-stream integral scales in similarity coordinates. For isotropic turbulence $\mathcal{L}_1 = 2\mathcal{L}_2$. Thus the fact that the ratio of $\Phi^{(1)}_{1,1}/\Phi^{1}_{2,2} > 2$ is greater than 2 is clearly a consequence of the anisotropy, both of the turbulence intensities and the integral scales.

In spite of the anisotropy of the lowest wavenumbers, however, the spectra behave similarly to their isotropic counterparts. The $\Phi^{(1)}_{2,2}$ spectrum crosses the $\Phi^{(1)}_{1,1}$ spectrum and both roll-off at approximately $\kappa^{-5/3}$ until about $\kappa \approx 300 - 500$. For isotropic turbulence, $\Phi^{(1)}_{1,1}/\Phi^{(1)}_{2,2} = 4/3$ in the $\kappa^{-5/3}$ range. This ratio is being approached in figure 5.5, but not quite reached before the roll-off cuts in, a roll-off consistent with the spatial filtering by the finite interrogation volumes. The approach to the 4/3 ratio can be interpreted as a trend toward isotropy with increasing wavenumber.

The cut-off wavenumber due to the averaging of the velocity across the interrogation volume is approximately π/l where l is the size of the interrogation window (see appendix II below). The values for the two cameras were 2.5 mm and 3 mm respectively, corresponding to physical cut-off wavenumbers of $1.25 \times 10^3 \mathrm{m}^{-1}$ and $1.05 \times 10^3 \mathrm{m}^{-1}$ respectively. These physical cut-off wavenumbers can be converted to the similarity wavenumber as $\kappa \approx k_1 \times (x - x_o)$. So for the most upstream position of $x/D = 30$, the cut-off is approximately at $\kappa_c \approx 375$; while at, $x/D = 95$, the most downstream position, $\kappa_c \approx 994$. The equally-spaced logarithmic coordinates in ξ-space are more densely spaced upstream in physical space. Since the spectra represent a composite of the measurement over the entire domain with the upstream data more heavily weighted, a nominal value of the cutoff wavenumber of about 400-500 is a reasonable estimate. Indeed $\Phi^{(1)}_{1,1}$ spectra appear to roll-off about about $\kappa \approx 500$, while $\Phi^{(1)}_{2,2}$ appears to roll-off a bit earlier. Approximately the same roll-offs will be seen to be exhibited by the other spectra for other values of η well.

Finally, the streamwise velocity spectra and the approximate $\kappa^{-5/3}$ slope, which corresponds to the usual $k_1^{-5/3}$-range in physical coordinates (see Appendix 1), presents the opportunity to test the universal inertial subrange) arguments put forth by Batchelor [54] using Kolmogorov's 1941 universal equilibrium range ideas. If the physical space one-dimensional spectra had a universal inertial subrange, it would be described by:

$$F^{(1)}_{1,1}(k_1) = \frac{9}{55} \alpha_{Kol}\, \varepsilon^{2/3} k_1^{-5/3} \tag{5.6}$$

where ε is the rate of dissipation of turbulence energy per unit mass and α_{Kol} is presumed to be a universal constant approximately equal to 1.5. Following

Appendix 1 this can be mapped into jet similarity coordinates as $k_1 = \kappa/(x - x_o)$ and $F_{1,1}^{(1)}(k_1) = \Phi_{1,1}^{(1)}(\kappa)U_c^2(x - x_o)$ to obtain the dimensionless spectrum resulting from the logarithmically transformed data as:

$$\Phi_{1,1}^{(1)}(\kappa) = \frac{9}{55}\alpha_{Kol}\ \tilde{\varepsilon}^{\,2/3}\ \kappa^{-5/3} \tag{5.7}$$

where $\tilde{\varepsilon}$ is the dimensionless rate of dissipation defined by:

$$\tilde{\varepsilon} = \frac{\varepsilon(x - x_o)}{U_c^3} \tag{5.8}$$

The best fit line to the inertial subrange in the streamwise spectrum of figure 5.6 corresponds to $\Phi_{1,1}^{(1)} = 0.1\kappa^{-5/3}$. Together with equation 5.7 yields an estimate for $\tilde{\varepsilon}$ as 0.26. This can be compared to the various efforts of Hussein et al. [16] to measure the dissipation directly using parallel flying hot-wires, albeit at a much higher jet exit Reynolds number (100,000 versus 30,000 here). Their preferred value using a local axisymmetry estimate (see George and Hussein [59]) was 0.35, but other estimates based on local isotropy were 0.23 (based on $\langle(\partial u/\partial y)^2\rangle$) and 0.28 ($\langle(\partial u/\partial x)^2\rangle$). Thus the estimate from the spectrum here is remarkably close, and the differences may be more due to the difference in Reynolds number than to the methodology.

As a final note, the dissipation rate in similarity variables can be used to define the local Kolomogorov microscale as $\eta_K(x) = (\nu^3/\varepsilon(x))^{1/4} = (\nu^3/\tilde{\varepsilon})^{1/4}(x - x_o)^{1/4}U_c(x)^{-3/4} = \tilde{\eta}_K(x - x_o)(BM_o^{1/2})^{-3/4}$ where $\tilde{\eta}_K = 3.38 \times 10^{-4}$ and $BM_o^{1/2} = 1.72$ was established for the current flow. Thus the local size of Kolmogorov microscale increases linearly downstream, and for this experiment is given by $\eta_K(x) \approx 2.25 \times 10^{-4}(x - x_o)$. At $x - x_o = 30D$ the dissipation range is at a physical scale of 6.74×10^{-5}m and at $x - x_o = 95D$ it is 2.14×10^{-4}m.

5.3.3 The off-axis spectra

Figures 5.7(a) through 5.7(f) show the velocity spectra at off-centerline positions across the jet corresponding to $|\eta| = 0.5,\ 1$ and 1.5. Note that such spectra have never been presented before, since hot-wire probes do not work reliably away from the jet core because the local turbulence intensity rises rapidly. Even flying hot-wires can not work since the traverse the flow too quickly to obtain a measurement record length long enough to avoid window effects. Burst-mode LDA cannot be used either, since Taylor's hypothesis fails at these very large local turbulence intensities.

All of streamwise and radial velocity spectra show almost the same characteristics as noted for the centerline. The major difference is the non-zero

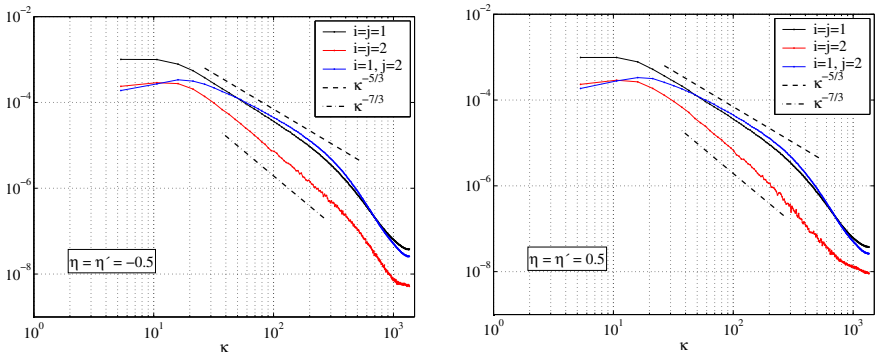

(a) at $\eta = -0.5$

(b) at $\eta = 0.5$

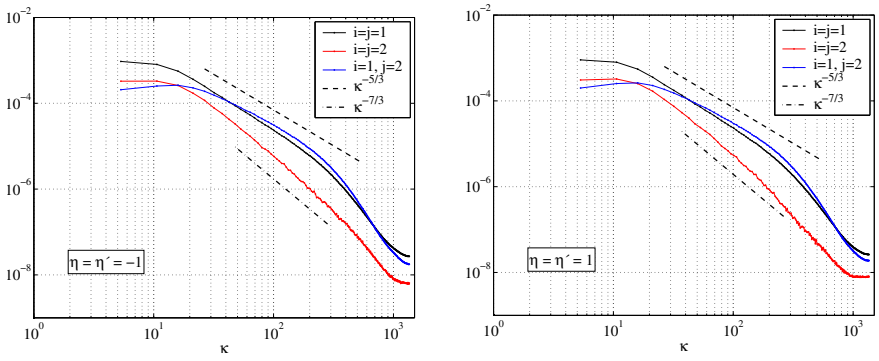

(c) at $\eta = -1$

(d) at $\eta = 1$

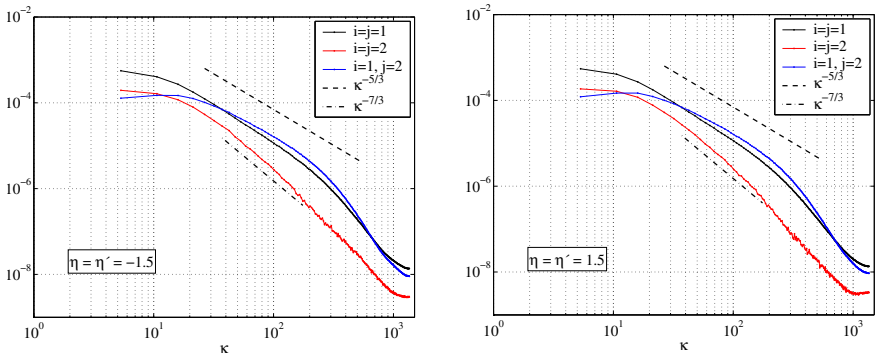

(e) at $\eta = -1.5$

(f) at $\eta = 1.5$

Fig. 5.7: One-dimensional spatial spectral tensor elements $\Phi^{(1)}_{i,j}(\kappa, \eta, \eta)$ at several radial positions. Black curves indicate $\Phi^{(1)}_{1,1}$, blue curves $\Phi^{(1)}_{2,2}$ and red curves $\Phi^{(1)}_{1,2}$. Dashed lines correspond to slope of $\kappa^{-5/3}$ and $\kappa^{-7/3}$ respectively.

cross-spectrum, the integral of which is the Reynolds shear stress. These show the $\kappa^{-7/3}$ inertial subrange behavior that has been previously noted for turbulent shear flows (like the atmosphere), c.f., Panofsky and Lumley [60]). The basic argument for this is that the Reynolds stress spectrum should be proportional to the mean velocity gradient (using an eddy viscosity argument), so the only possibility using ε and κ as parameters is $\kappa^{-7/3}$. As a qualitative overview of the overall radial distribution of the three one-dimensional single point spectra, figures 5.8(a), 5.8(b) and 5.8(c) show the spectral estimates on logarithmic axes.

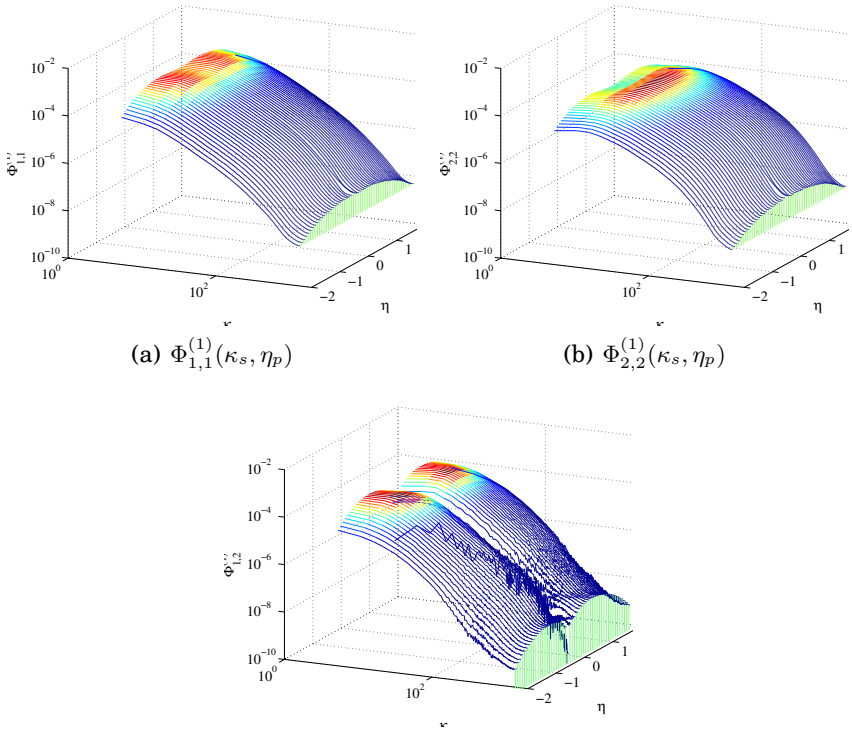

(a) $\Phi^{(1)}_{1,1}(\kappa_s, \eta_p)$ (b) $\Phi^{(1)}_{2,2}(\kappa_s, \eta_p)$

(c) $\Phi^{(1)}_{1,2}(\kappa_s, \eta_p)$

Fig. 5.8: Elements of the single point one-dimensional spectrum tensor $\Phi^{(1)}_{i,j}(\kappa_s, \eta_p)$.

5.4 Contribution of noise to the spectral estimates

The predominant adverse effect on the spectra presented in this chapter has been recognized to the be the spatial filtering resulting from the finite interro-

gation volume size. The filtering removes energy from the highest wavenumbers so the the overall turbulence energy captured is reduced. Since the spatial interrogation volumes for the two cameras is fixed while the scales grow downstream, the amount of energy removed is progressively less so the turbulence intensities appear to grow downstream. The net result is that the energy is slightly less than might have been expected from the Hussein et al. [16] measurements with LDA and flying hot-wire. As a consequence any contributions from noise are not obvious. Since these data will be used in the next section for POD analysis, it is important to estimate what the contribution of the noise are, and where it appears in the spectrum. The primary sources of noise in this experiment are three-fold: first, the noise which arises from the turbulence itself due to the finite number of particles on which the individual velocities are estimated by the PIV; second, the noise added to the process by the distorting effect of imperfections of the imaging of particles on the PIV correlation peak, and finally, the quantization, i.e., the rounding off of the measured signal value by the smallest available level quantification. For standard PIV data obtained under good conditions, an total rms error on the order of 0.1 pixel can be expected.

The total measurement uncertainty is considered by Foucaut et al. [57] to manifest as a random noise that is filtered by the PIV interrogation window. It should thus appear in the spectra as a constant multiplied to the spectrum of the interrogation window (a $sinc^2(k_1 l/2)$, l window dimension) which is added to the true spectrum, see equation 4.32, possibly distorted by the convolving effect of a finite domain window. It should be noted that while the spectra estimated by Foucaut et al. [57] show distinct evidence of the lobes of the cardinal sine function at the higher end of their spectra, this feature has note been observed in the spectral estimates calculated herein. The reason for this difference is possibly due to a spectral ´smearing' effect when Fourier transforming a signal subject to locally linearly varying filtering.

In the analysis below the last two sources of measurement uncertainty will be considered to have been added to the velocity data and therefore treated independently from the it. It is also considered to be uncorrelated from the velocity estimates. The unique problem for this experiment is that the data have been re-scaled, both in amplitude and space by logarithmically transforming it and by dividing each realization by the mean centerline velocity. Thus, although the mean square value of the quantization noise, for example, can be estimated as $\epsilon^2/12$ and its spectrum to be white, the contribution to the transformed data is not so simple. Moreover, unlike the original errors, the errors in the transformed environment are not even homogeneous (since they have been divided by the centerline velocity which diminishes downstream as $(x - x_o)^{-1}$). Nonetheless, as shown in Appendix 3 of this chapter, the contribution to the ξ-space spectra can still be shown to be white, but with a spectrum which depends on the domain and is given by:

$$\Upsilon^{L_\xi}(\kappa) = \frac{\epsilon^2}{48\pi B^2 M_o}\left[\frac{e^{2L_{\xi_{max}}} - e^{2L_{\xi_{min}}}}{4\pi L_\xi}\right] \tag{5.9}$$

In discrete spectral computations the quantization noise variance is spread evenly over the spectral domain from $(-\pi/\Delta_\xi, \pi/\Delta_\xi)$. For the spectra shown above the computed quantization level assuming a resolution of 0.01 pixel corresponds below the level at which the spectra flattens out at the highest wavenumbers, or nearly an order of magnitude less than the conventional value of 0.1 pixels. It also dominates the spectrum only at wavenumber well beyond those at which spatial filtering dominates the measured spectrum. Thus the contributions from white noise sources would appear to be negligible. Note also that (as observed) the effect of quantization noise on the Reynolds stress spectrum would be expected to be significantly less (or perhaps even zero), since there is little to no correlation between the quantization of one velocity component and another. For the cross-spectra (not shown here) the quantization noise would be expected to be identically zero.

Another contribution to the spectral noise arises from the finite and random number of particles on which an individual realization is based. This has recently been considered theoretically by George (2009, private communication) who estimates the mean square contribution to be $var\{u\}/N$ where N is the average number of particles in the interrogation volume. The spectrum of this contribution has a shape determined by the Fourier transform of the interrogation volume and is given by:

$$\Upsilon^{turb}(\kappa) = \frac{1}{4\pi N}\frac{\langle u_i u_j\rangle}{U_c^2}\frac{\Delta}{(x - x_o)}\left[\frac{sin(k_1 l/4)}{k_1 l/4}\right]^2 \tag{5.10}$$

For even a nominal number of particles (say $N = 10$) this is several orders of magnitude below the spectra shown above for all values below the cut-off wavenumber.

Thus in summary: the sources of noise we have been able to consider to not significantly affect the spectral data presented herein. In part this is because these noise levels are low, and in part because the spatial filtering restricts our wavenumbers of interest to those well below any wavenumber at which their effects would be felt.

5.5 Summary

The two-point correlations and spectra (including cross-spectra) of the logarithmically transformed data in similarity variables are remarkably consis-

tent, both with other experiments in the same facility and with prevailing theory and conventional wisdom. Thus both the PIV methodology and the two-point similarity theory would seem to have been well-substantiated. The former is particularly gratifying given the extraordinary large windows used, which very much stretched the limits of the hardware.

6. STREAMWISE EXPERIMENT POD

As explained in Chapter 3, the optimal decomposition in the radial direction of the turbulent jet is the so-called 'classical' proper orthogonal decomposition (POD). In many ways, the radial extent of the jet this the the perfect application for the POD, since the the fundamental constraints on its use are that the region be of finite total energy, which the jet in the radial direction satisfies. Moreover the ratio of lateral extent to the integral scale is relatively small ($L/I \approx 4-5$), so the number of eigenvectors necessary to capture most of this energy is quite small. This can be contrasted the streamwise direction where the ratio is effectively infinite, hence the need for as continuous wavenumber Fourier representation.

6.1 POD analysis of two-point velocity cross - spectra

The implementation of the POD begins by first decomposing the field into streamwise Fourier modes for each wavenumber, κ, then using the two-point cross-spectra for different values of normalized radial position as the kernel in the POD integral; i.e.,

$$\int_0^\infty \Phi_{i,j}^{(1)}(\kappa_s, \eta, \eta')\phi_j(\kappa, \eta')\eta' d\eta' = \lambda(\kappa)\phi_i(\eta, \kappa) \tag{6.1}$$

Thus for each value of κ, a separate eigenvalue problem must be solved. Since the field in the η-direction has finite total energy (for each wavenumber), the integral problem reduces to the classical Karhunen-Loéve expansion discussed in Chapter 3. There are in principle a countably infinite number of eigenvectors, say $\phi_i^{(n)}(\eta, \kappa)$, and eigenvalues, say $\lambda_n(\kappa)$. These solutions are optimal in the sense that $\lambda_1 1 > \lambda_2 > \lambda_3$, etc. Moreover, the sum over all the eigenvalues yields the energy for a given wavenumber, κ. The kernel can be reconstructed as:

$$\Phi_{i,j}^{(1)}(\kappa,\eta,\eta') = \sum_{n=1}^{\infty} \lambda_n \phi_i^{(n)*}(\eta,\kappa)\phi_j^{(n)}(\eta,\kappa) \tag{6.2}$$

Finally, and most importantly from the perspective of understanding the physics, the instantaneous Fourier transformed velocity field can be also reconstructed from the eigenfunctions using coefficients determined by projecting the eigenfunctions onto it; i.e.,

$$\hat{v}_i(\eta,\kappa) = \sum_{n=1}^{\infty} a_n(\kappa)\phi_i^{(n)}(\eta,\kappa) \tag{6.3}$$

where the $a_n(\kappa)$ are random coefficients given by:

$$a_n(\kappa) = \int_0^{\infty} \phi_i^{(n)*}(\eta,\kappa)\hat{v}_i(\eta,\kappa)\eta d\eta \tag{6.4}$$

This chapter is about the application of this theory to the streamwise experiment, and the results of doing so.

6.2 Implementation over a finite, discretely sampled domain

The techniques applied herein have previously been applied to jets by Glauser et al. 1991, Citriniti and George [37], Jung et al. [61]and Gamard et al. [8], but using frequency data obtained from rakes of hot-wire probes. This is believed to be the first time it has been applied to actual spatial wavenumber cross-spectra, at least without the need to invoke Taylor's hypothesis.

The first major difference from the theory outlined in the introduction above is that the domain itself is not only of finite total energy, it is spatially finite and truncated at $\eta = 2$. The corresponding integral equation is:

$$\int_0^2 \Phi_{i,j}^{(1)}(\kappa_s,\eta,\eta')\phi_j(\kappa_s,\eta')\eta' d\eta' = \lambda(\kappa_s)\phi_i(\eta,\kappa_s) \tag{6.5}$$

where the subscript s indicates the discrete nature of the wavenumber space. As noted in the previous chapters, it would perhaps have been better had the integral been truncated at $\eta = 2.5$, although it is not obvious immediately what the effect would be.

Second, solution by standard matrix techniques requires a Hermitian symmetric kernel. Because of the radial metric, the kernel $\eta'\Phi_{i,j}^{(1)}(\kappa,\eta,\eta')$ is not

symmetric with respect to both η and η'. However, if, as first suggested by Glauser et al. [], the kernel can be symmetrized by re-defining the basis function as:

$$\tilde{\phi}_i(\kappa_s, \eta) = \eta^{1/2}\phi_i(\kappa_s, \eta) \tag{6.6}$$

and absorbing the remaining dependence on η and η' into the kernel as:

$$\tilde{\Phi}^{(1)}_{i,j}(\kappa_s, \eta, \eta') = \eta^{1/2}\eta'^{1/2}\Phi^{(1)}_{i,j}(\kappa_s, \eta, \eta') \tag{6.7}$$

Lastly, the integral equation 6.5 must be approximated by a discrete sum as:

$$\sum_{q=0}^{P} \tilde{\Phi}^{(1)}_{i,j}(\kappa_s, \eta_p, \eta_q)\tilde{\phi}_j(\kappa_s, \eta_q)\Delta\eta = \lambda\tilde{\phi}_i(\kappa_s\eta_p) \tag{6.8}$$

where $\eta_p = p\Delta\eta,\ \ p, q = 1, 2, ..., P$ and P is the total number of grid points in η.

The corresponding matrix equation can be solved with a matrix eigenvalue solver in matlab. If the matrix $\mathbf{A}_s$ is formed as

$$\mathbf{A}_s = \Delta\eta \begin{bmatrix} \tilde{\Phi}^{(1)}_{1,1}(\kappa_s, \eta_p, \eta_q) & \tilde{\Phi}^{(1)}_{1,2}(\kappa_s, \eta_p, \eta_q) \\ \tilde{\Phi}^{(1)}_{2,1}(\kappa_s, \eta_p, \eta_q) & \tilde{\Phi}^{(1)}_{2,2}(\kappa_s, \eta_p, \eta_q) \end{bmatrix} \tag{6.9}$$

the eigenvalue solver outputs matrices $\mathbf{V}_s$ and $\mathbf{D}_s$ such that

$$\mathbf{A}_s\mathbf{V}_s = \mathbf{V}_s\mathbf{D}_s \tag{6.10}$$

where $\mathbf{D}_s$ is a diagonal matrix with the eigenvalues $\lambda_n(\kappa_s)$ of $\mathbf{A}_s$ as diagonal elements and where the columns of $\mathbf{V}_s$ contain the vector elements of corresponding $2P$ eigenvectors $\tilde{\phi}^{(n)}_i(\eta_p)$. The desired eigenvectors $\phi^{(n)}_i(\kappa_s, \eta_p)$ of the discrete kernel $\Delta\eta\Phi^{(1)}_{i,j}(\kappa_s, \eta_p, \eta_q)\eta_q$ are then found from equation 6.6 as

$$\phi^{(n)}_i(\kappa_s, \eta_p) = \eta_p^{-1/2}\tilde{\phi}^{(n)}_i(\kappa_s, \eta_p) \tag{6.11}$$

It should be noted that the division of the modified eigenvectors $\tilde{\phi}^{(n)}_i(\kappa_s, \eta_p)$ by $\eta^{1/2}$ would correspond to dividing by zero at the origin. Therefore the values of $\phi^{(n)}_i(0)$ are instead determined from the definition of the POD integral, which for $\eta = 0$ is:

$$\phi^{(n)}_i(\kappa_s, 0) = \frac{1}{\lambda_n}\int_0^\infty F_{i,j}(\kappa_s, 0, \eta')\phi^{(n)}_j(\kappa_s, \eta')\eta' d\eta' \tag{6.12}$$

This operation is possible to perform, despite lack of knowledge of $\phi^{(n)}_i(\kappa_s, 0)$, since the integrand of 6.12 is zero at the lower boundary $\eta' = 0$. For the discrete case, this operation corresponds to

$$\phi_i^{(n)}(\kappa_s, \eta_0) = \frac{\Delta\eta}{\lambda_n} \sum_{q=1}^{P} F_{i,j}(\kappa_s, 0, \eta_q)\phi_j^{(n)}(\kappa_s, \eta_q)\eta_q \tag{6.13}$$

The only drawback of this method is that the last eigenvalue, λ_{2P}, is zero, causing the values of $\phi_i^{(2P)}(\kappa_s, 0)$ to be undefined. These are however the very least energy relevant modes to be determined by the analysis and as can be seen in figures 6.5(a) through 6.9 in section 6.4, the radial grid resolution has long since been unable to resolve the shape of the modes. In summary, the end result of the POD decomposition is that the correlation tensor has been expanded on a composite Fourier and POD mode basis so that

$$\Phi_{i,j}^{(1)}(\kappa_s, \eta_p, \eta_q) = \sum_{n=1}^{2P} \lambda_n(\kappa_s)\phi_i^{(n)*}(\kappa_s, \eta_p)\phi_j^{(n)}(\kappa_s, \eta_p) \tag{6.14}$$

6.3 Eigenspectra

The spectral energy density per POD mode number $n = 1, 2, ..., 2P$, where $P = 26$ is the number of radial grid points, and wavenumber κ_s, $s = 0, 1, ..., S$ where $S = 255$ is simply $\lambda_n(\kappa_s)$. The distribution over all the combinations of n and s is presented on linear axes in figure 6.1(a). This representation is not particularly illuminating, since the magnitude of the eigenvalues appear to drop quite rapidly with both POD mode number n and wavenumber κ_s. If instead the axes are made logarithmic, as in figure 6.1(b), the variation of spectral density over the basis functions is more evident.

More specific comparisons of the POD eigenvalues, their rate of convergence and the variation over wavenumbers space can be made if the eigenvalues are normalized. The energy of the Fourier transformed field is, in the continuous case,

$$\begin{aligned}
\int_0^\infty \langle v_i(\eta)v_i(\eta)\rangle\eta d\eta &= \int_0^\infty d\eta \int_{-\infty}^\infty \eta\Phi_{i,i}^{(1)}(\kappa, \eta, \eta)d\kappa \\
&= \int_{-\infty}^\infty d\kappa \sum_{n=1}^\infty \lambda_n(\kappa) \int_0^\infty \phi_i^{(n)*}(\kappa, \eta)\phi_i^{(n)}(\kappa, \eta)\eta d\eta \\
&= \int_{-\infty}^\infty \sum_{n=1}^\infty \lambda_n(\kappa)d\kappa
\end{aligned} \tag{6.15}$$

In the the current discrete case this infinite integral over an infinite sum of POD eigenvalues is a finite sum and the total energy represented in the field

is:

$$\mathcal{E} = \Delta\eta \sum_{p=0}^{P} \langle \upsilon_i(\xi_s, \eta_p)\upsilon_i(\xi_s, \eta_p)\rangle \eta_p = \Delta\kappa \sum_{s=0}^{S}\sum_{n=1}^{2P} \lambda_n(\kappa_s) \tag{6.16}$$

so that the relative energy per POD mode and Fourier mode is simply $\lambda_n(\kappa_s)/\mathcal{E}$.

The rate of convergence of the POD expansion 6.14 can be evaluated by the slope of a partial sum over the mode numbers: the steeper the the slope of the curve formed by the partial sum, the less POD modes must be retained in order to represent the spectral density at a given wave number. Defining a partial sum over POD mode numbers per wavenumber as :

$$\Lambda_N(\kappa_s) = \sum_{n=1}^{N} \lambda_n(\kappa_s) \tag{6.17}$$

the rate at which each POD expansion converges to the relative spectral density is

$$\chi_N(\kappa_s) = \frac{\lambda_N(\kappa_s)}{\mathcal{E}} \tag{6.18}$$

Figure 6.3 shows such a distribution on linear axes. While it appears that the POD expansions for the lower wavenumbers converge quickly, the rate appears to slow down with increasing wavenumber.

In order to highlight the varying convergence rates at different wavenumbers the ratio of the eigenvalue magnitude relative to the spectral density per wavenumbers can be formed as:

$$\gamma_n(\kappa_s) = \frac{\lambda_n(\kappa_s)}{\Lambda_{2P}(\kappa_s)} \tag{6.19}$$

Forming $\Gamma_N\kappa_s$, the partial sum over $\gamma_n(\kappa_s)$ as:

$$\Gamma_N(\kappa_s) = \sum_{n=1}^{N} \gamma_n(\kappa_s) = \frac{\Lambda_N(\kappa_s)}{\Lambda_{2P}(\kappa_s)} \tag{6.20}$$

The relative rate of convergence of the POD expansion per wavenumber is visualized in figure 6.3. From the figure it is clear that the rate of convergence for the POD expansions does indeed decrease with increasing wavenumber in the interval $0 \leq \kappa \leq 450$, but that the rate of convergence then increases for the rest of the wavenumbers. Figure 6.3 shows a more detailed curve for $\Gamma_1(\kappa_s)$ from which it is evident that the relative fraction of energy drops from about 60% to about 7% between $\kappa = 0$ and $\kappa = 450$. Based on the arguments made for the spectral roll-off due to the filtering of the finite PIV interrogation window, it is likely that this also affects the POD decomposition results. Thus the apparent increase in POD expansion convergence rate evident in the interval

$450 \leq \kappa \leq 1350$ is not believed to be physically representative. As will be seen from the inspection of the eigenvectors in the following chapter, the character of the eigenvectors changes markedly a about $\kappa = 450$.

At the low wavenumber end of the interval $0 \leq \kappa \leq 450$ the values of Γ_N are the highest in the entire distribution and the rate of convergence is rapid. However, as the wavenumber increases towards the higher end of the sub-interval, the values of Γ_1 drop radically and, as noted above, appear to be approaching a constant value. That means that the lowest order POD mode in each expansion captures less and less of the available spectral density. Since the theory dictates that each POD mode eigenvalue is larger than the following ones, it also means that the relative difference in magnitude among the POD eigenvalues decreases. This in turn indicates that a truncated representation of the flow requires higher and higher orders of the expansion. As will be seen in the following section, the POD modes themselves exhibit higher and higher sequency values (i.e. number of zero-crossings per unit length). In combination with the decreasing rate of convergence observed in the partial sums of the magnitudes of the eigenvalues, this could be consistent with the idea that the turbulence develops locally homogeneous features at the small scales so that a Fourier representation would be suitable.

6.4 Eigenvectors

The number of eigenvectors produced by the POD matrix decomposition is 2P = 52 per wavenumber κ_s. The real parts of the eigenvectors for all POD mode numbers for $\kappa_1 = 5.3$ are presented in figures 6.5(a) through 6.9. As the POD mode number n increases, the sequency, i.e., the number of zero-crossings of the radial modes, appears to increase as well. In fact for $n = 10$ and higher, the eigenfunctions resemble Fourier modes. This is quite consistent with the idea of *local homogeneity* of the small scales of motion, and the historical use of spectra and Fourier analysis to characterize them (c.f. Tennekes and Lumley [18]).

In order to properly display a discrete curve which exhibits zero-crossings as a smooth curve, the number of grid points per zero-crossing should be 10 (at least without using an interpolation formula). Since the number of grid points is fixed at P=26, it is inevitable that the higher order POD modes which exhibit high sequency have the appearance of saw-tooth functions. This is noted for $n > 30$. It is also seen that the eigenvector components become more and more singular at the extremes of the radial domain and approach zero inside the domain. It is thought that this behavior is due to the numerical method of finding linearly independent vectors rather then representative of some property of the turbulence.

Another interesting feature of the decomposition is the variation of eigenvector shape per POD mode number and wavenumber. In order to investigate this feature of the basis, the magnitude of the real and imaginary parts of the components of the 12 first POD eigenvectors are plotted as surfaces in figures 6.10(a) through 6.17(d) below.

Before trying to interpret these result, first recall that spatial filtering dominates the wavenumber spectra on which the POD analysis is based for wavenumbers beyond $\kappa \approx 300 - 500$, as discussed in detail in the preceding chapter. Low-pass filtering almost always brings with it significant phase shifts as well. All of the surface plots show a significant change in character beyond about $\kappa = 400$, consistent with the spatial filtering and also consistent with the change in the partial POD eigenvalue sums for $\kappa > 450$, see figure 6.3. Thus nothing beyond this value is of interest.

What is of considerable interest, however, is the nature of the eigenfunctions for both the streamwise and cross-stream components below $\kappa \approx 50$: the horizontal columns in the figures mean that the shape of the eigenfunctions is relatively independent of wavenumber. Moreover the eigenfunctions are almost pure real-valued. This behavior persists through all of the plots below $\kappa \approx 50$, even to the highest POD mode. This has important implications for how the Reynolds shear stress is produced, since from equation 6.2,

$$\Phi_{1,2}^{(1)}(\kappa, \eta, \eta) = \sum_{n=1}^{N} \lambda_n(\kappa) \phi_1^{(n)}(\eta, \kappa)^* \phi_2^{(n)}(\eta, \kappa) \tag{6.21}$$

It is clear that the eigenfunctions must produce Reynolds shear stress in proportion to the turbulence energy density at a given wavenumber if they do not have a significant complex part.

The change in character of the eigenfunctions at about $\kappa \approx 50$ corresponds to where the turbulence component energy spectra appeared to be beginning to develop an inertial subrange (or $k^{-5/3}$-range). First the distance between the surfaces gets smaller with increasing n. Second the basic character remains nearly wavenumber independent until the filtering begins to affect the data. Third, and perhaps most importantly, the higher the mode number and wavenumber within these limits, the more significant the complex parts. This is very consistent with the observation above about the Reynolds shear stress, and explains (or at least correlates with) the fact that the Reynolds shear stress cross-spectrum falls faster than either velocity component ($\kappa^{-7/3}$ versus $\kappa^{-5/3}$). It is also consistent with the long-alleged trend toward local isotropy (and zero Reynolds stress) with increasing wavenumber, since the real and imaginary parts become nearly equal. This can also be taken to be supportive of the idea that the scales of motion smaller than those characteristic of the inertial subrange might be nearly universal, at least statistically speaking.

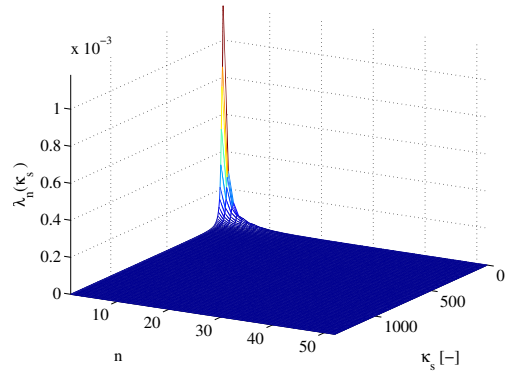

(a)

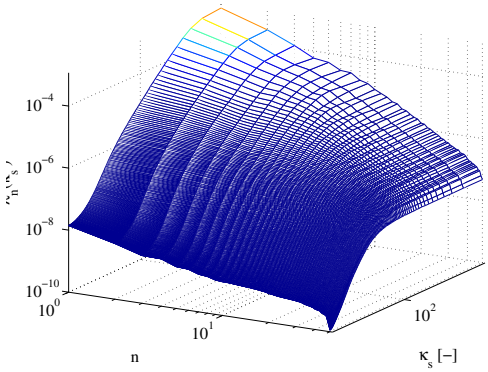

(b)

Fig. 6.1: Distribution of the eigenvalues $\lambda_n(\kappa_s)$ over streamwise wavenumber κ_s and radial POD mode number n on linear axes in (a) and on logarithmic axes in (b).

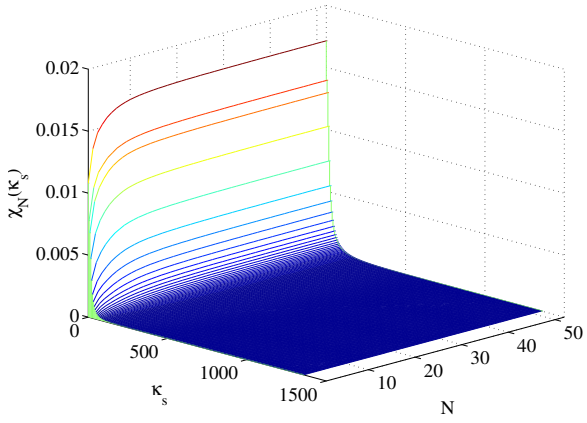

Fig. 6.2: Distribution of $\chi_N(\kappa_s)$, the partial sums over POD mode number n per wavenumber κ_s, normalized by the total energy of the field.

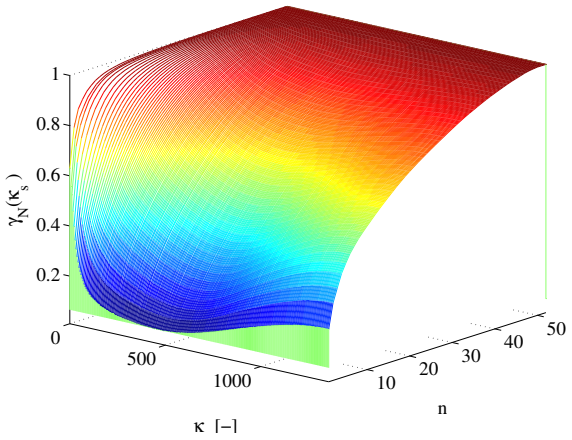

Fig. 6.3: Distribution of $\Gamma_N(\kappa_s)$, the partial sums of the POD eigenvalues normalized by the total spectral density available at each wavenumber κ_s.

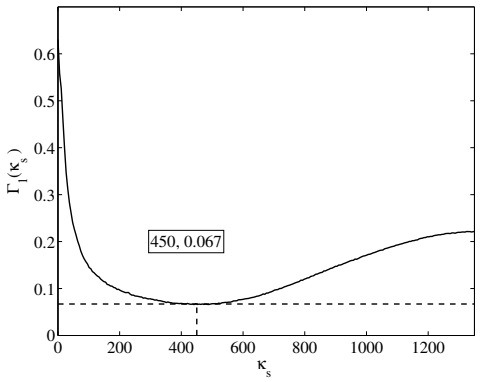

Fig. 6.4: Variation of $\Gamma_1(\kappa_s)$, corresponding to the first POD eigenvalue per wavenumbers κ_s, normalized by the total spectral density available at each wavenumber.

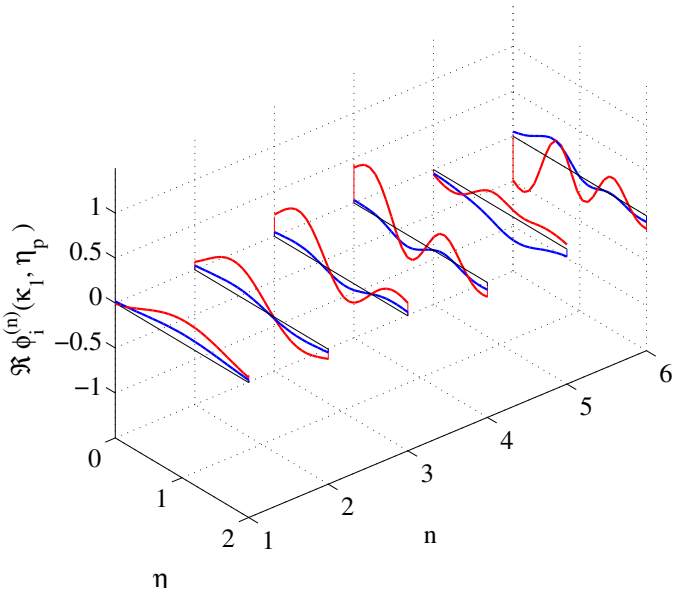

(a) $1 \leq n \leq 6$

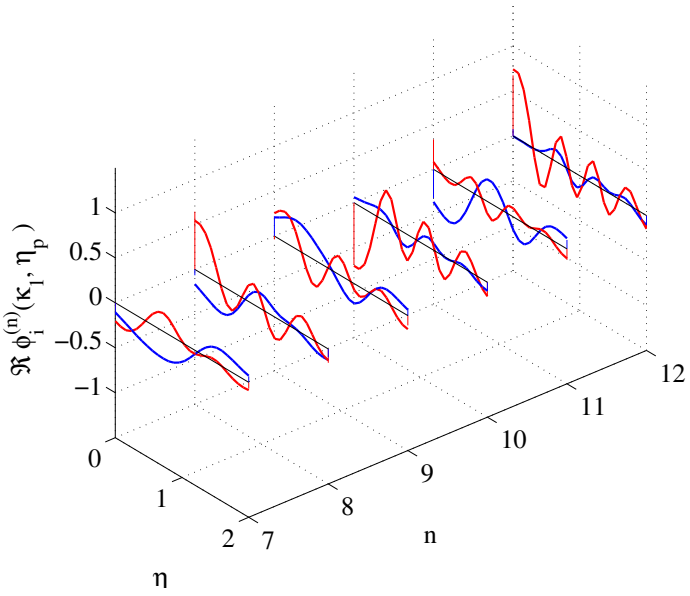

(b) $7 \leq n \leq 12$

Fig. 6.5: Real parts of eigenvectors $\phi_i^{(n)}(\eta,\kappa_1)$, $1 \leq n \leq 12$. (-) $\phi_1^{(n)}(\eta,\kappa_1)$, (-) $\phi_2^{(n)}(\eta,\kappa_1)$.

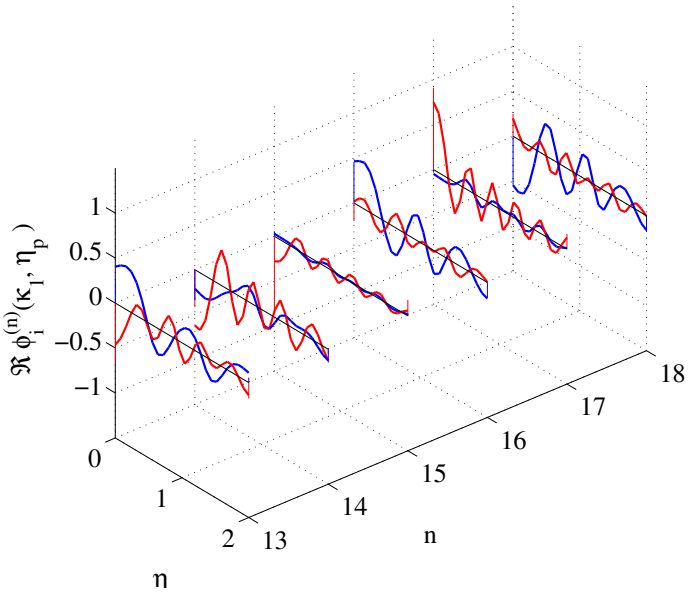

(a) $13 \leq n \leq 18$

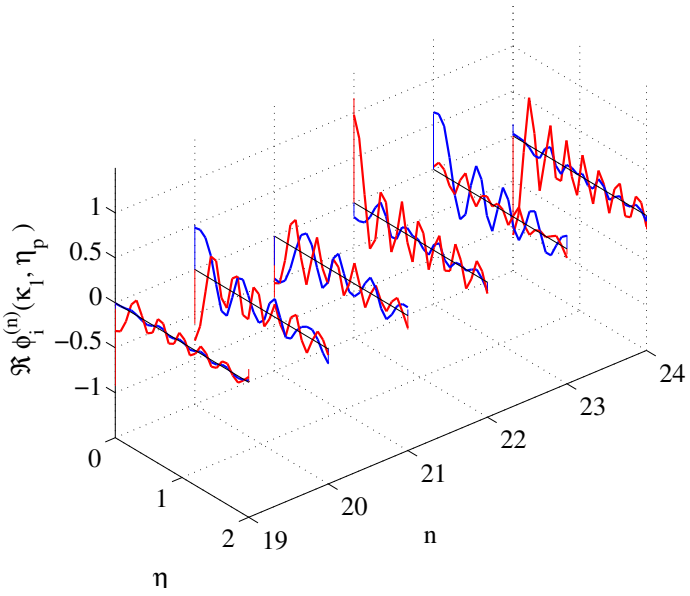

(b) $19 \leq n \leq 24$

Fig. 6.6: Real parts of eigenvectors $\phi_i^{(n)}(\eta, \kappa_1)$, $13 \leq n \leq 24$. (-) $\phi_1^{(n)}(\eta, \kappa_1)$, (-) $\phi_2^{(n)}(\eta, \kappa_1)$.

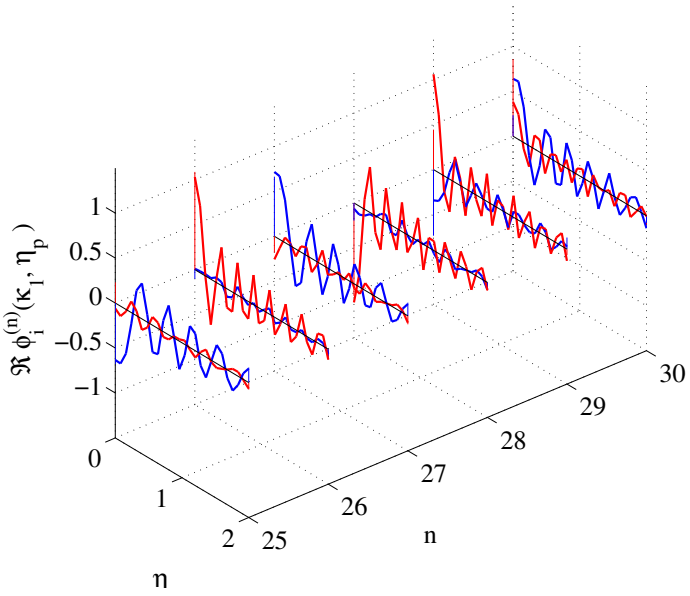

(a) $25 \leq n \leq 30$

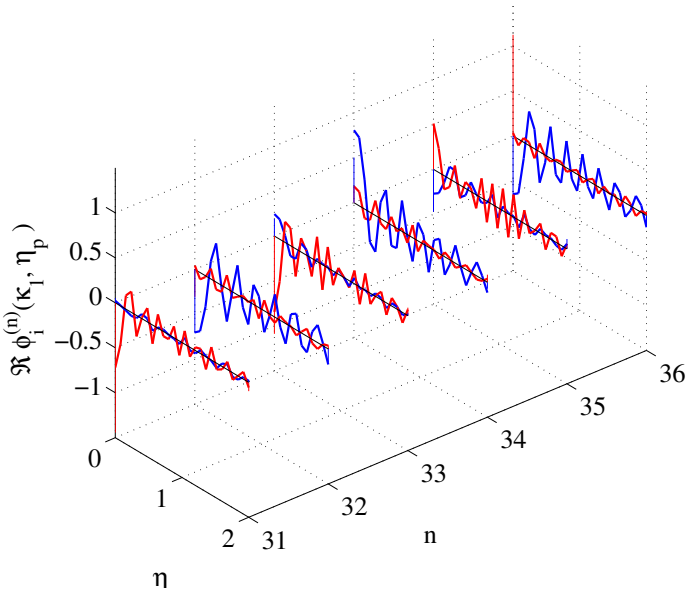

(b) $31 \leq n \leq 26$

Fig. 6.7: Real parts of eigenvectors $\phi_i^{(n)}(\eta,\kappa_1)$, $25 \leq n \leq 36$. (-) $\phi_1^{(n)}(\eta,\kappa_1)$, (-) $\phi_2^{(n)}(\eta,\kappa_1)$.

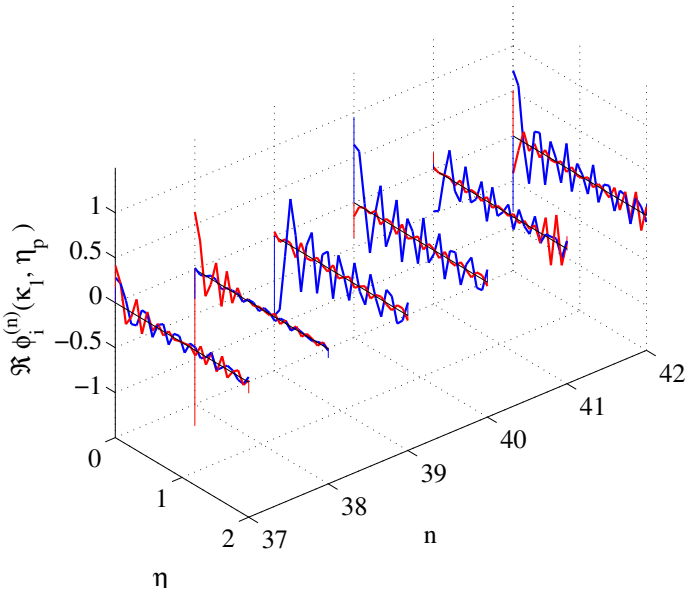

(a) $37 \leq n \leq 42$

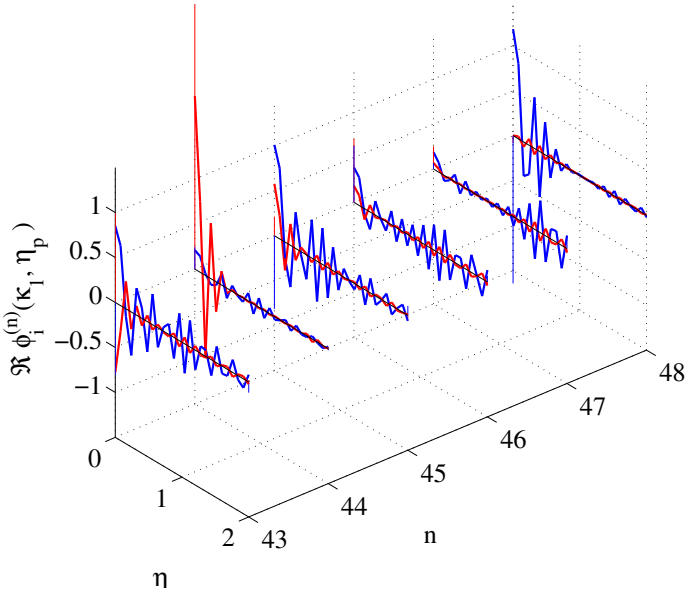

(b) $43 \leq n \leq 48$

Fig. 6.8: Real parts of eigenvectors $\Re_p hi_i^{(n)}(\eta, \kappa_1)$, $37 \leq n \leq 48$. (-) $\phi_1^{(n)}(\eta, \kappa_1)$, (-) $\phi_2^{(n)}(\eta, \kappa_1)$.

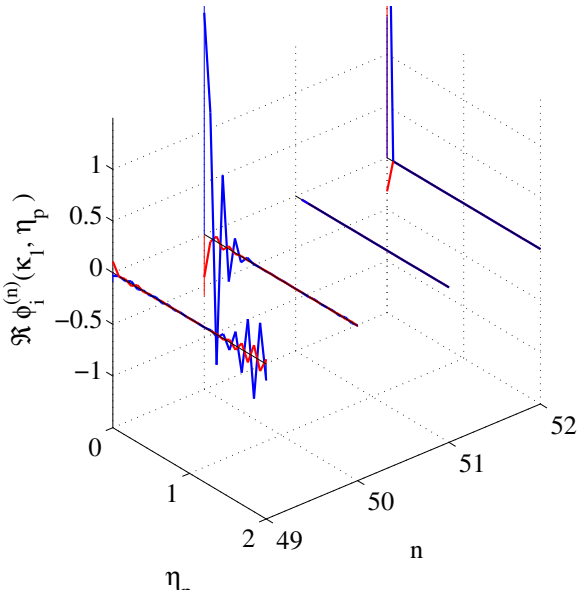

Fig. 6.9: Real parts of eigenvectors $\phi_i^{(n)}(\eta, \kappa_1)$, $49 \leq n \leq 52$. (-) $\phi_1^{(n)}(\eta, \kappa_1)$, (-) $\phi_2^{(n)}(\eta, \kappa_1)$.

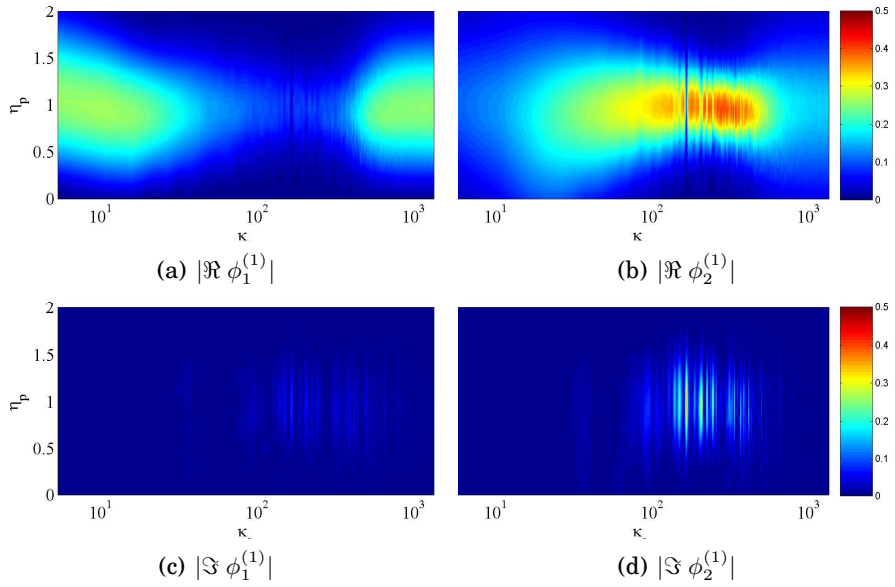

(a) $|\Re\ \phi_1^{(1)}|$ (b) $|\Re\ \phi_2^{(1)}|$

(c) $|\Im\ \phi_1^{(1)}|$ (d) $|\Im\ \phi_2^{(1)}|$

Fig. 6.10: Magnitudes of the real and imaginary parts of the eigenvector $\phi_i^{(n)}(\eta, \kappa_s)$, $n = 1$.

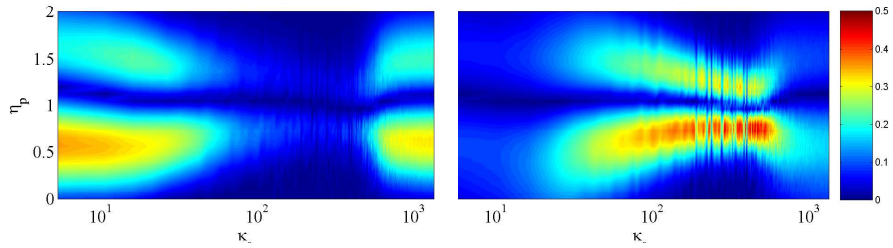

(a) $|\Re\ \phi_1^{(2)}|$ (b) $|\Re\ \phi_2^{(2)}|$

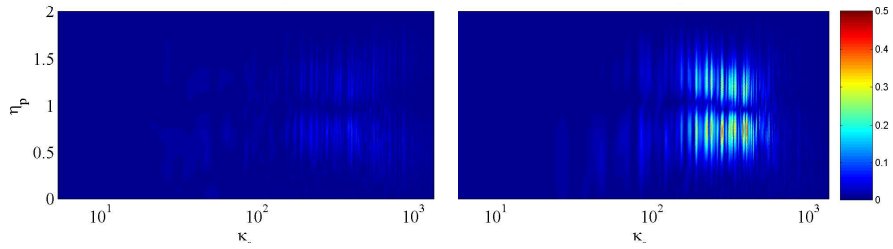

(c) $|\Im\ \phi_1^{(2)}|$ (d) $|\Im\ \phi_2^{(2)}|$

Fig. 6.11: Magnitudes of the real and imaginary parts of the eigenvector $\phi_i^{(n)}(\eta, \kappa_s)$, $n = 2$.

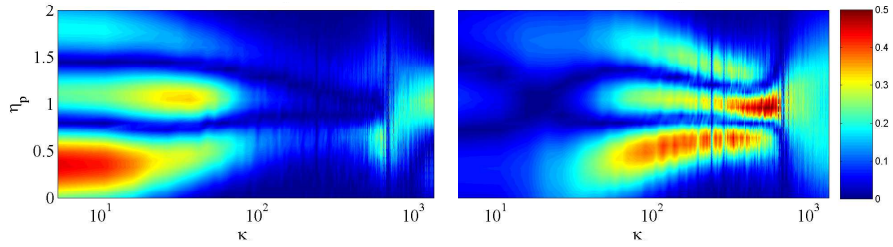

(a) $|\Re\ \phi_1^{(3)}|$ (b) $|\Re\ \phi_2^{(3)}|$

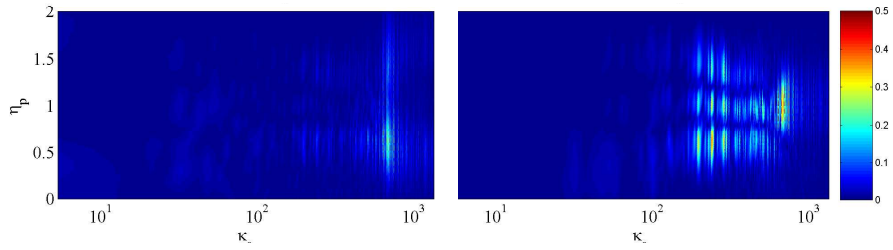

(c) $|\Im\ \phi_1^{(3)}|$ (d) $|\Im\ \phi_2^{(3)}|$

Fig. 6.12: Magnitudes of the real and imaginary parts of the eigenvector $\phi_i^{(n)}(\eta, \kappa_s)$, $n = 3$.

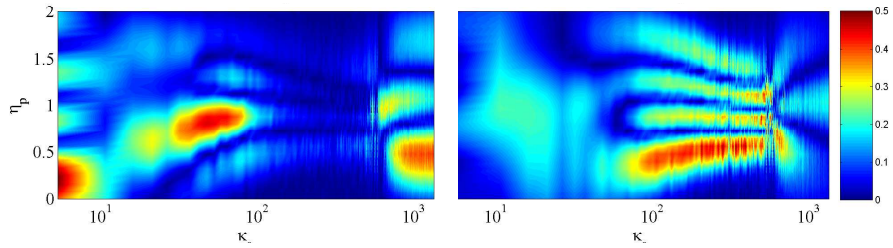

(a) $|\Re\ \phi_1^{(4)}|$ (b) $|\Re\ \phi_2^{(4)}|$

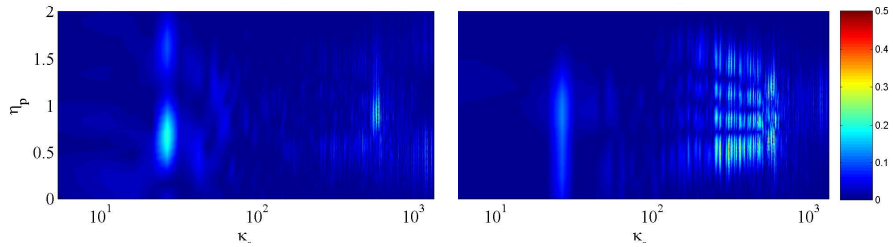

(c) $|\Im\ \phi_1^{(4)}|$ (d) $|\Im\ \phi_2^{(4)}|$

Fig. 6.13: Magnitudes of the real and imaginary parts of the eigenvector $\phi_i^{(n)}(\eta, \kappa_s)$, $n = 4$.

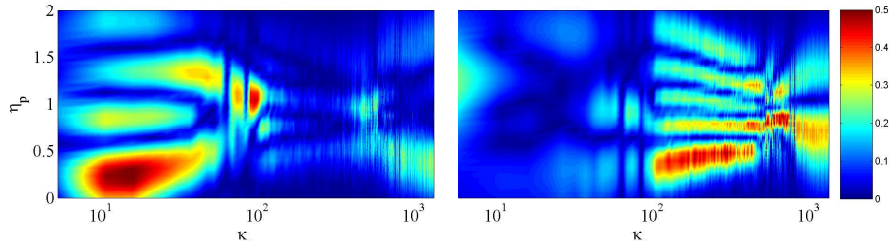

(a) $|\Re\ \phi_1^{(5)}|$ (b) $|\Re\ \phi_2^{(5)}|$

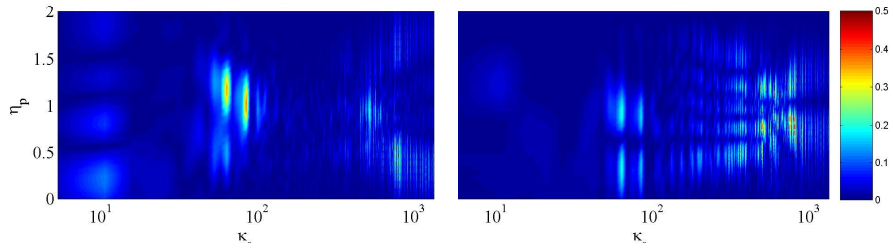

(c) $|\Im\ \phi_1^{(5)}|$ (d) $|\Im\ \phi_2^{(5)}|$

Fig. 6.14: Magnitudes of the real and imaginary parts of the eigenvector $\phi_i^{(n)}(\eta, \kappa_s)$, $n = 5$.

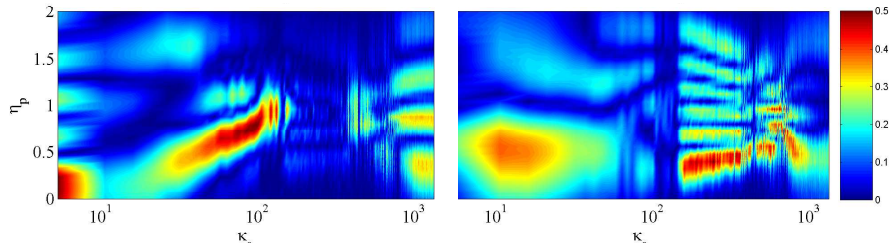

(a) $|\Re\ \phi_1^{(6)}|$ (b) $|\Re\ \phi_2^{(6)}|$

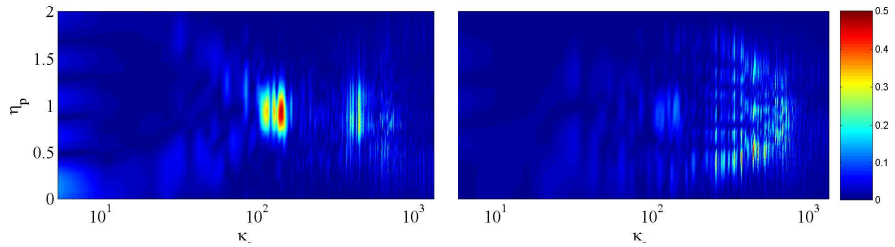

(c) $|\Im\ \phi_1^{(6)}|$ (d) $|\Im\ \phi_2^{(6)}|$

Fig. 6.15: Magnitudes of the real and imaginary parts of the eigenvector $\phi_i^{(n)}(\eta, \kappa_s)$, $n = 6$.

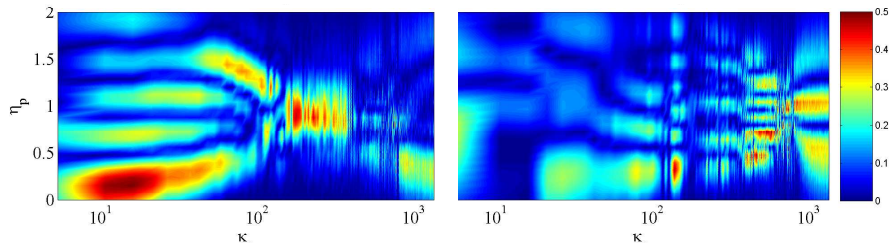

(a) $|\Re\ \phi_1^{(7)}|$ (b) $|\Re\ \phi_2^{(7)}|$

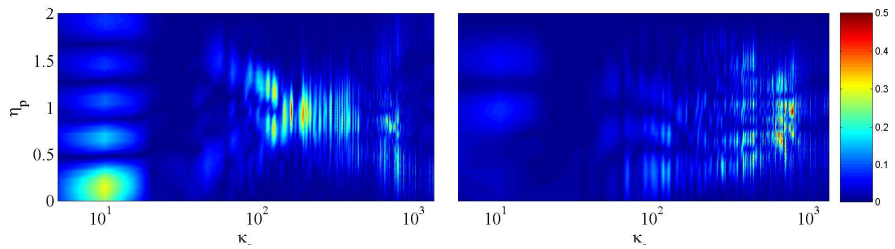

(c) $|\Im\ \phi_1^{(7)}|$ (d) $|\Im\ \phi_2^{(7)}|$

Fig. 6.16: Magnitudes of the real and imaginary parts of the eigenvector $\phi_i^{(n)}(\eta, \kappa_s)$, $n = 7$.

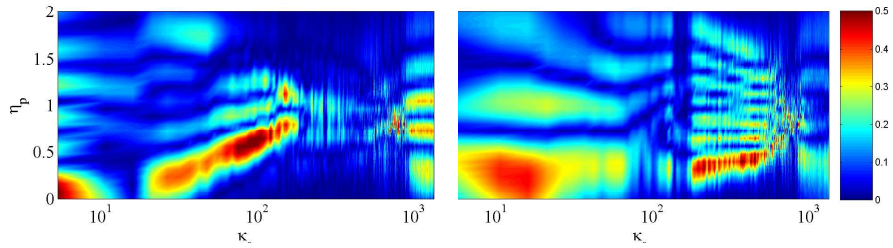

(a) $|\Re\ \phi_1^{(8)}|$ (b) $|\Re\ \phi_2^{(8)}|$

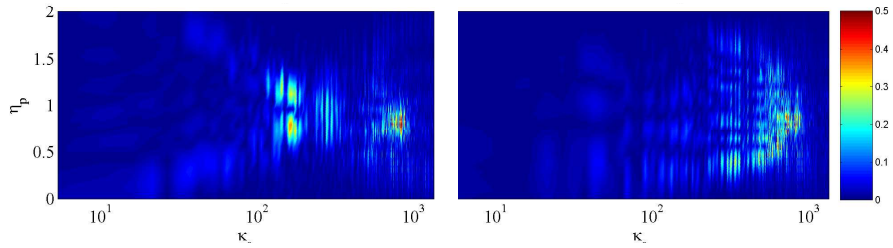

(c) $|\Im\ \phi_1^{(8)}|$ (d) $|\Im\ \phi_2^{(8)}|$

Fig. 6.17: Magnitudes of the real and imaginary parts of the eigenvector $\phi_i^{(n)}(\eta, \kappa_s)$, $n = 8$.

Part II

CROSS-PLANE EXPERIMENT

7. INTRODUCTION TO PART II

The second part of this thesis continues a series of experimental investigations which have been carried out on incompressible axisymmetric jets in the Turbulence Research Laboratory over the past 25 years, beginning with Glauser and George [33], Citriniti and George [37], and most recently represented by the papers of Jung et al. [62] and Gamard et al. [63]. Earlier versions of this work were presented by Wänström et al. [64], [65], [66]. The common purpose of the above experiments has been the application of Proper Orthogonal Decomposition (POD) techniques to this canonical flow, a methodology which aims at uncovering statistically identifiable azimuthal and radial constituents of the flow so that further insight into the dynamic interactions within the flow may be gained. The particular goal of this ongoing study was to enhance understanding how of the dynamical processes by which turbulence is produced and sustained via interaction with the mean flow.

Evolution of flow measuring equipment and methodology has made possible measurements that were previously impossible, with the result that each generation of experiments has extended our ability to probe the dynamics of turbulent flow. Attention should be brought to a number of parallel studies, for example Ukeily and Seiner [67, 68], Glauser et al. [69], Tinney [70] and Iqbal [71]. Earlier versions of the work presented in this chapter have appeared in Wänström et al [64, 72, 66] and Tutkun et al.[73].

7.1 Historical Review

The early studies (e.g., [33, 37] focussed on the jet mixing layer (i.e., at $x/D = 3$) and showed clearly evidence for a vortex ring-like structures. They suggested it was the breakdown of these rings into azimuthal modes between 4 and 6 that were the natural process for the turbulent jet mixing layer, and perhaps even the asymptotic jet (c.f., Grinstein et al.[74]).[1] Figure 7.1 from Jung et al.[62] presents the main characteristics.

[1] The recent success of chevrons, especially 6, at reducing jet noise can in part trace its origins to these observations.

> "At at $x/D = 2.0$...the azimuthally coherent 'volcano-like' eruption described by [37] is clearly present in the uppermost figure, and it evolves in the same manner they described. It was suggested by [37] that this was the result of the attempted leap-frogging of the azimuthally coherent vortex rings proposed by [74]. The eruption (figure 7.1 a) forces high-velocity fluid through its center along with the remnants of mode-6 in the potential core, while a new azimuthal mode-6 structure appears outside. The 'volcano' passes quickly leaving an azimuthally coherent structure (mode-6) in the potential core. Note that the higher modes (4 to 6) dominate the temporal pictures since they are mostly outside the core of the flow and are therefore swept past the probes more slowly. But it is the eruption that has most of the energy. The animation at higher Reynolds number shows the same evolution, but with more velocity fluctuation..."

Subsequently Gamard et al.[8] were able to extend the 138-hotwire-rake measurements to downstream locations as well. As is clear from figure 7.2, the picture of a single vortex ring like structure breaking down (or volcano-like event) was clearly too simplistic. In their words:

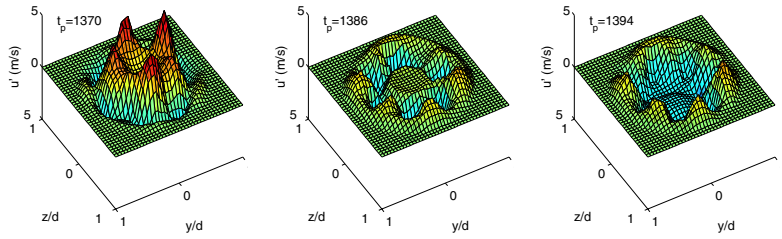

Fig. 7.1: Time sequence of reconstructed velocity field at $x/D = 2$ for Re_D= 117 600 using only the first POD mode, and azimuthal mode numbers m = 0, 3, 4, 5, 6, 7. From [62].

> "Unlike the reconstructions at $x/D = 2$ and 3, those at $x/D = 4$ are quite different, as shown in figure 7.2. The 'volcano-like' eruption still exists, but it is very weak. The most evident azimuthal mode changes from mode-4 to mode-3, consistent with eigenspectra ...."

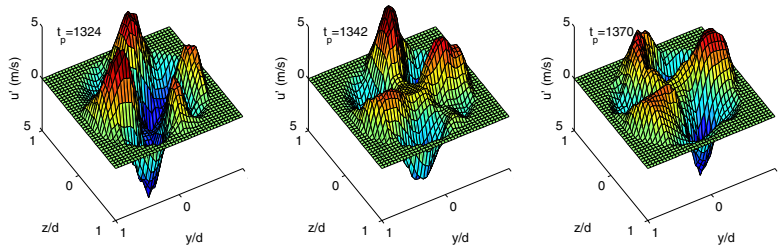

Fig. 7.2: Time sequence of reconstructed velocity field at $x/D = 4$ for Re_D= 117 600 using only the first POD mode, and azimuthal mode numbers m = 0, 1, 2, 3, 4, 5. From [62].

And they continued:

> "By 5 diameters downstream for all Reynolds numbers, the features show disorganized evolution, and are not periodic. Mode-0 is very small and has almost disappeared. Unlike the volcano-like eruptions, a 'propeller-like' motion is observed, which rotates (or precesses) slowly from frame to frame. By $x/D = 6.0$, the structure is simpler. Mode-0 is almost gone, and only lower mode numbers are observed for all Reynolds numbers. Azimuthal mode-2 and mode-3 appear in figure 7.3, showing quite large-scale structure. Energy shifting from one peak to another is quite obvious. Various mode numbers are observed, but the lower mode numbers dominate the evolution."

Inferences from inviscid linear stability theory had long predicted that the most unstable mode should be governed by mode-1 [12]. However, the study by Gamard et al. [63] found that the evolution of the dominant modes in the near jet did not continue all the way to mode-1 in the far jet (as expected). Instead, eigenspectra of the time-resolved streamwise velocity showed that the modal distribution of energy evolved towards dominance of azimuthal mode-2 in the far jet. Figure 7.4 from [63] shows the evolution of the azimuthal modes of the POD eigenspectra. Both the [62] and [63] studies were based on POD of two-point two-time correlations of the streamwise velocity fluctuations and their corresponding cross-spectra.

Almost simultaneously with the Gamard findings, Freund and Colonius [75] found supporting results for their low Reynolds number jet DNS, and

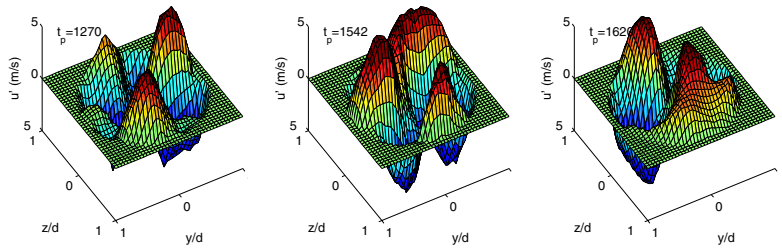

Fig. 7.3: Time sequence of reconstructed velocity field at $x/D = 6$ for Re_D= 117 600 using only the first POD mode, and azimuthal mode numbers m = 0, 1, 2, 3, 4, 5. From [62].

Kopiev and co-workers [76] discovered mode-2 dominating the radiated noise spectrum beyond a few jet exit diameters downstream. The implications of this on the theoretical questions were quite significant, since a majority of the community had assumed that the linear stability theory would capture the basic instability that drives the dynamics of even fully developed turbulent shear flows. Subsequent re-examination of the linear theory by George et al. [77] showed the possibility of mode-2 disturbance growth, but numerical studies by Chomaz and others (private communication) showed these disturbances to be stable. Liang and Maxworthy [78] were able to show that swirling flows could be unstable to mode-2, but there was no evidence of swirl in any of the jets subject to study. Nevertheless, the result of Gamard clearly showed that the turbulence kinetic energy of the streamwise fluctuations settles into an azimuthally modal variation best represented by mode-2 after the breakdown of the jet potential core, where mode-0 had most energy (which was itself consistent with linear theory because of the near top-hat profile at the exit). This would indicate that mode-2 could only arise from non-linear interactions.

In the light of these findings, the measurements by Thomas et al. [80, 79], seemed only to add to the confusion. As shown in figure 7.5 taken from their paper, they found that the eigenspectra peak at azimuthal mode 1 when the POD basis functions are found from the full velocity spectral tensor. This was in direct contrast to the results of [32, 33], who found no significant difference between the three-component and streamwise component decompositions for the jet mixing layer.

There were a number of differences among the experiments which complicated a direct comparison. First, the [79] jet was at much higher Reynolds exit

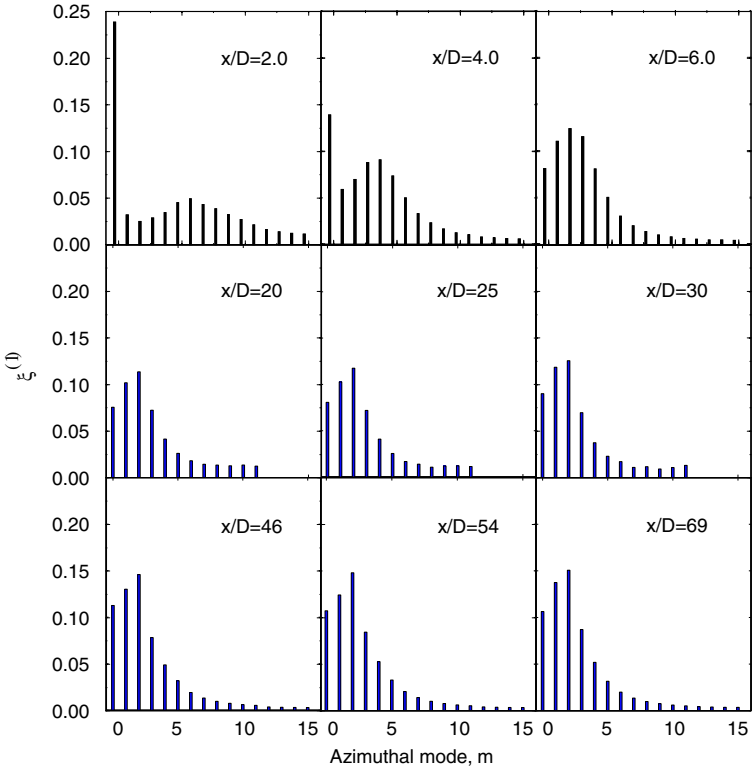

Fig. 7.4: Relative fraction of energy contained in the first eigenspectrum as a function of mode number. First row, near field results, second row 2.54 cm jet with 15 hot-wire array, third row 1 cm jet with 139 hot-wire array. From [63].

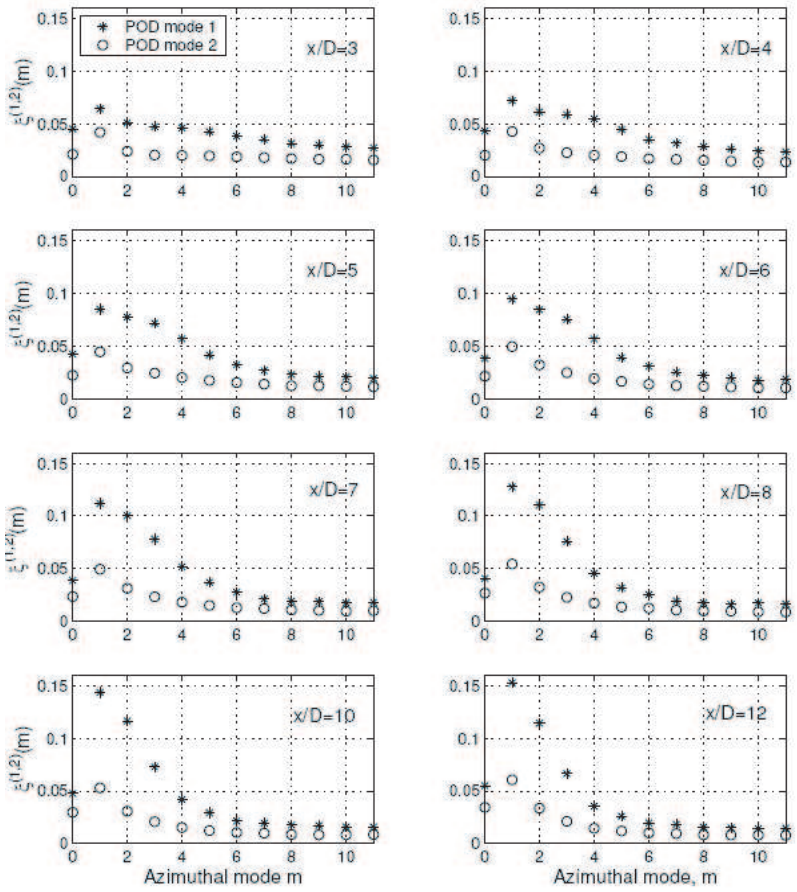

Fig. 7.5: Azimuthal mode distribution $\psi^{(n)}(m)$ for POD modes $n = 1$ and $n = 2$ where $\psi^{(n)}$ is the fraction of energy in each azimuthal mode. From [79], figure 14.

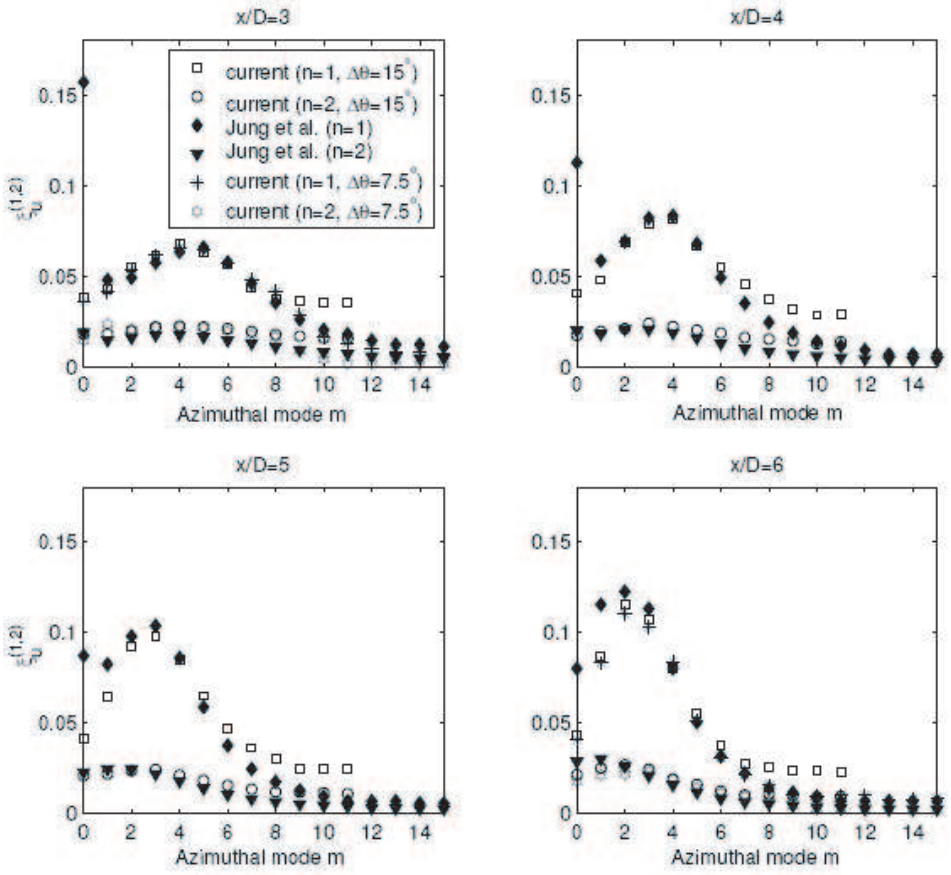

Fig. 7.6: Comparison of the azimuthal mode number dependence of u-component eigenspectra. From [79], figure 16.

number, 380,000, compared to the [63] experiments which ranged from 40,000 to 84,700. The [80, 79] experiments used cross-wire probes in two rakes (in the manner of [32]), and was thus not able to look at an entire cross-section simultaneously. The relevant cross-spectra were obtained sequentially by moving one of the rakes azimuthally. While in principle the results of this should be satisfactory, [45] showed that aliasing from one mode to another could occur if the azimuthal grid was too coarse, and they illustrated this with two experiments in the jet mixing layer. The earlier [80] experiment was performed on the coarser grid, thereby leaving open the possibility that the results were grid dependent. This concern was addressed in a subsequent experiment by [79], which used a finer measurement grid and achieved essentially the same results. Also lending further credibility to their findings was the result shown in figure 7.1 from their paper: they achieved the same results as the [62] and [63] experiments when only the streamwise component of velocity was used. Even so it was not at all clear whether lower Reynolds number jets would behave in a similar manner, especially since the DNS results of Freund and Colonius [75] found the snapshot POD eigenspectra to peak at azimuthal mode-2.

A major concern about the hot-wire results from all previous experiments was whether the spatial resolution in the radial and azimuthal directions was adequate, since all of the hot-wire experiments used a limited number of probes (typically 6 to 13). Also, the use of hot-wires in any far jet flow is problematical because of the cross-flow and rectification errors arising the the high local turbulence intensity. (The minimum local turbulence intensity is nearly 30%, and away from the centerline it rises rapidly, c.f. Hussein et al.[81].) These problems are much more severe for multi-wire probes than for single-wire probes, c.f. [82]. High turbulence intensities also complicate the use of Taylor's frozen field hypothesis, which was used in at least the Glauser et al.[32, 33] and Thomas et al.[80, 79] experiments to obtain the $\langle u_r u'_\theta \rangle$ cross-spectra from the continuity equation.

7.2 The goal of the SPIV cross-plane study

The objective of the work reported herein was to attempt to establish which of the previously reported conflicting results are correct. With the use of stereo PIV it was thought that the following questions could be answered :

- Are similar differences between the three-component and streamwise-only decompositions observed at Reynolds numbers below 100,000?
- Was the number of probes (or measurement locations) and lateral spatial extent of the hot-wire experiments adequate to properly perform the POD?

- Were the previous results significantly influenced by the relatively high turbulence intensities on the hot-wire probes?

The same jet facility as in Part I of this thesis was used. It is also the same jet as was used by Gamard et al.[63]. Three-component velocity estimates were obtained in cross-streamwise planes. From an ensemble of 1000 statistically independent PIV snapshots, all independent components of the Reynolds stress tensor, $R_{i,j}(\vec{x},\vec{x}') = \langle u_i(\vec{x},t)u_j(\vec{x}',t)\rangle$, which forms the POD kernel, were estimated. In addition, the spatial resolution exceeded that possible with hot-wire probes, and the hot-wire technique problem with high turbulence intensities was avoided. The goal was to answer all of the above stated questions. As will be clear the use of stereo-PIV proved to be a substantial challenge.

8. CROSS-PLANE EXPERIMENTS

As was stated in the previous chapter, measuring the far jet with stereoscopic PIV proved to be quite a challenge. In fact, two independent investigations of the jet cross-planes have been performed. The first data set was analyzed and reported on in Wänström[72], but upon subsequent inspection was found to exhibit features that are incompatible with the flow under investigation, namely lack of azimuthal symmetry in the second order velocity moments. An extensive search for possible sources of the asymmetry was initiated. The process and its conclusions are described in the following section, since it provides a context for the design and execution of the second measurement campaign, the results of which will be given in detail in the following chapter. It is also relevant in the sense that it highlights several of the difficulties of attempting to measure free shear flows with stereoscopic PIV. Primarily, attention is directed towards possible sources of artificial azimuthal variations due to relative misrepresentation of the in-plane fluctuation intensities. Earlier versions of this chapter appeared as [66]. Note that in the following sections 'Cross-plane Experiment 1' will refer to the flawed first measurement campaign and 'Cross-plane Experiment 2' as the subsequent attempt to improve on it. Note that while in previous chapters the notation for the polar coordinate system velocities were denoted as u, v, w, in this chapter the they will be referred to as u_x, u_r, u_θ to distinguish from the Cartesian coordinate ones.

8.1 Cross-plane Experiment 1

The same jet facility as in Part I of this thesis was used. For further details on the facility, see section **??**.

8.1.1 Stereoscopic PIV setup

The stereoscopic setup used in Experiment 1 was of the side-view type is shown in figure 8.1.

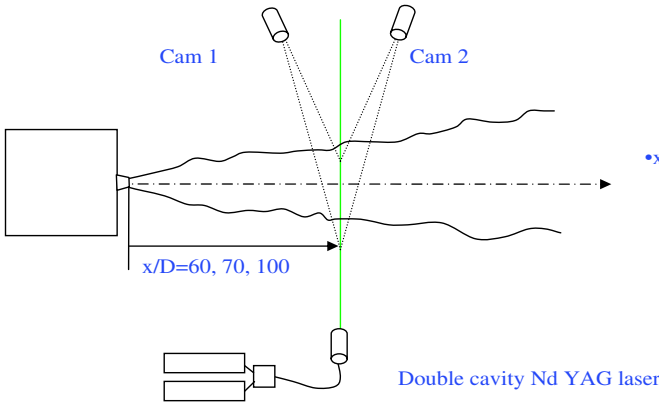

Fig. 8.1: Stereoscopic PIV setup for Experiment 1.

The nominal exit Re_D of the jet was 17,700. The air in the tent was seeded with glycerine droplets generated by an atomization device producing particles of 2-3 μm mean diameter. Illumination of the measurement plane was provoded by a Continuum Surelite I-10 double-cavity Nd:YAG laser delivering coherent 532 nm wavelength light with an energy of 150 mJ/pulse. The optical configuration for laser sheet formation produced a light sheet of approximately 3 mm in thickness.

Two Kodak MegaPlus ES1.0 1Mpxl CCD cameras, both fitted with 60 mm Nikkon camera lenses, were operated in dual frame single exposure mode. The cameras were positioned relative to the laser sheet so that they viewed the measurement plane at approximately plus and minus 30 degrees respectively. In order to satisfy the Scheimpflug condition, both camera backplanes were rotated relative to the respective lenses' field of view, allowing the plane illuminated by the laser to be fully in focus.

The SPIV system was controlled via a Dantec FlowMap processor and a PC operating with Dantec FlowManager 4.4 software. The software handled the calibration image processing and data acquisition as well as subsequent validation of the raw images. The sampling frequency was 1 Hz. The Eulerian integral time scale can be estimated as $T_E = L_\epsilon/U_c$ where $L_\epsilon = u'^3/\epsilon$ is the pseudo-integral length scale. At $x/D = 100$, $T_E \approx 0.07$s, so each snapshot could be assumed to be an independent realization.

Particle image displacements were evaluated with Dantecs Flowmanager 4.4 which provdes standard FFT-based correlation methods, including window shifting and adaptive multi-pass interrogation. The final interrogation area

was 32×32 pixels and the interrogation window overlap was 50%. The particle image displacements were validated by a moving average. A mapping from the image space to the object space was obtained by stereoscopic calibration using the Soloff method and was estimated by the Dantec software. The resulting common camera field of view had physical dimensions of $L_y = 0.28$m and $L_z = 0.15$m and spatial resolution was approximately $\Delta y = 3m$m and $\Delta z = 6m$m.

8.1.2 Single point statistics

Figure 8.2 shows contours of mean streamwise velocity at $x/D = 100$. The centreline mean velocity at x/D = 100 was found to be $U_c(x) = 1.72$m/s and the half-width $\delta_{1/2}(x) = 0.094$m, both in excellent agreement with previous experiments from Hussein et al.[16].

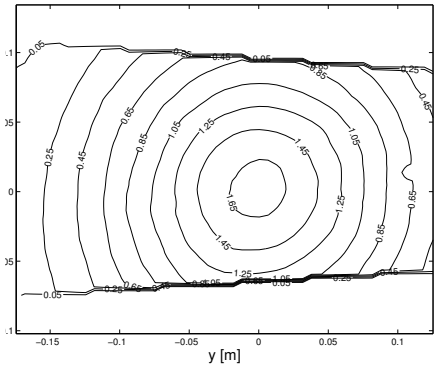

Fig. 8.2: $x/D = 100$Contour plot showing mean streamwise velocity.

The Cartesian velocity data was rotated to evaluate the polar coordinate vector components and the second moments of the velocity was estimated using $N = 1000$ independent samples. In an axisymmetric, azimuthally homogeneous jet, the single-point statistics are expected to be symmetric as well. While the out-of plane streamwise velocity component variance, $\langle u_x u_x \rangle$, appeared normal to within statistical errors, inspection of the in-plane radial and azimuthal normal stresses, $\langle u_r u_r \rangle$ and $\langle u_\theta u_\theta \rangle$, exhibit strong azimuthal asymmetry, as seen in figures 8.3(a) and 8.3(b).

As no known disturbance to the flow itself, such as swirl, could have caused the distortion evident in the variances, it was clearly some feature of the measurement of the data that caused the errors. In fact it can be shown that the radial and azimuthal statistics will be rotationally symmetric only if the Cartesian coordinate system statistics, from which they are derived, are of ellipsoids

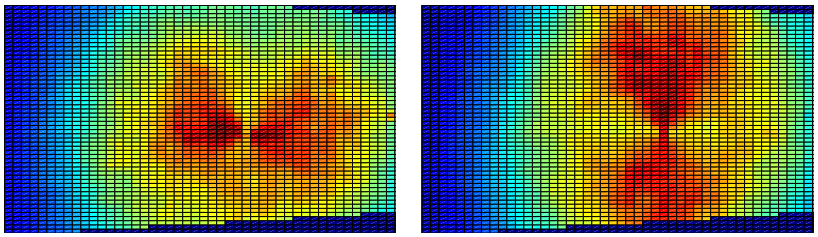

(a) $\langle u_r u_r \rangle$ (b) $\langle u_\theta u_\theta \rangle$

Fig. 8.3: Variation of the variance of the radial and azimuthal velocity components, $\langle u_r u_r \rangle$ and $\langle u_\theta u_\theta \rangle$. Both are expected to exhibit rotational symmetry. Instead a lobed pattern is in evidence.

of equal magnitude rotated by 90° relative to each other. This is evident from the following relations, where x, y, z and u, v, w denote coordinate positions and velocity components along the out-of-plane streamwise, horizonal and vertical axes respectively and $r^2 = y^2 + z^2,\ \tan\theta = z/y$.

$$\begin{aligned} u_x(x,r,\theta) &= u(x,y,z) \\ u_r(x,r,\theta) &= v(x,r,\theta)\cos\theta + w(x,r,\theta)\sin\theta \\ u_\theta(x,r,\theta) &= v(x,r,\theta)\cos\theta - w(x,r,\theta)\sin\theta \end{aligned} \tag{8.1}$$

The corresponding rotation from polar to Cartesian coordinates is given by:

$$\begin{aligned} v(x,r,\theta) &= u_r(x,r,\theta)\cos\theta - u_\theta(x,r,\theta)\sin\theta \\ w(x,r,\theta) &= u_\theta(x,r,\theta)\cos\theta + u_r(x,r,\theta)\sin\theta \end{aligned} \tag{8.2}$$

It follows immediately that the in-plane second moments of velocity can be expressed in terms of their Cartesian counterparts as

$$\begin{aligned} \langle u_r^2 \rangle &= \langle v^2 \rangle \cos^2\theta + \langle w^2 \rangle \sin^2\theta + 2\langle vw \rangle \sin\theta\cos\theta \\ \langle u_\theta^2 \rangle &= \langle w^2 \rangle \cos^2\theta + \langle v^2 \rangle \sin^2\theta - 2\langle vw \rangle \sin\theta\cos\theta \end{aligned} \tag{8.3}$$

and since the radial and azimuthal velocities are uncorrelated, i.e., $\langle u_r u_\theta \rangle = 0$, the corresponding polar coordinate variances are

$$\begin{aligned} \langle v^2 \rangle &= \langle u_r^2 \rangle \cos^2\theta + \langle u_\theta^2 \rangle \sin^2\theta \\ \langle w^2 \rangle &= \langle u_\theta^2 \rangle \cos^2\theta + \langle u_r^2 \rangle \sin^2\theta \end{aligned} \tag{8.4}$$

Thus only the sum of the Cartesian in-plane single point statistics is expected to be axisymmetric, since $\langle v^2 \rangle + \langle u_3^2 \rangle = \langle u_r^2 \rangle + \langle u_\theta^2 \rangle$. Individually, the variance of Cartesian fluctuations in a cross-plane must each be described by

the same family of ellipsoids, where the major axis are perpendicular to the Cartesian coordinate direction of the respective velocity component. These constraints can be visualized by substituting the in-plane variance profiles of Hussein et al. [16] into equation 8.4 and the result is shown in figures 8.4(a) and 8.4(b) below.

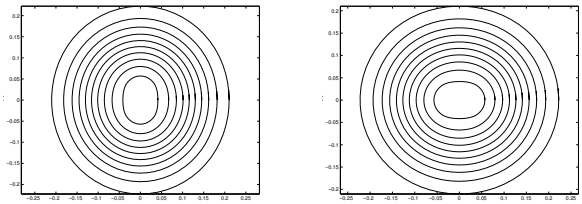

(a) $\langle v^2 \rangle$ (b) $\langle w^2 \rangle$

Fig. 8.4: Contours of the horizontal and vertical velocity variances, $\langle v^2 \rangle$ and $\langle w^2 \rangle$, in axisymmetric jet.

The in-plane Cartesian variances estimated from Experiment 1 data are in fact not of equal magnitude, the horizontal variance $\langle vv \rangle$ being significantly larger than the vertical $\langle ww \rangle$, see figure 8.1.2 where they are shown as radial profiles. The discrepancy is particularly obvious at zero radius, where

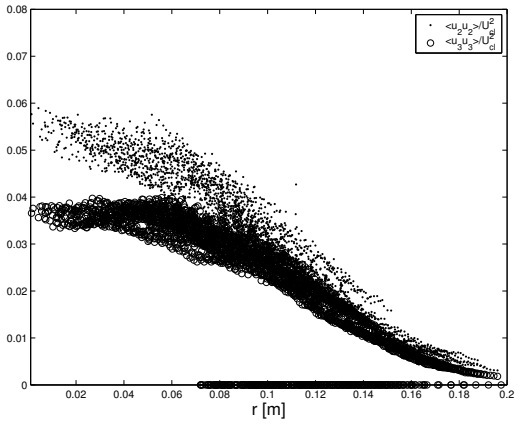

Fig. 8.5: Radial profiles of in-plane Cartesian variances from Experiment 1, which must be of equal magnitude to obtain axisymmetric polar coordinate variances. (·) $\langle vv \rangle$,(○) $\langle ww \rangle$.

the individual in-plane variances, in both coordinate systems, should be equal.

Instead, the horizontal variance is about 40% larger than the vertical one. Clearly, either the vertical velocity component is underestimated relative to the real one, the horizontal is overestimated, or a combination of both.

One possibility is that the in-plane velocity components are spatially resolved unequally, due to the non-cubic interrogation window in physical coordinates, and thus that the turbulent velocity are subjected to differing degrees of filtering. This hypothesis was tested using a simple energy spectrum model for homogeneous isotropic turbulence, including a window function corresponding to the physical lengths of the PIV window. Another possibility is that the signal noise levels are different for v and w. The presence of different size uncertainties in the two components will show up as increased variance in the signal, masquerading as turbulence. A third possible explanation is that there is something fundamentally wrong about the experimental setup and calibration of the PIV instrumentation, for example misalignment of the light sheet relative to the jet flow and misalignment of hte calibration plane and the laser light sheet.

8.1.3 Underestimation of vertical turbulent fluctuations due to spatial filtering

This section will examine whether the results displayed in Figures 8.3(a) and 8.3(b) can be explained by the spatial filtering introduced by the finite interrogation volume of the SPIV, and especially that fact the dimensions of the volume are different in different directions. The filtering effect of the PIV interrogation window on the turbulent velocity filed was modeled as the local average of isotropic turbulence by a volume with physical Cartesian dimensions l_1, l_2, l_3. As described in a previous section, spatial filtering corresponds to multiplication of the three-dimensional turbulence spectrum by $sinc^2(k_i l_i/2)$. The resulting filtered variances of the initially isotropic model are obtained by integrating the filtered spectral tensor.

The computational wavenumber grid was equidistant and equal in all three spectral space coordinate directions $\tilde{k}_i = k_i L/k_e L$. The grid spacing $\Delta\tilde{k}_i = \Delta\tilde{k} = 0.5$ was chosen small enough that grid independence was ensured. Truncation of the wave number spectrum is inevitable, but the filtering itself causes the spectrum to roll off faster, which increases the rate of convergence at high wave numbers. At the maximum wave number used, $\tilde{k}_{max} = 150$, the ratio between filtered and unfiltered variances is virtually unchanged by further increase in integration interval length. The values for the filtering volumes were $l_1 = 3m$m, $l_2 = 6m$m and $l_3 = 3m$m and the integral scale L in $\tilde{k}_i = k_i L/k_e L$ corresponds to the local longitudinal length scale at $x/D = 100$, which for $D = 0.01$ gives $L_1(x) = 53m$m. The von Karman/Howarth energy spectrum model parameters were $k_e L = 0.7468$ and $C = 6.2528$.

The resulting values for the spatially averaged turbulence variances are $\langle v_m^2 \rangle / u^2 = 0.88$ $\langle w_m^2 \rangle / u^2 = 0.87$, which is a difference of about 1%. Clearly the spatial filtering due to lack of symmetry in the interrogation volume $l_1,\ l_2,\ 2l_3$ cannot account for the 40% difference in the variances of the horizontal and vertical velocity components.

8.1.4 Overestimation of horizontal turbulent fluctuations due to noise

Figures 8.6(a) through 8.6(b) show the two-point correlations computed using a single location near the centerline as reference. Since the spatial resolution was approximately equal to the Taylor microscale, the value of these correlations at zero lag should be nearly equal to that at the first non-zero lag. Clearly this is not the case. This suggests that instead of representing the mean square of the filtered velocity component, the value for zero lag represents the filtered mean square velocity plus any noise added to it. This interpretation presumes that any measurement errors are uncorrelated at different spatial locations, so the noise only appears at zero lag. An example of such noise quantization noise due to the inability to fully represent the actual value of the particle image displacement, causing round-off errors. Inspection of the data shows that the

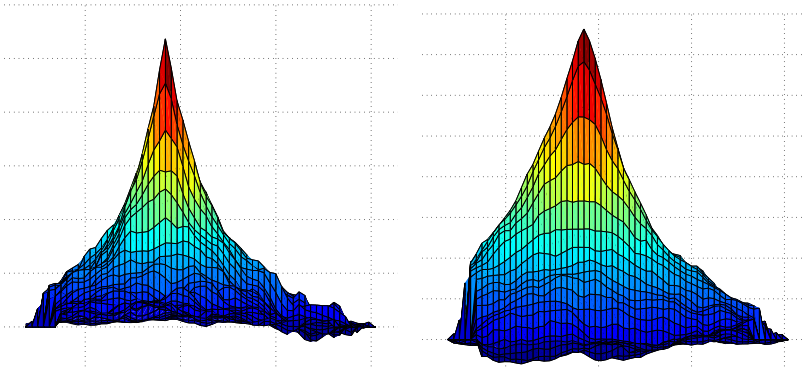

(a) (b)

Fig. 8.6: Correlation functions showing sharp peaks at zeros lag, indicative of uncorrelated self-noise. The different levels of noise are indicated by the slopes near zero. (a) $R_{2,2}(y, z, y, z')$, (b) $R_{3,3}(y, z, y, z')$.

added contribution to the horizontal component is substantially larger. This section examines whether the answer lies in different levels of relative errors of the two in-plane velocity components, and the resulting additive 'noise'.

8.1.5 The displacements with uniform errors

If X_1, Y_1 and X_2, Y_2 are the image plane coordinates of cameras 1 and 2, one can estimate the reconstructed object space displacements $\Delta x, \Delta y, \Delta z$ of the camera configuration in Experiment 1 as (c.f., van Doorne and Westerweel [83]):

$$\begin{aligned} \Delta x &= (-\Delta X_1 - \Delta X_2)/2cos(\alpha)\Delta & (8.5)\\ \Delta y &= (\Delta X_1 - \Delta X_2)/2sin(\alpha) & (8.6)\\ \Delta z &= (\Delta Y_1 + \Delta Y_2)/2 & (8.7) \end{aligned}$$

where the angle angle α is the angle between the field of view and the camera. In the current setup the cameras are positioned $\alpha = 30^\circ$ to either side of the laser sheet. If one assumes that every displacement found in the image plane is associated with a fixed uncertainty, say ϵ, which is the same for all displacements in both cameras, we can express the measured displacements as:

$$\begin{aligned} \Delta x_m &= (-[\Delta X_1 + \epsilon] - [\Delta X_2 + \epsilon])/2\cos\alpha \\ \Delta y_m &= ([\Delta X_1 + \epsilon] - [\Delta X_2 + \epsilon])/2\sin\alpha \\ \Delta z_m &= ([\Delta Y_1 + \epsilon] + [\Delta Y_2 + \epsilon])/2 & (8.8) \end{aligned}$$

In the absence of errors, squaring and averaging yields the mean square displacements as:

$$\begin{aligned} \langle\Delta x^2\rangle &= (\langle\Delta X_1^2\rangle + \langle\Delta X_2^2\rangle + 2\langle\Delta X_1\Delta X_2\rangle)/4\cos^2\alpha \\ \langle\Delta y^2\rangle &= (\langle\Delta X_1^2\rangle + \langle\Delta X_2^2\rangle - 2\langle\Delta X_1\Delta X_2\rangle)/4\sin^2\alpha \\ \langle\Delta z^2\rangle &= (\langle\Delta Y_1^2\rangle + \langle\Delta Y_2^2\rangle + 2\langle\Delta Y_1\Delta Y_2\rangle)/4 & (8.9) \end{aligned}$$

If there are errors present in the displacement estimates and if these errors are uncorrelated with both each other and the displacements, it is straightforward to show that the mean square 'measured' displacements are given by:

$$\begin{aligned} \langle\Delta x_m^2\rangle &= \langle\Delta x^2\rangle + \langle\epsilon^2\rangle/2\cos^2\alpha \\ \langle\Delta y_m^2\rangle &= \langle\Delta y^2\rangle + \langle\epsilon^2\rangle/2\sin^2\alpha \\ \langle\Delta z_m^2\rangle &= \langle\Delta z^2\rangle + \langle\epsilon^2\rangle/2 & (8.10) \end{aligned}$$

Since the camera and laser configuration in Experiment 1 corresponds to $\alpha = 30^\circ$, $\sin^2\alpha \approx 1/4$ and $\cos^2\alpha \approx 3/4$ and the relative magnitude of the errors on the in-plane components of the displacements should be:

$$\begin{aligned} \frac{\langle\Delta x_m^2\rangle - \langle\Delta x^2\rangle}{\langle\Delta z_m^2\rangle - \langle\Delta z^2\rangle} &\approx 2/(3/2) = 4/3 \\ \frac{\langle\Delta y_m^2\rangle - \langle\Delta y^2\rangle}{\langle\Delta z_m^2\rangle - \langle\Delta z^2\rangle} &\approx 2/(1/2) = 4 & (8.11) \end{aligned}$$

Thus the mean square 'noise' (or quantization noise) added to the horizontal in-plane component is 4 times that added to the vertical in-plane component. In Experiment 1, it was estimated that the typically the displacement associated with the mean out-of-plane velocity is about 5 pixels. If the turbulence intensity associated with the vertical velocity components is nominally 20%, then the number of pixels associated with the rms vertical displacement is about 2pixels. Given a sufficient number of particle image pairs in the interrogation area, a particle image size of two pixels or more and an appropriate correlation peak fitting algorithm, the rms uncertainty of the displacement can be expected to be about 0.1 pixel, (Raffel et al.[50] and Westerweel [84]) so $(\langle\epsilon^2\rangle/2)/\langle\Delta z^2\rangle \approx ((0.1)^2/2)/2^2$. Thus the increase in the mean square $\langle {w_m}^2\rangle$ due to the quantization (or pixel) noise can be estimated as approximately 0.125 %. Because of the geometry of the imaging system, represented by equation 8.11, this corresponds to a 0.5% contribution to $\langle {v_m}^2\rangle$. Even with a somewhat less accurate correlation peak fit, the contribution to the mean squares is far too small to account for the nearly 30-40 % increased value of $\langle {v_m}^2\rangle$ relative to $\langle {w_m}^2\rangle$.

8.1.6 Noise from the turbulence itself

As discussed previously, the finite number of scattering particles in the interrogation volume at any instant, which are used to estimate the local average over the Eulerian turbulent velocity field, also gives rise to a kind of error in the estimated velocity field. When the average particle image displacement of an interrogation window is evaluated, the output is representative only of the average of the displacements of the particles. In a turbulent flow, even if the particles follow the flow perfectly, the continuous Eulerian velocity field is then represented by a finite number of scattering particles. The displacements obtained from detecting the average particle motion can be considered as a finite sample estimate of the volume average of the actual continuous velocity field present in the interrogation volume. This estimate can be expected to deviate from the local average since only a subset of the volume is represented by the particles present therein, and thus an error is incurred. Intuitively, the magnitude of this error due to sparse representation of the Eulerian velocity should be inversely proportional to the square root of the number of particles present in the interrogation volume. In fact, recent analysis by W.K. George (private communication), indicates that the net effect of this representability error on the single-point moments is to increase them relative to their spatially filtered values by a factor proportional to the inverse of the average number of particles N_p in the volume ; i.e.

$$\langle u_i u_j\rangle_{PIV} = \left[1 + \frac{1}{N_p}\right] \langle u_i u_j\rangle_{E,f} \tag{8.12}$$

where the subscript E, f indicates the perfectly represented Eulerian velocity field evaluated as the local average over the PIV volume, i.e., spatially filtered. This was source of noise empirically recognized earlier by Foucaut et al. [57], but was expressed instead in terms of interrogation volume area (which is proportional to N_p for fixed particle concentrations). In practice N_p is not easy to determine but is typically at least 10. (Foucaut et al. [57] suggest that approximately 0.03 particles per pixel is optimal, which would correspond to 30 particles per interrogation volume for the experiment under discussion here.) The two-point correlation of this noise can be approximated by:

$$\langle n_i(\vec{x},t)n_j(\vec{x}+\vec{r},t)\rangle = \frac{1}{N_p}\langle u_i(\vec{x},t)u_j(\vec{x}+\vec{r},t)\rangle W(\vec{r}) \tag{8.13}$$

where $W(\vec{r})$ is the triangle function given by:

$$W(\vec{r}) = \begin{cases} (1-\frac{|r_1|}{l_1})(1-\frac{|r_2|}{l_2})(1-\frac{|r_3|}{l_3}) & , \quad |r_3| \le l_1, |r_2| \le l_2, |r_3| \le l_3 \\ 0 & , \quad otherwise \end{cases}$$

As noted earlier, this 'turbulence' noise manifests itself in the one-dimensional spectrum as being of broadband with amplitude proportional to the interrogation volume length times the Fourier transform of sinc-function squared.

Because of the small spatial dimensions of the interrogation volume, the contribution from this noise source is approximately just a contribution at $|\vec{r}| \approx 0$. In fact, it is of both the magnitude and character to account for the correlation anomalies at zero lag in figures 8.6(a) and 8.6(b). Note that the corresponding contribution to the spectra is quite small because it is spread over a very wide band.

Since the additive noise contribution is proportional the volume-averaged moments themselves, this means that this noise source cannot disturb the relative balance. Thus it cannot explain the asymmetries since it cannot change the components relative to each other. So part of the mystery is solved, the origin of the correlation peaks, but not main question of what is causing the asymmetries noted at the beginning of this chapter.

8.1.7 Disparity errors due to misalignment between the calibration plane and the laser sheet

In stereo PIV there will always be a small misalignment between the calibration target plane and the actual position of the laser sheet. Since the mappings

from the two image planes of the cameras to the common object plane is derived from an object space defined relative to the position of the calibration target, even small misalignment between the target plane and the laser sheet can cause significant distortion in the reconstructed displacement field. For example, Willert [85] cites misalignment errors of only 0.6 degrees between the laser sheet and the calibration plane which yielded up to a 10 pixel shift between the interrogation areas seen by the two cameras. In brief, such a misalignment causes a particle located at the midplane of the laser sheet to be interpreted (from the image to object mapping from the stereo calibration) as though it were at a different position for the two cameras. While the particle image displacements can be estimated accurately for each camera individually, they will be erroneously combined in the reconstruction of the three-dimensional displacement, since the reconstruction mapping associates the location of a given point in the laser sheet plane to two different, displaced points in the calibration plane. If velocity gradients are large enough to cause a detectable change of the velocity between these two points, a significant measurement error occurs.

The effect and how to correct for it is well-understood (v. Coudert and Schon [86], Raffel et al. [50]). However, at the time of the execution of Cross-plane Experiment 1, the author was not aware of the problem. The magnitude and direction of such the disparity between the calibration plane and measurement plane can be estimated by cross-correlation of images from the two cameras exposed at the same time and to which their individual mappings have been applied. A perfect match between the laser sheet and calibration plane should result in best correlation at zero displacement everywhere in the common field of view of the cameras. If non-zero displacement is found the disparity between the planes can be found and is readily corrected for by adjusting the calibration mappings of the cameras relative to each other.

In the case of Experiment 1, the horizontal in-plane velocity component v will be much more sensitive to this type of error since it is constructed as the difference between the difference between the two horizontal displacements seen by the cameras and at the same time is much smaller than the other horizontal component u. When cross-correlation was applied to the images of the two cameras as described above, the disparity found was horizontal in the camera coordinate system and varied linearly from bottom to top (from 0 to -14 pixels), corresponding to a tilt of about 1.4 degrees. This in turn corresponds to 3-4 mm near the location corresponding to the jet center. For the camera angles used, that would imply a 2 mm misalignment between laser sheet and calibration plane or about half the laser sheet thickness.

The effect on the velocity measurement can be estimated by Taylor expanding the velocity around a point (say at a location between that seen differently by the two cameras): i.e., considering only a horizontal displacement varying

in the vertical direction yields:

$$u_i(x, y + \Delta y) = u_i(x, y) + \frac{\partial u_i}{\partial y}\Delta y + \cdots \tag{8.14}$$

The increase in the apparent turbulence mean square can thus be estimated as:

$$\langle \Delta v^2 \rangle \approx \langle \left[\frac{\partial v}{\partial y}\right]^2 \rangle \Delta^2 \approx \langle v^2 \rangle \frac{2\Delta^2}{\lambda^2} \tag{8.15}$$

where λ_2 is the transverse Taylor microscale. Using the estimate $\lambda_2 \approx 0.008(x - x_o)$ the resulting increase in the variance of v is approximately

$$\langle u_{2m}^2 \rangle \approx \langle v^2 \rangle \left(1 + 2\left[\frac{\Delta y}{0.008(x - x_o)}\right]^2\right) \tag{8.16}$$

A horizontal misalignment Δy of 3-4 mm at $x/D = 100$ (estimated virtual origin of x0 = 3D) would then yield a measured horizontal variance 30 to 50% larger than the actual turbulent one, which is indeed on the order of the observed 40%. Thus the asymmetry observed in the SPIV data of the cross plane is very nearly entirely due to a tilt of the calibration target relative to the laser light plane. After failed attempts to correct for the disparity it was decided to redo the measurements, paying more close attention to the calibration procedure.

8.1.8 Summary and Conclusions

The lack of axisymmetry in the single point statistics obtained with SPIV in the far field of a turbulent round jet has been discussed in detail. The velocity moments in Cartesian coordinates were shown to be elliptical, quite unlike those in polar coordinates which were circular. It was demonstrated that only if the measurements in Cartesian coordinates are measured to the same relative accuracy will the polar coordinate moments computed from them be axisymmetric.

Velocity moment data from an initial SPIV jet experiment [72] were used to demonstrate the problems this presents for measurement. In particular, the vertical and horizontal velocity moments do not fulfill the requirements of being identical ellipses but rotated 90 degrees with respect to each other. A number of possible reasons for this were explored, among them varying degrees of spatial filtering, quantization noise addition, finite particle representation noise and disparity between the calibration of laser plane. Only the

latter could be shown to incur a large enough effect on the data to cause the asymmetries observed and is interpreted as the sources of the error. In the time between the first and second rounds of experiment, the software provider of the laboratory had developed a calibration correction scheme similar to the ones described above, which was applied in the subsequent data processing. In addition, extra care was taken during calibration, making sure that the focus settings were not disturbed and calibrating before and after measurements.

8.2 Cross-plane Experiment 2

The jet facility used in these experiments was the same as in the streamwise experiment and is described in section **??**. Therefore only changes in the experimental setup will be discussed below. The nominal exit velocity chosen was $U_e = 30.3m/s$, corresponding to an exit Reynolds number of $Re_D = U_e D/\nu = 20000$, where ν is the kinematic viscosity defined as $\nu = \mu/\rho$ for air at standard temperatures and pressure.

8.2.1 SPIV Setup

In order to facilitate measurements of cross-planes at several downstream locations, the SPIV configuration used in Cross-plane Experiment 2 was modified relative to that used Cross-plane Experiment 1. Both the laser and the camera rig was mounted rigidly onto the base plate of the traverse so that the entire unit could be traversed together, see figures 8.7(b) and 8.7(a).

Seeding particles were droplets of DEHS with an average particle diameter was $d_p = 2\mu$m. The illumination was provided by the same New Wave double-cavity 120 mJ YAG laser. As indicated by the sketch, the laser sheet was reflected by a mirror positioned below the jet axis and thus provided a sheet perpendicular to it. The position of the mirror could be adjusted to allow for variable distance L from the cameras to the laser sheet. The thickness in sheet at the hight of the field of view of the cameras was approximately 3 mm.

Two HisSense MkII cameras were positioned horizontally and at 45° relative to the jet axis and laser sheet. The cameras were supported by a cross-beam and could be shifted laterally in order to facilitate several sizes of the field of view while maintaining the same angle to the laser light. The sensor dimensions of the cameras were 1280 pixels by 1024 pixels and the pixel pitch was 6.5μm. The senors were rotated to for as large as vertical field of view as possible. In the three data sets presented here, efforts were made to maintain the same distance L from the jet nozzle to the camera rig cross-beam. This was done in order to keep any blockage of the flow constant in the three cases and

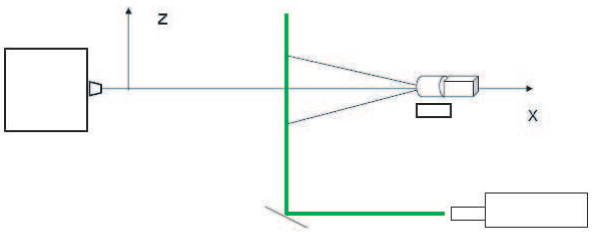

(a) Side view.

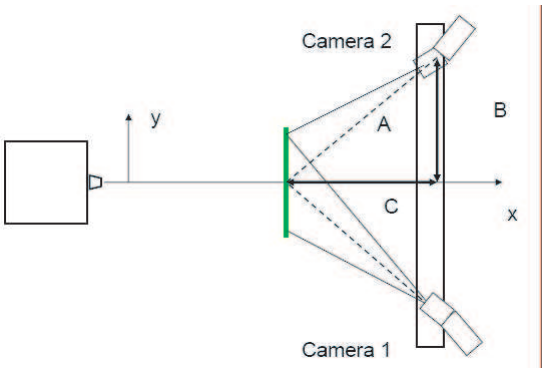

(b) Top view.

Fig. 8.7: Sketch of experimental setup in Cross-plane Experiment 2.

was facilitated by using lenses with different focal lengths while adjusting the distance A from the camera sensor to the laser sheet by changing the distance B from the camera to the jet axis and the distance L. The downstream locations of the measured cross-planes were $x/D = 31$, 46 and 71 respectively and were chosen to since the focal lengths of the lenses available were $f = 35, 60$ mm. The 35 mm lens was used to evaluate the cross-plane at x/D = 71, the 60 mm lens for x/D = 46 and with the use of teleconverters, the focal length was doubled to $f = 120$mm at x/D=31. Since the length scales of hte jet grows linearly, the relative resolution of the three data set are held approximately

constant. It should be noted that for the most downstream location, $x/D = 71$, the position of the mirror could not be adjusted enough to correspond to viewing angles of 45° so the viewing angles were decreased to 41°. This decreased the aspect ratio of this data set relative to the other two.

In order to be able to correct for the inevitable disparity between the calibration target plane and the light sheet, careful calibrations were made with displacements in the out-of-plane direction that spanned $\pm$ 10 laser sheet thicknesses. The calibration target was a white plane with black dots that could be fixed to the flow generating box at the time of calibrations. By traversing the entire camera/laser/mirror unit until the laser light intersected the calibration target the relative angles could be maintained. The calibration correction supplied by the Dantec software Dynamic studio was used to find the disparity between the camera mappings and correct for them. It should be noted that the method used assumes that the light sheets given by the two laser pulses overlap completely and if they do not an error will be incurred. Therefor no attempt to shift the laser pulses relative to each other was made. This could otherwise have been used to increase the dynamic range of the measurements, which is constrained by the large out-of-plane velocity component. Instead, particle drop-out was minimized by shrinking the time between pulses Δt at the different downstream locations.

The sampling frequency was 3 Hz, which allowed for independent samples at all downstream locations. A total of $N = 1000$ samples were acquired at each downstream location. Once acquired, the particle images were evaluated with the Dynamic Studio software. The interrogation window size was 64 pixels $\times$ 64 pixels for all downstream locations. With 50 % of interrogation windows were and the particle image displacements were estimated with a standard FFT-based multi-pass interrogation with window shifting and moving median validation. Spurious vectors were replaced with the local mean of the surrounding displacements. Sub-pixel accuracy was obtained with the 'High-Accuracy' setting in Dynamic Studio, which is believed to based on a centrioding method. The apertures were adjusted to give particle image diameters of 2 pixels in each camera. After the individual planar PIV processing, the three-component displacements were found by stereoscopic reconstruction based on a pin-hole model. Table 8.1 summarizes the output for the three downstream locations. It should be noted that the spatial resolution obtained with the 64 $\times$ 64 pixel interrogation area is quite low, and thus the filtering of the PIV volumes, following the reasoning presented earlier, should be quite sever. This is confirmed in the variances estimated in the following section. The choice of the present interrogation window dimension was dictated by time constraints on the part of the author. Any future work with the present database will be performed with a smaller interrogation window size.

x/D	f [mm]	$L_y[mm]$	$L_z[mm]$	$l_y[mm]$	$l_z[mm]$	M	$N_y \times N_z$
31	120	107	105	3.9	2.7	0.085	29×40
46	70	186	183	6.2	4.7	0.049	29×40
71	35	273	290	11.4	7.2	0.039	25×41

Tab. 8.1: Fields of view and resolution for SPIV output.

8.2.2 Single Point Statistics

In order to define the polar coordinate system, the deviation of the data coordinate system from that defined by the jet flow mean centerline velocity must be corrected for, i.e., $r = ((y - y_o)^2 + (z - z_o)^2), \theta = atan((z - z_o)/(y - y_o))$ where y_o, z_o is due to the filed of view being imperfectly centered around the jet axis. The in-plane origin shift, along with the local centerline velocity $U_c(x)$ and half-width $\delta_{1/2}(x)$, was found from non-linear least square optimization of the mean streamwise velocity relative to a

$$U_{fit} = U_c(x) sech^2 \left[c \frac{((y - y_o)^2 + (z - z_o)^2)^{1/2}}{\delta_{1/2}(x)} \right] \tag{8.17}$$

for each cross-plane data set individually. The results of the optimization is shown in table 8.2.

x/D	U_c[m/s]	$\delta_{1/2}$[mm]	y_o [mm]	z_o [mm]
31	5.9	26.9	-8.8	-8.1
46	3.7	42.1	-7.6	-6.6
71	2.4	65.9	-2.8	-5.1

Tab. 8.2: Scaling parameters, $U_c(x)$ and $\delta_{1/2}(x)$, and origin shift found from optimization.

Figure 8.8(a) shows the inverse of the variation of the centerline velocity, the variation of the half-width and figure 8.8(b) shows the square of their product, normalized by the value at x/D =31.

The radial profiles of the mean streamwise velocity are presented in single-point similarity variables, where it is also compared with the curve-fit of the LDA measurements of Hussein et al. [16] from a much larger Re_D. The collapse of the SPIV profiles is excellent. The profiles do not quite resemble that of [16], but this can be attributed to the difference in Re_D.

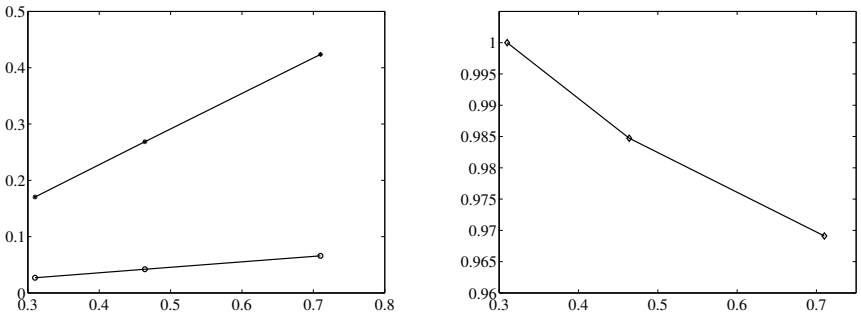

(a) $U_c(x)^{-1}$ and $\delta_{1/2}(x)$ (b) $(U_c\delta_{1/2})^2$

Fig. 8.8: Figure (a) shows the downstream variation of the inverse of the centerline velocity ($*$) $U_c(x)^{-1}$ and half-width ($\circ$). Figure (b) shows the product $U_c^2\delta^2$, which should be constant in a momentum conserving flow, normalized by the value at $x/D = 31$. The decline of this curve indicates a slight momentum loss, possibly due to the blockage of the camera rig cross bar.

The normal stresses in polar coordinates are shown in figure 8.2.2. Clearly, the effect of the filtering of the PIV interrogation window is significant,since it removes about 40% of the available variance from the velocity components. This is consistent with the modeling of the analysis presented earlier, and also with previous work by the author, [44], where the local spatial resolution was similar. Since this amount of filtering is not optimal for the subsequent analysis, it should be considered a preliminary result.

As it appears that the disparity errors have been handles by the calibration correction, the azimuthal asymmetries in the polar coordinate variances observed in Cross-plane Experiment 1 should be missing from the ones produced in the subsequent Cross-plane Experiment 2 data. Figure 8.2.2 shows contours of the radial and azimuthal variances. While some azimuthal variation is still exhibited, it is not at all as significant as in the previous experiment with large disparity errors and it appears that the asymmetry has been largely avoided in two two first downstream cross-planes. Surprisingly, the data form x/D=71 shows an axisymmetric distribution of radial variance, but the azimuthal variance has a distinct lobed pattern. At the present time, no explanation can be given for this discrepancy.

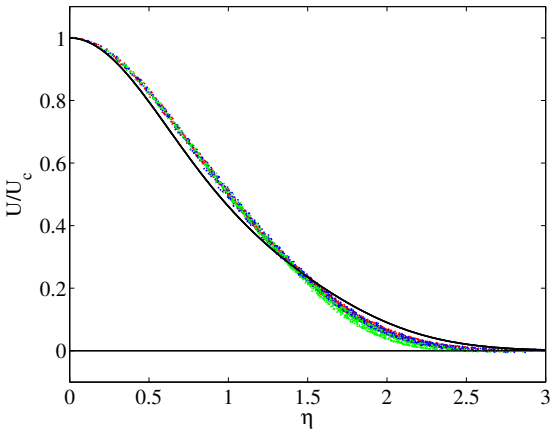

Fig. 8.9: Radial profile of the mean steamwise velocity in similarity coordinates, U/U_c. Red symbols corresponding to x/D =31, blue to x/D =46 and green to x/D =71. Solid line indicates the profile of [16].

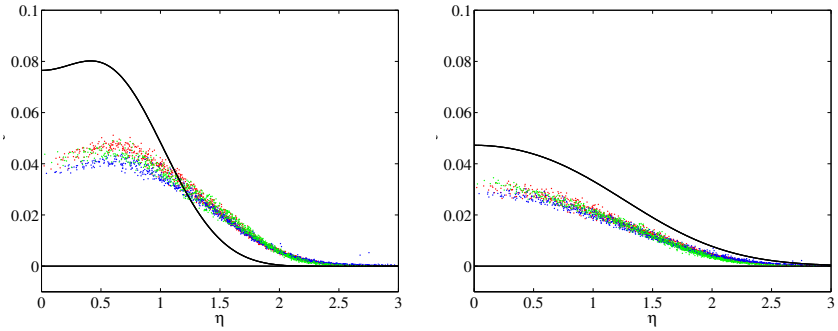

(a) $\langle u_x^2 \rangle / U_c^2$

(b) $\langle u_r^2 \rangle / U_c^2$

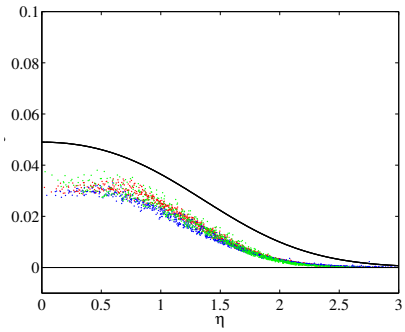

(c) $\langle u_\theta^2 \rangle / U_c^2$

Fig. 8.10: Radial profiles of the normal Reynolds stresses in similarity coordinates. Red symbols corresponding to x/D =31, blue to x/D =46 and green to x/D =71. Figure (a) $\langle u_x^2 \rangle / U_c^2$, figure (b) $\langle u_r^2 \rangle / U_c^2$, figure (b) $\langle u_\theta^2 \rangle / U_c^2$. Solid lines indicates the corresponding profiles of [16].

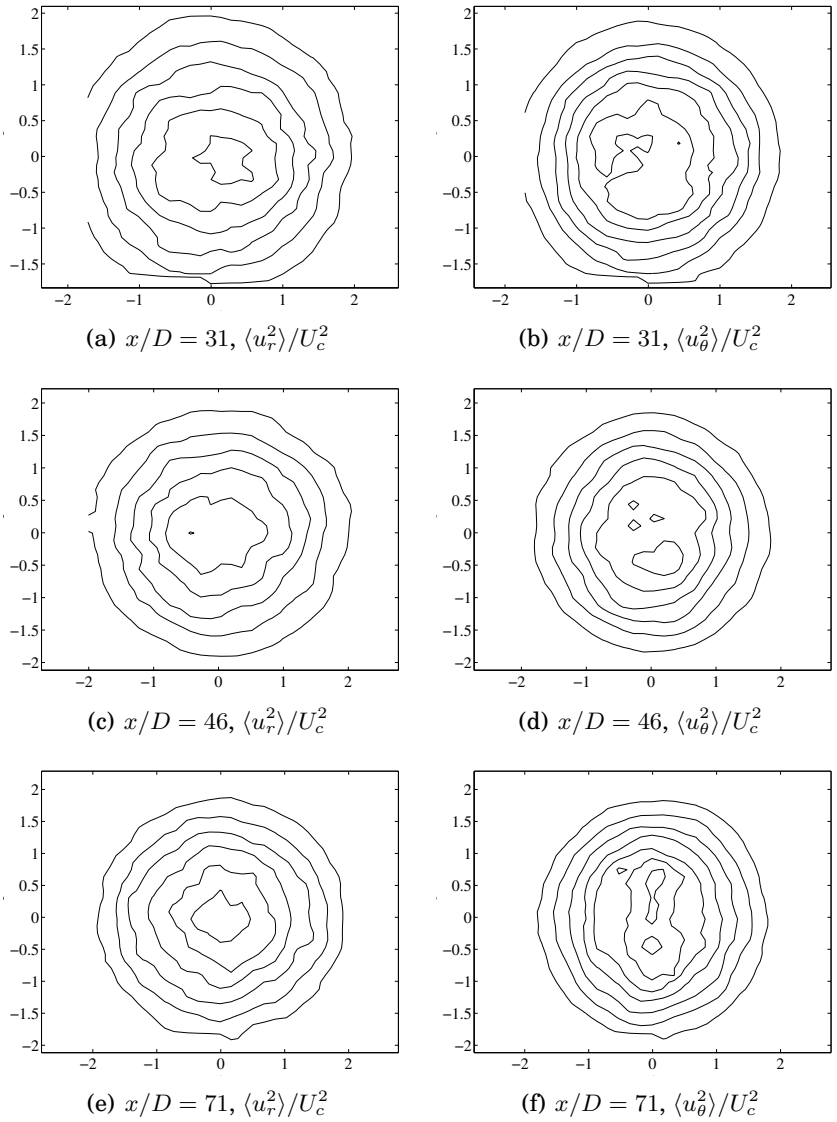

(a) $x/D = 31$, $\langle u_r^2 \rangle / U_c^2$ (b) $x/D = 31$, $\langle u_\theta^2 \rangle / U_c^2$

(c) $x/D = 46$, $\langle u_r^2 \rangle / U_c^2$ (d) $x/D = 46$, $\langle u_\theta^2 \rangle / U_c^2$

(e) $x/D = 71$, $\langle u_r^2 \rangle / U_c^2$ (f) $x/D = 71$, $\langle u_\theta^2 \rangle / U_c^2$

Fig. 8.11: Contours of the variances of the radial and azimuthal velocity. Left column is the radial variances and right column the azimuthal ones. Rows, from top to bottom, correspond to the downstream locations x/D=31, 46 and 71 respectively.

9. AZIMUTHAL FOURIER EXPANSION OF CROSSPLANE DATA

Velocity data sampled at the three downstream positions $x/D = 31, 46, 71$ were scaled by the local mean velocity $Uc(x)$ and the radial positions scaled by the local half-width $\delta_{1/2}(x)$. Then the velocity components were interpolated onto a polar coordinate grid with a cubic interpolation scheme. The extent and resolution of the grid is listed in table 9.1.

The purpose of the dense grid is to be able to facilitate grid sensitivity with respect to changes both in radial resolution and extent and azimuthal extent of the combined Fourier and POD analysis. However, at the time of the measurement campaign, the importance of the radial domain extent was not fully appreciated appreciated. In hindsight, it is clear that radial extent of the data set is vital to the output of the POD analysis. The reason for this is that in order to uniquely determine the radial eigenvectors of the covariance of the flow, the magnitude of turbulence kinetic energy integrand must be zero at the outer radial boundary point η_b, that is $\eta_b \langle \upsilon_i(\eta_b) \upsilon_i(\eta_b) \rangle = 0$. From previous work on the current jet facility by both Gamard et al. [8] and the author herself [44], it is clear that this occurs at $\eta_b = 3$, i.e., at three jet half-widths from the centerline. In fact, the effect of partial radial domain extent was directly studied by Gamard et al. by comparing the the results of their analysis from a case of $\eta = 1$ and one of $\eta = 4.3$. The conclusion was that the peaks in the spectral spaces and the POD space shifted when the coverage was low - clearly indicating that the analysis is not robust with respect to the choice of domain. However, no direct conclusions regarding the general coverage requirements were drawn in Gamard et al., since their comparison test was unable to isolate the radial extent factor from the radial and azimuthal resolution of the flow field. In fact, beside this one test case, none of the measurements presented in Gamard et al. extend beyond $\eta = 1.5$, and neither do the results of Iqbal and Thomas [71].

x/D	η_a	η_b	N_η	Δ_η	N_θ	Δ_θ
31.0	0	1.70	36	0.05	129	2.7
46	0	1.90	38	0.05	129	2.7
71.0	0	1.85	37	0.05	129	2.7

Tab. 9.1: Equidistant polar grids for the three downstream locations.

9.1 Two-point cross velocity Fourier coefficients

The the coefficients of the azimuthal Fourier series expansion of the two-point velocity correlation tensor function $R_{i,j}(\eta,\eta',\Delta\theta)$, $B_{i,j}^{(m)}(\eta,\eta')$, was estimated as the finite sample ensemble average of the Fourier series coefficients of the azimuthal variation of the instantaneous fluctuating velocity components $\upsilon_i(\eta,\theta) = u_i(\eta,\theta)/U_c(x)$. These Fourier coefficients were evaluated with an FFT algorithm corresponding to

$$\hat{\upsilon}_i^{(m)}(\eta_q,x_s,t_k) = \frac{1}{2\pi}\sum_{P=0}^{P-1}\upsilon_i(\eta_q,\theta_p,x_s,t_k)e^{-im\theta_p}\Delta\theta \tag{9.1}$$

where $\theta_p = -\pi + p\Delta\theta$, $\Delta\theta = 2\pi/(N_\theta - 1)$, $p = 0,1,2,\ldots,P-1$ and $m = 0,\pm1,\pm2,....$ The standard notation of for Fourier series coefficients has been modified in order to facilitate the velocity vector index notation. Thus $B_{i,j}^{(m)}(\eta,\eta',x)$ is estimated as

$$B_{i,jN}^{(m)}(\eta_p,\eta_q,x_s) = \frac{1}{N}\sum_{k=1}^{N}\hat{\upsilon}_i^{(m)*}(\eta_p,x_s,t_k)\hat{\upsilon}_j^{(m)}(\eta_q,x_s,t_k) \tag{9.2}$$

where subscript 's' indicates the different measurements planes and 'k' the independent samples. Note that as the velocity field is by definition 2π-periodic in θ, no unlike the streamwise spectral analysis in the preceding chapter, the no spectral leakage will incurred by a finite azimuthal window (unless only a partial domain is used). In addition, aliasing should be minimal, since the PIV was done with 50% overlap of the interrogation windows and the streamwise variation of velocity was is completely suppressed by averaging over all particle variation in that direction. As in the streamwise experiments case, the velocity data has been filtered (the relative amount should be the same for all data sets) and noise as consequence of measuring with PIV. There is also the possibility of introducing error via the calibration procedure and stereoscopic imaging. This was commented on in the previous section. In addition, there is the effect of slight momentum loss described in section 8.2.2. However, as the velocities of the three data sets are scaled by the local mean centerline velocity, this difference should also be suppressed in a comparison of the data analysis

results. In fact, the only quantitative difference is the slightly varying radial coverage.

9.2 Fourier coefficients of the two-point correlation

While the primary reason for obtaining the Fourier series expansion of the azimuthally homogeneous and periodic two-point similarity scaled correlation tensor, $B_{i,j}^{(m)}(\eta,\eta')$, is that it facilitates the subsequent POD decomposition, it also has it's own theoretical merits. As has been explained in the previous section, a somewhat heated debate regarding the turbulence kinetic energy manifestation of particular Fourier modes have been on-going in the community. The argument has been centered on the primacy of azimuthal Fourier mode $m = 1$ versus $m = 2$. The hypothesis underlying the argumentation is that there should be one azimuthal mode that dominates distribution of turbulent kinetic energy and that it does so because it has access to the energy source of the flow, i.e., it is able to extract turbulent kinetic energy form the radial mean flow gradient. The remainder of the modes are then expected to receive their energy through some cascade of turbulent kinetic energy within the basis. However, it can be shown experimentally that several azimuthal modes exhibit the necessary property for tapping into the mean flow kinetic energy, namely significant levels of the primary Reynolds shear stress $\langle B_{1,2}^{(m)}(\eta,\eta)\rangle$. Such evidence is presented in figures 9.1(a) through 9.3(c), which also show the distributions of the Fourier coefficients three normal Reynolds stresses over the radial domain and azimuthal mode number $0 \leq m \leq 24$. Note that only the real parts are presented. The normal stresses are real due to their symmetric correlation functions and the imaginary part of the shear stress is very small.

From the figures one could draw the conclusion that there are several low order azimuthal modes that should have access to the turbulent kinetic energy source. Thus they are active participants in any energy cascade and not simply passive receivers of energy passed by some single predominant energy-dense mode. From this perspective the arguments about the energy dominance of a particular modes appears obsolete. This will be substantiated with the POD analysis in the following chapter.

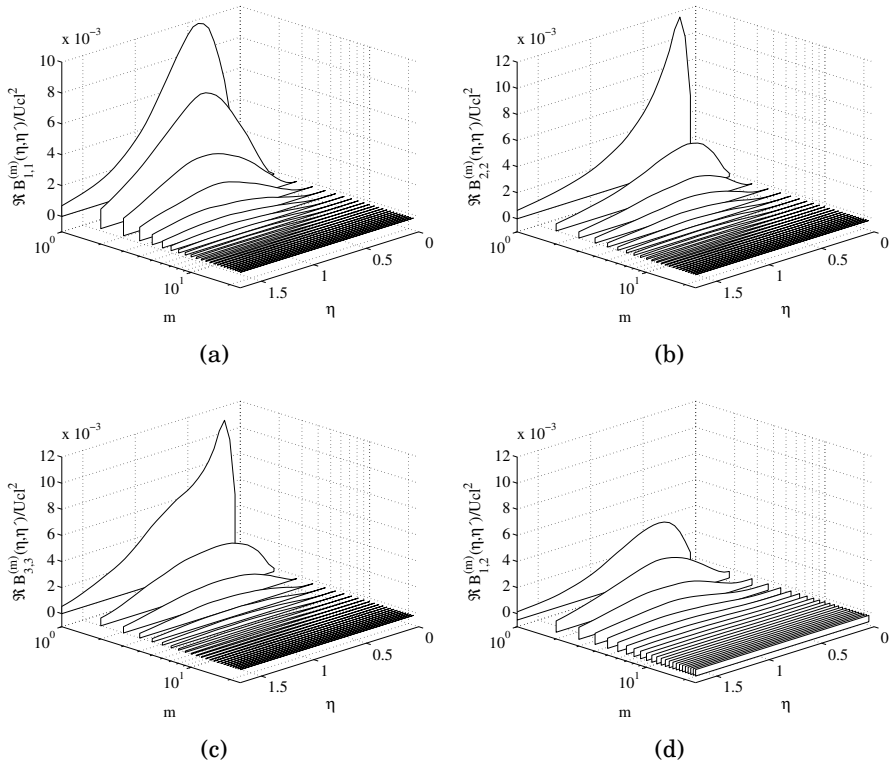

Fig. 9.1: Radial variation $B_{i,j}^{(m)}(\eta,\eta)$, the Fourier coefficients of azimuthal series expansion of the two-point Reynold stress tensor, evalauted at $\eta = \eta'$ and presented on mode number axis. (a) $B_{1,1}^{(m)}$, (b) $B_{2,2}^{(m)}$, (c) $B_{3,3}^{(m)}$, (d) $\Re\, B_{1,2}^{(m)}$. Streamwise position is $x/D = 31$.

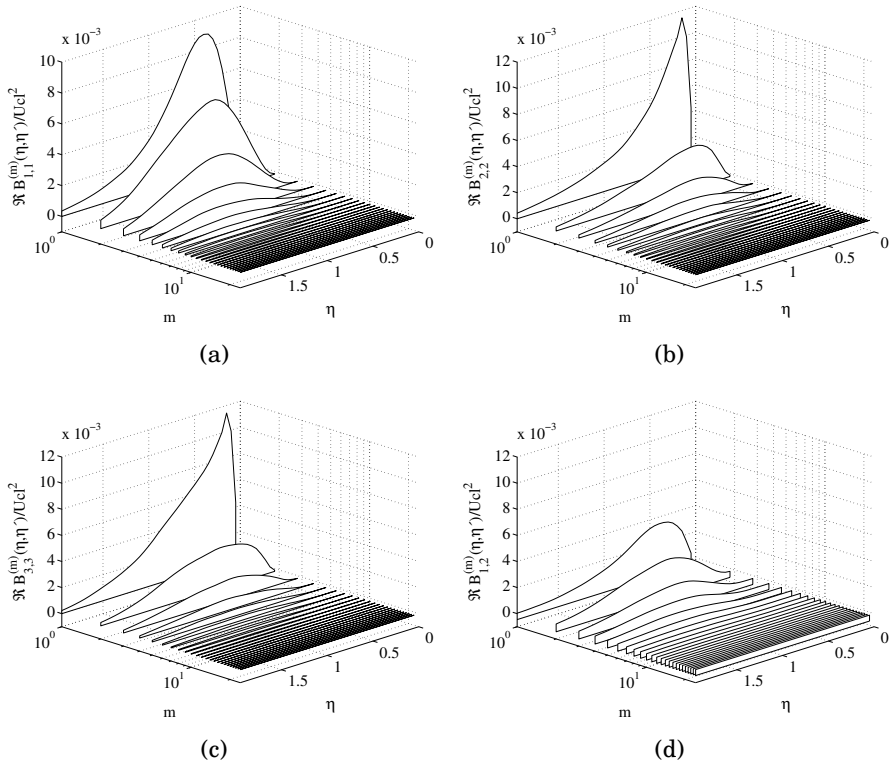

Fig. 9.2: Radial variation of $B_{i,j}^{(m)}(\eta,\eta)$, the Fourier coefficients of azimuthal series expansion of the two-point Reynold stress tensor evalauted at $\eta = \eta'$ and presented on mode number axis. (a) $B_{1,1}^{(m)}$, (b) $B_{2,2}^{(m)}$, (c) $B_{3,3}^{(m)}$, (d) $\Re\, B_{1,2}^{(m)}$. Streamwise position is $x/D = 46$.

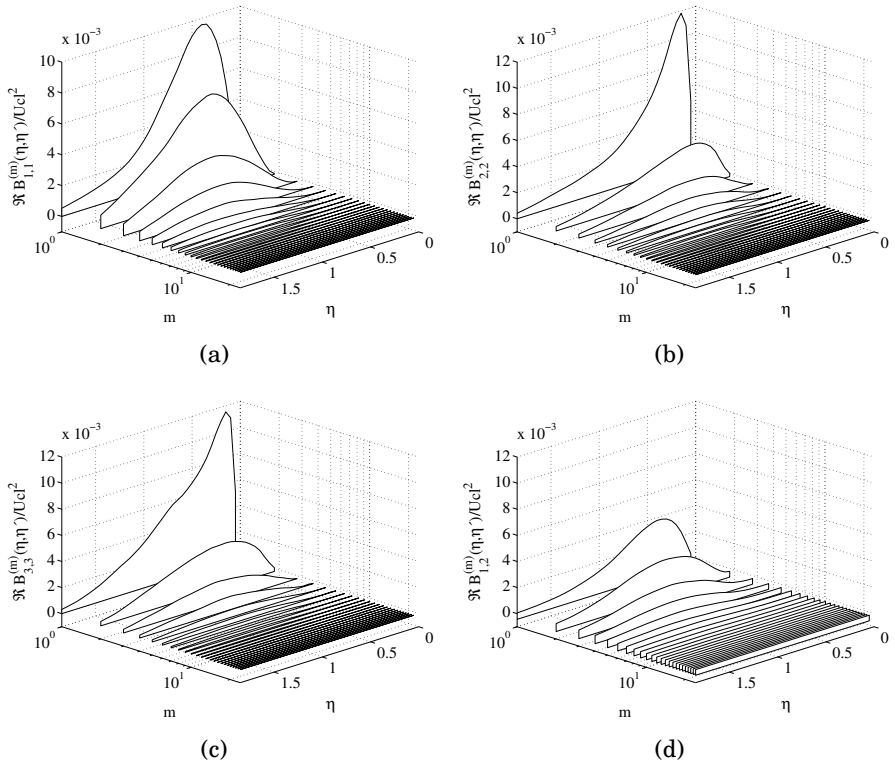

Fig. 9.3: Radial variation of $B_{i,j}^{(m)}(\eta,\eta)$, the Fourier coefficients of azimuthal series expansion of the two-point Reynold stress tensor evalauted at $\eta = \eta'$ and presented on mode number axis. (a) $B_{1,1}^{(m)}$, (b) $B_{2,2}^{(m)}$, (c) $B_{3,3}^{(m)}$, (d) $\Re\, B_{1,2}^{(m)}$. Streamwise position is $x/D = 71$.

10. CROSS-PLANE EXPERIMENT POD

10.1 POD Implementation

The Fourier coefficients of the correlation tensor function is then formed as:

$$B_{i,j}^{(m)}(\eta_p, \eta_q) = \langle \upsilon_i^{(m)*}(\eta_p) \upsilon_j^{(m)}(\eta_q) \rangle \tag{10.1}$$

and a basis of mutually orthogonal radial modes was found for each azimuthal Fourier modes by solving the discrete version of the POD integral equation

$$\int_0^\infty B_{i,j}^{(m)}(\eta, \eta') \eta' \phi_j^{(m,n)}(\eta') d\eta' = \lambda_{m,n} \phi_i^{(m,n)}(\eta) \tag{10.2}$$

where the integer mode number azimuthal dependence is indicated by m. Similarly to the procedure outlined in the previous chapter on streamwise planar PIV experiement, the radial basis functions were found by solving the matrix corresponding to $\tilde{B}_{i,j}^{(m)}(\eta, \eta') = \eta^{1/2} \eta'^{1/2} B_{i,j}^{(m)}(\eta, \eta')$ for the data sets from the three downstream positions $x/D = 31, 46$ and 71. The major difference compared to the previously implemented case is that the stereoscopic PIV setup allows for all elements of the set of eigenvectors to be estimated. This induces the matrix solver to obtain a set of $3P$ orthogonal eigenvectors, where P is the number of radial grid points. However, as was also the case in the streamwise experiment, the full radial extent of the jet was not covered by the field of view. As will be shown later, this affects the eigenvalue spectra that are obtained.

10.1.1 Eigenspectra

As in the analysis of the streamwise experiment, the distribution of the eigenvalues of the POD matrices are shown in figure 10.1.1. Only the subset of positive series expansion mode numbers are presented, the distribution being hermitian symmetric in m. In comparison with the eigenspectra of the streamwise wavenumber distribution POD analysis, figure **??** in chapter 6, the azimuthal series expansion distribution appears to be more compact, with more of the available spectral density in the lower modes. From this representation, the distributions also appear to be unchanging in steamwise location

x/D, which is consistent with the similarity theory of the far jet. In order to evaluate the convergence rate of the POD expansion, the partial sums of the eigenvalues can be inspected.

The energy of the Fourier expanded cross-plane fields are, in the continuous case,

$$\begin{aligned}\int_0^\infty \langle \upsilon_i(\eta)\upsilon_i(\eta)\rangle \eta d\eta &= \int_0^\infty d\eta \sum_{m=-\infty}^{\infty} \eta B_{i,i}^{(m)}(\eta,\eta) \\ &= \sum_{m=-\infty}^{\infty}\sum_{n=1}^{\infty} \lambda_{m,n} \int_0^\infty \phi_i^{(m,n)*}(\eta)\phi_i^{(m,n)}(\eta)\eta d\eta \\ &= \sum_{m=-\infty}^{\infty}\sum_{n=1}^{\infty} \lambda_{m,n} \end{aligned} \tag{10.3}$$

In the the current discrete case this double infinite sum over of POD eigenvalues $\lambda_{m,n}$ is a finite double sum and the total energy represented in the field is:

$$\mathcal{E} = \Delta\eta \sum_{p=0}^{P} \langle \upsilon_i(\eta_p, x_s)\upsilon_i(\eta_p, x_s)\rangle \eta_p = \sum_{m=-M}^{M}\sum_{n=1}^{3P} \lambda_{m,n} \tag{10.4}$$

so that the relative energy per radial POD mode and azimuthal Fourier mode is simply $\lambda_{m,n}/\mathcal{E}$.

The rate of convergence of the POD expansion 10.2 can be evaluated by the slope of a partial sum over the mode numbers: the steeper the the slope of the curve formed by the partial sum, the less POD modes must be retained in order to represent the spectral density at a given azimuthal mode number. Defining a partial sum over POD mode numbers per Fourier mode number as :

$$\Lambda_{m,N} = \sum_{n=1}^{N} \lambda_{m,n} \tag{10.5}$$

the rate at which each POD expansion converges to the relative spectral density is

$$\chi_{m,N} = \frac{\lambda_{m,N}}{\mathcal{E}} \tag{10.6}$$

Figures 10.2(a) through 10.2(c) show such distributions on linear axes for the three downstream cross-plane locations and it appears that the convergence rate of the radial expansion decays with azimuthal mode number.

In order to highlight the variation in convergence rates at different Fourier modes and downstream location, the ratio of the eigenvalue magnitude relative to the spectral density per azimuthal Fourier mode number can be formed as:

$$\gamma_{m,n} = \frac{\lambda_{m,n}}{\Lambda_{m,3P}} \tag{10.7}$$

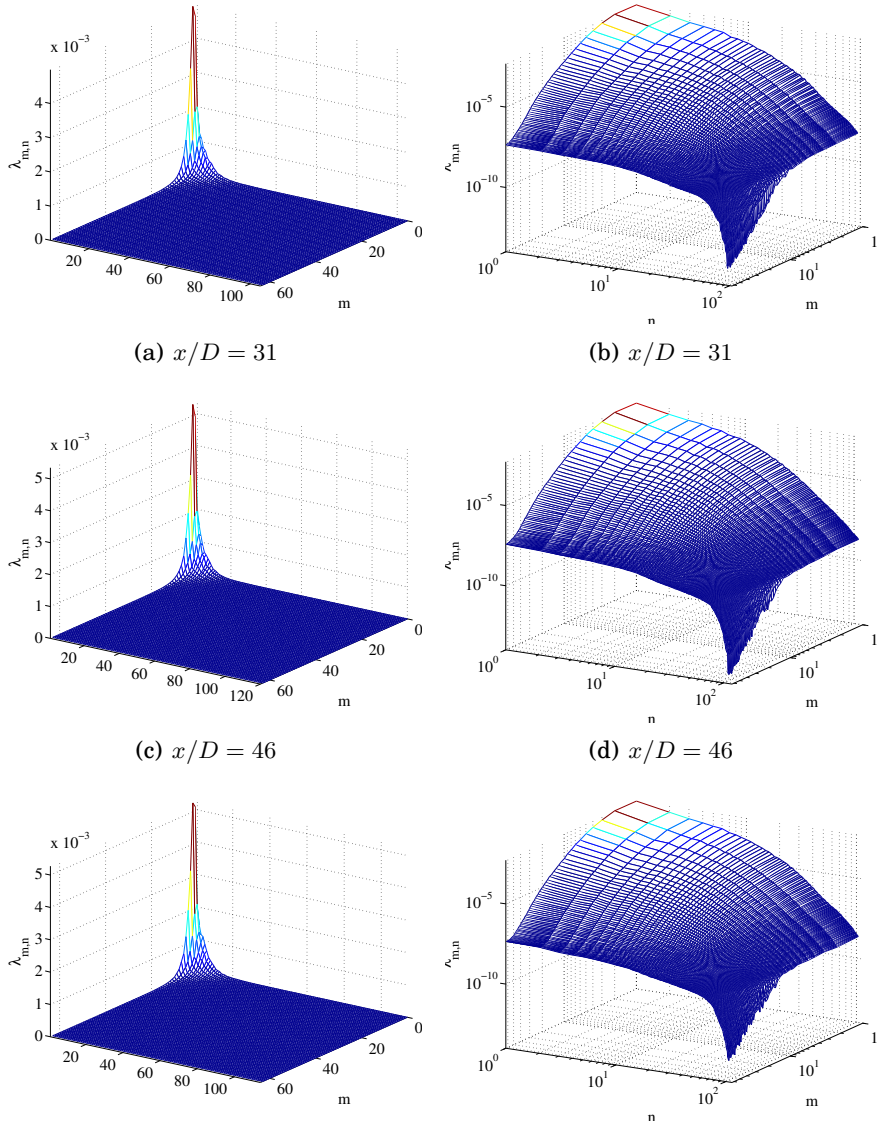

(a) $x/D = 31$ (b) $x/D = 31$

(c) $x/D = 46$ (d) $x/D = 46$

(e) $x/D = 71$ (f) $x/D = 71$

Fig. 10.1: Distribution of the radial POD eigenvalues $\lambda_{m,n}$ over POD mode number n over azimuthal mode number m. (a) $x/D = 31$, linear axes, (b) $x/D = 31$, logarithmic axes, (c) $x/D = 46$, linear axes, (d) $x/D = 46$, logarithmic axes, (c) $x/D = 71$, linear axes, (f) $x/D = 71$, logarithmic axes.

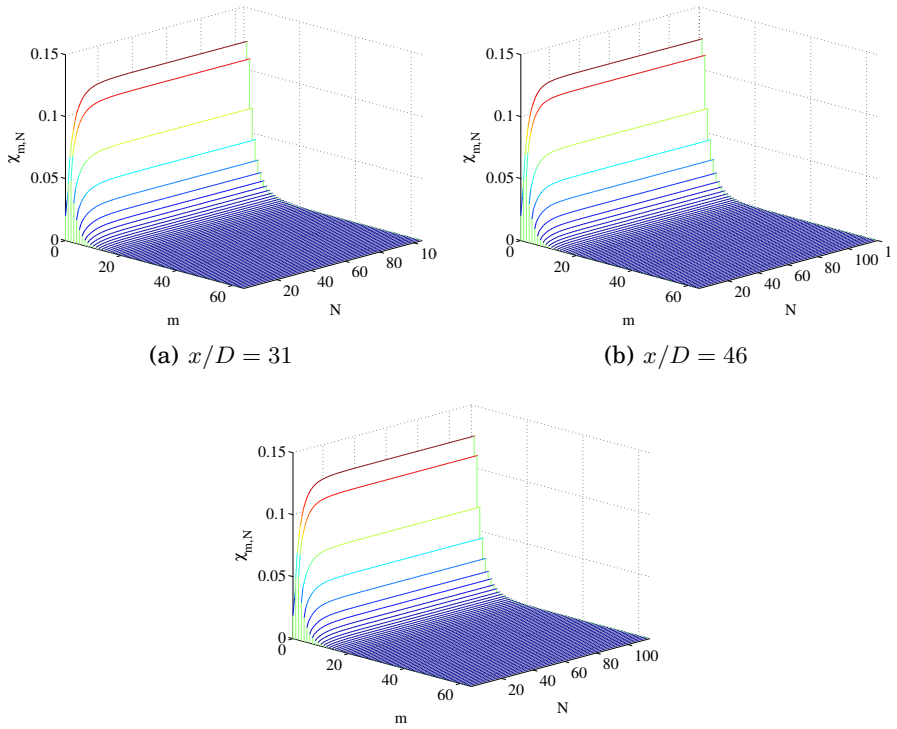

(a) $x/D = 31$

(b) $x/D = 46$

(c) $x/D = 71$

Fig. 10.2: Distribution of $\chi_{m,N}$, the partial sums over POD mode number n per azimuthal mode number m normalized by the total energy of the field. (a) $x/D = 31$, (b) $x/D = 46$, (c) $x/D = 46$.

Evaluating $\Gamma_{m,N}$, the partial sum over $\gamma_{m,n}$ as:

$$\Gamma_{m,N} = \sum_{n=1}^{N} \gamma_{m,n} = \frac{\Lambda_{m,N}}{\Lambda_{m,3P}} \tag{10.8}$$

The relative rate of convergence of the POD expansion per Fourier mode number is visualized in figures 10.3(a) through 10.3(c).

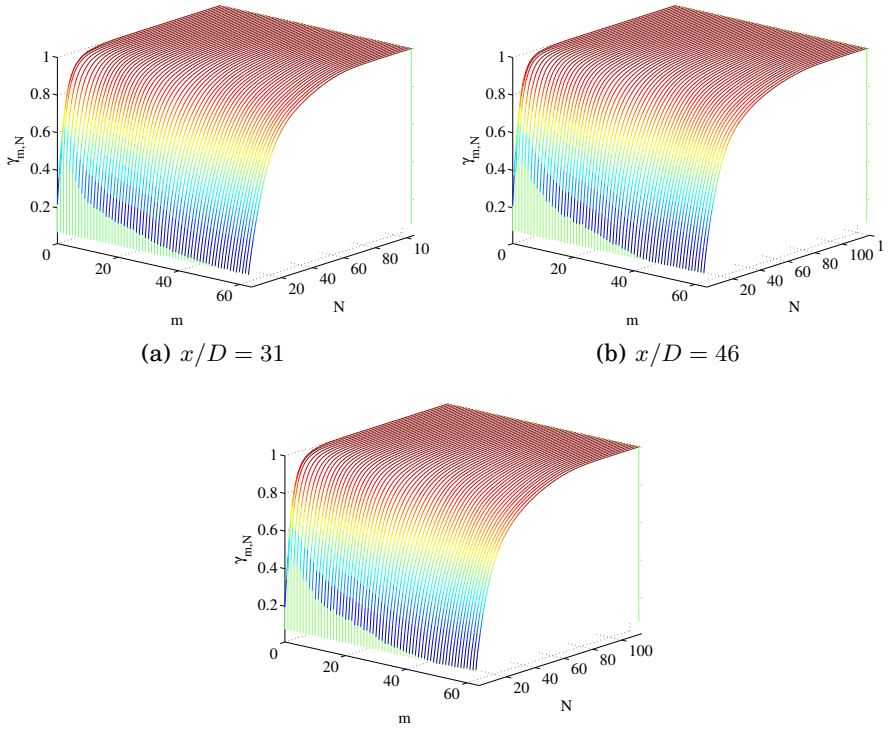

(a) $x/D = 31$ (b) $x/D = 46$

(c) $x/D = 71$

Fig. 10.3: Distributions of $\Gamma_{m,N}$, the partial sums of the POD eigenvalues normalized by the total spectral density available at each azimuthal Fourier modes m.

From the slopes of the distributions of $\Gamma_{m,N}$ is evident that the convergence rate of the POD modes do decay with azimuthal mode number, so that less and less of the available spectral density in each Fourier mode is captured by the same number of POD modes. However, the decay in convergence rate is not as drastic at that found in the streamwise analysis, see figure 6.3. Also, the changing character of the distribution noted in figure 6.3 and attributed to the PIV filtering of the streamwise spectra is not present in the azimuthal Fourier expansion. Since it is obvious that the SPIV data is heavily filtered, it can

perhaps indicates that it is the varying degree of filtering in the streamwise experiment that causes the problem.

Lastly, the customary graphs that show the azimuthal mode variation of the magnitude of the first POD mode eigenvalue relative to the total energy presented in figures 10.9(d) through 10.4(c) together with an indication of the sum of all POD eigenvalues. Note that this corresponds to distributions of $\chi_{m,1}$ and $\chi_{m,3P}$ as defined earlier. If one chooses to consider only the first and largest POD mode, it is clear that the azimuthal modes 1 and 2 are very close. As indicated by the figures, the total sum of the POD modes per azimuthal mode number compared to the total available energy is peaks at azimuthal mode 1, which would substantiate the results of Thomas and Iqbal [79].. Again, the

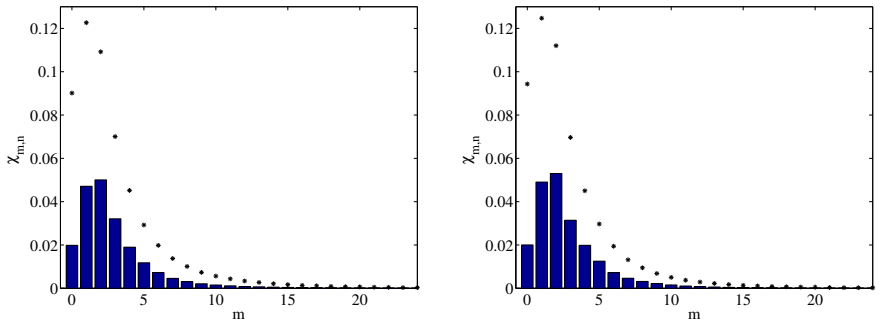

(a) $x/D = 31$

(b) $x/D = 46$

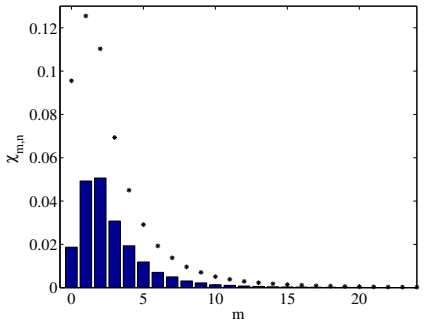

(c) $x/D = 71$

Fig. 10.4: Distributions of $\chi_{m,1}$, the first POD mode eigenvalues normalized by the total energy in the field and varying over azimuthal Fourier mode number m. The symbols $(*)$ indicate the values of $\chi_{m,2P}$, the ratio of energy represented by all the POD modes relative to the total energy.

high dimensionality of the jet turbulence is confirmed by the distribution of

the total energy over the POD and Fourier modes.

10.1.2 Eigenvectors

The number of eigenvectors produced by the POD matrix decomposition is 3P = 105 per azimuthal Fourier mode m. Figures 10.6(a) and 10.6(b) show the variation over POD mode number n of the real parts of the 0^{th} order Fourier mode eigenvectors $\phi_i^{(0,n)}(\eta)$ for $1 \leq n \leq 16$. As in the streamwise case, the sequency of the POD eigenvectors increase with the POD mode number n and resemble tapered Fourier modes. From close inspection of the component-to-compopenent variation oft he eigenvectors it seems that there is a tendency of their magnitude to alternate, so that when one vector component is large, the other two are small. Also, for azimuthal mode numbers $m > 20$, the values of the vectors at the radial position closest to the origin blow up. The cause for this is currently not known.

In order to compare the POD decompositions for the three cross-planes, figures 10.7(a) through 10.7(f) shows, for all three cross-planes, the three eigenvector components of the first and second order POD mode for azimuthal Fourier mode $m = 0$. The subsequent figures 10.8(a) through 10.8(f) show the same POD modes for azimuthal mode $m = 1$.

10.1.3 Grid radial extent sensitivity study

It has been noted previously by Gamard et al[8] that the degree to which the measurement covered the radial extent of the jet influences the eigenspectra. In order to investigate this aspect of the POD decomposition, the radial extent of the data sampled at $x/D = 46$ was reduced from $\eta = 1.9$ to 1.8, 1.6, 1,4 and 1.2 respectively. It should be noted that the results of Thomas and Iqbal[79], part of which are which are presented in figure 7.5, indicate strongly that the energy relative energy distribution between azimuthal modes 1 and 2 shift towards mode 1 as the flow develops downstream. However, their radial extent was shrinking as the probe rig moved moved downstream. Already at their $x/D = 8$ location, the radial extent is no more than $\eta = 1.2$. The figures below show the effect of on POD mode 1 and 2 as functions of azimuthal mode number for the different radial extents.

Clearly the results of the analysis is sensitive to the radial coverage. This makes sense, since the inner product on which the POD is based gets worse and worse approximated as the radial extent decreases. This brings to the question also the data sampled in this study, since none of the data presented here actually covers the jet beyond $\eta = 1.9$. Still, from the perspective of the far

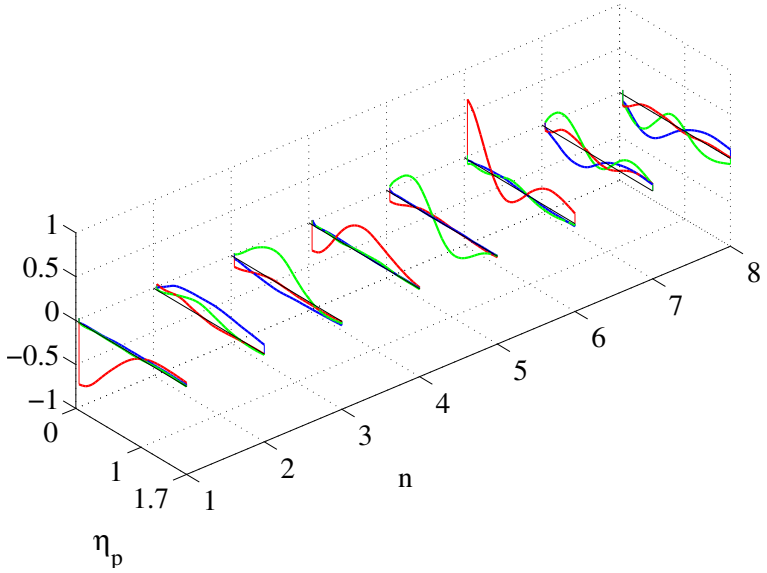

(a) $m = 0,\ 1 \leq n \leq 8$

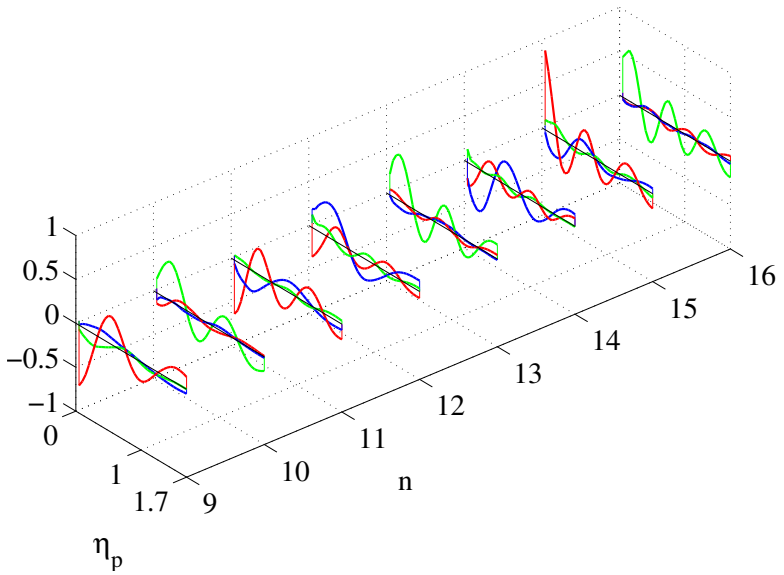

(b) $m = 0,\ 9 \leq n \leq 16$

Fig. 10.5: Real parts of eigenvectors $\phi_i^{(0,n)}(\eta)$, (a) $1 \leq n \leq 8$, (b) $9 \leq n \leq 16$. Color indication for the eigenvector components: (-) $\phi_1^{(0,n)}(\eta)$, (-) $\phi_2^{(0,n)}$,(-) $\phi_3^{(0,n)}$. Cross-plane at $x/D = 31$.

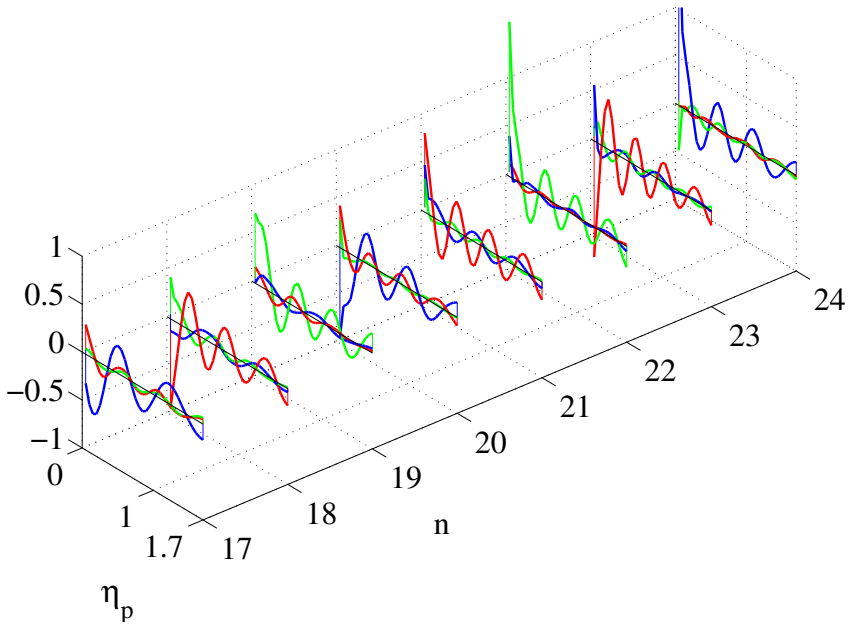

(a) $m = 0,\ 17 \leq n \leq 24$

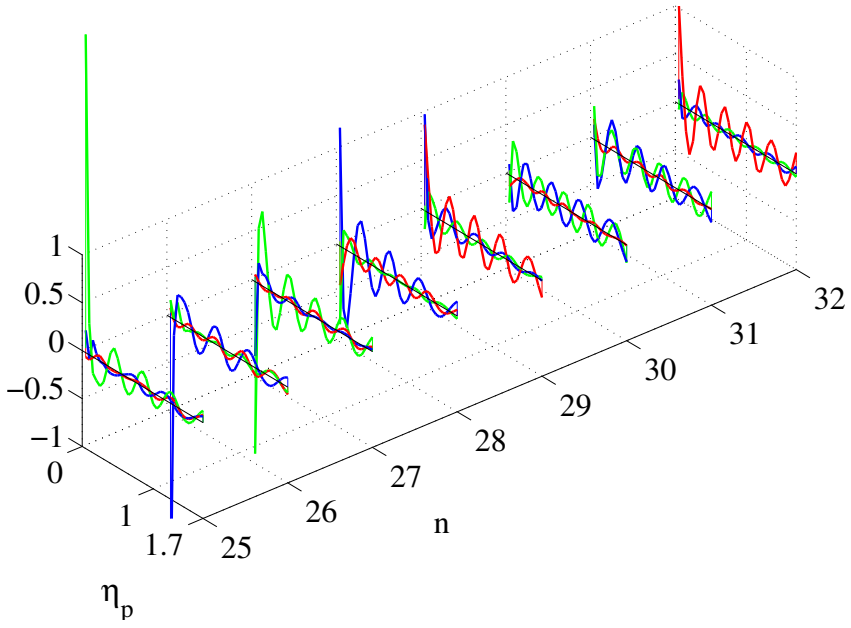

(b) $m = 0,\ 25 \leq n \leq 32$

Fig. 10.6: Real parts of eigenvectors $\phi_i^{(0,n)}(\eta)$, (a) $17 \leq n \leq 24$, (b) $25 \leq n \leq 32$. Color indication for the eigenvector components: (-) $\phi_1^{(0,n)}(\eta)$, (-) $\phi_2^{(0,n)}$,(-) $\phi_3^{(0,n)}$. Cross-plane at $x/D = 31$.

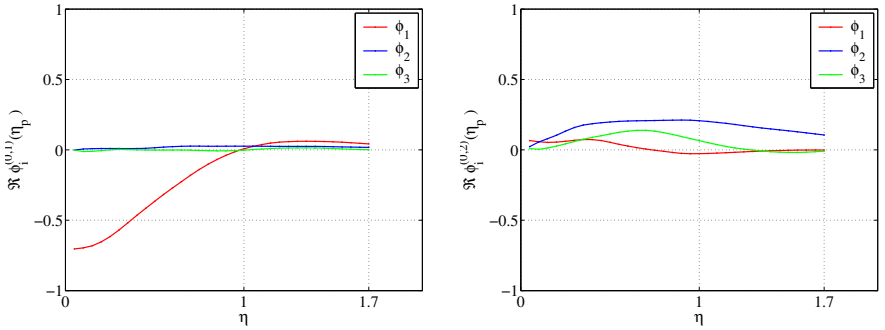

(a) $x/D = 31$

(b) $x/D = 31$

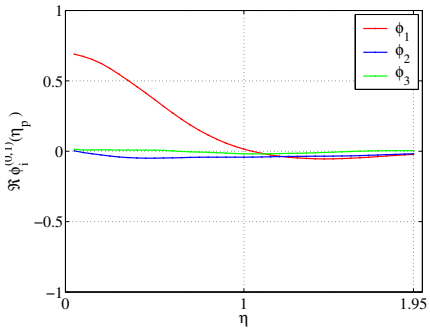

(c) $x/D = 46$

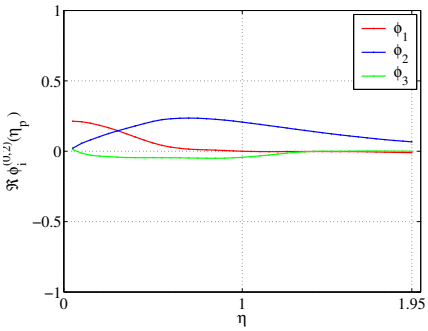

(d) $x/D = 46$

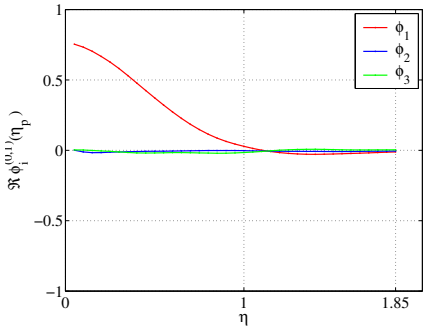

(e) $x/D = 71$

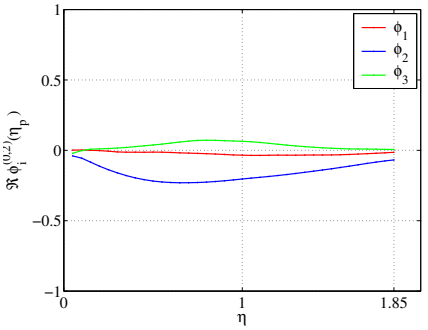

(f) $x/D = 71$

Fig. 10.7: Real parts of eigenvectors $\phi_i^{(m,n)}(\eta)$ for $m = 0$ and $n = 1, 2$. Rows correspond to the three cross-plane locations and column corresponds to $n = 1$ and $n = 2$,respectively. (-) $\phi_1^{(0,n)}(\eta)$, (-) $\phi_2^{(0,n)}(\eta)$, (-) $\phi_3^{(0,n)}(\eta)$.

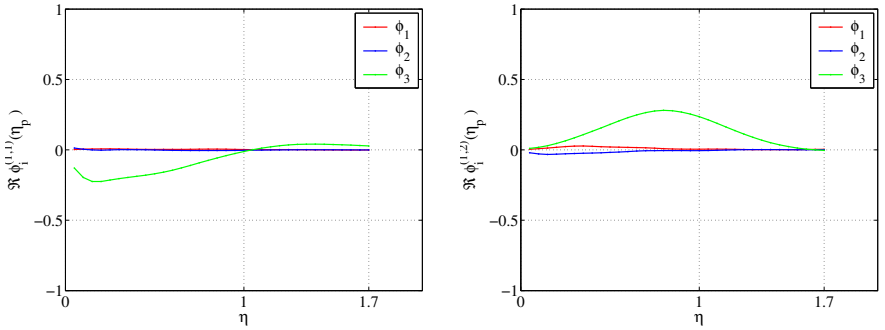

(a) $x/D = 31$

(b) $x/D = 31$

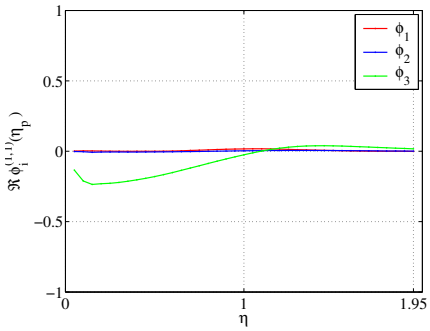

(c) $x/D = 46$

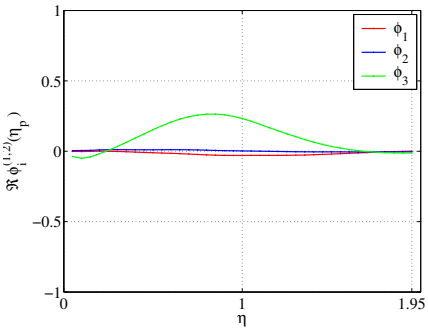

(d) $x/D = 46$

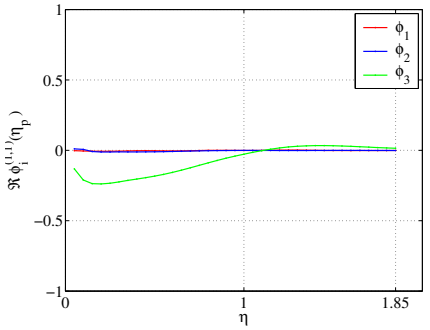

(e) $x/D = 71$

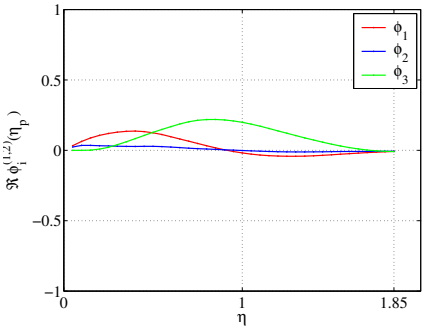

(f) $x/D = 71$

Fig. 10.8: Real parts of eigenvectors $\phi_i^{(m,n)}(\eta)$ for $m = 1$ and $n = 1, 2$. Rows correspond to the three cross-plane locations and column corresponds to $n = 1$ and $n = 2$,respectively. (-) $\phi_1^{(1,n)}(\eta)$, (-) $\phi_2^{(1,n)}(\eta)$, (-) $\phi_3^{(1,n)}(\eta)$.

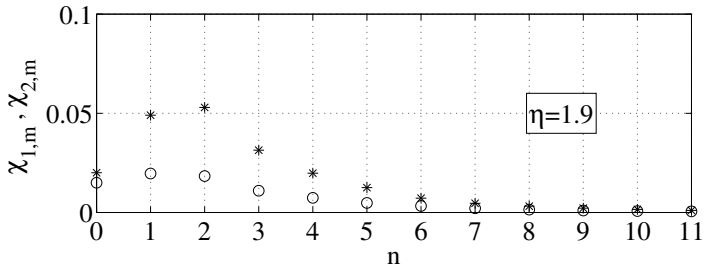

(a) $\eta = 1.2$

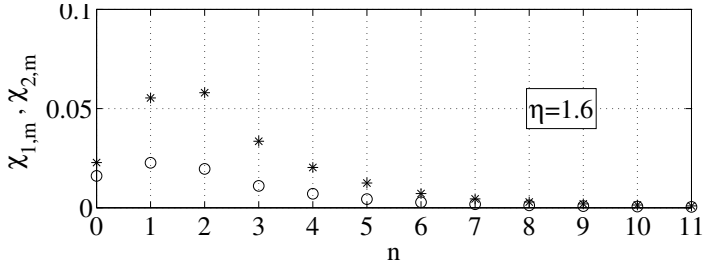

(b) $\eta = 1.2$

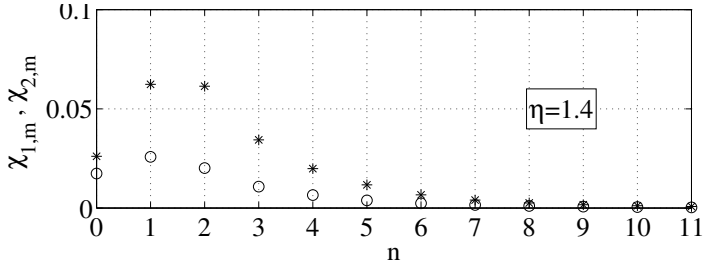

(c) $\eta = 1.2$

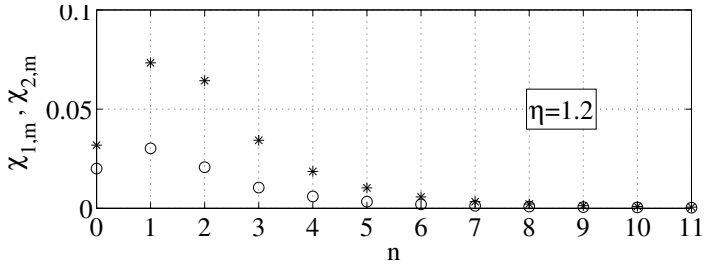

(d) $\eta = 1.2$

Fig. 10.9: (∗) $\chi_{m,1}$ and (○) $\chi_{m,2}$ for varying radial extent, showing how the reduced coverage shifts distribution from azimuthal mode 2 to mode 1.

jet, one must ask oneself what the gain in attempting to determine what mode is more dominant - clearly a whole spectrum of modes is required to represent the turbulence in the far jet.

11. SUMMARY AND CONCLUSIONS

11.1 The experiments

Two experiments were carried out in fully-developed flow downstream of a 10 cm top-hat jet at exit Reynolds number of 20,000. The jet was operated in air at a nominal exit velocity of 30 m/s. The primary interest of both experiments was in the scales of the turbulence that produce the Reynolds shear stress and which contain most of the turbulence energy. The value of the Reynolds number was chosen to be near the minimum for which one could expect the characteristics of high Reynolds number jets to be manifested. The most important of these was to insure the existence of a spectral gap between the small dissipative scales and those containing most of the energy and producing the Reynolds shear stress. The similarity of the single point statistics to earlier measurements at much higher Reynolds number, as well as the limited inertial subrange in the spectral measurements themselves, suggest that the flow indeed satisfied this requirement. The scale of the experiment was also the smallest in air that was consistent with being able to resolve the physical scales of interest and for which the scattering particles could be assumed to follow the flow to at least the time scales of interest.

The streamwise experiment used two-component PIV to examine the entire flow field simultaneously in the $x-r$-radial plane from $30 \leq x/D \leq 95$. The cross-stream experiment used stereo PIV to examine the flow in cross-sectional $(r-\theta)$-planes at three downstream distance. Both experiments exploited the single and two-point equilibrium similarity theory of [7] and [11], and provided independent experimental confirmation of it.

11.2 The measurement difficulties

A considerable effort was made in both experiments to understand the sources of error and noise arising from the PIV itself. These problems are intrinsic to any instrument, but exacerbated in these experiments because of the large

physical extent of the flow that had to measured simultaneously: $0.4m \times 0.7m$ in the streamwise experiment and $0.4m \times 0.4m$ in the cross-stream experiment. Also complicating measurement was the large dynamic range of velocities that had to be measured simultaneously. In spite of the difficulties, the success of the measurements makes clear the unique value of such an instrument: the ability to look at large scale experimentally realized exact solutions of the Navier-Stokes equations.

The major adverse effect on the second moment and spectral measurements was the spatial filtering from the finite interrogation volume. This problem was analyzed using the established methodologies for spatial filtering, and estimated to have reduced the turbulence intensities by approximately 10-15 %. The effect on the spectrum was obvious, and caused a sharp departure from the inertial subrange behavior at wavenumbers corresponding to the inverse of the interrogation volume dimension. Since the effect was primarily to remove the small scales by averaging them out, it did not affect the measurements (or inferences from them) at the wavenumbers and scales of interest.

Of the many sources of error considered, two dominated. The first was a consequence of bad experimental practice and inexperience (but corrected for the final measurements with great effort); namely, the disparity errors which very much contaminated our early attempts at SPIV. These errors result when the calibration plane and the light plane are not perfectly aligned. These 'registration errors' were well-understood by the PIV community, but were initially discounted as not being important for measurement of the large scales of our experiments since the mean flow gradients were small. Nothing could have been further from the truth. In fact, as argued in chapter 8.1.7, the higher the Reynolds number, the smaller the Taylor microscale relative to the misalignment (for fixed large scales), and the more critical the alignment becomes. The Taylor microscale enters since it measures the fluctuating velocity gradients in the flow. Such errors were easily spotted in the jet measurements because they introduced asymmetries into what should have been azimuthally symmetric contour plots.

The second source of source of error was the noise arising from the fact that each PIV realization is based on a relatively small number of individual scattering particles, typically 10 to 30. This source of noise had also been previously recognized by the PIV community, but was overlooked by us (in part because the observations were reported as an interrogation area dependence instead of number of particles and we did not see the significance). The net effect is to increase the turbulence moments by a factor of $(1 + 1/N_p)$, and add a broadband spectrum proportional to Fourier transform of the interrogation window function squared (i.e., sinc-squared) times the interrogation volume dimension. In our experiments the contribution to the mean square velocity from this source was estimated to be approximately 3-5 percent, but fortu-

nately spread over a very large band so its contribution to the spectra (and cross-spectra) was negligible.

In part the problems encountered were a consequence of inexperience. But in part they must also be attributed to the unique nature of these jet investigations. Much of the focus in PIV books and meetings is on improving the signal processing to provide more accurate velocity determination. As a result our focus was entirely on things that, while important, were simply overwhelmed by other considerations intrinsic to the device. The nuances in performance from different algorithms were simply buried by the large and poorly resolved fields-of-view with which we were forced to work to investigate a flow that was interesting. That these experiments succeeded in spite of the difficulties can largely be attributed to effective use of statistics and flow theory - and very large statistical ensembles. In many ways, this may be a harbinger of the future of PIV, at least in applications, since if application of the PIV is restricted to only small experiments at relatively low Reynolds number that can be measured to great accuracy, then it can only provide a fraction of the information available at the same Reynolds numbers with a DNS.

11.3 Insights into flow scaling

As noted above, both experiments, especially the streamwise one, provided strong support for the equilibrium similarity theory of [**?** **?**], and as well for the extension to two-point similarity by [6**?**]. The thesis carried those ideas one large step forward by exploring the consequences for instantaneous velocity fields, in particular the re-mapping of the velocity field by the local mean centerline velocity, normalizing the radial coordinate by the local half-width, and stretching the streamwise axis logarithmically. From all observable quantities the velocity field was effectively homogeneous in the streamwise direction.

While such a mapping may seem a great leap of faith it follows naturally from the fact that the original (in this case mapped field) can be recovered from its POD and Fourier modes. These modes can be entirely determined from second-order quantities. So if these satisfy equilibrium similarity conditions, then so must reconstructions based on them. In fact, it is possible to show by a simple scale analysis that the instantaneous equations for a fully developed, axisymmetric jet are also scale invariant. Moreover, this applies to all of the terms in the equations, including the neglected terms in a first or second-order boundary layer-type analysis. This means that the flow at any cross-section, if scaled up or down, also represents a possible realization of the flow at any upstream or downstream position. It is not entirely clear at the present time what the implications of this may be, but they might be profound.

All of the above depended crucially on the fact that as consequence of conservation of momentum in the axisymmetric jet, $[U_c\delta_{1/2}]^2 = constant$ once the flow becomes fully-developed (typically $x/D \geq 30$). Hence the local Reynolds number for the turbulent jet, $U_c\delta_{1/2}/\nu$ is also constant. This means that all of the turbulence length and time scales, no matter how defined and from integral scale to Kolmogorov microscale, maintain the same ratio as the flow develops downstream. Only one other flow, the plane wake appears to share this property.

11.4 Insights into how the jet sustains itself

An extensive decomposition of cross-stream planes was carried out using Fourier series and slice-POD decompositions. Previous experiments have had to depend on measurements with rakes of individual probes. These have, of necessity, been limited in number by the physical constraints of how many can be squeezed into a given space without blocking the flow, and as well by the sheer difficulty of operating them (139 is the record for a jet investigation). For example, the smallest angle for azimuthal correlation separations is typically $7.5\,\mathrm{deg}$ and often more. (For the PIV experiments here it was $1.5\,\mathrm{deg}$.) Also these previous investigations have had to depend on heuristic arguments more than experiment to determine parameters like spatial extent and probe density. Moreover most probes (especially hot-wires) are operating well beyond their comfort level in jets, where the local minimum turbulence intensity is 25 % at the centerline and rises rapidly with increasing radius from it. Finally, it was virtually impossible to adjust the fixed probe rakes to the growing shear layer, so for each position a different spatial discretization was realized, and a different largest dimension.

For the PIV experiments reported herein, the domain and discretization were adjusted to the local domain size. Moreover, the effective number of probes was equal to the number of overlapping interrogation volumes, the overlap minimizing aliasing. As a consequence, not only was the field better resolved, it was possible to investigate the effect of changing the domain and discretization. Not surprisingly, some of the results proved to be quite sensitive, and it was possible to resolve a number of outstanding issue and explain the reason why different investigators saw what they reported. Of particular interest was whether the azimuthal decomposition of the jet peaked at mode-1 or mode 2. It appears that mode-2 wins by a very small amount, and any significant reduction in radial extent of the field tips the balance the other way.

This issue has been of historical importance only because of the attempt to create simplistic views of turbulence based on linear (or non-linear) stability theories. Of far greater importance to the field than mode-1 versus mode-2 and

to the future theories was the observation that there is a virtual continuum of modes, a spectrum of them if you will. Moveover, it was possible to show that each of these modes has Reynolds shear stress that it is in direct proportion to its energy. This means that each mode is directly receiving a significant (and relatively equal) percentage of its energy directly from the mean flow! Since this balance is maintained (by similarity) for all downstream positions, does this means that the non-linear energy transfer has effectively shut-down, or at least makes no net contribution? This question appears to be quite profound, and gets the core of what it means for a flow to have achieved an equilibrium similarity state. A consequence of this is that perhaps linear theories might indeed be able to predict after all how each mode receives its energy, consistent with the suggestion of Morris et al.[87] many years ago.

BIBLIOGRAPHY

[1] W. K. George. The self-preservation of turbulent flows and its relation to initial conditions and coherent structures. In *Advances in Turbulence*, pages 39–73. Hemisphere, NY, 1989.

[2] J. Cater and J. Soria. The evolution of round zero-net-massflux jets. *Journal of Fluid Mechanics*.

[3] Nathan G. J. Wong C. Y. and O'Doherty T. The effect of initial conditions on the flow exiting from a fluidic precessing jet nozzle. *Experiments in Fluids*, 36:0723–4864, 2003.

[4] *Journal of Fluid Mechanics*, pages 115–138, 1998.

[5] D. Ewing and W. K. George. Implication of a similarity hypothesis on the application of the proper orthogonal decomposition. In Hanjalic and Pereira, editors, *Proc. ICHMT Symposium on Turbulence, Heat and Mass Transfer, Lisbon, Portugal (1994)*. Elsevier, Amsterdam, 1995.

[6] D. Ewing. *On Multi-point Similarity Solutions in Turbulent Free Shear Flows*. PhD thesis, University at Buffalo, SUNY, 1995.

[7] D. Ewing, B. Frohnapfel, W.K. George, J.M. Pedersen, and J. Westerweel. Two-point similarity in the round jet. *Journal of Fluid Mechanics*, 557:309–330, 2007.

[8] S. Gamard, D. Jung, and W.K. Goerge. Downstream evolution of the most energetic modes in a turbulent axisymmetric jet at high reynolds number. part 2. the far-field region. *Journal of Fluid Mechanics*, 2004.

[9] W. K. George. Some thoughts on similarity, the POD, and finite boundaries. In A. Gyr, W. Kinzelbach, and A. Tsinober, editors, *Fundamental Problematic Issues in Turbulence*, Trends in Mathematics (from the Second Monte Verita Colloquium on Turbulence, Centro Stefano Francini, Switz., Mar. 22 – 27, 1998), pages 117–128. Birkhauser, Switzerland, 1999.

[10] J. L. Lumley. The structure of inhomogeneous turbulent flows. In A. M. Yaglom and V. I. Tatarsky, editors, *Atmospheric Turbulence and Radio Wave Propagation*, pages 166–176, Moscow, USSR, 1967. Publishing House Nauka.

[11] W. K. George. The self-preservation of turbulent flows and its relation to initial conditions and coherent structures. In *Advances in Turbulence*, pages 39–73. Hemisphere, NY, 1989.

[12] G. K. Batchelor and E. A. Gill. Analysis of the instability of axisymmetic jets. *Journal of Fluid Mechanics*, 14:529–551, 1962.

[13] A. Michalke. On spatially growing disturbances in an inviscid shear layer. *Journal of Fluid Mechanics*, 23:521–544, 1965.

[14] Nonlinear roll-up of externally excited free shear layers.

[15] X. Wu and P. Huerre. Low frequency sound radiated by a nonlinearly modulated wavepacket of helical modes in a subsonic circular jet. *Journal of Fluid Mechanics*, In press, 2009.

[16] H. J. Hussein, S. P. Capp, and W. K. George. Velocity measurements in a high-reynolds-number, momentum-conserving, axisymmetric, turbulent jet. *Journal of Fluid Mechanics*, 258:31–75, 1994.

[17] G. K. Batchelor. *An Introduction to Fluid Dynamics*. Cambridge University Press, Cambridge, UK, 1967.

[18] H. Tennekes and J. L. Lumley. *A First Course in Turbulence*. MIT Press, Cambridge,MA, 1972.

[19] A. A. Townsend. *The Structure of Turbulent Shear Flow*. Cambridge University Press, Cambridge, UK, second edition, 1976.

[20] W.K. George. Is there an asymptotic effect of initial and upstream conditions on turbulence? *2008 Freeman Lecture, Proc. ASME 2008 Fluids Engineering Meeting.*, 2008.

[21] P. B. V. Johansson, W. K. George, and M. J. Gourlay. Equilibrium similarity, effects of initial conditions and local reynolds number on the axisymmetric wake. *Physics of Fluids*, 15(3):603 – 617, 2003.

[22] W. K. George. Some new ideas for similarity of turbulent shear flows. In J. C. F. Hanjalic, K.and Pereira, editor, *Proceeding of the Symposium on Turbulence, Heat and Mass Transfer 1, Lisbon, Portugal 9-12 August 1994)*. Begell House, 1995.

[23] W. K. George. Another look at the log (or is it a power law?) velocity profile for a zero-pressure gradient boundary layer. 3rd Joint ASME/ASCE Mech. Conf. LaJolla, CA July 9-12, 1990.

[24] W. K. George. The decay of homogeneous isotropic turbulence. *Physics of Fluids A*, 4(7):1492–1509, 1992.

[25] W.K. George and H.L. Wang. The exponential decay of homogeneous turbulence. *Physics of Fluids*, 2008.

[26] W. K. George and M. M. Gibson. The self-preservation of homogeneous shear flow turbulence. *Experiments in Fluids*, 13:229–238, 1992.

[27] J. O. Hinze. *Turbulence*. McGraw-Hill, New York, NY, 1975.

[28] J. L. Lumley. *Stochastic Tools in Turbulence*. Academic Press, New York, NY, 1970.

[29] W.K. George. *Lectures in Turbulence for the 21st Century (available from www.turbulence-online.com)*. 2009.

[30] A.D. Polyanin and A.V. Manzhirov. *Handbook of integral equations*. CRC Press LCC, 1998.

[31] W. K. George, S. J. Leib, and M. N. Glauser. An application of lumley's orthogonal decomposition to the axisymmetric jet mixing layer. In *American Physical Society, Division of Fluid Dynamics*, Houston, TX, 1983.

[32] M. N. Glauser. *Coherent Structures in the Axisymmetric Turbulent Jet Mixing Layer*. PhD thesis, Dept. of Mechanical and Aerospace Eng., State University of New York at Buffalo, 1987.

[33] M. Glauser and W. K. George. An orthogonal decomposition of the axisymmetric jet mixing layer utilizing cross-wire measurements. In *Proceedings of the Sixth Symposium on Turbulent Shear Flow*, pages 10.1.1–10.1.6, Toulouse, France, 1987.

[34] J. Delville, L. Ukeiley, L. Cordier, J. P. Bonnet, and M. Glauser. Examination of large–scale structures in a turbulent plane mixing layer. Part 1. Proper orthogonal decomposition. *Journal of Fluid Mechanics*, 391:91–122, 1999.

[35] J.H. Citriniti. *Experimental investigation into the dynamics of the axisymmetric mixing layer utilizing the proper orthogonal decomposition*. PhD thesis, Dept. of Mechanical and Aerospace Eng., State University of New York at Buffalo, 1996.

[36] S. Gordyev and F. O. Thomas. Coherent structure in the turbulent planar jet. Part 1. Extraction of proper orthogonal decomposition eigenmodes and their similarity. *Journal of Fluid Mechanics*, 414:145–194, 2000.

[37] J. H. Citriniti and W. K. George. Reconstruction of the global velocity field in the axisymmetric mixing layer utilizing the proper orthogonal decomposition. *Journal of Fluid Mechanics*, 418:137–166, 2000.

[38] C. E. Tinney, M.N Glauser, and L. S. Ukeiley. Low-dimensional characteristics of a transonic jet. part 1: Proper orthogonal decomposition. *Journal of Fluid Mechanics*, 612:107–141, 2008.

[39] B.R. Noack, K. Afansiev, M. Morzynski, G. Tadmor, and F. Thiele. A hierarchy of low-dimensional models of the transient and post-transient cylinder wake. *Journal of Fluid Mechanics*, 497:335–363, 2003.

[40] B.R. Noack, P. Papas, and P.A. Monkewitz. The need for a pressure-term representation in empirical galerkin models of incompressible shear flow. *Journal of Fluid Mechanics*, 523:339–365, 2005.

[41] B. Frohnapfel. Multi-point similarity of the axisymmetric turbulent far jet and its implication for the pod. Master's thesis, Friedrich-Alexander-Universität Erlangen-Nurnberg Lehrstuhl fur Strömungsmekanik, 2003.

[42] M. Wänström, W.K. George, K.E. Meyer, and C. Westergaard. Identifying sources of stereoscopic piv measurement errors on turbulent round jets. *5th Joint ASME/LSME Fluids Engineering Conference, July 30 - August 2, San Diego, Symposium paper FEDS2007-37256*.

[43] A. Spenser and D. Hollis. Correcting for sub-grid filtering effects in particle image velocimetry data. *Meas. Sci. Technol*, 16:2323–2335, 2005.

[44] M. Wänström. Modal composition of a far turbulent axisymmetric jet, Lic. Thesis, Chalmers Univeristy of Technology. 2006.

[45] M. N. Glauser and W. K. George. Application of multipoint measurements for flow characterization. *Experimental Thermal and Fluid Science*, 5:617–632, 1992.

[46] W.K. George, P.D. Beuther, and J.L. Lumley. Processing of random signals. pages 757–800, 1978.

[47] C.M. Velte. *Characterization of Vortex Generator Induced Flow*. PhD thesis, Technical University of Denamrk, Dept. of Mechanical Eng., 2009.

[48] S. Gamard. *The axisymmetric turbulent jet*. PhD thesis, Dept. of Thermo and Fluid Dynamics, Chalmers University of Technology, Gothenburg, Sweden, 2002.

[49] S. Gamard. *Application of the Slice POD to the Far region of an Axisymmetric Jet*. PhD thesis, Dept. of Mechanical and Aerospace Eng., State University of New York at Buffalo, 2002.

[50] Willert C.E. Wereley S.T. Raffel, M. and J. Kompenhaus. *Particle Image Velocimetry - A Practical Guide. Second Edition.* Springer-Verlag, Berlin Heidelberg, 2007.

[51] P. Buchhave, W. K. George, and J. L. Lumley. The measurement of turbulence with the laser-doppler anemometer. In Van Dyke, Wehausen, and Lumley, editors, *Annual Review of Fluid Mechanics*, volume 11, pages 443–503. Academic Press, Palo Alto, CA., 1979.

[52] N. R. Panchapakesan and J. L. Lumley. Turbulence measurements in axisymetric jets of air and helium, part 2 helium jets. *Journal of Fluid Mechanics*, 246:225–247, 1993.

[53] G. Comte-Bellot and S. Corrsin. Simple eulerian time correlation of full nad narrow band velocity signals in grid-generated ´isotropic turbulence'. *Journal of Fluid Mechanics*, 48:273 –337, 1971.

[54] G. K. Batchelor. *The Theory of Homogeneous Turbulence*. Cambridge University Press, Cambridge, UK, 1953.

[55] D. Ewing. *On Multi-Point Similarity Solutions in Turbulent Free-Shear Flows*. PhD thesis, Dept. of Mechanical and Aerospace Eng., State University of New York at Buffalo, 1995.

[56] Chester S. Kang, H.S. and C. Meneveau. Decaying turbulence in an active-grid-genreated flow and comparison with large-eddy simulation. *Journal of Fluid Mechanics*, 480:129–160, 2004.

[57] Carlier J. Foucaut, J.M. and M. Stanisals. Piv optimization for the study of turbulent flow using spectral analysis. *Meas. Sci. Technol*, 15:1046 – 1058, 2004.

[58] S. Herpin. *Study of the influence of the Reynolds number on the organization of wall-bounded turbulence*. PhD thesis, Ecole Centrale de Lille, Dept. of Mechanical Eng., 2009.

[59] W. K. George and H. J. Hussein. Locally axissymmetric turbulence. *Journal of Fluid Mechanics*, 233:1–23, 1991.

[60] *The structure of atmospheric turbulence*. Interscience, NY, NY, 1964.

[61] D. Jung, S. Gamard, and W. K. George. Downstream evolution of the most energetic modes in a turbulent axisymmetric jet at high reynolds number. Part 1. The near field region. *Journal of Fluid Mechanics*, 2004.

[62] D. Jung, S. Gamard, and W. K. George. Downstream evolution of the most energetic modes in a turbulent mixing layer at high reynolds number. part 1: the near field region. *Journal of Fluid Mechanics*, 514:173–204, 2004.

[63] S. Gamard, D. Jung, and W. K. George. Downstream evolution of the most energetic modes in a turbulent mixing layer at high reynolds number. part 2: the far jet. *Journal of Fluid Mechanics*, 514:205–230, 2004.

[64] M. Wänström, K. E. Meyer, and W.K. George. Stereoscopic piv and pod applied to the far turbulent axisymmetric jet. *APS/DFD Ann. Mtg., Chicago, IL*, 2005.

[65] M. Wänström, W.K. George, and K. E. Meyer. Stereoscopic piv and pod applied to the far turbulent axisymmetric jet. *AIAA Fluid Dynamics Meeting, San Francisco, June 3-7*, (2006-4332), 2006.

[66] M. Wänström, W.K. George, and K. E. Meyer. Identifying effects of stereoscopic piv measurements errors on turbulent round jets. *5th Joint ASME/JSME Fluids Engineering Conference, 30 July -2 August, San Diego, CA, USA*, (FEDSM2007-37256), 2007.

[67] L. Ukeiley and J. Seiner. Examination of large scale structures in a transonic jet mixing layer. *ASME FEDSM98-5234*, 1998.

[68] L. S. Ukeiltey, J. M. Seiner, and M. K. Ponton. Azimuthal structure of an axisymmetric jet mixing layer. In *ASME FEDSM99-7252*, 1999.

[69] M.N. Glauser, J.A. Taylor, L.S. Ukeiley, W.K. George, and J.H. Citriniti. A low dimensional description of the axisymmetric turbulent jet: an update. *ERCOFTAC Bulletin*, 46:53–61, 2000.

[70] C. Tinney. *Low Dimensional Techniques for Sound Source Identification in High Speed Jets*. PhD thesis, Syracuse University, 2004.

[71] M.O. Iqbal and F.O. Thomas. Coherent structure in a turbulent jet via a vector implementation of the proper orthogonal decomposition. 2005.

[72] M. Wänström. Using stereoscopic piv to investigate the crossplane modal composition of a far turbulent axisymmetric jet. *Licentiate Thesis, Thermo and Fluid Dynamics, Chalmers University of Technology, Gothenburg, Sweden*, 2006.

[73] M. Tutkun, M. Wänström, and W. K. George. Comparison of the turbulence structure in fully developed wakes and jets. *Proceedings of the 4th Ankara International Aerospace Conference, 10-12 September, 2007, Middle East Technical University, Ankara, Turkey*, (AIAC-2007-018), 2007.

[74] F.F. Grinstein, M.N. Glauser, and W.K. George. *Turbulent Jets*. Kluwer, 1995.

[75] J. B. Freund and T. Colonius. Pod analysis of sound generation by a turbulent jet. *AIAA Paper*, 2002-0072, 2002.

[76] V. F. Kopiev. Private Communication, 2001.

[77] W. K. George, P.B.V. Johansson, and S. Gamard. How has the study of coherent structures contributed to our understanding of turbulent free shear flows? In *Workshop on Coherent Structures in Turbulence: FEDSM'02/ASME Fluids Engineering Division Summer Meeting, Montreal*. ASME, 2002.

[78] H Liang and T Maxworthy. An experimental investigation of swirling jets. *Journal of Fluid Mechanics*, 525:115 – 159, 2005.

[79] F. Thomas and M. Iqbal. Coherent structure in a turbulent jet via a vector implementation of the proper orthogonal decomposition. *J. Fluid Dynamics*, 2005.

[80] F. Thomas, M. Iqbal, and T. Corke. An experimental vector implementation of the proper orthogonal decomposition in a turbulent axisymmetric jet. 49 no. 10, 2004.

[81] H. J. Hussein, S. P. Capp, and W. K. George. Velocity measurements in a high-reynolds-number, momentum-conserving, axisymmetric, turbulent jet. *J. Fluid Mech.*, 258:31–75, 1994.

[82] N.K. Tutu and R. Chevray. Cross-wire anemomety in high intensity turbulence. *J. Fluid Dynamics*, 71:785–800, 1975.

[83] C.W.H. C.W.H. van Doorne and J. J. Westerweel. The laser doppler velocimeter and its application to the measurement of turbulence. *Exp. Fluids*, 42:259–279, 2007.

[84] Fundamentals of digital particle image velocimetry. *Meas. Sci. Technol.*, pages 1379–1392, 1997.

[85] C. Willert. Stereoscopic digital particle image velocimetry for application in wind tunnel flows. *Meas. Sci. Technol.*, 8:1465–1479, 1997.

[86] J.M.S. Coudert and Schon J-P. Back-projection algorithm with misalignment corrections for 2d3c stereoscopic piv. *Meas. Sci. Technol.*, 2001.

[87] P. J. Morris, M. G. Giridharan, and G. M. Lilley. On the turbulent mixing of compressible free shear layers. *Proc. R. Soc. Lond. A.*, 431:219–243, 1990.

[88] W.K. George and J.L. Lumley. The laser doppler velocimeter and its application to the measurement of turbulence. *J. Fluid Mech.*, 60(FEDSM2007-37256):321–363, 1973.

APPENDIX

A. INCOMPRESSIBLE NAVIER-STOKES EQUATIONS IN CYLINDRICAL COORDINATES

Assuming a incompressible flow in a Newtonian fluid medium, conservation of mass for a fluid volume element requires that

$$\frac{\partial \rho}{\partial t} + \nabla \cdot (\rho \tilde{u}) = 0 \tag{A.1}$$

$$\rho = \rho_o \Rightarrow \nabla \cdot \tilde{u} = 0 \tag{A.2}$$

Conservation of momentum for a fluid volume element requires that

$$\frac{\partial \tilde{u}}{\partial t} + \tilde{u} \cdot \nabla \tilde{u} = -\frac{1}{\rho_o} \nabla p + \nu \nabla^2 \tilde{u} \tag{A.3}$$

Expression the differential operators in cylindrical coordinates one obtains the following set of four equations that governs the fluid motion :

$$\frac{\partial u_x}{\partial x} + \frac{1}{r}\frac{\partial}{\partial r} r u_r + \frac{1}{r}\frac{\partial u_\theta}{\partial \theta} = 0 \tag{A.4}$$

$$\frac{\partial u_x}{\partial t} + \tilde{u} \cdot \nabla u_x = -\frac{1}{\rho_o}\frac{\partial p}{\partial x} + \nu \nabla^2 u_x \tag{A.5}$$

$$\frac{\partial u_r}{\partial t} + \tilde{u} \cdot \nabla u_r - \frac{u_\theta^2}{r} = -\frac{1}{\rho_o}\frac{\partial p}{\partial r} + \nu(\nabla^2 u_r - \frac{u_\theta}{r^2} - \frac{2\partial u_\theta}{r^2 \partial \theta}) \tag{A.6}$$

$$\frac{\partial u_\theta}{\partial t} + \tilde{u} \cdot \nabla u_\theta + \frac{u_r u_\theta}{r} = -\frac{1}{r\rho_o}\frac{\partial p}{\partial \theta} + \nu(\nabla^2 u_\theta + \frac{2\partial u_\theta}{r^2 \partial \theta} - \frac{u_\theta}{r^2}) \tag{A.7}$$

Reynolds decomposition separates the steady mean parts of the fluid velocity and expresses the turbulence as a fluctuation relative to the mean, i.e., $\vec{u}' = \vec{U} + \vec{u}$. The continuity equation becomes:

$$\frac{\partial U_x}{\partial x} + \frac{1}{r}\frac{\partial}{\partial r} r U_r + \frac{1}{r}\frac{\partial U_\theta}{\partial \theta} = 0 \tag{A.8}$$

$$\frac{\partial u_x}{\partial x} + \frac{1}{r}\frac{\partial}{\partial r} r u_r + \frac{1}{r}\frac{\partial u_\theta}{\partial \theta} = 0 \tag{A.9}$$

The mean momentum conservation equations are: ’

$$\frac{\partial U_x}{\partial t} + \tilde{U} \cdot \nabla U_x + \langle \tilde{u} \cdot \nabla u_x \rangle = -\frac{1}{\rho}\frac{\partial P}{\partial x} + \nu \nabla^2 U_x \tag{A.10}$$

$$\frac{\partial U_r}{\partial t} + \tilde{U} \cdot \nabla U_r + \langle \tilde{u} \cdot \nabla u_r \rangle - \frac{U_\theta^2}{r} - \frac{\langle u_\theta^2 \rangle}{r} = -\frac{1}{\rho}\frac{\partial P}{\partial r} + \nu(\nabla^2 U_r - \frac{U_\theta}{r^2} - \frac{2\partial U_\theta}{r^2 \partial \theta}) \tag{A.11}$$

$$\frac{\partial U_\theta}{\partial t} + \tilde{U} \cdot \nabla U_\theta + \langle \tilde{u} \cdot \nabla u_\theta \rangle + \frac{U_r U_\theta}{r} + \frac{\langle u_r u_\theta \rangle}{r} = -\frac{1}{r\rho}\frac{\partial P}{\partial \theta} + \nu(\nabla^2 U_\theta + \frac{2\partial U_\theta}{r^2 \partial \theta} - \frac{U_\theta}{r^2}) \tag{A.12}$$

Due to azimuthal homogeneity all terms involving $\frac{\partial}{\partial \theta}$ drop out and no swirl causes all terms explicit in U_θ to be zero. Stationarity causes time derivatives of mean quantities to be zero.

Continuity eqns:

$$\frac{\partial U_x}{\partial x} + \frac{1}{r}\frac{\partial}{\partial r} r U_r = 0 \tag{A.13}$$

$$\frac{\partial u_x}{\partial x} + \frac{1}{r}\frac{\partial}{\partial r} r u_r + \frac{1}{r}\frac{\partial u_\theta}{\partial \theta} = 0 \tag{A.14}$$

Mean momentum conservation equations:

$$U_x \frac{\partial U_x}{\partial x} + U_r \frac{\partial U_x}{\partial r} + \langle \tilde{u} \cdot \nabla u_x \rangle = -\frac{1}{\rho}\frac{\partial P}{\partial x} + \nu \nabla^2 U_x \tag{A.15}$$

$$U_x \frac{\partial U_r}{\partial x} + U_r \frac{\partial U_r}{\partial r} + \langle \tilde{u} \cdot \nabla u_r \rangle - \frac{\langle u_\theta^2 \rangle}{r} = -\frac{1}{\rho}\frac{\partial P}{\partial r} + \nu \nabla^2 U_r \tag{A.16}$$

$$\langle \tilde{u} \cdot \nabla u_\theta \rangle + \frac{\langle u_r u_\theta \rangle}{r} = 0 \tag{A.17}$$

B. SPECTRAL ANALYSIS DERIVATIONS

B.1 Windowing

A spectral estimate for a finite sampling domain width (window) of an infinite domain signal corresponds to the convolution of the true infinite domain spectrum and the Fourier transform of the symmetric convolution of the window function with itself, i.e.,

(B.1)

This can be shown via the finite domain estimator: where and Thus

$$\hat{u}^{[L]}(k) = \frac{1}{2\pi}\int_0^L u(x)e^{-ikx}dx = \frac{1}{2\pi}\int_{-\infty}^{\infty} u(x)w_L(x)e^{-ikx}dx \tag{B.2}$$

While the infinite length window would generate the true spectrum as the Fourier transform of $B_{uu}(r)$, the statistical correlation function of a homogeneous signal u(x), according to equation 4.5, we can only estimate the spectrum based on a finite record length. Recalling the convolution theorem B.2 and its special case the correlation theorem B.2, the estimator 4.6 corresponds to:

$$\begin{aligned}
F_{uu}^L(k) &= \frac{2\pi}{L}\langle \hat{u}^L(k)^* \hat{u}^L(k)\rangle \\
&= \frac{2\pi}{L}\frac{1}{2\pi}\int_{-\infty}^{\infty}\int_{-\infty}^{\infty}\langle u(x)u(x+r)\rangle w_L(x)w_L(x+r)dxe^{-ikr}dr \\
&= \frac{2\pi}{L}\frac{1}{2\pi}\int_{-\infty}^{\infty} B_{uu}(r)\int_{-\infty}^{\infty} w_L(x)w_L(x+r)dxe^{-ikr}dr \\
&= \frac{2\pi}{L}\left[\frac{1}{2\pi}\int_{-\infty}^{\infty} B_{uu}(r)e^{-ik'r}dr \otimes \frac{1}{2\pi}\int_{-\infty}^{\infty} W_L(r)(r)e^{-ik'r}dr\right](k) \\
&= \frac{2\pi}{L}[F_{uu}(k') \otimes \hat{W}_L(k')](k) = \frac{2\pi}{L}[F_{uu}(k') * |\hat{w}_L(k')|^2](k)
\end{aligned} \tag{B.3}$$

where $W_L(r)$ is the auto-correlation of the window function $w_L(x)$. Note that this is *n*ot the same definition as of a correlation function of a stochastic variable. As an example, the auto-correlation of the rectangular unity window of length L is a unity peak triangular window of length $2L$. The rectangular

window has a Fourier transform of :

$$\hat{w}_L(k) = \frac{\sin(kL)}{kL} \tag{B.4}$$

Thus the standard sampling window will, when estimated with 4.6, generate a spectrum as

$$\begin{aligned} F_{uu}^L(k) &= \frac{1}{2\pi}\int_{-\infty}^{\infty} F_{uu}(k')\hat{W}_L(k-k')dk' \\ &= \frac{1}{2\pi}\int_{-\infty}^{\infty} F_{uu}(k')\left(\frac{sinL(k-k')}{L(k-k')}\right)^2 dk' \\ &= F_{uu}(k) \otimes \left(\frac{\sin(Lk)}{Lk}\right)^2 \end{aligned} \tag{B.5}$$

Due to the curvature variation of the correlation function, the net effect of the windowing will be to redistribute spectral energy from lower wavenumbers to higher wavenumbers, a process labeled 'spectral leakage'.

B.2 Spatial Filtering due to finite probe volume

As a probe length cannot be infinitely small, each probe approximates a point measurement of the local velocity by spatial integration over a length l_p. The spatial integration of the local process effectively discards the contributions from structures smaller than l_p (leaving less aliased energy to claim wrong wavelengths). Thus the probe integration can ameliorate the effect of spatial aliasing, which is why low-pass filters are called anti-aliasing filters. If the probe spacing was the same size as l_p the effect of aliasing would be minimal. Consider a 1D case. Let the random velocity signal to be sampled be $u(x)$, $x \in [-\infty, \infty]$. The velocity field is homogenous, so that the auto-correlation function, i.e. the expected value of any product of a realization $u(x)$ with the realization at a spatial separation r, is

$$B_{uu}(x, x+r) = \langle u(x)u(x+r)\rangle = B_{uu}(r) \tag{B.6}$$

The Fourier transform of the correlation function is :

$$F_{i,j}(k) = \frac{1}{2\pi}\int_{-\infty}^{\infty} drB_{uu}(r)e^{-ikr} \tag{B.7}$$

When sampling the field $u(x)$ with a finite sized probe in such a way as to obtain a local average of the velocity field one effectively performs a running

convolution with a spatial sampling window $w_l(x)$. The window is symmetric about $x = 0$ and non-zero only if $|x| \leq \frac{l}{2}$. Note that the window is normalized by it's own dimension in order to resemble the local average. Thus the sampled velocity is filtered as:

$$u^l(x) = \int_{-\infty}^{\infty} u(y)w_l(y-x)dy \tag{B.8}$$

$$= \int_{-\infty}^{\infty} u(y)w_l(x-y)dy \tag{B.9}$$

$$= [u(y) \otimes w_l(y)](x) \tag{B.10}$$

where the shift in variables between equations B.8 and B.9 is possible due to the mirror symmetry around $y - x = 0$ of the window.

The resulting filtered signal is of infinite extent and has a corresponding filtered expected correlation function $B^l_{uu}(r)$:

$$B^l_{uu}(x, x') = \langle u^l(x)^* u^l(x + r)\rangle = \langle [u \otimes w_l](x)[u \otimes w_l](x + r)\rangle \tag{B.11}$$

The convolution theorem states that if:

$$h(r) = g(x) \otimes f(x) = \int_{-\infty}^{\infty} g(x)f(r - x)dx \tag{B.12}$$

then

$$\hat{h}(k) = 2\pi\hat{g}(k)\hat{f}(k) \tag{B.13}$$

where $\hat{h}$ indicates the Fourier transform of h. A special case of B.2 is the correlation Theorem which states that if

$$h(r) = g(x) \odot f(x) = \int_{-\infty}^{\infty} g(x)f(x + r)dx \tag{B.14}$$

then

$$\hat{h}(k) = 2\pi\hat{g}(k)^*\hat{f}(k) \tag{B.15}$$

where $*$ indicates a complex conjugate. B.2 reduces to B.2 if f or g is symmetric in x.

Let the filtered velocity $u^l(x)$ be the inverse Fourier transform of $\hat{u}^l(k)$ so that

$$B^l_{uu}(x, x') = \left(\langle \int_{-\infty}^{\infty} \hat{u}^l(k)e^{+ikx}dk\right)^* \int_{-\infty}^{\infty} \hat{u}^l(k')e^{+ik'x'}dk'\rangle \tag{B.16}$$

$$= \int_{-\infty}^{\infty} dk \int_{-\infty}^{\infty} \hat{e}^{-ikx}e^{+ik'x'}\langle \hat{u}^l(k)^*\hat{u}^l(k')\rangle dk' \tag{B.17}$$

Since the filtered velocity is the result of a convolution in space, it's Fourier transform is the product of the individual functions transforms respectively, e.g.,

$$\hat{u}^l(k) = 2\pi\hat{u}(k)\hat{w}_l(k) \tag{B.18}$$

Inserted into B.17, it gives

$$B^l_{uu}(x,x') = (2\pi)^2 \int_{-\infty}^{\infty} dk \int_{-\infty}^{\infty} dk' \hat{e}^{-ikx} e^{+ik'x'} \hat{w}^*_l(k)\hat{w}_l(k')\langle \hat{u}^*(k)\hat{u}(k')\rangle \tag{B.19}$$

As the expected value of the product of Fourier transforms in non-overlapping wavenumber bands is zero, and equal to the power spectrum $\langle \hat{u}^*_i(k)\hat{u}_j(k')\rangle = F_{uu}(k)\delta(k'-k)$ in overlapping ones, the integral over dk' will eliminate all functional dependence on k' in the expression B.19, lest $k' = k$, resulting in:

$$B^l_{uu}(x,x') = (2\pi)^2 \int_{-\infty}^{\infty} F_{uu}(k)\hat{w}^*_l(k)\hat{w}_l(k)e^{+ik(x'-x)}dk \tag{B.20}$$

As $x' - x = r$, and invoking again the convolution theorem, we have:

$$\begin{aligned} B^l_{uu}(x,x+r) &= 2\pi \int_{-\infty}^{\infty} F_{uu}(k)e^{+ikr}dk \otimes \int_{-\infty}^{\infty} |\hat{w}_l(k)|^2 e^{+ikr}dk && \text{(B.21)} \\ &= B_{uu}(r) \otimes [w_l(x) \odot w_l(x)](r) && \text{(B.22)} \\ &= B_{uu}(r) \otimes W_l(r) && \text{(B.23)} \end{aligned}$$

where $W_l(r) = [w_l(x) \odot w_l(x)](r) = \int_{-\infty}^{\infty} w_l(x)w_l(x+r)dx$

The above yields a filtered spectrum that, again according to the convolution theorem, consists of the true spectrum multiplied in with the modulus squared of the filter window, i.e.,

$$F^l_{uu}(k) = 2\pi F_{uu}(k)\hat{W}_l(k) = (2\pi)^2 F_{uu}(k)|\hat{w}_l(k)|^2 \tag{B.24}$$

A rectangular probe window would be

$$w_l(x) = \begin{cases} 1/l & , \quad |x| \le l/2 \\ 0 & , \quad |x| > l/2 \end{cases} \tag{B.25}$$

$$\hat{w}_l(k) = \frac{1}{2\pi}\frac{sin(kl/2)}{kl/2} \tag{B.26}$$

and the velocity spectrum and correlation function obtained from it would be respectively

$$F_{uu}^{l}(k) = F_{uu}(k)\left[\frac{sin(kl/2)}{kl/2}\right]^2 \tag{B.27}$$

and

$$B_{uu}^{l}(r) = B_{uu}(r) \otimes [l - |r|/l]/l \tag{B.28}$$

Filtering model for isotropic turbulence sampled with 3D rectangular probe Isotropic turbulence is three-dimensionally homogenous turbulence that is also invariant of rotation. Since homogenous, the turbulence can be represented in the spectral domain as $F_{i,j}(\vec{k})$. From this three-dimensional tensor quantity one can extract the energy spectrum $E(k)$ by integrating out two of three spectral space coordinates. The variable $k = |\vec{k}|$ is a radial distance in a spherical polar coordinate system and at every value of k the values of the spectrum tensor trace are $F_{i,i}$ are integrated over the angles, i.e.,

$$E(k) = \frac{1}{2}\int_{-\pi}^{\pi} d\theta \int_{-\pi/2}^{\pi/2} F_{i,i}(\vec{k})k^2 d\psi \tag{B.29}$$

The integral of the energy spectrum is the average turbulence kinetic energy,

$$\int_0^{\infty} E(k)dk = \frac{1}{2}\langle q^2\rangle = \frac{1}{6}\langle(u_1^2 + u_2^2 + u_3^2)\rangle \tag{B.30}$$

Isotropy, together with incompressibility, enables the solving of $F_{i,j}(\vec{k})$ in terms of $E(k)$:

$$F_{i,j}(\vec{k}) = \frac{E(k)}{4\pi k^4}[k^2\delta_{ij} - k_i k_j] \tag{B.31}$$

Clearly, if a model for $E(k)$ was available, one could easily compute $F_{i,j}$. THe model that is utilized here is the von Karman/Howarth model, which is representative for the large scale turbulence and the spectral gap, but fails to decrease sufficiently fast enough with wavenumber to accurately predict the purely dissipative range of scales. George & Wang [25] models the von Karman/Howarth spectrum as

$$E(k) = C\frac{(kI)^4}{[1 + (kI/k_eI)^2]^{17/6}} \tag{B.32}$$

where I is the integral length scale of the turbulent flow, $C = 6.2528$ is a constant and $k_eI = 0.7468$ is non-dimensional wavenumber where the energy spectrum peaks. George & Wang list several choices for the set of parameters, the one choice here represents $p = 4$.

The modeled spectral tensor function scan be integrated over the three-dimensional spectral space to yield the average turbulence kinetic energy $\langle q^2\rangle$

or the space coordinate components. Changing the the variable k_i to $y_i = k_i I/k_e I$ gives:

$$\frac{1}{2}\langle q^2\rangle = \frac{(k_e I)^7}{I^3}\frac{C}{2\pi}\int\int\int d\vec{y}\frac{y^2}{[1+y^2]^{17/6}} \tag{B.33}$$

and

$$\langle u_1^2\rangle = \frac{(k_e I)^7}{I^3}\frac{C}{4\pi}\int\int\int d\vec{y}\frac{[y_2^2+y_3^2]}{[1+y^2]^{17/6}} \tag{B.34}$$

$$\langle u_2^2\rangle = \frac{(k_e I)^7}{I^3}\frac{C}{4\pi}\int\int\int d\vec{y}\frac{[y_1^2+y_3^2]}{[1+y^2]^{17/6}} \tag{B.35}$$

$$\langle u_3^2\rangle = \frac{(k_e I)^7}{I^3}\frac{C}{4\pi}\int\int\int d\vec{y}\frac{[y_1^2+y_2^2]}{[1+y^2]^{17/6}} \tag{B.36}$$

Introducing a finite probe window of dimensions l_1, l_2, l_3 in the three space dimensions gives:

$$\frac{1}{2}\langle q^2\rangle = \frac{(k_e I)^7}{I^3}\frac{C}{2\pi}\int\int\int d\vec{y}\frac{y^2}{[1+y^2]^{17/6}}sinc^2(y_1 d_1)sinc^2(y_2 d_2)sinc^2(y_3 d_3) \tag{B.37}$$

where $sinc(x) = sin(x)/x$ and $d_i = (k_e I)(l_i/2I)$. The components are. and

$$\langle u_1^2\rangle = \frac{(k_e I)^7}{I^3}\frac{C}{4\pi}\int\int\int d\vec{y}\frac{[y_2^2+y_3^2]}{[1+y^2]^{17/6}}sinc^2(y_1 d_1)sinc^2(y_2 d_2)sinc^2(y_3 d_3) \tag{B.38}$$

$$\langle u_2^2\rangle = \frac{(k_e I)^7}{I^3}\frac{C}{4\pi}\int\int\int d\vec{y}\frac{[y_1^2+y_3^2]}{[1+y^2]^{17/6}}sinc^2(y_1 d_1)sinc^2(y_2 d_2)sinc^2(y_3 d_3) \tag{B.39}$$

$$\langle u_3^2\rangle = \frac{(k_e I)^7}{I^3}\frac{C}{4\pi}\int\int\int d\vec{y}\frac{[y_1^2+y_2^2]}{[1+y^2]^{17/6}}sinc^2(y_1 d_1)sinc^2(y_2 d_2)sinc^2(y_3 d_3) \tag{B.40}$$

Thus any ratio of the filtered variances can be estimated for any value of the ratio between the filter dimensions l_i and the integral scale I by direct computation. From such an analysis it was found that in order resolve 88% of the available energy in each component, the probe window dimension must be a tenth of the integral scale, see also Wanstrom et al[42].

C. SINGLE POINT VERSUS "HOMOGENIZED" SPECTRA

What is the relation between the spectra one would measure at a single point, x, using Taylor's hypothesis, say $F^1_{i,j}(k_1(x), x)$, and the spectra we determine from our 'homogenized' jet, say $\Phi(\kappa)$? The connection between the two is the two-point correlation function,

$$B_{i,j}(x, x+r) = \langle u_i(x) u_j(x+r) \rangle. \tag{C.1}$$

Note that we have used on the streamwise coordinate and suppressed the other coordinates (at least for now). From the two-point similarity hypothesis,

$$\langle u_i(x) u_j(x+r) \rangle = U_c(x) U_c(x+r) \langle \upsilon_i(\xi) \upsilon_j(\xi + \Delta\xi) \rangle \tag{C.2}$$

where

$$\xi = \ln x/D, \tag{C.3}$$

$$\upsilon_i(\xi) = \frac{u_i(x)}{U_c(x)} \tag{C.4}$$

and $U_c(x)$ is the centerline velocity at x. Note that x should be taken to be the distance from some virtual origin x_o.

The single point spectrum really only makes sense if the flow is homogeneous, but we follow convention, ignore that and write anyway the inverse transform relation:

$$\langle u_i(x) u_j(x+r) \rangle = \int_{-\infty}^{\infty} e^{ik_1(x)r} F^{(1)}_{i,j}(k_1(x), x) dk_1 \tag{C.5}$$

For a truly homogeneous flow both sides would be independent of x.

Our transformed field is in fact homogeneous so we can write exactly:

$$\langle \upsilon_i(\xi) \upsilon_j(\xi + \Delta\xi) \rangle = \int_{-\infty}^{\infty} e^{i\kappa\Delta\xi} \Phi^{(1)}_{i,j}(\kappa) d\kappa \tag{C.6}$$

Multiplying equation C.6 by $U_c(x)U_c(x+r)$, expressing $\Delta\xi$ as a function of x and r, and equating equations C.5 and C.6 yields:

$$\int_{-\infty}^{\infty} e^{ik_1 r} F^{(1)}_{i,j}(k_1, x) dk_1 = \int_{-\infty}^{\infty} e^{i\kappa \ln(1+r/x)} \left[U_c(x) U_c(x+r) \right] \Phi^{(1)}_{i,j}(\kappa) d\kappa \tag{C.7}$$

The idea of 'local homogeneity' is that one only consider small values of spatial separation r, the exact definition of 'small' being in general rather vague. But in the current case it is possible to be quite precise and expand the exponential in equation C.7 for small values of the physical local relative separation r/x. First regroup the terms to obtain:

$$e^{i\kappa \ln(1+r/x)} \approx e^{i\kappa r/x} e^{i\kappa[\ln(1+r/x)-r/x]} \tag{C.8}$$

Then expand the second exponential to obtain to second order in r/x:

$$e^{i\kappa[\ln(1+r/x)-r/x]} \approx 1 + i\kappa(r/x)^2 + \dots \tag{C.9}$$

Similarly we can expand $U_c(x+r)$ about the point x to obtain:

$$U_c(x+r) \approx U_c(x) + \left[\frac{dU_c}{dx}\right|_x r + \frac{1}{2}\left[\frac{d^2U_c}{dx^2}\right|_x r^2 \tag{C.10}$$

where for reasons which hopefully will become obvious later we have kept the second term.

Combining both of the expansions above and substituting into equation C.7 and keeping only the leading terms in r/x yields:

$$\int_{-\infty}^{\infty} e^{ik_1 r} F_{i,j}^{(1)}(k_1, x) dk_1 \approx \int_{-\infty}^{\infty} e^{i(\kappa/x)r} \left[U_c^2(x)\Phi_{i,j}^{(1)}(\kappa)\right] d\kappa \tag{C.11}$$

Dividing and multiplying the RHS by x, regrouping and identifying $k_1 = \kappa/x$ yields immediately:

$$\int_{-\infty}^{\infty} e^{ik_1 r} F_{i,j}^{(1)}(k_1, x) dk_1 \approx \int_{-\infty}^{\infty} e^{ik_1 r} \left[xU_c^2(x)\Phi_{i,j}^{(1)}(k_1/x)\right] dk_1. \tag{C.12}$$

Comparing the two sides, it is obvious that our one-point one-dimensional local spectrum is related to the 'true' decomposition by:

$$F_{i,j}^{(1)}(k_1) \approx \left[xU_c^2(x)\right] \Phi_{i,j}^{(1)}(k_1/x) \tag{C.13}$$

Or alternatively, to a first approximation to our true homogenized spectrum is given by:

$$\Phi_{i,j}^{(1)}(\kappa) \approx \frac{1}{[xU_c^2(x)]} F_{i,j}^{(1)}(k_1 x) \tag{C.14}$$

The RHS is exactly the normalized form used by Gamard (2002), Gamard et al. (2004), and Frohnapfel (2003).

Note that it should be possible to evaluated the effect of the higher order of the local expansion by integration by parts. That way the effects of jet flow physical space inhomogeneity on the single point one-dimensional spectra can be investigated.

D. PROOF THAT FINITE DOMAIN SPECTRUM OF SIMILARITY SCALED UNCORRELATED NOISE IS WHITE

The noise on the local velocity measurements is absolute at some level independent of the position (if one disregards the fact that the two cameras are different). However, as the similarity scaling is applied to form $\upsilon_i(\xi) = u_i(x)/U_c(x)$, the noise level gets scaled up as $(x - x_o)$. The estimation of finite domain velocity spectral densities of the resulting homogeneous velocity plus an inhomogeneous noise is considered below. It should be noted that the reasoning applies to random noise of the round-off quantization type.

The *finite* domain Fourier transform in the logarithmically transformed coordinate system of the noise, $\nu^L(\xi)$, given by:

$$\begin{aligned} \hat{\nu}_L(\kappa) &= FT_L\{\nu(\xi)\} \\ &= \frac{1}{2\pi}\int_0^L e^{-i\kappa\xi}\nu(\xi)d\xi \end{aligned} \tag{D.1}$$

The noise, $\nu(\xi)$, relates to the original discretization error of the PIV in the following way:

$$\nu(\xi) = \frac{n(x)}{U_c(x)} \tag{D.2}$$

where $x = De^{\ln x/D}$ (i.e., $\xi = ln\ x/D$, D is the jet diameter, and $U_c(x)$ is the mean centerline velocity at the downstream location in physical space, x, which is assumed measured from a virtual origin. We know that the centerline velocity varies inversely with distance downstream from the virtual origin; i.e.,

$$U_c = BM_o^{1/2}x^{-1} \tag{D.3}$$

where B is a constant (about 6.5 from Hussein et al. 1994) and M_o is the rate at which kinematic momentum is added at the source. For a top-hat jet, $M_o = \pi U_o^2 D^2/4$.

We also know that the noise itself is *homogenous in physical space* and *uncorrelated from one location to another*; i.e.,

$$\langle n(x)n(x')\rangle = C_n(x'-x) = \langle n^2\rangle \Delta\, x\delta(x'-x) \tag{D.4}$$

where L is a length scale providing the necessary dimensions to the delta function (Note that we will not need it later when we move to dimensionless coordinates).

The mean square value of the noise is given by $\langle n^2\rangle = \Delta^2/12$ where Δ is the quantization level which is assumed x-independent. It follows immediately that the mean square value of ν is:

$$\begin{aligned}\langle \nu^2\rangle &= \frac{\Delta^2}{12U_c^2} \\ &= \left[\frac{\Delta^2}{12}\right]\left[\frac{x^2}{B^2M_o}\right] \\ &= \left[\frac{\Delta^2}{12}\right]\left[\frac{D^2}{B^2M_o}\right]e^{2\xi}\end{aligned} \tag{D.5}$$

We can put all of this together and express the noise correlation directly in the transformed coordinate system as:

$$\langle \nu(\xi)\nu(\xi')\rangle = \left[\frac{\Delta^2}{12}\right]\left[\frac{D^2}{B^2M_o^2}\right]e^{2\xi}\ \Delta\xi\ \delta(\xi'-\xi) \tag{D.6}$$

Note that the noise is *not* homogeneous in the transformed coordinate system (because of the presence of the exponential which depends on ξ.

D.1 The finite spectrum of the transformed noise

The spectrum computed from the finite Fourier transform (the finite spectrum) is given by:

$$
\begin{aligned}
F_{\nu L}(\kappa) &= \frac{2\pi}{L}\langle\hat{\nu}_L(\kappa)\hat{\nu}_L(\kappa)\rangle \\
&= \left[\frac{\Delta^2}{12}\right]\left[\frac{D^2}{B^2M_o^2}\right]\left[\frac{1}{2\pi L}\right]\int\int_0^L e^{-i\kappa(\xi'-\xi)}e^{(\xi+\xi')}\Delta\xi\delta(\xi'-\xi)d\xi d\xi' \\
&= \left[\frac{\Delta^2}{12}\right]\left[\frac{D^2}{B^2M_o^2}\right]\left[\frac{\Delta\xi}{2\pi L}\right]\int_0^L e^{2\xi}d\xi \\
&= \left[\frac{\Delta^2}{12}\right]\left[\frac{D^2}{B^2M_o^2}\right]\left[\frac{\Delta\xi}{2\pi L}\right]\left\{\frac{1}{2}[e^L-1]\right\} \qquad \text{(D.7)}
\end{aligned}
$$

The noise is clearly independent of wavenumber, so is indeed white. BUT it also clearly depends on the size of the domain, clearly a consequence of the fact that it is not homogenous (and consistent with the infinite domain analysis).

E. THE 'DROPOUT' PROBLEM

This section[1] looks at the problem of '*dropout*' caused by the generation of spurious vectors for whatever reason, usually poor signal quality. There has been much written about how to detect and replace the missing information. Here our interest is only the single and two-point statistics. We begin by creating a mathematical model for the actual snapshot the PIV produces. Let $\tilde{u}_i(\vec{x},t)$ represent the actual instantaneous velocity vector at any point $\vec{x}$ in the flow at the time of the snapshot t. Following George and Lumley [88] (see also Buchhave et al. [51]) we define a random function $\tilde{g}(\vec{x},t)$ which 'locates' the spurious vectors. The statistical properties of $\tilde{g}$ will be discussed below, but it is perhaps helpful for the moment to think of it as a classical delta-function $\delta(\vec{x}-\vec{x}_o)$ which simply locates the spurious vectors at $\vec{x}_o$ and turns on when integrated over. At these locations the actual velocity is not available, but instead another random variable, say $\tilde{a}_i(\vec{x},t)$, has been substituted for it. Using these the instantaneous velocity field available from the PIV can be written as:

$$\tilde{v}_i(\vec{x},t) = \tilde{u}_i(\vec{x},t) + \tilde{g}_i(\vec{x},t)\left[-\tilde{u}_i(\vec{x},t) + \tilde{a}_i(\vec{x},t)\right] \tag{E.1}$$

We can now treat $v_i(\vec{x},t)$ as a continuous random function of space and time, as long as we recognize that it must be treated as a generalized function.

E.1 The velocity statistics

Of particular interest herein are the statistical properties of the $\tilde{v}_i$, and their relation to those of $\tilde{u}_i$. For example, consider the mean value, $V_i(\vec{x},t) = \langle\tilde{v}_i(\vec{x},t)\rangle$. What is its relation to the same statistics property of the original velocity field, $U_i(\vec{x},t) = \langle\tilde{u}_i\rangle$? The symbols $\langle\rangle$ imply an ensemble average, which in principle demands an infinite number of statistically independent realizations.

In general, the averages are dependent on both time and space. But in practice this will be usually performed (at least for statistically stationary

[1] This appendix and the one following it were taken from [72] with only slight modifications.

flows) by averaging over snapshots (or realizations) which are separated by more than two integral time scales. For such situations, the averages are time-independent, so we will drop the implicit dependence of the statistics on time, and keep only the space dependence.

Since almost all flows of interest are turbulent, the properties of the fluctuating velocity, $v_i(\vec{x},t)\tilde{v}_i(\vec{x},t) - V_i(\vec{x})$ and its counterpart in the original field $u_i(\vec{x},t) = \tilde{u}_i(\vec{x},t) - U_i(\vec{x})$ are also of interest. Of primary interest below is the two-point (single time) correlation, $W_{ij}(\vec{x},\vec{x}') = \langle v_i(\vec{x},t)v_j(\vec{x}',t)\rangle$ and its counterpart $R_{ij} = \langle u_i(\vec{x},t)u_j(\vec{x}',t)\rangle$.

E.2 Statistics of the g's

Before averaging of any kind we must agree on whether the location of the spurious vector and the original velocity field are statistically independent. We assume in all subsequent analysis that they are. We further assume that the occurrence and locations of the spurious vector are statistically independent of each other. The mean value of $\tilde{g}$ is then given by:

$$\langle \tilde{g} \rangle = \mu(\vec{x}), \tag{E.2}$$

where in general the expected number of spurious vectors can be location-dependent. If the field is statistically stationary in time, $\mu(\vec{x})$ can be computed by counting the relative number of snapshots in which spurious vectors occur. Note there is no reason to assume at this point that μ is location independent.

We have assumed occurrences of spurious vectors to be at least uncorrelated from one interrogation volume to the next, and from snapshot to snapshot. It follows immediately that (c.f. George and Lumley [88] that the two-point correlation of the fluctuations of the g's is given by:

$$\langle g(\vec{x},t)g(\vec{x}',t)\rangle = \mu(\vec{x})\delta(\vec{x}' - \vec{x}) \tag{E.3}$$

or

$$\langle \tilde{g}(\vec{x},t)\tilde{g}(\vec{x}',t)\rangle\mu(\vec{x})\mu(\vec{x'}) + \mu(\vec{x})\delta(\vec{x}' - \vec{x}) \tag{E.4}$$

E.3 The mean velocity

Using these the mean value of the snapshot velocities is given by:

$$V_i(\vec{x}) = \langle u_i(\vec{x},t)\rangle[1-\langle\tilde{g}(\vec{x},t)\rangle] + \langle\tilde{g}(\vec{x},t)\rangle\langle\tilde{a}_i\rangle \quad \text{(E.5)}$$

$$= U_i(\vec{x})[1-\mu(\vec{x})] + \mu(\vec{x})A_i(\vec{x}) \quad \text{(E.6)}$$

where $A_i(\vec{x}) \equiv \langle\tilde{a_i}(\vec{x},t)\rangle$.

Equation E.6 suggests two alternative strategies which could have achieved the same end.

- The first requires replacing the spurious vectors by the *mean* value at that location, since clearly if $A_i = U_i$, then the net effect is zero, regardless of the number of bad vectors (i.e., the value of μ). The problem with this is that the mean value is not known *a priori*, *and its determination is the reason for the measurement in the first place*.
- A second strategy is to replace the spurious vectors by simply setting them equal to zero, then correcting the measured mean by dividing it by the factor $[1-\mu(\vec{x})]$. In many situations the estimate of the average is computed by simply summing the different realizations (from snapshot to snapshot) and then dividing by the number of them; i.e.

$$AVG_N = \frac{1}{N}\sum_{n=1}^{N}(realiztion)_n \quad \text{(E.7)}$$

  where N is the number of snapshots. Thus this zero-replacement alternative can be implemented by simply replacing the N in the denominator by the number of non-zero realizations, say $N - N_o(\vec{x})$ where $N_o(\vec{x})$ is the number zeroed for each x-position. This also allows a simple determination of $\mu(\vec{x}) = N_o(\vec{x})/N$ as the fraction of discarded data for each x-position. This will be seen below to be quite important for determination of the two-point and higher order single-point statistics.

E.4 The two-point correlations

In turbulent flows, the single point correlations (like intensities and Reynolds stress) are of course of considerable interest. But they are a special case of the two-point correlations that not only contain information on them, but also on the various scales of motion and the spatial coherence of the field. These are of particular interest herein, since the POD-based algorithms below depend on them.

The instantaneous fluctuating velocity available to the PIV can be obtained by subtracting equation E.6 from equation E.1. Multiplying the fluctuating velocity at one location, $\vec{x}'$, by that at another, $\vec{x}$, and averaging yields the two-point, single time velocity correlation tensor as:

$$\langle v_i(\vec{x},t)v_j(\vec{x}',t)\rangle = \langle u_i(\vec{x},t)u_j(\vec{x},t)\rangle[(1-\mu(\vec{x}))^2 + \mu(\vec{x})\delta(\vec{x}'-\vec{x})] \quad \text{(E.8)}$$

$$+\mu(\vec{x})U_i(\vec{x},t)U_j(\vec{x}',t)\delta(\vec{x}'-\vec{x}) + \mu(\vec{x})A_i(\vec{x},t)A_j(\vec{x}',t)\delta(\vec{x}'-\vec{x}) \quad \text{(E.9)}$$

$$-\mu(\vec{x})A_i(\vec{x},t)U_j(\vec{x}',t)\delta(\vec{x}'-\vec{x}) - \mu(\vec{x})U_i(\vec{x},t)A_j(\vec{x}',t)\delta(\vec{x}'-\vec{x}) \quad \text{(E.10)}$$

$$+\mu(\vec{x})\langle a_i(\vec{x},t)a_j(\vec{x}',t)\rangle[\mu(\vec{x}) + \delta(\vec{x}'-\vec{x})] \quad \text{(E.11)}$$

$$+\langle u_i(\vec{x},t)a_j(\vec{x}',t)\rangle\mu(\vec{x})[1-\mu(\vec{x}) + \mu(\vec{x})\delta(\vec{x}'-\vec{x})] \quad \text{(E.12)}$$

$$+\langle a_i(\vec{x},t)u_j(\vec{x}',t)\rangle\mu(\vec{x})[1-\mu(\vec{x}) + \mu(\vec{x})\delta(\vec{x}'-\vec{x})] \quad \text{(E.13)}$$

It is easy to show that this reduces to just $\langle u_i(\vec{x},t)u_j(\vec{x},t)\rangle$ if either there are no bad vectors, or if the replacement is exactly equal to the true velocity. It is immediately clear what the primary problem is: All of the mismatch between the true velocity and the measured field shows up at zero displacement; i.e., $\vec{x} = \vec{x}'$. The delta functions have important implications for both spatial spectral analysis and application of the POD. In particular, they imply that all of the errors show up in the means, the turbulence intensities, or the diagonal elements of the cross-correlation tensor. The mean velocities can, in principle, be fixed by setting the replacement vectors to zero and correcting for the number of samples used, $(1-\mu)$. Unfortunately the contributions to the standard deviations of this strategy will drown the actual turbulence. So to the cost of a small reduction in spatial resolution (being equivalent to spatial filtering), one may interpolate to compensate for an invalid data point. It seems evident that replacement by neighboring data points is the way to proceed. However, if, more than one vector is missing from a neighborhood, the reliability of the interpolated value could decrease drastically.